Laser-generated, plane-wave, broadband ultrasound sources for metrology

Srinath Rajagopal

A dissertation submitted in partial fulfilment
of the requirements for the degree of
Doctor of Philosophy
of
University College London.

Department of Medical Physics and Biomedical Engineering
University College London

September 24, 2019

I, Srinath Rajagopal, confirm that the work presented in this thesis is my own. Where information has been derived from other sources, I confirm that this has been indicated in the work.

Abstract

The accurate quantification of ultrasound fields generated by diagnostic and therapeutic transducers is critical for patient safety. This requires hydrophones calibrated to a traceable national measurement standard over the full range of frequencies used. At present, the upper calibration frequency range available to the user community is limited to a frequency of 60 MHz. However, there is often content at frequencies higher than this, e.g., through nonlinear propagation of high-amplitude pulses or tone-bursts for therapeutic applications, and the increasing use of higher frequencies in diagnostic imaging. To reduce the uncertainties and extend the calibrations to higher frequencies, a source of high-pressure, plane-wave and broadband ultrasound fields is required. This is not possible with current piezoelectric transducer technology, therefore laser-generated ultrasound is investigated as an alternative. This consists of an ultrasound wave generated by the pulsed laser excitation of a thin, planar, layer of light absorbing carbon-polymer nanocomposite materials. The work described in this thesis can be divided into three parts. The first part consisted of the fabrication of various nanocomposites in order to study the effect of different polymer types, composite thickness, laser fluence, and concentration of carbon nanotubes, on the ultrasound generated, as well as their stability. This included an investigation into the nonlinear propagation of MPa range laser-generated ultrasound, and the effect of the bandlimited hydrophone response, using a numerical wave solver (k-Wave). In the second part, the effects on the signal of acoustically reflective and matched backings (the substrates onto which the nanocomposite was coated) were studied. It was found experimentally that the backing material can significantly affect the pressure amplitude when the duration of the laser pulse is longer than the acoustic transit time across the thin nanocomposite layer. An analytical model was developed to describe how the signal generated depends on the backing material, absorbing layer thickness, and laser pulse duration. The model agreed well with measurements performed with a variable pulse duration fibre-laser. Finally, in the third part, a laser-generated, plane-wave, broadband ultrasound source device superficially resembling a standard piezoelectric piston source was designed, fabricated, and tested. The source produced quasi-unipolar pressure-pulse of 9 MPa peak-positive pressure with a bandwidth of 100 MHz, and the ultrasound beam is sufficiently planar to reduce uncertainties due to diffraction to negligible levels for hydrophones up to 0.6 mm in diameter.

Impact Statement

In this thesis, a laser-generated, plane-wave, broadband ultrasound source device has been developed, which will be used to calibrate medical hydrophones at the National Physical Laboratory – the National Measurement Institute of U.K. The laser-generated ultrasound source has been developed with the aim to overcome the shortcomings of piezoelectric transducers, and thereby expand hydrophone calibrations beyond the current upper limit of 60 MHz to as high as 100 MHz. First, at the highest level, the impact of this research on end users of hydrophones such as medical device manufacturers and academic researchers, will be the availability of accurate calibrations to higher frequencies. Diagnostic imaging device manufacturers, especially those operating with a centre frequency in the 40–70 MHz range, have been demanding access to calibration frequencies up to 100 MHz and beyond. The availability of higher calibration frequencies will allow these manufacturers to assess the performance and safety of their devices more accurately. Secondly, when performing hydrophone calibration, the uncertainty due to spatial averaging errors is one of the highest contributions in the uncertainty budget, currently 7% at 60 MHz in a focused field. In a laser-generated ultrasound beam the error is less than 1% at all frequencies. Therefore, it is estimated that the overall calibration uncertainty will reduce from 15% (expressed at 95% coverage probability) at 60 MHz to 10%. The reduced uncertainty may benefit the medical device manufacturers in the following way. Manufacturers of diagnostic ultrasound imaging devices must limit the acoustic output power to within the specified safe limits by considering the upper uncertainty bound of the hydrophone calibration data. If the uncertainty on the hydrophone calibration is reduced, then this will allow the manufacturers to use higher acoustic powers leading to improved image quality while still operating within the safe limits.

Historically, researchers working on carbon-polymer type nanocomposites have been predominantly focused on increasing the concentration of nanocomposites in the polymer to maximise light absorption. With everything else held constant, this leads to increased acoustic pressure. However, through nonlinear propagation, this pressure-pulse can steepen over a relatively short propagation distance of 1 mm. The experimental observations on this described in this thesis were confirmed with simulations using a numerical model.

The other effect of increased optical absorption is that the depth of light penetration decreases and consequently the duration of the laser pulse must also decrease to ensure the stress confinement time is satisfied i.e., the acoustic transit time across the optical absorption depth must be greater than the laser pulse duration. It was found experimentally that when the duration of the laser pulse is

longer than the stress confinement time, there is a significant increase in the ultrasound pressure from a nanocomposite source backed on an acoustically hard material relative to a source backed on an acoustically matched material. The experiments carried out using various laser pulses, which spanned from stress confined to unconfined durations was also validated with an analytical, and numerical models. The above two effects have not been studied before and it is expected that future researchers working on laser ultrasound from nanocomposites are likely to consider the consequence of increased optical absorption and source backing material in their intended application of the nanocomposites.

Acknowledgements

First and foremost, I would like to sincerely thank my principal supervisor Ben Cox for his continual support throughout my PhD. His passion for continuous learning, patience, unbiased and inquisitive nature was truly inspiring, and it kept me on my toes over the last five years. I am also grateful for his many supervisory visits he made to my place of work, the National Physical Laboratory (NPL).

I am indebted to my former colleague, Toby Sainsbury of Materials group at NPL who trained me on the preparation of nanocomposites and provided unfettered access to his lab. Without such freedom this work would have been far more difficult to complete. I also thank the former group leader, Tamaryn Shean for facilitating a meeting with Toby.

I would also like to thank my second supervisor Bradley Treeby for helpful discussions and his continual support throughout my PhD.

I would also like to sincerely thank Bajram Zeqiri, science leader of Ultrasound and Underwater Acoustics (UUA) group at NPL, who supported my wish and sought the necessary approvals to take up the doctoral studies with UCL.

I am thankful to former UUA operational group leaders Susan Dowson, Pete Theobald, Stuart Kitney, and current group leader Alice Harling for allowing me to flexibly manage both work and the PhD. I am also thankful to Ian Severn, head of capability at NPL for his enthusiastic support and approval for starting my PhD.

My deepest gratitude to Geoff Stammers, head of Engineering Services and Michael Parfitt, Keith Burgon and Paul Stevens who always accommodated my many requests to make parts for the experimental setup at short notice, and for their help in refining my source design and its fabrication.

I am thankful to Thomas Allen of UCL's Photoacoustic Imaging Group for his help with setting up the experiment to investigate the effect of source backing using his variable pulse duration fibre-laser.

I am also thankful to my colleagues at NPL, Chris Fury for his help with LabVIEW programs for controlling the motorised stages for the automated field scanning software, Piero Miloro for providing the hydrophones and their calibrations, Christian Baker for hydrophone directivity measurements, Mark Hodnett for writing the reference letter for my PhD application, Stephen Robinson for discussion on acousto-optic corrections, Maria Lodeiro and Tony Maxwell of the Materials group for optical thickness measurements of the nanocomposites.

I am also thankful to Andrew Hurrell, my former colleague, and a friend and Paul Morris of Precision Acoustics Ltd, who provided the source code of their Ultrasound Measurement System software to help setup the automated scanning system.

I also thank members of the UCL's Photoacoustic Imaging Group Adrien Desjardins, Sacha Noimark, Erwin Alles and Richard Colchester for useful discussions on nanocomposite preparation at the beginning of my PhD.

The UK Department for Business, Energy & Industrial Strategy's funding of the National Measurement System is gratefully acknowledged through which this PhD was funded.

Finally, my family, my mother who has always encouraged my educational pursuits and has been a source of inspiration throughout my life. My late father would have been immensely proud to see both me and my sister for the lives we have made for ourselves. I am also thankful and indebted to my sister and brother-in-law for the love and care they have given me over the years. I am also lucky to have the love and affection of my little nephew, having been inspired by my work wants to become a Marine biologist!

Contents

List of Figures

List of Tables

Abbreviations

LGUS	Laser-generated Ultrasound
CNT	Carbon Nanotubes
MWCNT	Multi-walled Carbon Nanotubes
rGO	Reduced Graphene Oxide
CT	Computed Tomography
MR	Magnetic Resonance
NM	Nuclear Medicine
HIFU	High Intensity Focused Ultrasound
PVDF	Polyvinylidene Difluoride
NPL	National Physical Laboratory
PAL	Precision Acoustics Ltd
DC	Direct Current
ITF	Interferometer Transfer Function
FP	Fabry–Pérot
FPI	Fabry–Pérot Interferometer
IEC	International Electrotechnical Commission
NMI	National Measurement Institute
SI	Système International or International System of Units
INMETRO	National Institute of Metrology, Quality and Technology
PTB	Physikalisch-Technische Bundesanstalt
NIM	National Institute of Metrology China
NMIJ	National Metrology Institute of Japan
PBS	Polarising Beam Splitter
BS	Beam Splitter
PD	Photodetectors
BC	Bragg Cell
Vis–NIR	Visible to Near Infrared
NDT	Non-destructive Testing
SAW	Surface Acoustic Waves

CHOT	Cheap Optical Transducer
g-CHOT	Generated Cheap Optical Transducer
d-CHOT	Detected Cheap Optical Transducer
CMUT	Capacitive Micro-machined Ultrasound Transducer
CB	Carbon Black
CSNP	Candle Soot Nanoparticles
SPR	Surface Plasmon Resonance
CNF	Carbon Nanofibers
PDMS	Polydimethylsiloxane
PU	Polyurethane
CVD	Chemical Vapour Deposition
CPN	Carbon-polymer Nanocomposite
PRR	Pulse Repetition Rate
ODI	Optical Diffuser
PMMA	Polymethyl Methacrylate
PCX	Plano-convex Lens
PCV	Plano-concave Lens
BW6	–6 dB Bandwidth
PML	Perfectly Matched Layer
FDTD	Finite-difference Time-domain
PSTD	Pseudospectral Time-domain
FD	Finite-difference
FFT	Fast/discrete Fourier Transform
CFL	Courant-Friedrichs-Lewy
PPW	Points per Wavelength
PPP	Points per Period
IPD	Initial Pressure Distribution
SNR	Signal-to-Noise Ratio
FWHM	Full-width at Half-maximum
EM	Electromagnetic
UCL	University College London
Nd:YAG	Neodymium-doped Yttrium Aluminium Garnet

List of Symbols

Quantity	Meaning	Units
μ_a	Optical absorption coefficient	m^{-1}
μ_s	Optical scattering coefficient	m^{-1}
Φ	Laser fluence	$\mathrm{J\ m}^{-2}$
H	Absorbed laser energy density	$\mathrm{J\ m}^{-3}$
$\mathcal{H}$	Absorbed laser power density	$\mathrm{W\ m}^{-3}$
Γ	Grüneisen parameter	—
₹	Laser-generated ultrasound conversion efficiency. The sign used here is the currency symbol for the Indian rupee.	—
β_v	Volume thermal expansion coefficient	K^{-1}
β_L	Linear thermal expansion coefficient	K^{-1}
c_0	Isentropic sound-speed	$\mathrm{m\ s}^{-1}$
C_p	Isobaric heat capacity	$\mathrm{J\ kg}^{-1}\ \mathrm{K}^{-1}$
C_v	Isochoric heat capacity	$\mathrm{J\ kg}^{-1}\ \mathrm{K}^{-1}$
k_T	Isothermal compressibility	$\mathrm{m}^2\ \mathrm{N}^{-1}$ or Pa^{-1}
κ_{th}	Thermal conductivity	$\mathrm{W\ m}^{-1}\ \mathrm{K}^{-1}$
α_{th}	Thermal diffusivity	$m^2\ s^{-1}$
t_p or τ	Full-width at half-maximum duration of laser pulse	s
τ_{th}	Thermal relaxation time	s
τ_{ac}	Acoustic relaxation time	s
ρ_0	Mass density	$\mathrm{kg\ m}^{-3}$
ρ	Acoustic mass density	$\mathrm{kg\ m}^{-3}$
B_s	Isentropic bulk modulus	Pa
$\underline{n}$	Complex refractive index	—
η	Photoacoustic conversion efficiency	—
E_{aco}	Acoustic energy	J
E_{opt}	Optical energy	J
$\underline{M_c}$	End-of-cable open-circuit complex sensitivity	$\mathrm{V\ Pa}^{-1}$

$\underline{M_L}$	End-of-cable loaded complex sensitivity	$\mathrm{V\ Pa^{-1}}$
U_L	End-of-cable loaded voltage	V
$\mathcal{F}$	Fourier transform	—
$\mathcal{F}^{-1}$	Inverse Fourier transform	—
f	Frequency	Hz
P_0	Ultrasonic power at the face of the transducer	W
P_z	Ultrasonic power measured at a distance z from the face of the transducer	W
α_{ac}	Frequency-dependent acoustic amplitude absorption coefficient of plane waves	$\mathrm{Np\ m^{-1}}$
λ_0	Laser wavelength	m
a_{eff}	Effective radius of the hydrophone	m
p	Acoustic pressure	Pa
p_+	Peak-positive acoustic pressure	Pa
$\mathbf{u}$	Particle velocity	$\mathrm{m\ s^{-1}}$
$\mathbf{d}$	Particle displacement	m
$\mathbf{k}$	Wavevector	$\mathrm{m^{-1}}$
k	Scalar wavenumber	$\mathrm{rad\ m^{-1}}$
$\hat{\kappa}_t$	First-order *k*-space operator	—
$\hat{\kappa}_{tt}$	Second-order *k*-space operator	—
Δt	Time-step	s
Δx, Δy, Δz	Grid spacing	m
B/A	Acoustic nonlinearity parameter of the medium	—
L	Linear integro-differential operator	—
N_x	Number of grid points	—

Chapter 1

Introduction

1.1 Motivation

Over the past five decades, ultrasound imaging has transformed itself into an essential diagnostic capability in our health care system. Globally, as many as 250 million scans are performed annually, which is more than X-ray computed tomography (CT), magnetic resonance (MR) imaging and nuclear medicine (NM) imaging combined [1]. This popularity is due to its unprecedented safety record, which is due to the non-ionising nature of ultrasound, and also because the devices are portable, economic to procure and operate, and provide images in real-time with finer spatial resolution than CT, MR or NM [1]. More recently, the clinically accepted use of *therapeutic* ultrasound has grown initially from applying it as an adjunct form of physiotherapy [2] in the treatment of soft tissue injuries to more advanced applications by using high intensity focused ultrasound (HIFU) to ablate localised prostate tumours [3]. As research into clinical applications of ultrasound continues to expand [4]–[7], the use of high-frequency ultrasound, particularly beyond 40 MHz, is increasing in areas such as ophthalmology, dermatology, paediatrics, and peripheral vascular imaging [8]–[11]. Also, the low frequency (< 10 MHz) and high amplitude (tens of MPa) ultrasound waves used in ablative therapies and lithotripsy propagate nonlinearly in water, generating harmonic frequency components up to 100 MHz and beyond [12].

Accurate characterisation of ultrasound fields is vital for patient safety due to the damaging thermal and mechanical bioeffects that can occur under certain conditions [13]. In HIFU, intense acoustic energy is deposited at the focus, which is located inside the tissue. The harmonic frequencies generated at the focus are rapidly attenuated resulting in localised heating. In *diagnostic* applications, prolonged exposure of low intensity ultrasound fields during Doppler blood flow measurements, for example may cause the temperature to elevate, which is undesirable. When driven at sufficient pressures, the microbubble contrast agents used for enhancing image quality may undergo inertial cavitation and the rapid collapse of the microbubble can erode the nearby tissue surface and lead to internal bleeding. Therefore, in order to ensure the effectiveness of the applied ultrasound field in its intended application it is important to measure its characteristics so that one can predict all the

possible bioeffects. This requires hydrophones calibrated to a traceable standard and currently the upper calibration frequency range available to the user community is limited to a frequency of 60 MHz [14]. Therefore, a need has arisen for end-users, such as medical device manufacturers and academic researchers, to have access to calibration data as high as 100 MHz. This will facilitate the accurate characterization required for patient safety [15], performance validation and compliance [16], [17], and the development of new high-frequency ultrasound technologies [18], [19].

Miniature hydrophones manufactured using the piezoelectric polymer polyvinylidene difluoride (PVDF) are the standard devices used in the characterisation of fields generated by medical ultrasound equipment [20]. Recently, robust hydrophones based on PVDF and Fabry–Pérot ultrasound sensors have been developed for the characterization of the high intensity fields used in therapeutic ultrasound [21]–[23]. For quantitatively accurate field characterisation, these devices need to be calibrated over as wide a range of frequencies present in the fields being measured. At present, the highest calibration frequency available from the National Physical Laboratory (NPL), UK, is limited to 60 MHz [14], [24]. The frequency limit is mainly imposed by the calibration technique currently employed, which is based on measuring the displacement of an acoustically transparent and optically reflective pellicle in an ultrasound field using an interferometer. The ultrasound displacements become progressively small with frequency – nanometre range to picometer range – for a constant acoustic pressure. The pressures can be increased by using a highly focused transducer, however, the errors due to hydrophone spatial averaging grow since the spectral beam-widths decrease with frequency [25]. The uncertainty in the calibration of a 0.5 mm diameter active element hydrophone in a moderately focused field on NPL's displacement interferometer is 25% at 60 MHz. Beyond 60 MHz, the uncertainties are currently too large for the calibration to be practically useful.

In this thesis, the use of laser-generated ultrasound for the calibration of hydrophones is examined. This introductory chapter describes the types of hydrophone that are available, the state-of-the-art in hydrophone calibration, and the challenges that need to be overcome in order to extend the current frequency limit to 100 MHz and beyond. Chapter 2 provides an overview of laser-generated ultrasound, governing equations, and findings from the literature review relevant to the present study. Chapter 3 and 4 describe the fabrication and testing of initial laser-generated ultrasound sources. In Chapter 5, the effect of the source backing material on laser generated ultrasound is examined. Chapter 6 describes the design and testing of the final source, assessment of temporal stability, measurement repeatability and hydrophone spatial averaging, and challenges that still remain. Overall summary and future work are discussed in Chapter 7.

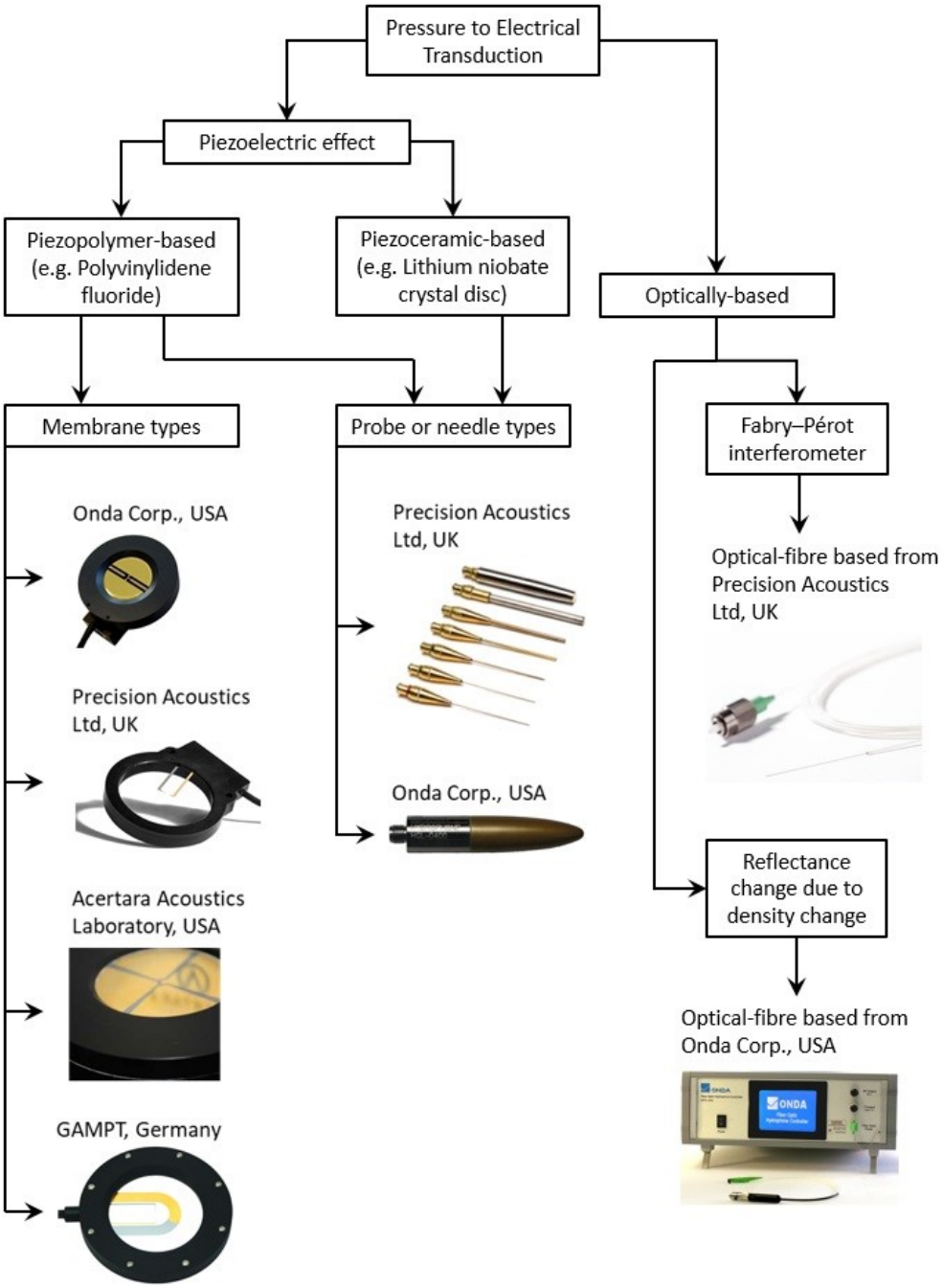

Figure 1-1: A broad classification of hydrophones based on their pressure to electrical transduction mechanism. The hydrophones identified in this figure are only a selection from commercial hydrophone manufacturers and does not necessarily represent every hydrophone available commercially or those used as research hydrophones.

1.1.1 Hydrophones

A classification of the different types of hydrophones currently available, based on their pressure to electrical transduction mechanism, is schematically shown in Figure 1-1. Irrespective of the hydrophone's transduction mechanism, its sensitivity (both magnitude and phase) is dependent on the acoustic frequency and angle of the incident wave relative to the transducer face. In practice, only the frequency response to a wave at normal incidence is usually reported. A brief description of widely-used hydrophone types are discussed in the subsequent sections.

1.1.1.1 Membrane Hydrophones

Membrane hydrophones are constructed from a thin sheet of unpoled polyvinylidene fluoride (PVDF) film in the thickness range of 9 μm to 25 μm. The film is stretched over an annular ring and then metal electrodes are deposited on either side of the film using a vacuum deposition method. A chromium layer is first deposited followed by gold since gold does not adhere well to the PVDF surface. Each metal layer is around 50 nm thick. A small overlapping electrode region defines the sensitive or active element shape, which is permanently polarised by the application of a high direct current (DC) electric field in an elevated temperature environment such as an oven, which is a few tens of degrees above the standard laboratory temperature. Upon cooling the PVDF, the polarisation freezes within the electrode area leaving the material both piezoelectric and pyroelectric [26]. This fabrication technique is commonly referred to as spot-poled design. The active element shape of membrane hydrophones are available in circular and square geometry. The standard circular element diameters are 0.2, 0.4 and 0.5 mm and for the square element, the standard side dimensions are 0.2 and 0.5 mm.

Membrane hydrophones fabricated from a single sheet of PVDF film are known as coplanar hydrophones. Membrane hydrophones can also be fabricated such that the active electrode is laminated between two PVDF sheets. During poling both sheets of PVDF become polarised thereby increasing the sensitivity of the hydrophone because the two sheets are configured electrically in parallel. These two-layer hydrophones are known as bilaminar hydrophones and were previously available from GEC Marconi Research Ltd. All modern hydrophones are based on coplanar design. The normal incidence frequency response of a hydrophone is determined by its thickness mode resonance given by $f_{pvdf} = c_{pvdf}/2d_{pvdf}$, where c_{pvdf} is the sound-speed of PVDF, which is 2300 m s^{-1} [27], d_{pvdf} is the thickness of the film(s) and f_{pvdf} is the resonance frequency. The frequency response varies smoothly with frequency and increases as it approaches the resonance frequency and then again decreases (see the responses of Marconi, Precision Acoustics Ltd, ONDA and SONORA hydrophones in Figure 1-2). Subsequent resonances occur at odd multiples of f_{pvdf}. However, the response continues to diminish for frequencies higher than f_{pvdf} since the ultrasonic absorption of PVDF rapidly increases with frequency [28]. In practice, f_{pvdf} is dependent on many fabrication parameters, for example the electrical impedance of the pair of thin metal strips deposited

on the membrane surface (which carry signal from the active electrodes), the length of interconnect cable, and the on-board electronics.

For the most part, commercially available hydrophones (membrane, probe and optical) contain integrated analogue signal processing electronics in order to suppress 50/60 Hz mains-borne noise, amplify the signal, flatten the resonance response, and match the electrical output impedance to 50 Ω so that it can be used with digital oscilloscopes and analogue-to-digital signal acquisition cards. In Figure 1-2, the magnitude sensitivity response of commercial membrane hydrophones from GEC Marconi Research Ltd, Precision Acoustics Ltd (PAL), Sonora, Onda Corporation, and Company for Applied Medical Physics and Technique (GAMPT) are shown. These hydrophones were calibrated on the National Physical Laboratory's (NPL) secondary calibration facility [29], [30].

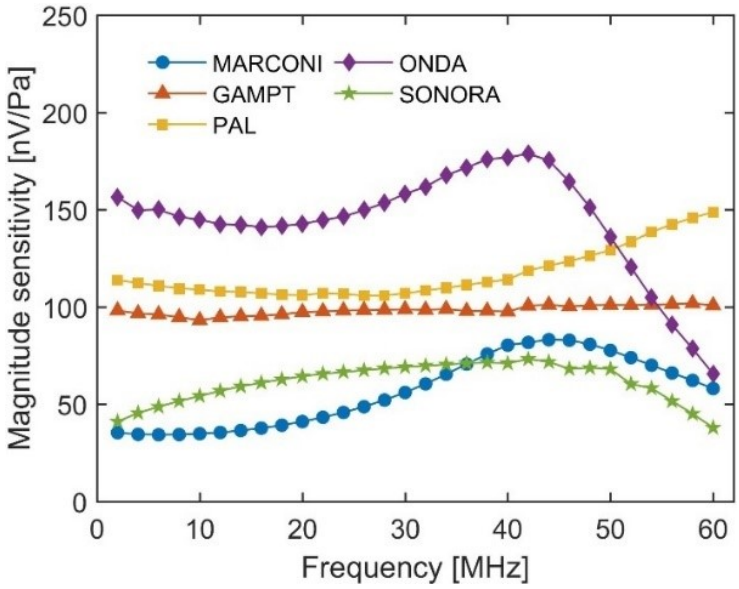

Figure 1-2: Magnitude sensitivity response of coplanar membrane hydrophones. MARCONI: 25 µm thick 0.5 mm active diameter with 75 Ω impedance coaxial cable of length 70 cm. GAMPT: 11 µm thick with 0.2 mm active diameter. PAL: 11 µm thick with 0.2 mm active diameter. ONDA: Unknown thickness with 0.2 mm square element. SONORA: Unknown thickness with 0.5 mm element diameter. These are National Physical Laboratory's reference hydrophones to which user hydrophones obtain their traceability via secondary calibration methods. The sensitivity response of the Marconi hydrophone is the end-of-cable open-circuit sensitivity whereas all other hydrophones comprised integrated analogue circuitry, which were terminated into a 50 Ω impedance and is known as the end-of-cable loaded sensitivity.

When transforming a hydrophone voltage signal from a membrane hydrophone to a pressure signal, using magnitude-only sensitivity results in smaller variation of the peak-positive or peak-

negative pressures compared to probe or fibre-optic hydrophones [31]–[33]. This is because the phase response of membrane hydrophones varies smoothly with frequency as does its magnitude response. But conventional membrane hydrophones suffer damage in HIFU fields due to the very high acoustic pressures, the temperature rise, and cavitation effects. Recently, robust membrane hydrophones have been developed, which have been shown to withstand HIFU pressures as high as 70 MPa peak positive pressure and 15 MPa peak negative pressure [34].

1.1.1.2 Probe Hydrophones

The diameters of the active elements of probe or needle type hydrophones used for medical ultrasound field characterisation range from 40 μm to 1 mm. The active element is supported on the tip of a cylindrical metal rod, which is placed inside a hollow cylindrical metal rod of slightly larger diameter. Electrical insulation is used so that there is no direct contact between the metal rods. The active element may be punched from a poled PVDF film, or a piezoelectric ceramic disc may be used. Since the acoustic impedance of the ceramic is much higher than PVDF, it is more resonant and so its bandwidth is narrower compared to PVDF film of similar dimensions. A wave incident on the tip of the needle hydrophone generates a complex pattern of waves in the active element, the housing, and in the surrounding fluid. The result is a hydrophone sensitivity that is dependent on both the frequency and angle of the incident wave, and that will change with tip geometry. Therefore, the frequency response of cylindrical probe hydrophones is not smooth [35]. The influence of the hydrophone on the measurement of the wavefield can be reduced by shaping of the probe tip resulting in a smoother frequency response [36]. The magnitude sensitivity response of 0.2 mm diameter element probe hydrophones from PAL and Onda are shown in Figure 1-3.

Probe type hydrophones are generally preferred over membrane hydrophones when measuring continuous or long tone-burst ultrasound fields. The large planar geometry of membrane hydrophones causes standing waves to setup between the transducer and hydrophone, which leads to erroneous estimates of the ultrasound pressure. Also, probe hydrophones can be, and have been, used for *in vitro* experiments. Robust probe hydrophones based on a ceramic active element are also available for HIFU fields.

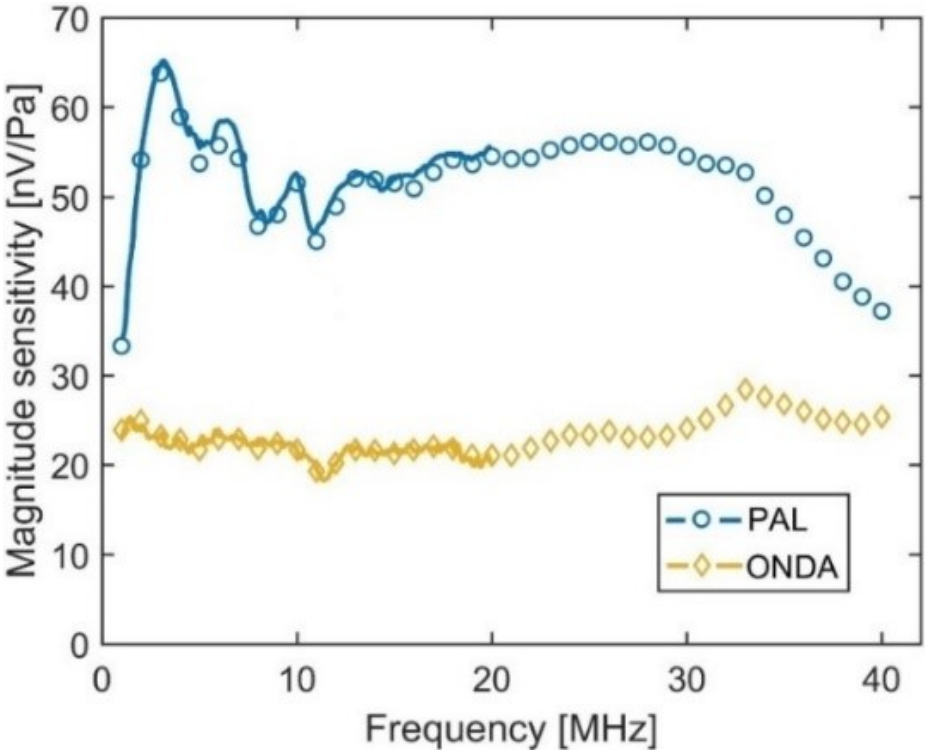

Figure 1-3: End-of-cable loaded magnitude sensitivity response of needle hydrophones. The active element diameters of PAL and ONDA hydrophones are both 0.2 mm. The continuous solid sensitivity response was obtained using a broadband ultrasound pulse via reference to a membrane referenced hydrophone.

1.1.1.3 Optical Hydrophones

There are currently two types of optical hydrophones commercially available. One is a Fabry–Pérot interferometer and the other is a reflectance hydrophone that is sensitive to the refractive index changes in water at the tip of an optical fibre. In a Fabry–Pérot (FP) interferometer, an optical reflecting cavity is fabricated on the tip of an optical fibre: A partially reflecting mirror is first deposited on the end of a bare fibre followed by a spacer and a fully reflecting mirror. The spacer is typically formed by chemical vapour deposition of type C, poly(p-xylylene) polymer commonly known as Parylene-C. The incident ultrasound wave changes the thickness of the optical cavity causing a change in the intensity of the light reflected back into the fibre, which is detected by a wideband photodiode and processed further to obtain a voltage signal. A tuneable laser is used to interrogate the sensor as the laser wavelength needs to be chosen such that the response of the hydrophone is linear with acoustic pressure, and to maximise the acoustic sensitivity. To find the optimal wavelength, the reflected optical power is measured in the absence of an ultrasound field as a function of wavelength, which is termed the Interferometer Transfer Function (ITF). Then the wavelength corresponding to the maximum slope of the ITF is chosen as the working wavelength.

The PAL FP fibre-optic hydrophone shown in Figure 1-4 uses a tuneable wavelength laser operating in the range 1520–1600 nm [37]. A representative magnitude sensitivity response is shown in Figure 1-5. Free-space, planar, FP hydrophones can also be made, using a glass, polymethyl methacrylate, or similar backing on which a FP cavity is fabricated [38]. This has allowed rapid spatial mapping of ultrasound fields in photoacoustic imaging and HIFU by using scanned laser beam [23], [38].

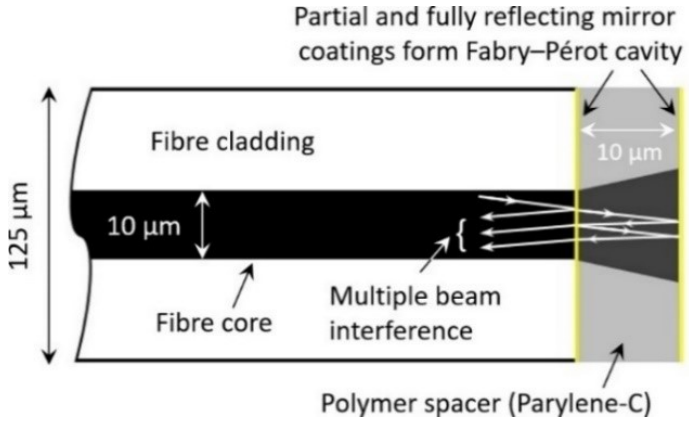

Figure 1-4: Precision Acoustics Ltd fibre-optic Fabry–Pérot interferometric hydrophone. The schematic was adapted from Ref [37].

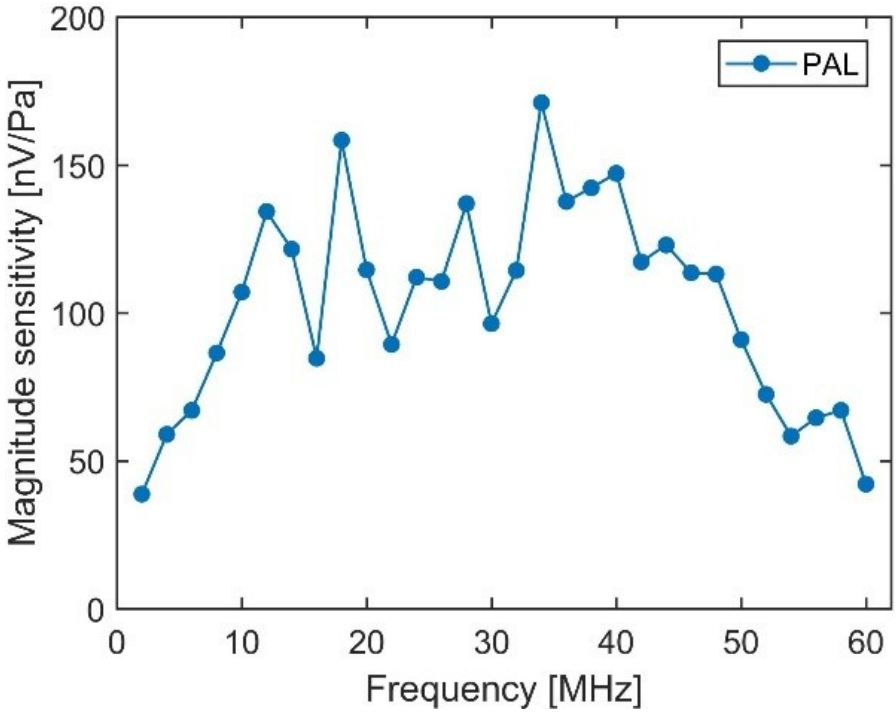

Figure 1-5: Representative end-of-cable loaded magnitude sensitivity response of a PAL fibre-optic Fabry–Pérot interferometric hydrophone.

Reflectance-based hydrophones were developed for use in very high-pressure fields such as cavitating and lithotripter acoustic fields whose peak-positive and peak-negative pressures can be in excess of 30 MPa and −10 MPa, respectively [39], [40]. In the reflectance-based fibre-optic hydrophone, also known as the Eisenmenger hydrophone [39], the optical refractive index changes in water at the end of a bare fibre due to the incident ultrasound wave are measured. The change in reflected laser light is measured by a photo-amplifier as a voltage change. The change in refractive index of water with pressure at a water temperature of 20 ℃ is 1.4×10^{-4} MPa^{-1} and for fused silica, from which the fibre core is made, it is 1.1×10^{-5} MPa^{-1} [22], a factor 10 lower due to its lower compressibility. Given the small change in refractive index of water with pressure, the acoustic sensitivity of reflectance-based fibre-optic hydrophones are the lowest amongst all hydrophones. Therefore, measurement-based calibration is not adequate since the peak-peak pressure amplitudes used in hydrophone calibrations are 5 MPa and below [14], [41], which means the uncertainty in the calibration will be large due to low signal-to-noise of the hydrophone. HIFU fields can be applied to increase the signal-to-noise but calibration techniques currently in use cannot cope with such high-pressure fields. Therefore, the acoustic sensitivity is derived theoretically [22].

In short, the measured pressure at the fibre end is derived using the method outlined in Ref. [40]. The dynamic refractive index of water due to ultrasound wave is recovered from the measured voltage response of the photo-amplifier and knowing the refractive index of water. Next, the dynamic refractive index of water is estimated using the empirical Gladstone-Dale relation. The refractive index of water is then related to the pressure using the modified equation of state of water. The estimated pressure at the fibre end is the sum of incident plane wave, diffracted waves and other elastic waves generated on the fibre. Since, only the incident pressure wave (free-field) is required for knowing the sensitivity response of the hydrophone, Ref. [22] only considers the effect of diffraction using a numerical model in which the average pressure at the fibre-water interface to an incident plane wave of ultrasound is computed. This method has been tested by comparing a weakly focused pressured field of 5.5 MPa peak-peak pressure with that measured using a membrane hydrophone.

1.1.2 Hydrophone Calibration Methods

The sensitivity of hydrophones is measured using primary standard techniques, which provide direct traceability to fundamental units of measurement, i.e., the SI (International System of Units). The ‘Primary Standard’ refers to the best currently available technique for measurements of this kind. This means measurements are undertaken under tightly controlled experimental conditions, for example, the temperature of the water must be known to an accuracy of 0.1 K, the instruments used for making the measurements are characterised for their linearity and stability, and there exists an unbroken chain of instrument calibrations traceable all the way to the top of the metrological hierarchy pyramid (see Figure 1-6).

Hydrophones calibrated on Primary Standard setups provide the best possible measurement available but the dissemination to the user community is undertaken on secondary methods, where hydrophones previously calibrated on the primary standard are used to calibrate test hydrophones. The secondary methods are based on a substitution technique, in which the response of the hydrophone under test and a reference hydrophone are compared when exposed to the same ultrasound field. This is lower in the hierarchy of best measurements (see Figure 1-6) since the test hydrophone is now traceable to the SI units only via hydrophones calibrated on the primary standard. Therefore, the test hydrophone inherits the uncertainties of the primary method and in addition, the uncertainties inherent to the secondary method. Nevertheless, secondary methods enable user accessibility to traceable calibrations, while remaining efficient in terms of the effort and resources (in time and cost) required to undertake a measurement.

The primary and secondary standard methods for the calibration of hydrophones briefly described in this section are those standardised by the International Electrotechnical Commission (IEC), which is an independent standard development organisation headquartered in Geneva, Switzerland. The Technical Committee (TC) 87 Ultrasonics is responsible for preparing standards related to the characterisation, methods of measurement, safety, and specification of fields. All calibrations are undertaken in a free-field condition. The free-field complex voltage sensitivity, $\underline{M}(f)$, is defined for two cases. (i) The sensitivity determined at the end of any integral cable or output connector of a hydrophone is known as *end-of-cable open-circuit sensitivity*, $\underline{M}_c(f)$, ii) The sensitivity determined at the end of any integral cable or output connector of a hydrophone or hydrophone-assembly, when connected to a specified load impedance, it is known as *end-of-cable loaded sensitivity*, $\underline{M}_L(f)$ [42]. The standardised definition for the *end-of-cable loaded sensitivity*, $\underline{M}_L(f)$, is given as the "quotient of the Fourier transformed hydrophone voltage-time signal $\mathcal{F}\big(U(t)\big)$ at the end of any integral cable or output connector of a hydrophone or hydrophone-assembly, when connected to a specified electric load impedance, to the Fourier transformed acoustic pressure-time signal $\mathcal{F}\big(p(t)\big)$ in the undisturbed free field of a plane-wave in the position of the reference centre of the hydrophone if the hydrophone were removed" [42]. In equation form this is given by

$$\underline{M}_L(f) = \frac{\mathcal{F}\big(U(t)\big)}{\mathcal{F}\big(p(t)\big)}. \tag{1.1}$$

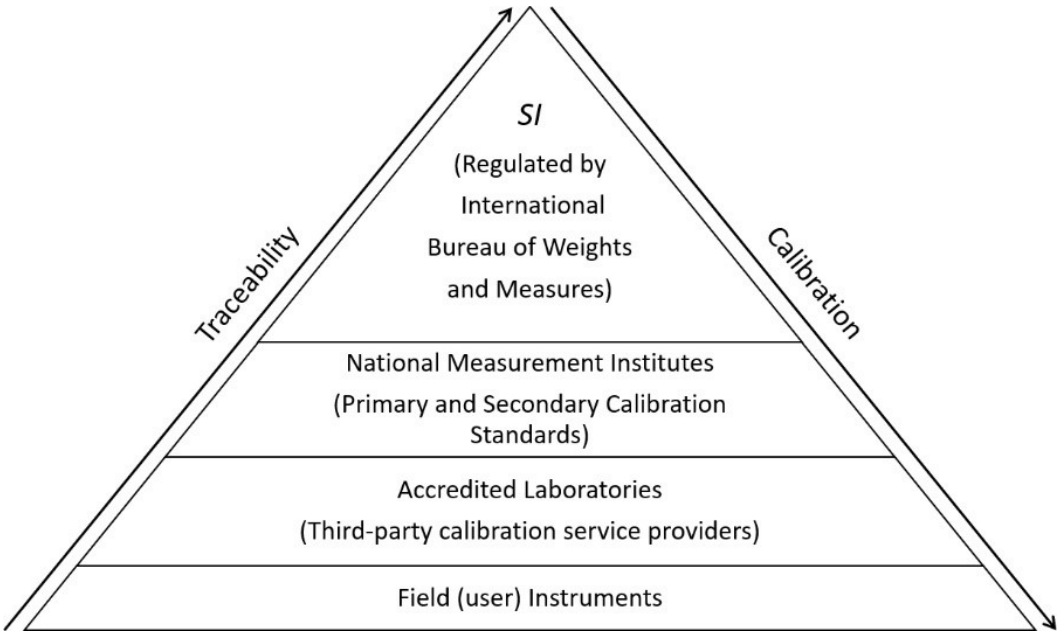

Figure 1-6: Metrological hierarchy pyramid. At the top are the SI units, which are established and maintained by the International Bureau of Weights and Measures. National Measurement Institutes (NMI) around the world are responsible for developing and maintaining their own primary standards to realise SI and the derived SI units for e.g., sensitivity unit, $\mathrm{V\,Pa^{-1}}$ of a hydrophone. The sensitivity unit is disseminated further by users obtaining traceability to the SI units via secondary calibration from NMIs or third-party calibration service providers.

In any given calibration method, some of the fundamental assumptions are that the hydrophone is a point receiver, the ultrasound beam is planar, measuring equipment is linear, and the signal to noise performance does not influence the measurement. In practice, such conditions are not perfectly met and therefore appropriate corrections for spatial averaging caused by the finite sized hydrophone, field non-planarity, and equipment nonlinearity need to be determined and applied to the measured data. The hydrophone calibration standard IEC 62127-2 [42] provides detailed guidelines on how to determine the individual corrections specific to each calibration method. In this thesis, only the general principle of the calibration methods is discussed in the subsequent sections.

1.1.2.1 Planar Scanning

In the planar scanning method, the relation between the total ultrasonic power and the ultrasonic intensity of the beam are utilised to derive the hydrophone sensitivity. The total ultrasonic power transmitted through a plane perpendicular to the direction of propagation when measured using a hydrophone can be written as

$$P_z = \frac{1}{T}\iiint_0^{T_i} \vec{I}(x,y,z,t)\,dt\,dx\,dy, \tag{1.2}$$

where T_i is the duration of integer number of cycles, P_z is the ultrasound power in W at the axial distance z, and $\vec{I}(x,y,z,t)$ is the instantaneous intensity in W m^{-2}.

The instantaneous intensity, $\vec{I}(x,y,z,t)$ is given by

$$\vec{I}(x,y,z,t) = p(x,y,z,t)\vec{u}(x,y,z,t), \tag{1.3}$$

where $\vec{u}(x,y,z,t)$ is the acoustic particle velocity. But, for a plane-wave or when z is at least twice the transducer radius and in the direction of propagation the vector components can be approximated by their equivalent scalar quantities [42]

$$I(x,y,z,t) = p(x,y,z,t)u(x,y,z,t), \tag{1.4}$$

and

$$p(x,y,z,t) = \rho_0 c_0 u(x,y,z,t), \tag{1.5}$$

where ρ_0 is the ambient mass-density of water in kg m^{-3} and the c_0 is the isentropic sound-speed of water in m s^{-1}.

Thus, the time-averaged intensity can be written as

$$\overline{I(t)} = \frac{\overline{p^2(t)}}{\rho_0 c_0}, \tag{1.6}$$

$$\overline{I(t)} = \frac{\overline{U_L^2(t)}}{\underline{M_L}_L^2\,\rho_0 c_0}, \tag{1.7}$$

where $\overline{p^2(t)}$ is the time-average of $p^2(t)$, $\overline{U_L^2(t)}$ is the time-average of the end-of-cable loaded voltage $U_L^2(t)$ of a hydrophone or hydrophone-assembly, and $\underline{M_L}$ is specified at the driving frequency, f, of the ultrasonic transducer.

Since the hydrophone sensitivity is derived from intensity and power measurements, it is not possible to determine the phase response of the hydrophone using the planar scanning method. From Eq. (1.7), the end-of-cable loaded magnitude sensitivity $M_L(f)$ is given by

$$M_L^2(f) = \frac{Power\ measured\ by\ hydrophone}{Power\ measured\ by\ R.F.B.} = \frac{1}{P_{z\_RFB}\rho_0 c_0 T_i}\iiint_0^{T_i} U_L^2(t)\,dt\,dx\,dy. \tag{1.8}$$

The ultrasound power, P_{z_RFB} in Eq. (1.8) is derived from measuring the total ultrasonic power, P_0 at the face of the transducer using radiation force method [43]. The reduced power at the hydrophone measurement distance, z is given by

$$P_{z\_RFB} = P_0 \exp(-2\alpha_{ac} z), \tag{1.9}$$

where α_{ac} is the frequency-dependent amplitude absorption coefficient of plane waves in water in units of Np m^{-1}.

The sensitivity of a hydrophone derived using planar scanning method is directly traceable to the SI base unit of mass via measurement of ultrasound power.

The planar scanning method is currently not practised by any of the National Measurement Institutes (NMI). The main disadvantage of this method is that it requires measurement of ultrasound power and planar scanning of the ultrasound beam for every frequency of interest. Therefore, it is only practical to do a calibration at large frequency steps of 1 or 2 MHz and consequently it is not suitable to calibrate a hydrophone whose frequency response varies rapidly within a narrow range of frequencies such as needle, probe, or fibre-optic type hydrophones.

1.1.2.2 Two-Transducer Reciprocity

The two-transducer reciprocity method requires that only one of the electroacoustic transducers being measured is reciprocal (the other transducer is usually a hydrophone), i.e., it satisfies the electromechanical reciprocity condition [42]:

$$\left|\frac{v}{I_{in}}\right| = \left|\frac{U}{F}\right| \tag{1.10}$$

where (in transmission) v is the uniform velocity of the radiating surface of the transducer for an input current I_{in} and (in reception) U is the open-circuit voltage produced by a force F acting on the transducer.

The reciprocal transducer is first calibrated by a self-reciprocity method in which a steel plate is used to reflect the emitted ultrasound waves back to the transducer to obtain its transmitting current response, S, at the driving frequency of the transducer, which under plane-wave measurement conditions is given by [42]

$$S = \frac{p}{I_{in}} = \sqrt{\frac{U_R}{I_{in} J_p}}, \tag{1.11}$$

where p is the amplitude of the acoustic pressure emitted by the reciprocal transducer, I_{in} and U_R are the amplitudes of the transmitting current and received voltage at the terminal of the reciprocal

transducer, respectively, and J_p is the reciprocity coefficient for plane waves which has units of $\mathrm{m}^4\ \mathrm{s}\ \mathrm{kg}^{-1}$. The reciprocity coefficient is given by [42]

$$J_p = \frac{2A}{\rho_0 c_0}, \tag{1.12}$$

where A is the surface area of the reciprocal transducer in m^2.

Once the transmitting current response of the reciprocal transducer is determined, the second transducer or the test hydrophone is then placed in the known sound field and its output voltage U_L is measured. The magnitude of the end-of-cable loaded sensitivity, $M_L(f)$ is given by

$$M_L(f) = \frac{U_L}{p} = \frac{U_L}{SI_{in}}. \tag{1.13}$$

The sensitivity of a hydrophone derived using two-transducer reciprocity method is directly traceable to the SI base unit of current via measurement of the transmitting current response, I_{in} of the reciprocal transducer.

A broadband source driven in a frequency-swept mode can be used to obtain a continuous magnitude sensitivity response of hydrophones overcoming the main limitation of the planar scanning method [44]. Also, recently, by accounting for the electrical transfer characteristics of the transmitting transducer and ultrasound diffraction effects, the phase response was determined for membrane type hydrophones from 1–7 MHz [45]. The reciprocity method is currently practised by the National Institute of Measurement (NIM), China and the National Institute of Metrology, Quality and Technology (INMETRO), Brazil.

The two-transducer reciprocity calibration method is relatively simple but is susceptible to small alignment errors at higher frequencies during the self-reciprocity calibration. Since the diameter of reciprocal transducers range from 6 mm to 25 mm [42] their directional response narrows significantly with increasing frequency. At 20 MHz and for a disc receiver of 3 mm radius the -6 dB directional response angles (see Sec. 1.1.3) calculated using Eq. (1.26) are $\pm\ 0.36^o$, which is a small range. Therefore, highly controlled positioning gantries are required to facilitate accurate alignments. Consequently, the two-transducer reciprocity method is limited to a calibration frequency of up to 20 MHz.

1.1.2.3 Optical Interferometry

In the late 1980s, two NMIs, the National Physical Laboratory (NPL), UK, and Physikalisch-Technische Bundesanstalt (PTB), Germany, developed primary standards based on optical interferometry. This was followed by the National Metrology Institute of Japan (NMIJ) in the 1990s [46]–[48] and more recently by the National Institute of Metrology (NIM), China [49]. The local displacement or local velocity in an acoustic field can be measured by using the principle of

superposition as implemented by optical interferometers in homodyne or heterodyne configurations. The primary standards implemented at NPL and NMIJ are based on a homodyne method and at PTB and NIM it is based on a heterodyne method.

For a single frequency plane wave, once the acoustic particle displacement, ξ or velocity, u are known then the acoustic pressure, p can be calculated as

$$p = 2\pi f \xi \rho_0 c_0, \tag{1.14}$$

$$p = u\rho_0 c_0. \tag{1.15}$$

The local pressure derived from the displacement or velocity measurement, together with the hydrophone voltage, U_L, measured at the same location in the ultrasound beam, are then used to obtain the sensitivity using Eq. (1.1).

Unlike planar scanning and reciprocity calibration, in interferometric methods nonlinearly-steepened tone-bursts and broadband pulses can be used, which extends the frequency range over 40 MHz to 60 MHz [24], [48], [49]. Recently PTB has tested their interferometer for both magnitude and phase to frequencies as high as 100 MHz [41]. The only limiting factor is the signal-to-noise ratio, the measurable displacement or velocity level above the noise floor, which is particular to the interferometer design and the sources of disturbance imposed by the environment in which the interferometer is operated.

1.1.2.4 Homodyne Interferometer

The basic principle of a homodyne interferometer of Michelson–Morley type is shown in Figure 1-7. Light from a monochromatic coherent source of wavelength λ_0 is divided equally using a beam-splitter or half-silvered mirror. One of the beams is reflected from a stationary mirror, M1, whilst the other is reflected from a moving mirror, M2. The two reflected beams are re-combined (superimposed) at the beam-splitter and directed towards a photodetector. The photodetector output voltage is dependent on the difference in the path-length (number of wavelengths) travelled by the reflected light from M2 to that from M1. If the path-length difference is an integer number of wavelengths then a constructive interference takes place and the voltage is proportional to the sum of maximum intensity in the two beams, and it is zero when the path-length difference is an odd number of half-wavelengths. For in-between values, the output voltage varies as shown in Figure 1-7, which are known as optical fringes. Since the wavelength of light is the SI unit of length, the measured voltage can be directly related to the acoustic displacement. The derived displacement is then used to estimate the acoustic pressure.

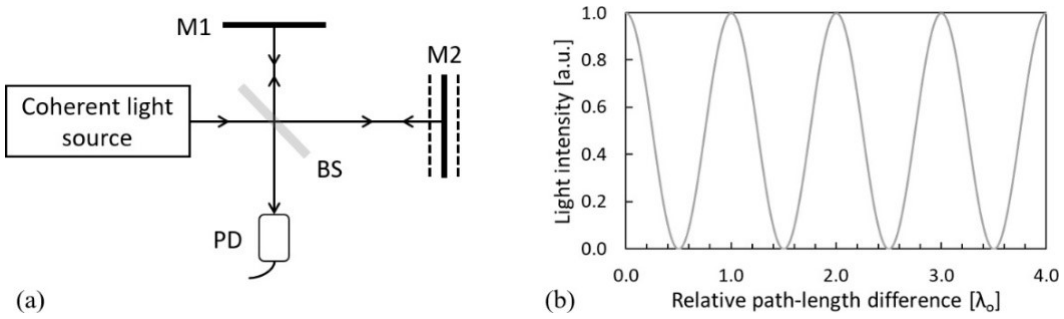

Figure 1-7: **a** Schematic of Michelson–Morley interferometer. BS: beam-splitter, M1: fixed mirror, M2: moveable mirror and PD: photodetector. **b** Intensity variation seen by PD as a function of relative path-length difference between M1 and M2. The dashed lines on either side of M2 represent motion of the moving mirror from an arbitrary position.

The wavelengths of the monochromatic source used in homodyne interferometry are in the green and red regions of the visible spectrum, typically 532 nm and 633 nm. However, the displacements produced in the medical ultrasound frequency range are small compared to the light source wavelength. The setup of the Michelson–Morley interferometer implemented at NPL to measure subwavelength displacements in the frequency range 100 kHz to 60 MHz is shown in Figure 1-8. The measurement beam is reflected from a thin pellicle (polyethylene terephthalate film of approximately 5 μm thickness) suspended in water and coated with a very thin layer of gold (< 25 nm) on the illumination side. The transducer exposes the pellicle to ultrasound from the opposite side. The thinness of the pellicle ensures it is acoustically transparent over the range of ultrasound frequencies of interest and it therefore moves in unison with the fluid as the sound wave passes through [46]. The focusing lens converges the optical beam to a diameter of 0.1 mm, which determines the spatial sampling of the acoustic field. If the optical beam diameter is kept sufficiently small, i.e., relative to the lateral extent of the applied acoustic field, then the measured displacements can be approximated to plane-wave displacements. The reflected beam from the pellicle is combined with the reference beam reflected from a stationary mirror (a corner cube reflector) mounted on a shaker (electromagnetic or piezo stack based). The combined beam is collected by a pair of photodetectors configured in a balanced detector arrangement to minimise the influence of laser power fluctuations. The balanced photodetectors produce an interferometer voltage signal, U_I, by detecting the phase change between the stationary reference beam (i.e., fixed path-length) and the measurement beam, which has been disturbed by ultrasound propagation. The shaker serves two functions: i) during the ultrasound displacement measurements, it applies an instantaneous phase correction detected by the balanced photodetectors due to disturbance of the pellicle caused by mechanical disturbances such as acoustic noise generated by equipment cooling fans, water surface

movement due to air drafts and movement of operating personal in the lab, and ii) it displaces the stationary mirror over tens of micrometres to form the full optical fringes, which are detected by the photodetectors as reference voltage, U_0, to enable the conversion of the displacement signal U_I to displacement in meters. The output of the Michelson interferometer, U_I, varies with displacement, ξ, according to the relationship:

$$U_I = U_0 \sin\left(\frac{4\pi n^* \xi}{\lambda_0} + \theta\right), \tag{1.16}$$

where, θ is the phase shift between the measurement and reference optical beams, n^* is the effective refractive index representing air and water mediums and U_0 corresponds to the amplitude of the reference voltage signal when the displacement exceeds $\lambda_0/2$.

If the feedback circuit of the shaker is adjusted so that θ is $\pi/2$ (plus an integral multiple of 2π), then the interferometer is operating in its most sensitive mode, i.e., the reference mirror is positioned exactly between a bright and dark optical fringe. By ignoring the constant amplitude part, Eq. (1.16) can be rewritten to give displacement

$$\xi = \sin^{-1}\left(\frac{U_I}{U_0}\right)\left(\frac{\lambda_0}{4\pi n^*}\right). \tag{1.17}$$

At NPL the interferometer is placed on a self-levelling antivibration platform in a draft proof enclosure, but still the audible noise generated by the equipment cooling fans and laboratory adjacency issues mechanically disturbs the shaker. The feedback circuit can compensate for this disturbance by applying an instantaneous voltage opposing the movement of the shaker. However, if the movement of the shaker is large or of high-frequency then the response time of the shaker cannot fully compensate for the disturbance, which means there is a limit on how small a displacement the interferometer can measure. NPL's interferometer can measure displacements as small as 110 pm, which was measured in the far-field of a plane piston transducer operating at 20 MHz [50]. As frequency increases the acoustic pressure must also increase to produce a constant displacement (see Eq. (1.14)). This is difficult to achieve using plane piston piezoelectric transducers and therefore, focused transducers are employed to increase the pressure level at higher frequencies. The highest frequency ever achieved on the NPL's interferometer was 60 MHz and this limit is mainly attributed to the laboratory noise conditions [14], [24]. Although tightly focused transducers could be employed to boost the pressure levels beyond 60 MHz, the hydrophone spatial averaging effects become significant elevating the uncertainty in the calibration to an unacceptable level.

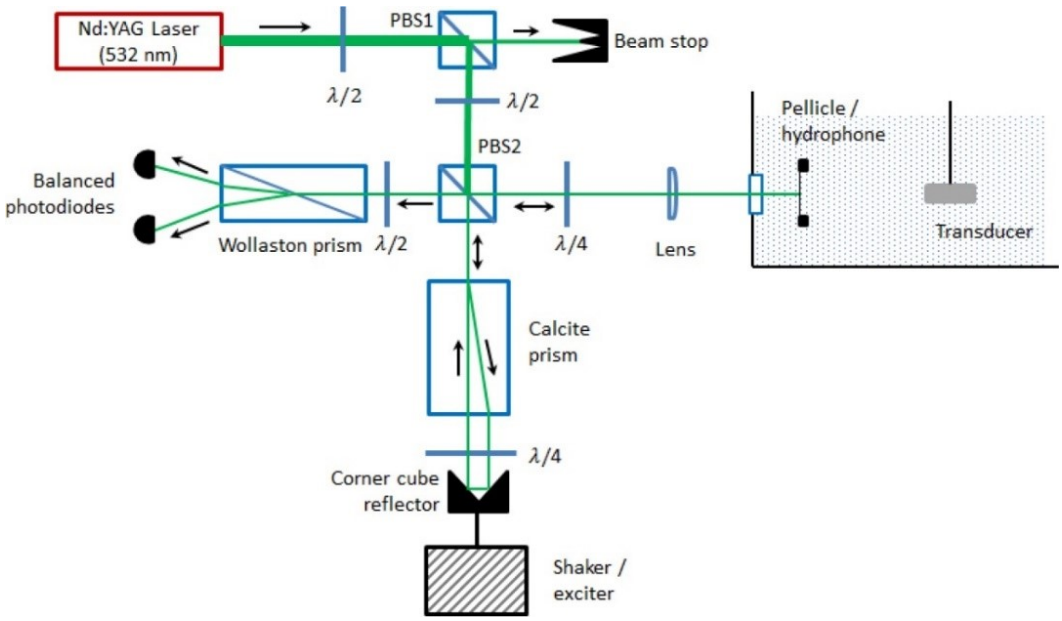

Figure 1-8: Schematic diagram of the NPL optical Michelson–Morley interferometer used for absolute displacement measurements at ultrasonic frequencies. PBS1 and PBS2 are polarising beam-splitters; λ/2 and λ/4 are half and quarter phase-retarder waveplates.

1.1.2.5 Heterodyne Interferometer

In a heterodyne interferometer, the displacement or velocity information is recovered from the phase of the reflected light using a Doppler technique. It is not possible to directly measure the phase changes from the reflected laser light of a moving surface since the frequency of the light is 429 THz to 750 THz in the visible wavelength range, which is beyond today's hardware measurement capability. Therefore, in order to overcome this limitation a heterodyne technique is used. Here, a portion of light from a monochromatic source is frequency shifted by a small amount, i.e., tens of MHz to few hundreds of MHz and then is reflected from a vibrating surface. The frequency shifted and the unshifted light beams are interfered and the resulting light is collected using a photodetector whose response is linear in energy. The photodetector transforms the optical power into oscillating current, which contains a component of the difference frequency corresponding to the heterodyne or beat frequency. There is also a component of the sum of two frequencies but the photodetector's response is too slow to detect the sum frequency [51], [52]. The difference frequency is essentially the shift frequency applied to the monochromatic source, which a photodetector can measure.

A schematic of a variant of the heterodyne interferometer or heterodyne laser Doppler vibrometer is shown in Figure 1-9. Light from a monochromatic laser source is divided using a polarising beam splitter (PBS). PBS1 is used to control the light intensity of the measurement and reference beams. The measurement beam with frequency f_m is incident on a moving target. The reflected measurement beam passes through PBS2 and at the non-polarising beam splitter (BS) the beam is equally divided and

detected by a pair of identical photodetectors (PD). The other beam from the PBS1 is frequency shifted by f_c using a Bragg-cell, which shifts the initial monochromatic source frequency to f_r, the reference beam. The reference beam is equally divided by the BS and collected by a pair of PD.

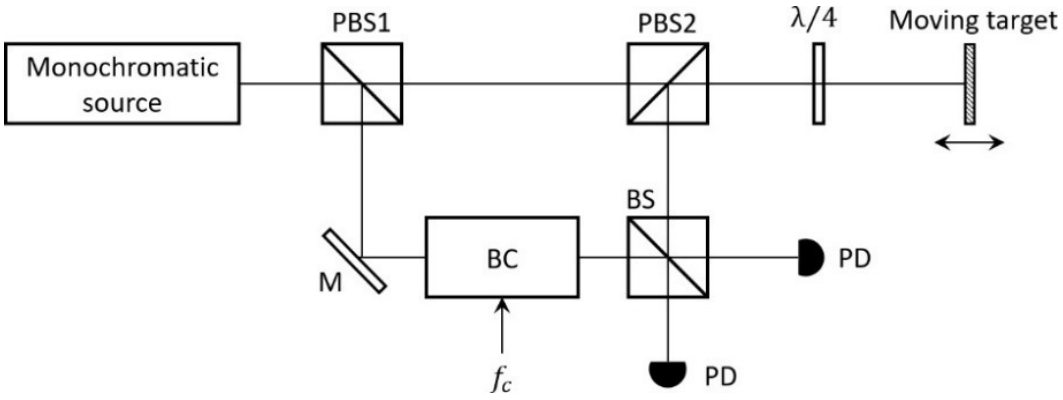

Figure 1-9: Schematic diagram of a laser Doppler heterodyne vibrometer. PBS1 and PBS2: Polarising beam splitters, M: mirror, BS: beam splitter, PD: photodetector, BC: Bragg cell, f_c: carrier frequency or shift frequency applied to the monochromatic source frequency. The schematic was adapted from Ref [51].

The heterodyne current, I_s generated by the photodetector can be given by [51]

$$I_s = K_{iP}\left[P_m + P_r + 2\kappa_h\sqrt{P_m P_r}cos\,(\omega_c t - \varphi(t) + \varphi_0)\right], \tag{1.18}$$

where P_m and P_r are the optical powers in Watts of the measurement and reference beams, respectively, $\omega_c = 2\pi f_c$ is the circular carrier frequency or shift frequency in rad, $\varphi(t)$ is the time-varying phase signal generated by the moving target that is proportional to target's instantaneous velocity, φ_0 is an arbitrary starting phase, $0 < \kappa_h < 1$ is the heterodyning efficiency, and K_{iP} is a conversion parameter, which describes the linear correlation of photocurrent and optical power given by [51]

$$K_{iP} = \frac{\eta_q q}{\omega}, \tag{1.19}$$

where η_q is the photodetector's quantum efficiency, defined as the ratio of incident photon to converted electron, q is the charge of electron, in Coulomb, and ω is the circular frequency.

The heterodyne current generated by the photodetectors is converted to a voltage signal using a transimpedance amplifier. The voltage signal is further processed to recover $\varphi(t)$ using analogue or digital demodulation methods. In the analogue demodulation method, a voltage proportional to velocity is produced by means a phase-locked loop circuit. The digital demodulation is based on an industry standard technique known as in-phase (I) and quadrature (Q) detection, which is widely used

in engineering applications such as radio communications, vector network analysers, and blood velocity measurements using ultrasound doppler. In IQ-demodulation, $\varphi(t)$ can be calculated using an arctangent method in which a pair of in-phase and quadrature signals are computed using the frequency modulated vibrometer or baseband signal and the original carrier signal used to shift the frequency of the monochromatic laser source. The I and Q signals are given by

$$I = \cos[\omega_c t + \varphi(t)] \times \cos(\omega_c t), \tag{1.20}$$

$$Q = \cos[\omega_c t + \varphi(t)] \times \sin(\omega_c t). \tag{1.21}$$

The instantaneous phase signal, $\varphi(t)$ is calculated by applying an inverse tangent to the I and Q signals

$$\varphi(t) = \tan^{-1}[Q/I]. \tag{1.22}$$

The instantaneous phase signal is low pass filtered to remove components of twice the carrier frequency and its harmonics. The filtered signal could be either processed to derive velocity information by numerical differentiation or displacement information by unwrapping the phase ambiguity introduced by the arctangent function [51].

1.1.3 Spatial Averaging and Directional Response

One idealisation of the hydrophone is that of a point receiver that does not affect the acoustic field it is measuring but just reports back the value of the acoustic pressure at that point. As it has no spatial extent, its response does not change with the angle or frequency of the wave. The frequency and angle-dependent response of a hydrophone indicates how far it is from being an ideal point receiver. While the dominant factor in the frequency response is the thickness of the sensitive element, as described above, the dominant effect on the hydrophone directionality is the spatial averaging of the acoustic field over the active region of the hydrophone.

Optical hydrophones exhibit the least spatial averaging, since the active element area is defined by the diameter of the laser beam or the diameter of the optical fibre, which can be made sufficiently small to be considered a point source at the frequencies currently used in biomedical ultrasound. But it also exhibits directionality influenced by its construction geometry as do membrane and probe hydrophones.

The directional response of a hydrophone can be measured for example by positioning the hydrophone in a nonlinear ultrasound field generated by finite amplitude distortion of a single frequency plane piston transducer [53]. A large separation distance between the hydrophone and transducer ensures that the ultrasound beam over the surface of the hydrophone is planar and still enough harmonics of the fundamental frequency are present to undertake measurements over a range of frequencies and incident

angles. Examples of the directional responses of a membrane and a probe hydrophone, whose nominal sensitive element diameters are 0.4 mm and 0.2 mm, respectively, are shown in Figure 1-10.

It has been empirically shown that the spatial averaging effects may be accurately estimated by integrating the free field over the surface area of an imaginary hydrophone calculated using the effective radius [20], [54]. The effective radius, $a_{eff}(f)$ is a frequency dependent property, often different from the physical dimensions of the sensitive element of a hydrophone, which is obtained from the directional response measurements and accounts for other effects on it as well as spatial averaging. For a given directional response, the angular difference between the left-hand −3 dB angle and the right-hand −3 dB angle and the angular difference between the left-hand −6 dB angle and the right-hand −6 dB angle $2\theta_3$ and $2\theta_6$, respectively, are obtained. The following formulas are then applied to estimate the effective radii, $a_{eff}(f)$ assuming circular geometry [55]:

$$a_{h3} = \frac{1.62\, c_0}{2\pi f \sin\theta_3}, \tag{1.23}$$

$$a_{h6} = \frac{2.22\, c_0}{2\pi f \sin\theta_6} \tag{1.24}$$

$$a_{eff} = \frac{a_{h3} + a_{h6}}{2} \tag{1.25}$$

where, c_0 is the temperature dependent isentropic sound-speed of water in m s^{-1}, a_{h3} and a_{h6} are the −3 dB and −6 dB effective radii in m, respectively, θ_3 and θ_6 are the −3 dB and −6 dB angular points on the directional response in radians, respectively and f is ultrasonic frequency in Hz.

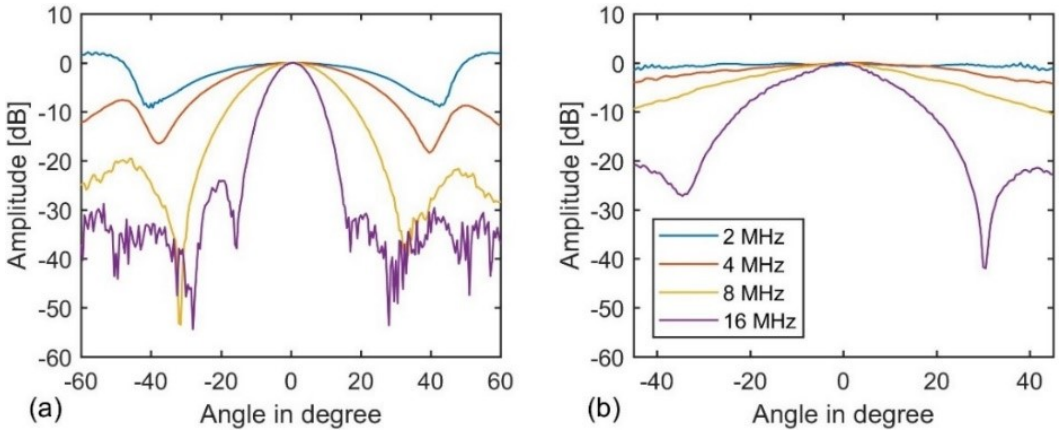

Figure 1-10: **a** Directional response of a nominal 0.4 mm geometrical diameter Precision Acoustics Ltd membrane hydrophone. **b** Directional response of a nominal 0.2 mm geometrical diameter Onda Inc probe hydrophone. The select few frequency dependent responses shown here correspond to harmonic content of a nonlinearly steepened tone-burst ultrasound waveforms generated from a 2 MHz fundamental plane piston source. The directional responses were measured by NPL.

It is also possible to find the effective element size by comparing the directional response measurements to the analytical model for a plane piston receiver in a rigid baffle model given by [20]

$$D(f,\theta) = \frac{2J_1(ka\sin\theta)}{ka\sin\theta}, \tag{1.26}$$

where, J_1 is the Bessel function of the first kind, a is the geometrical hydrophone radius in m, θ is the angle in radians, $k = 2\pi/\lambda$ is the circular wavenumber, and λ is the wavelength of the ultrasound wave in m. The effective radius, a_{eff}, is determined by varying a until it gives the best fit to the experimental directional response data. For membrane hydrophones, at lower frequencies and large incident angles, Eq. (1.26) does not fit accurately to the measured data due to heightened behaviour of the side lobes as seen in Figure 1-10(a). This is due to the initiation and propagation of slow-moving Lamb waves across the membrane, which affect its angle dependent reflectivity thus affecting the side lobes [27], and which are not included in the simple plane-piston model.

1.1.3.1 Methods for Correcting for Non-planar Wavefield

Hydrophone spatial averaging has been studied extensively. The Refs. [25], [54], [56]–[59] and the references contained therein provide a detailed account of work done in this area. This thesis makes a brief reference to the work currently identified in the IEC standard and that practised at NPL. Spatial averaging has the effect of underestimating the true pressure. Therefore, the correction factor can be thought of as a quantity greater than one, which, when multiplied by the quantity derived from the measured hydrophone, e.g., peak-positive, or peak-negative pressure, results in the recovery of that true quantity.

1.1.3.2 Quadratic Approximation

A widely used method to correct for the spatial averaging error was developed at NPL [56], [57], which is also the prescribed method by the IEC standard 62127-1: Measurement and characterization of medical ultrasonic fields up to 40 MHz [20]. The method approximates the radial beam profile at the focal plane of the transducer (last axial maximum in the case of a plane piston transducer) very close to the transducer axis (same as the hydrophone's active radius) as a quadratic relationship

$$p(r) = 1 - br^2, \tag{1.27}$$

where r is the radial distance from the transducer axis and b is a constant.

The following two correction methods defined below were based on empirical studies involving various hydrophone diameters ranging from 0.1 to 1.0 mm and frequencies in both linear and nonlinear pressure fields.

The first spatial averaging correction factor, K_{sa}, in the focal plane of a transducer in a linear field is defined by

$$K_{sa} = (3 - \beta_{SA})/2, \tag{1.28}$$

where the parameter β_{SA} is defined as

$$\beta_{SA} = \frac{\text{signal at one hydrophone radius from the axis}}{\text{signal on axis}}. \tag{1.29}$$

The second spatial averaging correction factor, K'_{sa}, for the case of a nonlinearly steepened field is defined by

$$K'_{sa} = (3 - 2\beta'_{SA}), \tag{1.30}$$

where, the parameter β'_{SA} is defined as

$$\beta'_{SA} = \frac{\text{signal at half a hydrophone radius from the axis}}{\text{signal on axis}}. \tag{1.31}$$

Since the radius of membrane hydrophones can be nearly a factor of two higher than its geometrical radius at low frequencies, i.e., below 3 MHz [54], the hydrophone radius in Eq. (1.29) and (1.31) should be replaced with effective hydrophone radius. Also, the correction factors must be calculated by making measurements in two orthogonal orientations of the active element.

1.1.3.3 Distorted Waveform Model

In the distorted waveform model [25], the spatial averaging correction is derived using the following empirical relationship

$$\delta_{SA} = 1 + \frac{0.3}{(\alpha_{SA}^2 - 0.3)}, \tag{1.32}$$

where

$$\alpha_{SA} = \frac{\text{measured} - 6\text{ dB beam width}}{\text{effective hydrophone diameter}}. \tag{1.33}$$

The above relationships have been validated using a theoretical model, in which various nonlinearly steepened acoustic waveforms (nonlinear distortion parameter, σ ranging from 0.5 to 2.0) have been investigated whose spectral beam widths varied with harmonic frequency. In comparison, the corrections in Sec. 1.1.3.2 have shown to significantly underestimate the corrections [25] and therefore, the IEC 62127-1 recommends using smaller size hydrophones where possible especially when $\alpha_{SA} < 1.5$ [20].

The spatial averaging corrections described here are only for the magnitude of the acoustic pressure. However, there have been recent developments in which the complex spatial transfer function has been theoretically investigated [59] with restricted experimental validation [60]. It is likely that the future improvements to the IEC 62127-1 standard will provide guidelines based on new developments in this area of study.

1.2 Challenges with High-frequency Calibration

Piezoelectric materials such as quartz crystals and lead zirconate titanate (PZT) ceramic are widely used in the generation of ultrasound due to their large piezoelectric strain coefficient. Unfortunately, the inherently resonant nature of the PZT transducers results in relatively narrow bandwidths. Acoustic damping improves the bandwidth but since some of the acoustic energy is lost in the damping material, the amplitude of the wave decreases. Capacitive micromachined ultrasound (CMUT) transducer arrays are also resonant devices and thus have similar problems. Therefore, a single piezoelectric or a CMUT transducer which covers a bandwidth of tens of MHz does not exist.

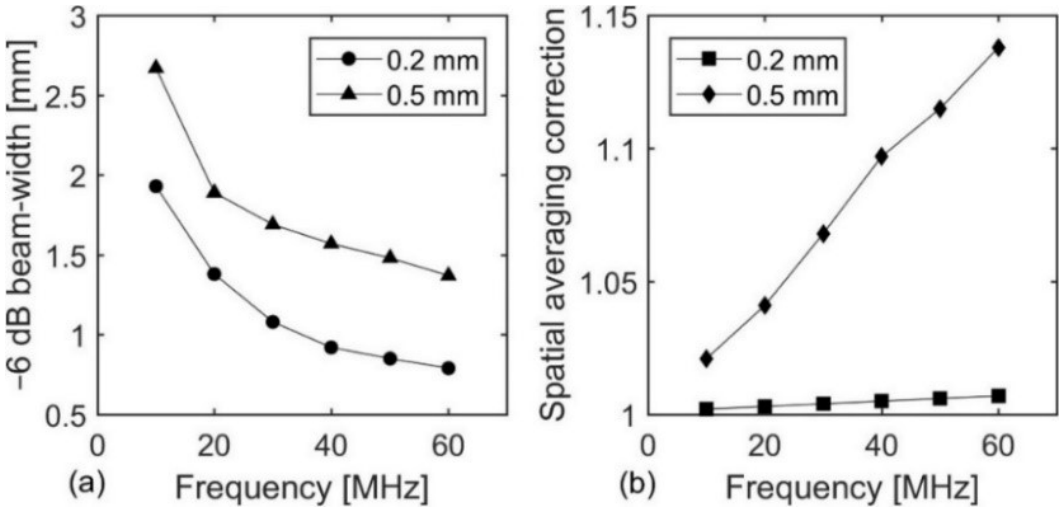

Figure 1-11: **a** −6 dB spectral beam-widths of a 10 MHz focused transducer measured using a 0.2 mm diameter probe hydrophone and a 0.5 mm diameter membrane hydrophone. **b** Spatial averaging corrections derived from Eq. (1.33) using beam-widths plotted in **a** and assuming geometrical diameter as the effective hydrophone diameter at all harmonics.

High-pressure and nonlinearly steepened ultrasound beams generated using focused PZT transducers have been the only way of calibrating hydrophones beyond 20 MHz for NPL, NIM and PTB. The harmonics of the nonlinearly steepened pressure fields at the focus have been used to calibrate hydrophones to a maximum frequency of 40 MHz to 100 MHz [14], [41], [49]. As discussed previously in Sec. 1.1.2, spatial averaging becomes significant in the presence of a focused field

because the confined pressure is not uniform on the surface of the hydrophone element and the error is dependent on the size of the active element. This can be seen in Figure 1-11(a) on the measured spectral beam-widths of a 10 MHz focused transducer (F# = 7.1) using a 0.2 mm probe hydrophone and a 0.5 mm membrane hydrophone. The corresponding spatial averaging corrections are shown in Figure 1-11(b). The uncertainty in the spatial averaging correction increases the overall uncertainty, which currently for NPL is in the range of 3% to 15% in the magnitude sensitivity over the frequency range of 0.5 MHz to 60 MHz expressed at 95% coverage probability. Since the user hydrophones are calibrated using secondary methods, it includes the uncertainty in the primary calibration as well as the secondary method, thus increasing the user hydrophone uncertainty to 6% to 25%. These uncertainties are also similar for PTB over the same frequency range and at 100 MHz the uncertainty in their magnitude sensitivity using the primary method is at least 40% [41].

1.3 Project Goal

In this chapter, the motivation for calibration of hydrophones to frequencies as high as 100 MHz and beyond was stated. A brief description of the commonly used hydrophone types used in medical ultrasound was given and the various techniques used to calibrate them, and their advantages and disadvantages were discussed. Interferometric calibration methods can be used to calibrate hydrophones up to 100 MHz and beyond, but focused ultrasound fields are required to generate high-frequency content via nonlinear propagation. However, hydrophone spatial averaging in the focused field become a significant uncertainty component, which is undesirable. Ideally, a planar and broadband field is required, which in not possible to generate using piezoelectric transducer technology.

Ultrasound generation via the photoacoustic effect could be a promising alternative to piezo transducer technology that may satisfy bandwidth, planarity, and high-pressure requirements. In photoacoustics, when a light absorbing medium is illuminated by an optical pulse, the photons are absorbed by chromophores in the medium and the subsequent thermalization of the energy leads to simultaneous increases in temperature and pressure within the absorption volume. If the medium is elastic, and the energy deposition is sufficiently rapid, the pressure rise will result in an ultrasound pulse. The amplitude, bandwidth and the spatial size of the ultrasound pulse can be controlled by varying the optical pulse duration and energy, the size of the illuminated region and the physical properties of the medium. The goal of this thesis is to first review the state-of-the-art photo-absorbing mediums used in photoacoustics via literature review. Next, to develop a reproducible photo-absorbing fabrication method followed by its characterisation to understand as to what properties constitutes the generation of a high-pressure, broad bandwidth and planar photoacoustic field suitable for a calibration application. Finally, to build a photoacoustic source device that could be applied in a laboratory environment in the same way as existing piezoelectric transducers.

1.4 List of Publications

The work contained in this thesis has previously been presented in the following journal and conference publications:

1. S. Rajagopal, T. Sainsbury, B. E. Treeby, B.T. Cox, Laser generated ultrasound sources using polymer nanocomposites for high frequency metrology, In: IEEE International Ultrasonics Symposium, Washington, DC, USA, 2017.

2. S. Rajagopal, T. Sainsbury, B. E. Treeby, B.T. Cox, Laser generated ultrasound sources using carbon-polymer nanocomposites for high frequency metrology, Journal of the Acoustical Society of America, 144(2), p.584, 2018.

3. S. Rajagopal, B. E. Treeby, B.T. Cox, Effect of Backing on Carbon-Polymer Nanocomposite Sources for Laser Generation of Broadband Ultrasound Pulses, In: IEEE International Ultrasonics Symposium, Kobe, Japan, 2018.

Chapter 2

Background to Laser-Generated Ultrasound

The earliest discovery of photoacoustics is credited to Alexander Graham Bell after the publication of his work titled “Upon the Production and Reproduction of Sound by Light” in the Journal of the Society of Telegraph Engineers in the year 1880 [61]. The discovery of photoconductivity of the non-metal selenium by Willoughby Smith in 1873 [62] led Bell to use this semiconductor in his sound transmission experiments. Bell devised an apparatus called the ‘photophone’ in which a flexible mirror was constructed by attaching a mica or a microscope glass to a diaphragm that could be excited using audible speech. The sunlight reflected from the vibrating mirror was collected at a distance using a parabolic mirror and at its centre a selenium solar cell was located. The rapid variation of light intensity on selenium generated an alternating current that was connected to a telephone, which reproduced the speech at transmission. Instrument maker Charles Sumner Tainter, a friend of Bell with whom he devised the photophone experiments, successfully transmitted the sound from the top of Franklin Schoolhouse to one of Bell’s laboratory on 1325, L Street in Washington, D.C., a distance of 213 meters.

The invention of the laser in the 1960s enabled widespread application of photoacoustics in many areas of science such as noncontact generation and detection of sound waves in materials for non-destructive testing [63], detection of trace gases [64], and biomedical imaging [65] by exploiting the spectroscopic absorption properties of molecules. In photoacoustics, although coherent light is not essential, lasers are extensively used to generate ultrasound because of its controllability: beam size, pulse energy / power, pulse duration. Therefore, it will henceforth be referred to as Laser-Generated Ultrasound (LGUS).

In this chapter, the physical principles of LGUS are described in Sec. 2.1, a review of the fabrication methodologies of LGUS sources and the current state-of-the-art is presented in Sec. 2.2, the characteristics of an ideal LGUS source are listed in Sec. 2.3 and in Sec. 2.4 a brief overview of the rest of the thesis is given.

2.1 Principles of Laser-Generated Ultrasound

There are broadly two mechanisms by which an ultrasound (or stress wave in solids) wave can be induced in a medium using pulsed lasers: the ablative regime and the thermoelastic regime. In the

ablative regime, the high energy density of the nanosecond or sub-nanosecond duration laser pulse when irradiated on the surface of a material causes it to fracture or fragment and vaporise. The recoil momentum associated with this physical action induces an acoustic wave in the intact material [66]. Since ablation involves continuous material loss for as long as it is being excited by laser pulses, it is not practical to design an ablative LGUS source for a metrology application.

LGUS in the thermoelastic regime occurs due to the sequence of events shown in Figure 2-1. The propagation and distribution of photons in a medium depends on both the absorption and scattering coefficients, μ_a [m^{-1}] and μ_s [m^{-1}], respectively. The distribution of light in a medium can be characterised by the fluence, Φ [$\mathrm{J\,m}^{-2}$], which is the flow of optical energy per unit area integrated over all directions and time. The amount of light absorbed within a medium, per unit volume, is the absorbed energy density, H [$\mathrm{J\,m}^{-3}$]. In LGUS, the photon energies correspond to the visible and near-infrared range wavelengths of the electromagnetic spectrum. A photon is absorbed only when the energy of the photon matches one of the quantised energy states (e.g., electronic, vibrational, or rotational). The time taken by the excited electron to return to the ground state determines whether there will be fluorescence, phosphorescence or thermalisation. Since there is re-radiation of the absorbed photon in fluorescence and phosphorescence, the return of the excited electron to the ground state is known as radiative relaxation. Thermalisation is a non-radiative collisional relaxation process, which occurs before fluorescence or phosphorescence, i.e., if the radiative relaxation time is longer then there is a greater probability for thermalisation to occur. In non-radiative relaxation, the excited electron gives away the energy it gained via small amounts to various lower energy levels of rotational and vibrational energy states. The excited rotational and vibrational energy states of the molecule collide with neighbouring molecules causing the transfer of kinetic energy, which at the macroscale is known as the thermalisation of the medium. Therefore, for the medium to thermalize the transition must happen to one of the vibrational or rotational energy states. Unabsorbed photons are scattered away from the molecule without loss of energy at least with elastic scattering. Inelastic scattering, called Raman scattering, does occur, but the proportion of the photons scattered in this way is small, and is negligible in this application. If the thermalisation happens in a sufficiently short time such that the density does not decrease, then the rise in pressure due to rise in temperature occurs simultaneously. The built-up pressure is known as the initial acoustic pressure distribution, p_0, which propagates away as an acoustic wave and the built-up temperature also diffuses to surrounding cooler regions, although on a different time scale [67]. This is also known as generation of ultrasound in the thermoelastic regime since it is the increase in pressure that causes an ultrasound wave.

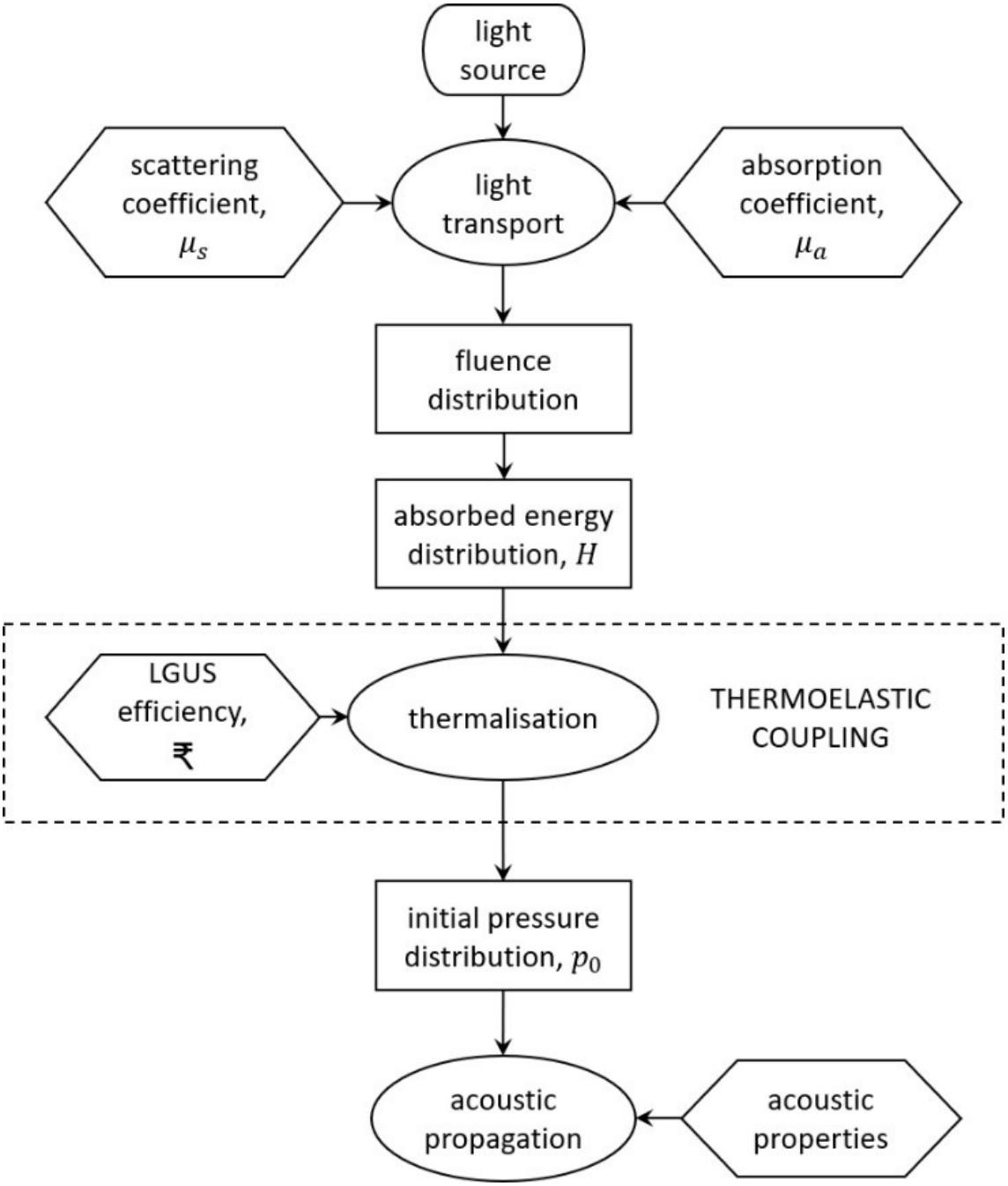

Figure 2-1: The light transport in a medium is dependent on its optical absorption, μ_a, and scattering, μ_s, properties, which determines how the fluence, Φ, is distributed. The subsequent absorption of all the photons gives rise to the absorbed energy distribution, $H = \Phi\mu_a$. The non-radiative relaxation of the excited photo-absorptive molecules heats the medium. The conversion of photon energy to acoustic energy is related to the medium's photoacoustic or laser-generated ultrasound efficiency parameter, ₹. Following a sufficiently short optical pulse, the simultaneous increase in temperature and pressure gives rise to initial pressure distribution, p_0, which propagates away as an acoustic wave in the medium. The figure is adapted from Ref. [67].

The amplitude of the initial pressure distribution, p_0 can be given by

$$p_0 = \Gamma H, \tag{2.1}$$

where, Γ is a unitless thermodynamic property of the medium known as the Grüneisen parameter. The Grüneisen parameter can be written in terms of other thermodynamic parameters, for example

$$\Gamma = \beta_v c_0^2 / C_p, \tag{2.2}$$

where, β_v $[K^{-1}]$ is the volume thermal expansion coefficient, c_0 [m s^{-1}] is the sound-speed and C_p [J Kg^{-1} K^{-1}] is the isobaric heat capacity. The absorbed energy density can be written as

$$H = \Phi \mu_a. \tag{2.3}$$

The spatial absorption profile of photons within the absorption region assuming plane-wave incidence and in the absence of scattering, is given by Beer–Lambert–Bouguer law

$$p_0(z) = \Phi_0 \mu_a ₹ \exp(-\mu_a z), \tag{2.4}$$

where, z is the perpendicular distance from the surface and Φ_0 is the laser fluence at the surface, $z = 0$ and ₹ (rupee – currency of India) is the photoacoustic conversion efficiency. Since the Grüneisen parameter is only strictly true for pure substances, the photoacoustic conversion efficiency parameter, ₹ represents the overall thermodynamic efficiency of a nanocomposite material including radiative losses, i.e., fluorescence and phosphorescence.

2.1.1 Wave Equation

Lasers can be used to generate all types of elastic waves i.e., bulk, surface and guided waves depending on the type of medium. When a solid LGUS source is excited with a laser pulse, along with compressional stresses, shear stresses may also be generated [63]. However, since hydrophones are used to measure the ultrasound waves propagating in a water medium in which only bulk compressional waves are supported, the following discussion is limited to wave propagation in a fluid media.

The coupled equations that describe the perturbations in the pressure, p, and temperature, T, can be written as [67]

$$\frac{\partial^2}{\partial t^2}(k_T p - \beta_v T) = \frac{1}{\rho_0}\nabla^2 p \tag{2.5}$$

and

$$\frac{\partial}{\partial t}\left(\rho_0 C_p T - T'\beta_v p\right) = \nabla \cdot (\kappa_{th}\nabla T) + \mathcal{H}, \tag{2.6}$$

where, $\mathcal{H}$ [W m^{-3}] is the optical energy deposited per unit volume per unit time or the optical power density, k_T [m^2 N^{-1} or Pa^{-1}] is the isothermal compressibility, C_p [J Kg^{-1} K^{-1}] is specific heat capacity at constant pressure, T' is the background temperature, T is the local temperature, p is the local pressure and κ_{th} [W m^{-1} K^{-1}] is the thermal conductivity. Eq. (2.5) and (2.6) must be solved together when thermal diffusion cannot be neglected. Since thermal diffusion from the absorbing region is a slower process compared to acoustic propagation time, the diffusion term in Eq. (2.6) can often be neglected. After some rearrangement of Eq. (2.5) and (2.6) a single wave equation can be given with the rate of change of absorbed power density as the source term [67]

$$\frac{1}{c_0^2}\frac{\partial^2 p}{\partial t^2} - \nabla^2 p = \frac{\beta_v}{C_p}\frac{\partial \mathcal{H}}{\partial t}, \tag{2.7}$$

or equivalently

$$\frac{\partial^2 p}{\partial t^2} - c_0^2\nabla^2 p = ₹\frac{\partial \mathcal{H}}{\partial t}. \tag{2.8}$$

The derivation of ₹, photoacoustic conversion efficiency or the Grüneisen parameter is described in Sec. 2.1.3.

Like the initial acoustic pressure, p_0, the initial temperature rise, T_0 can be given when thermal diffusion is negligible [68]:

$$T_0 = \frac{H}{\rho_0 C_v} = \frac{\Phi \mu_a}{\rho_0 C_v}, \tag{2.9}$$

where, C_v [J Kg^{-1} K^{-1}] is specific heat capacity at constant volume.

2.1.2 Thermal Confinement

The rate at which the rise in temperature within the absorbing region diffuses away is related to the thermal diffusivity, α_{th} [$m^2\ s^{-1}$] of the absorbing medium. To ensure thermal confinement, the duration of the laser pulse, t_p should be much shorter than the thermal relaxation time, τ_{th}, of the absorbing medium i.e., $t_p \ll \tau_{th}$. For a planar absorber (slab) the thermal relaxation, τ_{th} can be given by [68]

$$\tau_{th} = 1/4\mu_a^2\alpha_{th}. \tag{2.10}$$

2.1.3 Stress Confinement

The rise in pressure within the absorption region (to ~ $1/\mu_a$ deep) is directly related to the rise in temperature. Consequently, for maximum conversion, all the absorbed photon energy must be converted to thermal energy. For this to happen, the deposition of the photon energy from a laser

source must be sufficiently rapid that the density of the absorption region has no time to decrease significantly, i.e., there is no immediate expansion. If this is not the case, then some of the absorbed energy is used in changing the density of the medium thereby decreasing the pressure rise due to temperature rise.

The rates of change of the local temperature, T, pressure, p, and density, ρ, can be related by the thermodynamic identity [67]

$$\frac{\partial p}{\partial t} = \left(\frac{1}{k_T \rho_0}\right)\frac{\partial \rho}{\partial t} + \left(\frac{\beta_v}{k_T}\right)\frac{\partial T}{\partial t}. \tag{2.11}$$

If the duration of the laser pulse is sufficiently short then stress confinement occurs, i.e., there is no time for density to decrease and $|\partial\rho/\partial t| \ll |\partial T/\partial t|$. Under this condition of no volume change (isochoric) the rate of increase in local pressure can be given by

$$\frac{\partial p}{\partial t} = \left(\frac{\beta_v}{k_T}\right)\frac{\partial T}{\partial t}. \tag{2.12}$$

Since thermal diffusion is negligible when stress confinement is satisfied then the rate at which the local temperature increases is given by

$$\frac{\partial T}{\partial t} = \frac{\mathcal{H}}{\rho_0 C_v}, \tag{2.13}$$

Inserting Eq. (2.13) into Eq. (2.12), the rate at which the pressure increases becomes

$$\frac{\partial p}{\partial t} = \frac{1}{\rho_0 C_v}\left(\frac{\beta_v}{k_T}\right)\mathcal{H}(z,t) = ₹\mathcal{H}(z,t), \tag{2.14}$$

where $₹ = \beta_v/(\rho_0 C_v k_T) = \beta_v c_0^2/C_p$ is the dimensionless Grüneisen parameter or photoacoustic conversion efficiency. The equivalent expression was obtained by using the thermodynamic relation $c_0 = \sqrt{B_s/\rho_0}$, where $B_s = \left(C_p/C_v\right)/k_T$ is the isentropic bulk modulus.

It is useful to know for what duration of the laser pulse stress confinement occurs. This can be given by the acoustic relaxation time of the medium i.e., the time taken by the acoustic wave to transit across the absorption region

$$\tau_{ac} = 1/(\mu_a c_0). \tag{2.15}$$

If the duration of the laser pulse is much shorter than the acoustic transit time across the absorption depth, $t_p \ll \tau_{ac}$, then the medium undergoes isochoric thermalisation, meaning that all the laser energy is deposited before the acoustic wave has propagated away from the absorption region, maximising the build-up of pressure. Stress confinement is a stricter condition to satisfy than thermal confinement, as the acoustic travel time will always be shorter than the thermal diffusion time.

2.1.4 Initial Value Problem

The source terms may be separated into spatial and temporal factors when the source is stationary, i.e., $\mathcal{H}(z,t) = H(z)h(t)$, where $h(t)$ is a temporal heating pulse, normalised so that $\int_0^\infty h(t)dt = 1$ and $H(z)$ is the heat deposited per unit volume or the absorbed energy density. Stress confinement is considered a sufficient condition for approximating $h(t)$ by a delta function, $\delta(t)$. Therefore, the source term in Eq. (2.8) can be rewritten as [67]

$$₹\frac{\partial \mathcal{H}}{\partial t}(z,t) = ₹H(z)\frac{\partial h(t)}{\partial t} = p_0(z)\dot{\delta}(t). \tag{2.16}$$

where, $\dot{\delta}(t)$ is the time derivative of the delta function. Inserting the source term from Eq. (2.16) into the LGUS wave equation in Eq. (2.8) gives

$$\left(\frac{\partial^2}{\partial t^2} - c_0^2\nabla^2\right)p(z,t) = p_0(z)\dot{\delta}(t). \tag{2.17}$$

This is equal to the initial value problem given by

$$\left(\frac{\partial^2}{\partial t^2} - c_0^2\nabla^2\right)p(z,t) = 0, \tag{2.18}$$

with initial conditions:

$$p(z,t=0) = p_0(z), \qquad \left.\frac{\partial p}{\partial t}\right|_{t=0} = 0. \tag{2.19}$$

The second condition is equivalent to assuming that the particle velocity is initially zero in the region of initial pressure distribution.

2.2 Sources of Laser-Generated Ultrasound

2.2.1 Metals

The non-contact method of ultrasound wave generation using lasers in metals is widely studied because of its many uses in non-destructive testing (NDT) of optically opaque materials. There are several advantages of using LGUS over piezoelectric transducers in NDT applications [63], [69]. i) The test specimen itself is a source for generating acoustic waves. ii) The detection of ultrasound waves using optical interferometry renders the method non-contact. iii) There is no need of a couplant material. iv) Hostile and difficult to access spaces can be probed. v) It is possible to generate all types of elastic waves (bulk, surface and guided) by altering the heating pattern on the surface of a metal [70]. For example, using a technique known as cheap optical transducers (CHOT), surface acoustic waves (SAW) of a desired frequency can be generated (g-CHOT) [69] with pulsed laser excitation.

Here, a striped pattern of absorbing and reflective structures (grating pattern) printed or attached to the surface of a specimen induces laterally modulated thermal stresses. The frequency of the SAW is determined by the width and spacing of these structures. The same structures also aid in the detection (d-CHOT) of SAWs optically. In a d-CHOT, the height difference in the structure creates the desired path-length difference. The reflected continuous-wave laser gets separated into various diffraction orders and using an iris filter only the zeroth order (main reflection) is retained. A SAW propagating beneath the structure modulates the reflected light, which is detected by a photodiode and post-processed to obtain the measurement of the SAW.

Metals have a very short optical absorption depth. For a thick metal most of the incident laser energy gets reflected. As the thickness of the metal approaches its absorption depth, then its reflectance, transmittance and absorptance are all a function of both thickness and laser wavelength. The absorption depth for metals in which the intensity of the laser drops to $1/e$ of the value at the surface (ignoring the reflected intensity) is given by [71]

$$\frac{1}{\mu_a} = \frac{\lambda}{4\pi Im\left[\underline{n}(\omega)\right]}, \tag{2.20}$$

where, λ is the wavelength of the laser light and $\underline{n}(\omega)$ is the complex refractive index. The real part of $\mathrm{Re}\left[\underline{n}(\omega)\right]$ is the refractive index and is related to the phase velocity, and the imaginary part $\mathrm{Im}\left[\underline{n}(\omega)\right]$ is the extinction coefficient and is related to the absorption. The extinction coefficient of aluminium at 532 nm is 8.2709 [72], which gives an absorption depth of 7.7 nm. Since the absorption depth is very short and at the surface, the rise in temperature may cause melting, vaporisation or combustion of the surface material depending on the laser pulse duration and peak power [63]. Thermal confinement is difficult to satisfy for metals due to very short absorption depth and the high thermal diffusivity, which is three orders of magnitude faster in metals [73] compared to tissue [74]. For $\mu_\mathrm{a} = 1.3 \times 10^8\ \mathrm{m}^{-1}$ i.e., the inverse of the absorption depth calculated above and $\alpha_{th} = 9.7 \times 10^{-5}\ \mathrm{m}^2\ \mathrm{s}^{-1}$ [73], τ_{th} is 153 fs, calculated using Eq. (2.10). Similarly, τ_{ac} is 1.2 ps calculated using Eq. (2.15) with $c_0 = 6374\ \mathrm{m\ s}^{-1}$ [75].

2.2.1.1 Thin Metal Film Sources

The stringent requirements on the duration of the laser pulse means readily available nanosecond lasers used in biomedical photoacoustics are inefficient for LGUS. However, a significant performance improvement can be obtained by coating metal films (10–100 nm thick) with a few microns' of polymeric material [76], [77]. Here, the metal film transfers the thermalized heat owing to its high thermal diffusivity to the adjacent polymer layer, which has a relatively low thermal diffusivity. Therefore, stress confinement can be achieved in the polymer layer via heat transfer from the metal film.

Kang *et al*. [76], fabricated a LGUS source consisting of a 100 nm thick chromium film sandwiched between a 0.5 mm thick glass substrate and a 2 μm thick polydimethylsiloxane (PDMS) polymer. For a 5 ns laser pulse operating at 532 nm and a fluence of 20 mJ cm^{-2}, they measured a peak-positive pressure of 3.86 MPa using a 0.5 mm element diameter membrane hydrophone at a distance of 0.37 mm. In another similar study, Lee and Gou [77] fabricated a multi-layered source in which a 10 nm thick chromium film was sandwiched between two layers of PDMS. One of the PDMS layers was backed by a glass substrate through which the chromium was illuminated. On the other layer of PDMS (<1 μm thick) a 50 nm thick layer of aluminium was deposited. Chromium acted as a partially reflecting mirror while aluminium was completely reflecting thus a resonant optical cavity was formed in which more light was trapped. In this arrangement, a peak-positive pressure of 1.82 MPa was reported for a 6 ns laser pulse operating at 532 nm and a fluence of 2.35 mJ cm^{-2}. A custom-made membrane hydrophone of 0.5 mm element diameter was used to measure the LGUS pulses. Since not all of the experimental details – laser illumination area, measurement distance and the bandwidth of hydrophones – are available, it is not possible to say whether the cavity source of Lee and Gou is more efficient than the chromium-PDMS sandwich source of Kang *et al*.

2.2.2 Nanocomposites

A nanocomposite material has the advantage that it can be fabricated on most surfaces such as on the tip of an optical fibre to facilitate minimally invasive and multimodality imaging [78]–[80]. By using a large planar nanocomposite and a fast galvanic mirror to steer the laser, dynamic source arrays can be synthesised [81], [82]. Very small focal volumes can be produced by coating the material on an optical lens for precision targeted therapies at the millimetre scale [83] and arbitrary far-field beam patterns can be created using diffractive elements [84]. Consequently, there has been a considerable body of work over the last decade with an emphasis on producing high-pressure and broad bandwidth LGUS sources [80], [85], [86].

Nanocomposites usually consist of metallic or non-metallic nanoparticles within a bulk substance, which is usually a transparent polymer at the wavelength(s) of interest. The nanoparticles and the polymer could be homogenously mixed, or the nanoparticles could be deposited (chemically or mechanically) on a substrate and a layer of polymer subsequently deposited on top or infused within the nanoparticle structure. Nanoparticles exhibit different properties compared to their bulk counterpart due to their large surface-to-volume ratio, i.e., a greater proportion of the atoms in a nanoparticle are surface atoms compared to macroscopic particles. The large number of surface atoms changes many properties such as its ability to make tight bonds with foreign atoms and molecules increases, melting temperature is reduced, and light absorption, fluorescence, catalytic activity and selectivity become size dependent [87]. For example, the measured thermal conductivity of an exfoliated and suspended graphene sheet ranges from 2000–5000 W m^{-1} K^{-1} [88], whereas for bulk graphite (in-plane) it is 100–400 W m^{-1} K^{-1} [89]. When nanoparticles are added in small fraction to

a polymer, the nanoparticles change some of its bulk property. For example, the thermal conductivity of cured epoxy is 0.25 W m^{-1} K^{-1} and an addition of 0.5% by-weight multi-walled carbon nanotubes (MWCNT) increases its thermal conductivity to 0.29 W m^{-1} K^{-1} [89].

Light absorbing nanoparticles used in nanocomposites for LGUS have been typically carbon-based or metal-based. Allotropes of carbon such as graphite powder [90], carbon black (CB) [79], [91], carbon nanotubes (CNT) [83], [92]–[95], carbon nanofibers (CNF) [96], candle soot nanoparticles (CSNP) [97] and reduced graphene oxide (rGO) [98], [99] have been used. Once photons enter such nanocomposites their intricate structure traps the photons, i.e., the nanoparticles increase the scattering which reduces the optical penetration. In metal nanoparticles such as gold (Au), light is absorbed via a resonance mechanism known as surface plasmon resonance (SPR) when the dimensions of the nanoparticle are less than the wavelength of photons. In SPR, the electric field of the photons polarises the surface electrons (or the conduction band). A net charge difference occurs due to the polarisation of the surface electrons with respect to the positively charged core of the nanoparticle. Therefore, a net restoring force arises, which in turn gives rise to a specific plasmon resonance that is dependent on the geometry of the particle. In the depolarisation phase, electrons lose the acquired energy via non-radiative relaxation thus heating the nanoparticle [100]. The nanocomposites used to generate LGUS pulses in the MPa range have predominantly been carbon-based because they are strongly absorbing across the whole visible spectrum and hence, they appear black. Metal-based nanoparticles on the other hand have peak absorption over a narrow wavelength range due to SPR behaviour and their LGUS output have always been found to be lower when compared to carbon-based nanoparticles [85].

The thermal conductivity of carbon nanoparticles are three to four orders of magnitude larger than polymers [89] and at least two orders of magnitude larger for metallic nanoparticles [101]. Since the thermal diffusivity is directly proportional to the thermal conductivity, the two different rates of heat diffusion mean that most of the thermal energy is concentrated at the nanoparticle-polymer interface. The continued deposition of the thermal energy in a small region of the polymer during pulsed laser excitation causes the temperature to rise, which results in simultaneous rise in pressure leading to stress confinement provided that $t_p \ll \tau_{ac} \ll \tau_{th}$.

Historically, PDMS is the most frequently used polymer in nanocomposite fabrication due to its highest volume thermal expansion coefficient, β_v = 960 × 10^{-6} K^{-1} among all polymers [102]. (For small temperature ranges, the linear thermal expansion coefficient, $\beta_L \cong \beta_v/3$). The reason as to why the volume thermal expansion coefficient is cited as more important constituent of the Grüneisen parameter is because β_v of polymers varies by a factor of nearly 10 [102] compared to C_p or c_0, whose variation is smaller.

Nanocomposite fabrication of LGUS sources is an elaborate process compared to the thin film metal sources discussed in Sec. 2.2.1.1. This is because nanoparticles agglomerate due to the

presence of van der Waals electrostatic attractive forces between individual particles or molecules. In addition, the aspect ratio of some nanoparticles such as CNT and CNF can be over 1000, so they tend to tangle and form clusters [103]. The dispersion uniformity also deteriorates when increased amounts of nanoparticles are added to the polymer [103], which is generally required to increase the optical absorption of the nanocomposite. Therefore, many source fabrication approaches have been tried to overcome or bypass the difficulties of dispersion. This is discussed by Lee *et al.* in the book chapter "Efficient Photoacoustic Conversion in Optical Nanomaterials and Composites" [86], and the references contained therein provide the rationale behind each of the approaches. For conciseness, brief details are provided in the subsequent sections classified into two broad approaches which have demonstrated the possibility of generating MPa range pressure and bandwidth of tens of MHz (of direct relevance to the work undertaken in this thesis). The ultrasound pressure and bandwidth from select sources is listed in Table 2-1 in Sec. 2.2.3.

2.2.2.1 Dispersion

In the dispersion approach, the nanoparticles and the polymer are homogenously mixed through a series of chemical and mechanical processes. The first step in this method is most frequently to functionalise the nanoparticle. Functionalisation is a process in which the surface of the nanoparticle is modified so that the effect of van der Waals forces is lessened. Depending on the modification done to the surface, a covalent bond may form with the polymer molecule or re-aggregation is otherwise prevented from occurring during the dispersion process [104]. Nanoparticles such as MWCNT functionalised with chemical groups such as carboxylic acid (COOH-group) are combined in a large quantity of organic solvents such as toluene or xylene i.e., 100 mg in 10 mL in a glass vial and then sonicated. Bubbles introduced during sonication are removed under vacuum. The mixture is then combined with PDMS and a curing agent. The uncured nanocomposite is coated on surfaces, such as the end of an optical fibre or a glass slide, and finally oven cured to complete the process [105], [106]. Further improvements to the dispersion process has resulted in peak-to-peak LGUS pressure as high as 21.5 MPa [92]. In another technique, a glass substrate deposited with rGO was coated with PDMS-carbon black nanocomposite. Here, the rGO layer absorbs light and transfers the heat to the nanocomposite. Due to incomplete optical absorption within the rGO, the carbonised PDMS provided further optical attenuation thus generating higher pressures than the PDMS-only coating [99].

2.2.2.2 Dense Network Infiltration

The term "dense network infiltration" was coined for the purpose of this thesis to encapsulate all those methods in which an intricate network of nanoparticles was formed on a substrate. The intricate network is then infiltrated with PDMS to fill the gaps followed by oven curing to complete the fabrication. In order to further increase the optical absorption, in some cases the intricate network was

sputtered with gold nanoparticles before PDMS infiltration or on the surface after the intricate network was infiltrated with PDMS. In the following paragraphs several such methods are described.

As-Grown CNT network: A dense network of MWCNT was grown on a fused silica substrate using a chemical vapour deposition (CVD) technique [107]. To facilitate MWCNT growth on fused silica, 2 nm Fe and 5 nm Al_2O_3 catalyst layers were deposited and placed in a high temperature furnace at 775 ℃. A mixture of ethylene, hydrogen and helium gases were blown over the substrate. The MWCNT growth density was dependent on how long the substrate was left in the furnace. A tightly packed vertically aligned MWCNT forest would not allow any PDMS infiltration when spin coated. Therefore, the growth time was limited so that a vertically aligned MWCNT forest could not have time to form. A laterally tangled network of MWCNT, just before the vertical growth phase, was found to be most suitable for PDMS infiltration. A modified, reduced viscosity, PDMS was used in the spin coating to enable permeation of PDMS down to the silica substrate, which ensured adherence of the nanocomposite to the substrate. The optical absorption of this nanocomposite was only 80%, therefore a 20–30 nm layer of Au was deposited to elevate the absorption to over 90%. Finally, a few micrometres of PDMS was deposited by spin coating for complete encapsulation. The ablation threshold of this nanocomposite was found to be 190 $\mathrm{mJ\,cm^{-2}}$ when tested using a 6 ns pulsed laser operating at a wavelength of 532 nm [107]. One possible disadvantage of this technique is that it is very process-intensive since the fabrication involves several controlled steps.

Chemical Vapour Deposition Spinning: CVD spinning is a technique developed for producing a continuous yarn of CNTs [95]. Here, a liquid carbon source containing acetone and methanol dissolved with ferrocene and thiophene catalysts is mixed with hydrogen and injected through a hot reaction flow chamber. The CNTs self-assemble via van der Waals interactions into a multi-layered sock in the flow chamber, which is captured and spun on a spindle. A multi-layered CNT yarn was laid on a substrate and 10 nm gold nanoparticles were sputtered sparsely on the surface. PDMS was spin-coated to infiltrate the CNT yarn. The thickness of the nanocomposite was 5 μm, which was backed with a PDMS-only layer of 40 μm [95]. Like the *As-Grown CNT network*, this technique is also process-intensive.

Electrospinning: This is a high electrostatic voltage driven polymer fibre formation process used to produce fibres of diameters from nanometre to micrometre range[108]. The setup comprises of a polymer fluid reservoir flowing through the tip of a blunt needle and a large collector plate. When a high DC electric field is applied between the needle tip and the plate, an electric charge is induced on the liquid surface. If the electric field is sufficiently high, then the repulsive electrical forces between the polymer molecules overcome the surface tension forces. The electric forces deform the meniscus at the needle tip to a cone shaped charged liquid, which is ejected unstably towards the plate forming fibre deposits [108]. Electrospinning has been used to form laterally tangled network of MWCNT and CNF fibres, on the tip of optical fibre and glass substrate, which was later infiltrated with PDMS [93], [96]. Using this technique, a greater control on the nanocomposite thickness was

demonstrated ranging from 2.3–41.4 μm [93]. This is advantageous since acoustic attenuation in the nanocomposites is significantly higher compared to water [109], [110]. Therefore, if the nanocomposite thickness is greater than the optical absorption depth (the depth required to absorb the light) then much of the wave is attenuated unnecessarily within the nanocomposite before it is coupled to water.

Vacuum Filtration and Transition: In this technique, MWCNT dispersed in 2% by-weight sodium dodecyl sulphate aqueous solution was filtered through an anodic aluminium oxide filter whose diameter and pore size were 47 mm and 0.2 μm, respectively [94]. After filtration, the filter paper with MWCNT was attached to a PMMA substrate and spin coated with PDMS to infiltrate the porous MWCNT network. A further PDMS-only layer was spin coated to facilitate stress confinement via heat transfer from the nanocomposite. The thickness of the nanocomposite was 0.3 μm and the PDMS-only layer was 4.5 μm [94]. The advantage of this technique is that the overall nanocomposite is inherently thin, which reduces the acoustic attenuation within the nanocomposite.

Candle Soot Nanoparticles: The incomplete combustion of candle wax produces impure carbon nanoparticles known as soot. The CSNP were captured by simply placing a glass slide above the candle flame [97]. The scanning electron microscopy images sized the particles to be around 50 nm. PDMS was infiltrated into the CSNP by a direct transfer approach in which a glass slide spin coated with uncured PDMS was put in contact with CSNP coated glass slide. The thickness of the PDMS infiltrated CNSP was 6 μm and the PDMS-only layer was 20 μm [97]. The technique is relatively simple and requires only a few standard pieces of laboratory equipment to fabricate the nanocomposite.

2.2.3 Performance Comparison

The LGUS peak-positive pressure and bandwidth (−6 dB) obtained from the nanocomposite sources discussed in Sec. 2.2.2 are summarised in Table 2-1. It is instructive to compare the LGUS output from various nanocomposite sources because it dictates the fabrication requirements for obtaining a maximum LGUS output. In this regard, LGUS conversion efficiency, η, a unitless parameter (not to be confused with Grüneisen, Γ or the LGUS efficiency parameter, ₹) was first provided by Biagi *et al* [90], which is frequently used in the literature for estimating the nanocomposite efficiency. The parameter, η, is defined as

$$\eta = \frac{E_{aco}}{E_{opt}}, \tag{2.21}$$

where, E_{opt} is the optical energy and E_{aco} is the acoustic energy, given by

$$E_{opt} = \Phi A, \tag{2.22}$$

$$E_{aco} = A \int \frac{p^2(t)}{\rho_0 c_0} dt. \tag{2.23}$$

Here, A, is the area. The integral in Eq. (2.23) is normally performed over the duration of the time-gated acquisition window.

Inserting Eq. (2.22) and (2.23) in Eq. (2.21) gives

$$\eta = \frac{1}{\Phi} \int \frac{p^2(t)}{\rho_0 c_0} dt. \tag{2.24}$$

Here, Eq. (2.24) assumes a single point measurement of the instantaneous acoustic pressure is sufficient to estimate the opto-acoustic efficiency. But in practice, neither the optical illumination on the nanocomposite nor the acoustic field at the measurement plane are uniform, which deems Eq. (2.24) not representative of the whole beam. Additionally, there are several shortcomings that prevent a comparison of nanocomposites accurately from a metrological perspective, such as the use of different hydrophones whose frequency responses (or bandwidth) were not known accurately, spatial averaging error, absorption of the LGUS pulse along the propagation path in water, wavelength dependent optical absorption of the nanocomposite, different laser pulse durations, and not knowing the extent to which the stress confinement criterion was satisfied in any of the nanocomposites.

Table 2-1: Summary of findings from literature review, which provides an account of the current state-of-the-art in the area of LGUS nanocomposite sources.

Optical absorbing source material			Laser excitation parameters				LGUS pulse parameters		
Ref.	Type	Source thickness [μm]	λ_p [nm]	t_p [ns]	Energy/ Power density/ Fluence	Spot-dia. [mm]	Meas. distance [mm]	Peak-positive pressure [MPa]	–6 dB BW [MHz]
[95]	PDMS/Au-CNT yarn-PDMS	6.0	532	6	45.0 mJ cm^{-2}	5.0	4.9	33.6	15*
[94]	PMMA/CNT-PDMS	0.7	532	8	180.0 mW cm^{-2}	40.0	–	3.2	15*
[93]	Fibre/MWCNT-PDMS	13.7	1064	2	35.0 mJ cm^{-2}	0.2	1.5	1.6	30*
[92]	Fibre/MWCNT-PDMS	20.0	1064	2	33.1 mJ cm^{-2}	0.2	3.0	1.4	29
[97]	Glass/CSNP-PDMS	24.4	532	6	3.6 mJ cm^{-2}	10.0	4.2	4.8	21
[99]	Glass/rGO-PDMS	11.0	532	5	35.7 mJ cm^{-2}	10.0	3.0	4.8	40*
[96]	Glass/CNF-PDMS	57.9	532	4	3.7 mJ cm^{-2}	12.0	3.7	12.2	10*
[79]	Fibre/CB film	1.0	1064	0.5	50.0 μJ	0.2	0.5	2.8	34*
[98]	Glass/rGO-Al layer	0.1	532	5	43.0 mJ cm^{-2}	–	2.8	4.5	30*
[83]	Glass/MWCNT-PDMS	16.0	532	6	42.4 mJ cm^{-2}	0.1	5.5	22.0	23

* *Estimated values from the data reported within each paper.*

In Ref. [83] the source material was fabricated on a concave lens.

Another form of Eq. (2.24) was derived recently by Lee *et al* [77] in which the pressure pulse, $p(t)$, was assigned a Gaussian shape assuming a long pulse regime, i.e., the LGUS pulse duration has the same temporal shape and duration as that of the laser pulse. Such a condition may be satisfied when $t_p \gg 1/c_0\,\mu_a$. For a Gaussian pressure pulse, the integral $\int_{-\infty}^{\infty} p^2(t)dt = 0.75 p_0^2 t_p$ and therefore, the photoacoustic conversion efficiency becomes

$$\eta = 0.75\frac{p_0^2 t_p}{\rho_0 c_0 \Phi}. \tag{2.25}$$

Although Eq. (2.25) overcomes the issues of hydrophone-based measurements its applicability is very restrictive since it holds for only long Gaussian pulses. Therefore, intercomparing the LGUS output from various nanocomposite sources using a single metric is not as trivial as suggested by Eq. (2.24) and (2.25).

2.3 LGUS Source Characteristics

It is clear from the literature review that LGUS has a potential as an alternate source over piezoelectric transducer technology for generating high amplitude and broadband acoustic field. Also, the acoustic field should be spatially broad relative to the maximum sensing dimension of the hydrophones such that errors related to spatial averaging can be ignored. It is of at most importance that the LGUS source is temporally stable during the course of the calibration of hydrophones on the interferometer. Since the calibration involves measurement of acoustic displacement or velocity and hydrophone voltage signals which are acquired sequentially, therefore the long-term stability of the LGUS over days, months or years is not relevant. The key characteristics required from a LGUS source is listed as follows:

1. The LGUS pressure-pulse should have a frequency range that makes measurements possible up to 100 MHz and the amplitude of the Fourier transform of the acoustic displacement signal at all frequencies within the bandwidth should be at least 50 pm.

2. The spatial averaging of the LGUS beam by the hydrophone being calibrated should produce significantly lower errors compared to the current best practice (focused ultrasound fields) at all frequencies i.e., errors should be 1% or below.

3. The variation in the calibration of a hydrophone arising from the temporal stability of LGUS pulses over six repeat measurements involving a pair of acoustic displacement and hydrophone voltage signals should be less than 2%, which is typical when using a piezoelectric source. Also, the long-time temporal stability should span at least three hours, which is the duration required to calibrate at least one hydrophone on the interferometer.

4. The LGUS source must not contaminate the water (e.g., affect its conductivity) i.e., the source must not release nanoparticles into water.

5. The LGUS source must not present a laser hazard to the user i.e., the laser beam should be completely enclosed.

6. The temperature rise in the LGUS source must not elevate the temperature of the water, thereby affecting the temperature dependent sensitivity of the hydrophone.

2.4 Thesis Content

The nanocomposites sources fabricated and tested in this thesis comprises of MWCNT dispersed in polymeric materials. The characterisation of the nanocomposite sources and the ultrasound generated from each of the sources forms the core aspect of this thesis. Unlike the fabrication methodologies described in Sec. 2.2.2, the dispersion method undertaken in this thesis is simpler, easily reproducible and the acoustic output is on par with many of the nanocomposites sources listed in Table 2-1.

Chapter 3 looks at the initial experimental work in which various nanocomposite sources were fabricated and tested based on previous work reported in the literature. A total of 27 different sources were fabricated by varying the amount of carbon nanotubes in three different polymers, over three thickness ranges, and were all backed on a laboratory grade glass slide. The effect of polymer type, the amount of carbon nanotubes in each polymer, source thickness and laser fluence were assessed. Unlike previous studies, the work presented in this chapter is distinct for three reasons: i) A broadband membrane hydrophone with extrapolated response up to 110 MHz was used to measure the LGUS and the details of hydrophone waveform deconvolution is provided ii) The long-time temporal stability of the nanocomposites was tested under sustained laser excitation for periods up to three hours for their suitability as a stable source of ultrasound and iii) Via numerical modelling (covered separately in Chapter 4) it was confirmed that the measured LGUS pressure-pulses under various laser fluences were all nonlinear at the measurement location.

In Chapter 4, an investigation into the nonlinear propagation of mega-Pascal range laser-generated ultrasound, and the effect of the bandlimited hydrophone response, using a numerical wave solver (k-Wave) was performed.

Chapter 5 investigates the effect of glass backing (acoustically hard) and polymer backing (acoustically soft) materials on LGUS from nominally identical nanocomposites. The experimental work led to a novel finding, which provides new insights on how LGUS is affected by the backing material. When the duration of the laser pulse does not satisfy stress confinement, the peak-pressure from the glass-backed nanocomposite sources can be significantly higher relative to the polymer-backed sources. The ratio of glass-backed over polymer-backed pressure amplitudes continues to increase with the duration of the laser pulse eventually reaching a limiting value, which is a function

of acoustic pressure reflection coefficients of the interfaces in which the source is positioned. The experimental findings were validated with analytical and numerical models.

Chapter 6 addresses the final design, fabrication and testing of a submersible, laser-generated, plane-wave, broadband LGUS source device. The device is based on a glass-backed nanocomposite source, which consists of four replaceable source elements. An assessment of the improvements gained in the measurement frequency range, spatial averaging errors, and measurement repeatability up to 100 MHz is made with piezoelectric sources used for the calibration of hydrophones at NPL.

The overall conclusions and future work are presented in Chapter 7.

Chapter 3

Initial Source Design

3.1 Introduction

In this chapter, the fabrication and testing of the nanocomposite sources is laid out in detail. In Sec. 3.2, the experiments used to determine the optimal values for the various fabrication parameters of the nanocomposite sources are described. The parameters include the amount of multi-walled carbon nanotubes (MWCNT) required to be dispersed in a polymer to reach mega-Pascal (MPa) acoustic pressures, and how best to put a thin layer of nanocomposite onto a glass backing. A dedicated test setup was put together to test various nanocomposites under different fluence conditions. The characteristics of the test setup, which consisted of an automated scanning tank, pulsed laser, and a broadband hydrophone, are described in Sec. 3.3. The laser-generated ultrasound (LGUS) pulses generated by various nanocomposites were measured and assessed as a function of the polymer type, CNT content in the polymer, nanocomposite thickness, laser fluence, and the stability of nanocomposite sources under sustained laser excitation. The results are discussed in Sec. 3.4. Nonlinear steepening was observed in the LGUS pressure pulses measured at a distance of 7.4 mm from the nanocomposite. Also, there were undulations on the trailing side of the pulse, an indication of the bandlimited hydrophone response, which is known to introduce ringing artefacts in the measured response. These observations are numerically investigated using a model of nonlinear propagation in Chapter 4.

3.2 Source Fabrication

The nanocomposite sources were fabricated by mechanically dispersing MWCNT in polymeric matrices, which will be henceforth referred to as carbon-polymer nanocomposite (CPN) sources. In order to arrive at a suitable CPN source, which can generate MPa range pressures and a frequency range that makes measurement possible up to 100 MHz, CPN fabrication parameters such as the polymer type, weight fraction of the MWCNT in the polymer, and the thickness of the CPN source were varied. Though polydimethylsiloxane (PDMS) is the predominant polymer matrix employed in the fabrication of nanocomposites for LGUS, the stability of PDMS-based nanocomposites under

sustained laser excitation is not known. Therefore, two other polymers were included in the scope of this exploratory work: (i) epoxy resin—given its widespread use in industrial applications due to its high mechanical strength, thermal and chemical resistance, and (ii) polyurethane—for its application as phantoms in ultrasound quality assurance measurements.

The MWCNT (Haydale Ltd., Ammanford, Carmarthenshire, U.K.) were mechanically dispersed in the polymer using a high-speed shear mixer (DAC 150.1 FV-K, SpeedMixer™, High Wycombe, U.K.). As per the specifications from Haydale Ltd., the diameter and the length of individual MWCNT were 10 nm and 1.5 µm, respectively. Although the supplied MWCNT were functionalised to contain carboxylic-acid (COOH) groups, the effect of functionalisation on the quality of dispersion or fabrication was not studied separately. The MWCNT, polymer, and catalyst (curing agent) were all combined by their weight fractions (wt. %). The MWCNT were dispersed in the polymer at 3500 rpm for 2 min followed by addition of the catalyst, and shear mixed again at 3500 rpm for 2 min. At 1.25 wt. % of MWCNT in polymer, the viscosity of the resulting mixture still resembled the viscosity of the base polymer and at 3.5 wt. % the mixture had become more like a thick paste. The stiffness of the paste rapidly increased beyond 3.5 wt. % MWCNT content therefore, at these high wt. % it was not possible to make thin films. A total of 27 variations of the CPN sources were fabricated. The polymer types were epoxy, polyurethane (PU) or PDMS; the three wt. % of MWCNT in polymer were 1.25, 2.5, or 3.5 wt. % and the thicknesses were 17–28, 51–55, or 71–85 µm. The MWCNT-polymer mixture was used to coat a laboratory-grade glass slide. The polymer types and their curing conditions are given in Table 3-1.

Table 3-1: Polymer types employed in the preparation of carbon-polymer nanocomposite sources. Mix ratios quoted in the table are for pure polymers only. To prepare the nanocomposite, the mass of the base material was adjusted to accommodate the required percent weight content of the MWCNT (1.25, 2.5, or 3.5 wt. %).

Polymer type (Product)	**Supplier**	**Mix ratio by weight (base:catalyst)**	**Curing conditions**
Epoxy resin (Araldite)	Huntsman Advanced Materials, Duxford Cambridge, UK	Araldite LY 564: 10 g Aradur 2954: 3.5 g	Oven cured for 12 hours at 70 C
Polydimethylsiloxane (SYLGARD® 184)	Dow Corning Corporation, Auburn, MI, USA	Elastomer: 10 g Cure accelerator: 2 g	Oven cured for 35 mins at 100 C
Polyurethane (Polycraft FC-6630)	MB Fibreglass, Newtownabbey, Northern Ireland, UK	Polyol (Part A): 5 g Isocyanate (Part B): 5 g	Oven cured for 12 hours at 40 C

3.2.1 Blade Film Applicator

Thin film applicators are precision wet film application devices used to meet the quality requirements of the coatings industry. The American Society for Testing and Materials, a non-profit voluntary standards development agency, has developed a standard [111] that outlines best practices for

applying uniform coatings such as paints and varnishes. The blade film applicator is one such technique in which a height adjustable knife-edged metal frame attached to a micrometre controls the gap clearance relative to a flat surface, e.g., a glass slide. A thin film is produced when the excess mixture spread on the glass slide is removed by sliding the knife-edged metal frame over the length of the glass slide. A glass-backed CPN source is formed after oven-curing the thin film. The length and width of the glass slides used here were 76 × 26 mm, respectively. The thickness of the glass sides were nominally 0.8 mm. A height adjustable blade film applicator with a 10 μm step resolution was procured from Sheen Instruments (West Molesey, Surrey, UK) for producing thin nanocomposite films.

The blade film applicator setup shown in Figure 3-1 consists of an aluminium flatbed with guide rails to assist a steady horizontal motion of the blade. A glass slide is placed between the height-adjustable knife edge, controlled by a pair of micrometres (10 μm resolution), and the flat surface. The glass slide was temporarily held on the surface using masking tape. The knife edge wass zeroed by pushing it down on to the glass surface and then raised to the required height, which determines the thickness of the CPN film to within the resolution of the micrometre. The film applicator is then carefully lifted out of the setup to allow a thick layer of CPN to be spread across the surface of the glass. The film applicator is placed back on the setup and is drawn across the length of the coated surface leaving a thin layer of CPN on the glass. The excess CPN on all the surfaces are wiped and cleaned using acetone and then methanol. The masking tape is removed, and the CPN coated glass slide is cured in an oven at the temperature listed for each polymer type in Table 3-1. The thickness of the cured film was determined by measuring the difference in thickness between the uncoated glass slide and the coated glass slide using a 1 μm resolution calibrated micrometre. This technique was found to be applicable for all three polymer types as their viscosities allowed application of thin films on glass slides.

It was found that the thickness uniformity of the purchased laboratory-grade glass slides could vary between 2 to 5 μm over the length of the glass slide, i.e., the thickness of the glass slide progressively decreased from one end to the other. This variation was not thought to be a limiting factor in this preliminary study. It is possible that the final source could be coated over an optical flat whose thickness variations are typically less than 100 nm. The variation in inter and intra thickness of the thin films of CPN on glass backings, fabricated using the method described above, is shown in Figure 3-2 for an epoxy-based CPN with 2.5 wt. % MWCNT. The aim was to produce CPN film thicknesses of approximately 25, 50 and 75 μm. The variations arise from measurement and experimental systematic effects such as the step resolution of the micrometre, variation in the thickness of the glass slides, and shrinkage of the CPN whilst curing. Given the variation in the thickness of the CPN source, at least three samples were produced for each of the 27 CPN source types to allow a selection such that the sources were close to the three distinct thickness values: 25, 50 and 75 μm. However, for the case of PDMS-based CPN sources, the thicknesses were found to be

consistently lower by 30%. Volumetric shrinkage of PDMS at a cure temperature of 120 ℃ for a polymer:catalyst ratio of 6:1 is reported to be only 2.75% [112]. Therefore, it appears that the addition of MWCNT may have interfered with the polymerisation process whilst curing and causing it to shrink by an unusually high factor. Also, CPN sources of approximately 10 µm thickness were fabricated, one sample each, for epoxy, PU and PDMS-based CPNs with 2.5 wt. % MWCNT.

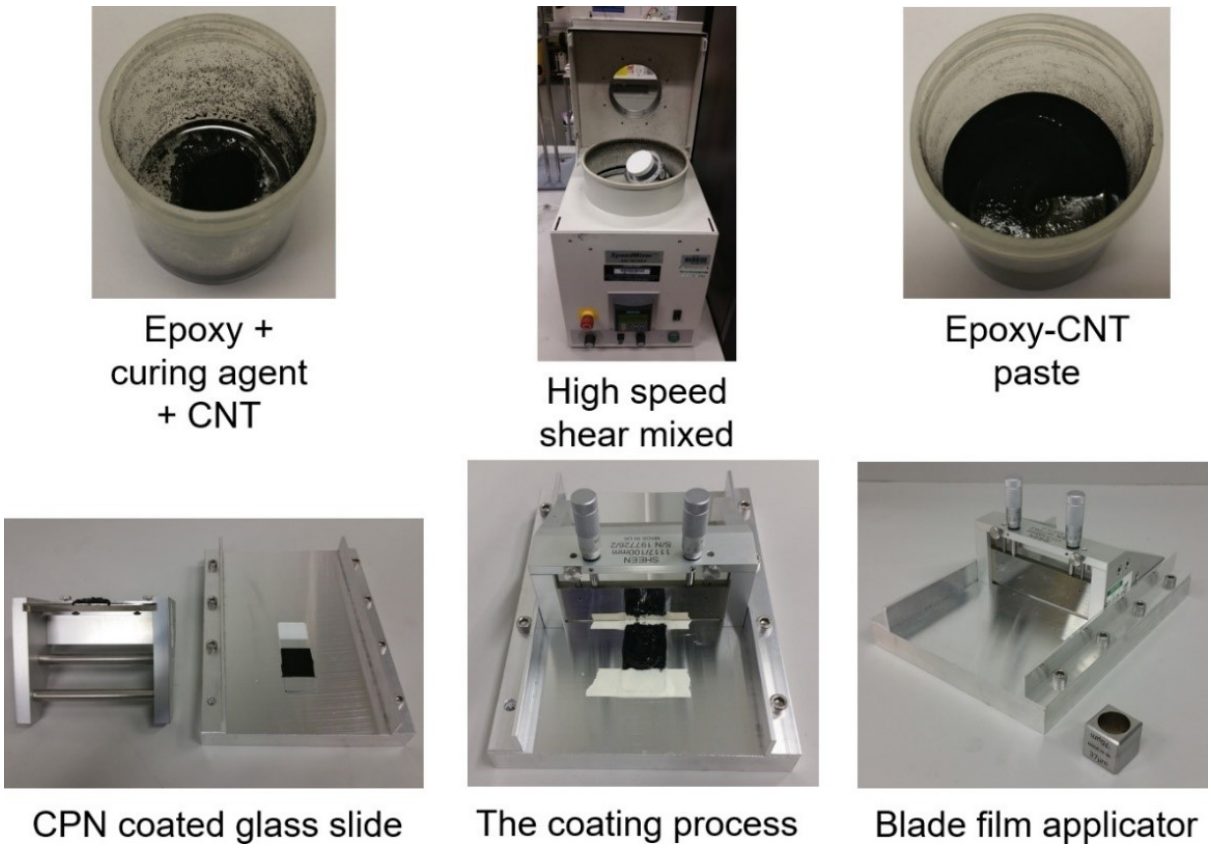

Figure 3-1: The CPN fabrication process is shown clockwise in the above images. The required amounts of epoxy, curing agent and CNT are added to a plastic jar. The jar is sealed and placed in a high-speed shear mixer. The mechanical shear mixing combines all the ingredients to form a paste. A blade film applicator is used to lay thin films of the paste on a glass slide. The film thickness is controlled by the two micrometres which moves the knife edged metal frame from the glass surface to the required height. The glass slide is held on the flat bed with masking tape and its surface spread with freshly prepared CPN paste. A CPN coated glass slide is formed after sliding the blade film applicator over the coated surface. The coated glass slide is oven cured, which completes the fabrication process.

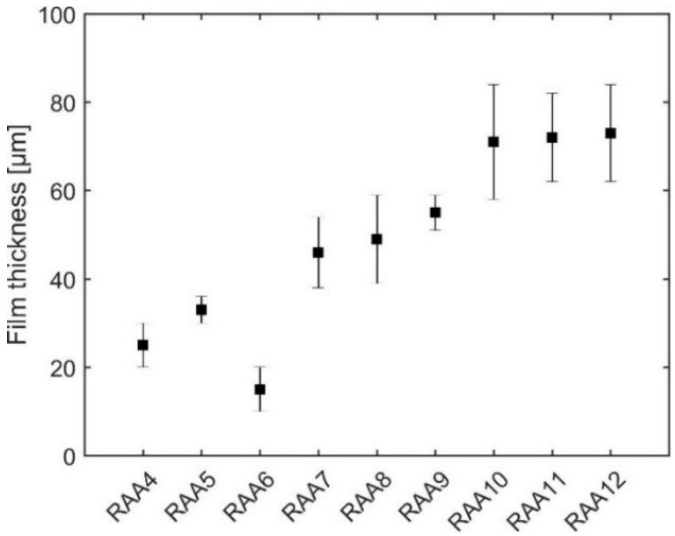

Figure 3-2: A range of film thicknesses produced using the blade film applicator for an epoxy-based CPN with 2.5 wt. % MWCNT. The aim was to produce CPN film thicknesses of approximately 25, 50 and 75 µm. The thickness of the CPN film was derived from differences in thicknesses of bare glass and glass coated CPN post curing. The error bars represent one standard deviation. The standard deviation was estimated from six measurements taken over an area of 20 × 20 mm in the central region of the coated area.

3.2.2 CPN Test Sources

The final set of glass-backed CPN sources fabricated by varying the polymer type, wt. % of MWCNT in the polymer, and the thickness are listed in Table 3-2. The experimental setup in which these sources were tested is described in Sec. 3.3.

Table 3-2: The final set of 27 CPN sources fabricated and tested in this study by varying the polymer type, MWCNT wt. % and CPN film thickness. The standard deviation in the film thickness was in the range of 4–10 µm.

Polymer type	1.25 wt. % MWCNT		2.50 wt. % MWCNT		3.50 wt. % MWCNT	
	id	Thickness (µm)	id	Thickness (µm)	id	Thickness (µm)
Epoxy	RAC3	27	RAA4	24	RAD1	26
	RAC4	55	RAA9	55	RAD7	55
	RAC9	71	RAA10	71	RAD9	59
PU	TAC2	28	TAA6	31	TAD4	27
	TAC6	51	TAA9	51	TAD7	54
	TAC8	85	TAA11	78	TAD8	75
PDMS	SAC1	17	SAA6	17	SAD3	19
	SAC4	36	SAA9	33	SAD4	34
	SAC7	51	SAA12	52	SAD8	55

3.2.3 Spectrophotometer Measurements

The optical absorption coefficient, μ_a, of the CPN sources was measured using a dual-beam spectrophotometer (Lambda 750, Perkin Elmer, Waltham, Massachusetts, USA) at University College London (UCL) over a wavelength range of 500–1100 nm in 10 nm steps. The measurements were repeated three times close to the centre of the CPN coated surface covering an area of 2 × 5 mm. The measurements were made only on samples of thicknesses 17–31 µm, as the optical transmittance for the other two thickness ranges was too low and hence the measurements were unreliable. The results are plotted in Figure 3-3 and listed in Table 3-3. The tabulated values are an average of 1060 and 1070 nm measurements, which is close to the experimental laser wavelength of 1064 nm.

From Table 3-3, it is seen that μ_a is approximately linear with wt. % for both epoxy and PDMS polymers. The coefficient of determination, R^2, for a linear regression fit with zero intercept was 0.99 and 0.98 for epoxy and PDMS, respectively. In case of PU, the relationship of μ_a with wt. % is not linear. These results were confirmed by making independent repeat measurements and using a different single-beam spectrophotometer (400–900 nm, Lambda 850, Perkin Elmer, Waltham, Massachusetts, USA) at National Physical Laboratory (NPL) to rule out potential measurement errors. It is possible that either the relationship is not expected to be linear or there was a user error when weighing the MWCNT for 2.5 wt. % inclusion into PU since the value of μ_a at 2.5 wt. % is low compared to epoxy and PDMS at the same wt. %.

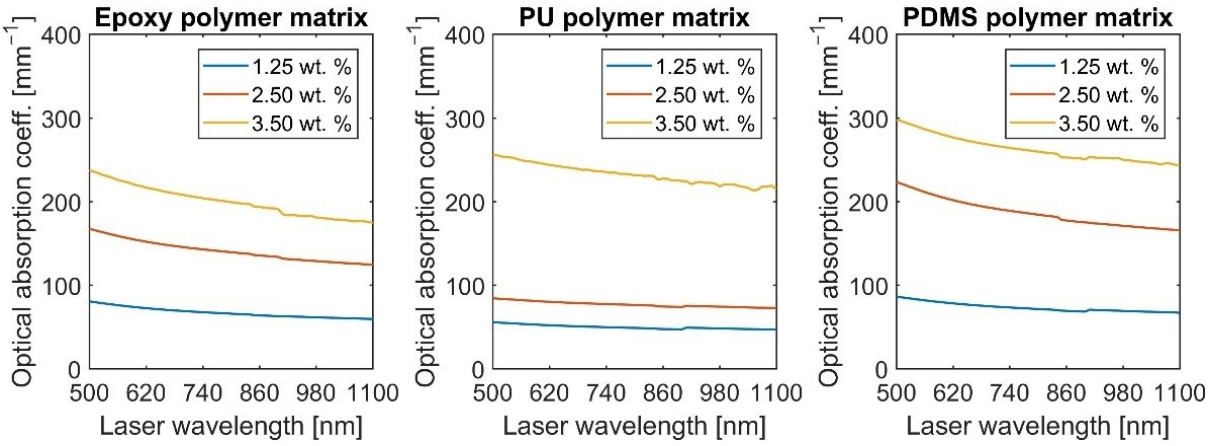

Figure 3-3: Optical absorption coefficients measurement, $\mu_a(\lambda)$, of epoxy, PU and PDMS-based CPN sources with 1.25, 2.5 and 3.5 wt. % of MWCNT over a wavelength range of 500–1100 nm in 10 nm steps. The measurements represent an average of three repeats approximately close to the centre of the CPN coated surface. The worst-case standard deviation across the measurements was 3%.

Table 3-3: The optical absorption coefficient, μ_a, of epoxy, PU, and PDMS-based CPN sources dispersed with 1.25, 2.5, and 3.5 wt. % MWCNT. The quoted values represent an averaged value of measurements at 1060 and 1070 nm.

Polymer matrix	Weight content of MWCNT		
	1.25 wt. %	2.50 wt. %	3.50 wt. %
	Optical absorption coefficient, μ_a [mm^{-1}]		
Epoxy	60	125	176
PU	47	73	216
PDMS	68	167	245

The measurement of optical absorption coefficients can be used to estimate the stress relaxation time, τ_s, thermal relaxation time, τ_{th}, initial temperature rise, T_o, and initial pressure amplitude, p_o, if the other relevant physical properties of the CPN sources are also known. The measurement of all the relevant physical properties of the nine CPN variants (three polymers and three MWCNT wt. %) was beyond the scope and means of this project, therefore, just the values of the polymer matrix available from manufacturer specifications sheet, online databases and via literature search were used. The one exception was the measurement of sound-speed and acoustic absorption, which were measured on NPL's acoustic characterisation facility [113]. The physical properties of the three polymer matrices are listed in Table 3-4. These values along with the three nominal values of optical absorption coefficients representing the three MWCNT wt. % were used in Eq. (2.1), (2.9), (2.10) and (2.15) to calculate the estimated parameters listed in Table 3-5.

It is interesting to see that the Grüneisen parameter is 25% higher for epoxy compared to PU or PDMS, both of which have similar values. Though the volume thermal expansivity is at least a factor of four higher for PDMS compared to epoxy, the sound-speed of epoxy, which is a factor of 2.5 higher than PDMS plays a significant role in elevating the Grüneisen parameter given that $\Gamma = \beta_v c_0^2 / C_p$. These calculations suggest that epoxy should produce higher LGUS output compared to PDMS for the same absorbed energy density. However, the high sound-speeds of epoxy and PU put a constraint on the laser pulse duration, which is required to be sufficiently lower than the stress relaxation time to ensure stress confinement, thereby maximising the acoustic pressure. Historically, PDMS has been the first choice in the fabrication of LGUS sources guided by polymer's largest thermal expansion coefficient. Therefore, no data exists where epoxy and PDMS nanocomposite sources were compared to demonstrate that epoxy was a better alternative over PDMS. In this thesis, the pulse duration of the laser, which is 4 ns is not adequate to satisfy stress confinement in any of the CPN sources and therefore, a like-with-like comparison of the CPN sources was not possible.

Table 3-4: Physical properties of polymer matrices, borosilicate glass and water*. The other values were obtained from manufacturer specifications sheets, online databases and via literature search [89], [102], [114]–[120].

Material	Volume thermal expansion coefficient, β_v	Specific heat capacity, C_p	Sound-speed @ 5 MHz, c_0	Calculated Grüneisen parameter, Γ	Mass density, ρ_0	Thermal conductivity, κ_{th}
	$[10^{-6}\,K^{-1}]$	$[J\,kg^{-1}\,K^{-1}]$	$[m\,s^{-1}]$	[Unitless]	$[kg\,m^{-3}]$	$[W\,m^{-1}\,K^{-1}]$
Epoxy	217	1600	2577	0.90	1097	0.19
PU	280	1800	2122	0.70	1050	0.15
PDMS	907	1350	1052	0.74	970	0.27
Glass	8.4	700	5640	0.38	2230	1.1
Water	214	4184	1482.5	0.11	998.2	0.56

* *The values reported are at laboratory temperatures and atmospheric pressure except water, which is quoted at 20* ℃.

Table 3-5: Estimated relaxation times, initial temperature rise and initial pressure amplitude of the nine variants of the CPN sources (three polymers each with three MWCNT wt. %). The physical properties tabulated in Table 3-4 along with nominal optical absorption coefficients representing the three MWCNT wt. % tabulated in this table and an assumed laser fluence of 100 $J\,m^{-2}$ (or 10 $mJ\,cm^{-2}$) were used in the calculations.

Polymer matrix	Optical absorption coefficient, μ_a	Thermal relaxation time, τ_{th}	Stress relaxation time, τ_{ac}	Initial pressure amplitude, p_0	Initial temperature rise, T_0
	$[m^{-1}]$	[μs]	[ns]	[MPa]	[K]
Epoxy	64000	564	6.1	5.8	3.6
PU		769	7.4	4.5	3.4
PDMS		296	14.9	4.8	4.9
Epoxy	146000	108	2.7	13.1	8.3
PU		148	3.2	10.2	7.7
PDMS		56.9	6.5	10.9	11.1
Epoxy	210000	52.4	1.8	18.9	12.0
PU		71.4	2.2	14.7	11.1
PDMS		27.5	4.5	15.6	16.0

3.3 Experimental CPN Test Procedure

3.3.1 The Test Setup

The LGUS experimental procedure used to characterise the CPN sources is described in this section. Broadly, this includes a test setup with an automated scanning tank, pulsed laser, a broadband membrane hydrophone, and a procedure to account for the hydrophone response to convert the measured hydrophone voltage pulse to units of pressure. The test setup used to measure the LGUS responses from the CPN sources is shown in Figure 3-4. A Q-switched, flashlamp-pumped, Nd:YAG (neodymium-doped yttrium aluminium garnet) pulsed laser (Nano 120-S, Litron Ltd, Rugby, U.K.) operating at 1064 nm with a full-width half-maximum of 4 ns, peak energy of 120 mJ per pulse and a maximum pulse repetition rate (PRR) of 20 Hz was used for the study. The expanded beam from the laser was homogenised using a 1500 grit ground glass optical diffuser (ODI). The homogenised beam was weakly converged using a plano-convex lens of 100 mm focal length to minimise the losses due to scatter caused by the ODI before passing through the clear polymethylmethacrylate (PMMA) wall of the water tank. A membrane hydrophone (UT1602, Precision Acoustics Ltd., U.K.) with a nominal element diameter of 0.2 mm was used to measure the LGUS response. A 5-axis gantry with rotation and tilt facilitated by a two-axis manual goniometer stage, and three motorised linear axes (LNR50S/M, Thorlabs, Ely, U.K.) was used for scanning the LGUS field, and was controlled by dedicated software (UMS2, Precision Acoustics Ltd., Dorchester, U.K.). A photodetector (PD) placed near the ODI provided a trigger to the digital oscilloscope (TDS7254, Tektronix, Beaverton, OR). The sampling rate and the record length were set to 2.5 GHz and 1250 sample points, respectively, which gives a spectral frequency resolution of 2 MHz (limitations in the oscilloscope settings meant that a short acquisition window was always accompanied with a high sampling rate). A thermocouple placed inside the PMMA tank was used to record the water temperature. The laboratory operating conditions maintained the temperature of the water to around 20 ± 1.0 ℃. Each measurement record consisted of acquiring 32 LGUS pulses sequentially using the UT1602 hydrophone and correcting each pulse for fluctuations in the laser energy (pulse-pulse variation was 2.5% after a one-hour warm-up period) using the peak voltage of the PD signal acquired simultaneously. The corrected LGUS pulses were averaged and stored for later analysis. All measurements were taken at an axial distance of 7.4 mm (or 5 μs time-of-flight) from the CPN source. The axis convention adopted in the IEC 62127-1 standard is used in this thesis: the propagation direction is the *z*-axis, vertical movement of the hydrophone is the *y*-axis, and the movement of the hydrophone with respect to the floor of the water tank is the *x*-axis.

3.3.2 Laser Fluence

It is essential that the CPN sources are tested under known illumination conditions in order to (a) characterise and compare the LGUS signals from various CPN source types, (b) understand the requirements of the excitation laser to achieve the desired pressure amplitude and bandwidth of the

eventual LGUS pulse, and (c) test the temporal stability of CPN sources under sustained laser excitation. Therefore, the fluence at the test position of the CPN source within the PMMA tank was characterised for various fractional output energy settings of the excitation laser, which was controlled by a custom fit motorised phase retarder $\lambda/2$ wave-plate. The laser energies at the CPN test position were measured using a 20 mm diameter pyroelectric energy sensor (ES220C, Thorlabs, Ely, U.K.). The laser beam-area was indirectly determined by scanning the LGUS beam from an epoxy-based CPN source using the hydrophone. A raster scan was completed over an area of 1.5 cm × 1.5 cm with 0.25 mm step size at an axial distance of 7.4 mm with the peak energy of the laser set to approximately 12 mJ. The beam-area of 0.8 cm^2 was estimated by summing the areas of all the pixels at which the beam energy was greater than or equal to 10% (or –20 dB) of the peak value in the image. This beam-area was then used to calculate the fluence, mJ cm^{-2}, at a number of energy settings of the laser. The beam-area was also determined at one other energy level of 25 mJ and using PU and PDMS-based CPN sources. The standard deviation in the beam-area from six sets of hydrophone raster scans was found to be around 5%. The raster scan of the LGUS field and the lateral profiles in the *x*- and *y*-dimensions at the peak position of the raster scan are shown in Figure 3-5. The laser fluence as a function of fractional energy setting is shown in Figure 3-6.

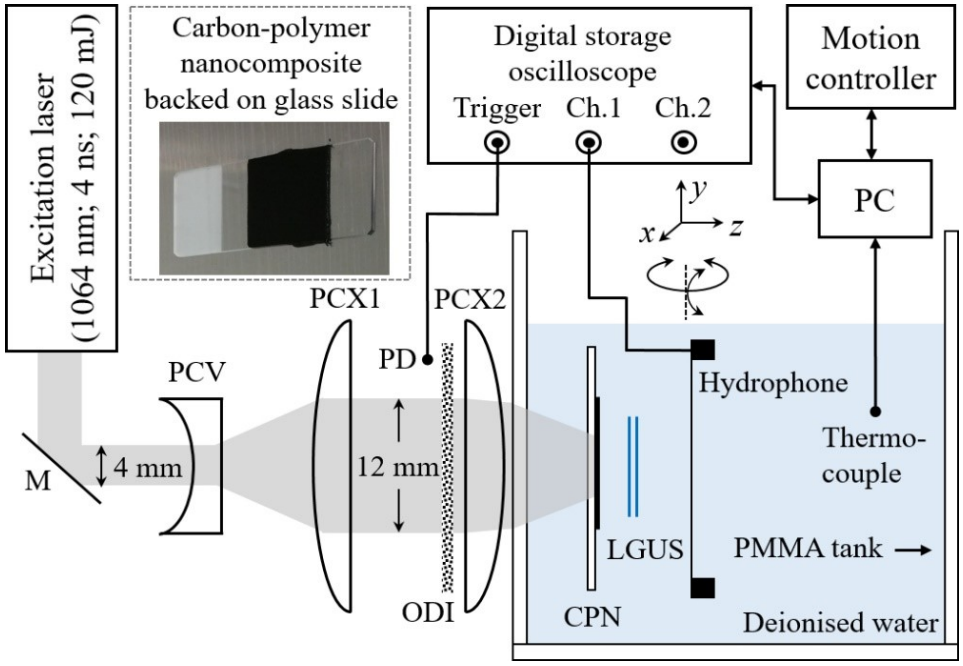

Figure 3-4: The experimental setup. The inset shows a carbon-polymer nanocomposite (CPN) source backed on a laboratory grade glass slide. The thickness of the CPN film is approximately 30 µm and was fabricated by dispersing 3.5 wt. % MWCNT in epoxy. M: Mirror, PCV: plano-concave lens, PCX: plano-convex lens, PD: photodetector, ODI: optical diffuser, LGUS: laser generated ultrasound, PMMA: polymethyl methacrylate, and PC: personal computer.

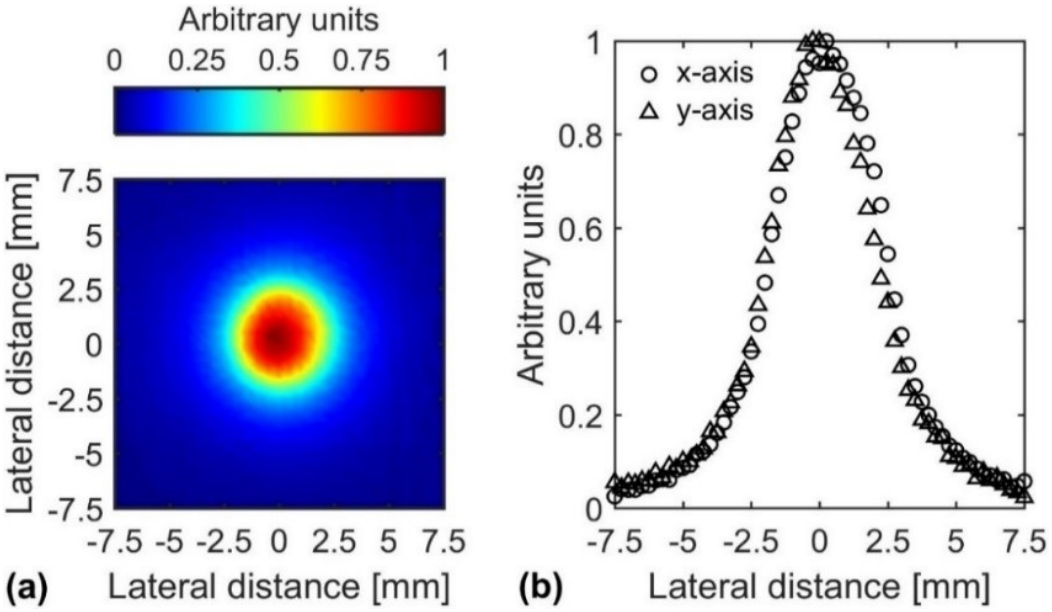

Figure 3-5: **a** Raster scan of the LGUS field measured from an epoxy-based CPN source at an axial distance of 7.4 mm. The peak hydrophone voltages recorded from the raster are rescaled between (0, 1). **b** Lateral profiles of the LGUS field in *x*- and *y*-dimensions at the peak position of the raster scan are represented by circles and diamonds, respectively.

The lateral beam profile of the LGUS beam shown in Figure 3-5 is Gaussian, not planar. Consequently, the pressure will not be uniform over the surface of the hydrophone, introducing a spatial averaging error in the measurement. Spatial averaging also occurs when the pressure is uniform but if the approaching wavefront has a curvature such as spherical, cylindrical, or complex wave patterns emitted by an imaging system. This is because the wavefront relative to the hydrophone surface will be nonuniform resulting in phase cancellation and hence reduction in the measured amplitude, which is dependent on the active element size of the hydrophone. Here, the CPN source is planar and is excited by a laser beam with a Gaussian lateral profile therefore, the uniformity of the pressure at the measurement location is more important since the phase effects are going to be smaller. The other advantage of the laser with a Gaussian beam profile is that the effect of diffraction can be nearly eliminated [121]. A laser beam with a uniform (top-hat) intensity profile leads to a sharp discontinuity in the absorbed optical energy density along the optically absorbed and unabsorbed surface of the CPN. This sharp discontinuity gives rise to boundary diffraction wave field (toroidal wave) that is radiated from the location of the edge of laser beam on the CPN surface [122] also known as the edge-wave. In order to isolate the effects of diffraction in calibration, the source-sensor separation must be very small, which is not always practical in an experiment or the laser beam needs to very wide such that in both cases the edge-wave arriving after the plane-wave can be clearly time-

gated. Also, several diffractive optical elements are normally required to transform a usual Gaussian laser beam profile to a top-hat profile, which increases the design complexity of the final LGUS source. For these reasons, a Gaussian beam profile is more practical and to ensure the pressure is uniform in the central region of the beam relative to the active element size of the hydrophone a simple diverging lens could be used to expand the laser beam.

A method developed by Zeqiri [25] for tone-burst acoustic waveforms previously discussed in Sec. 1.1.3.3 was applied to estimate the size of the spatial averaging error. The –6 dB spectral beam-width averaged in the *x*- and *y*-dimensions up to 100 MHz was 6.5 mm with a standard deviation of 1.1 mm. The frequency dependent effective hydrophone diameter was calculated using an empirical relation $a_{eff}(f) = \mathrm{sqrt}(a_g^2 + 1/4f^2)$, where $a_{eff}(f)$ is the frequency dependent effective radius, a_g is the geometrical radius and f is frequency in MHz [123]. For the UT1602 hydrophone the calculated effective hydrophone diameter, $2 \times a_{eff}(f)$, at the two extreme frequencies of 2 and 100 MHz were approximately 0.54 and 0.2 mm, respectively. Using a lower limit of 5.4 mm for the beam-width, the magnitude of the spatial averaging error at 2 MHz and 100 MHz were calculated to be around 0.3% and 0.04%, respectively. Since the spatial averaging errors are small, no corrections were applied to the measured LGUS responses from the CPN sources.

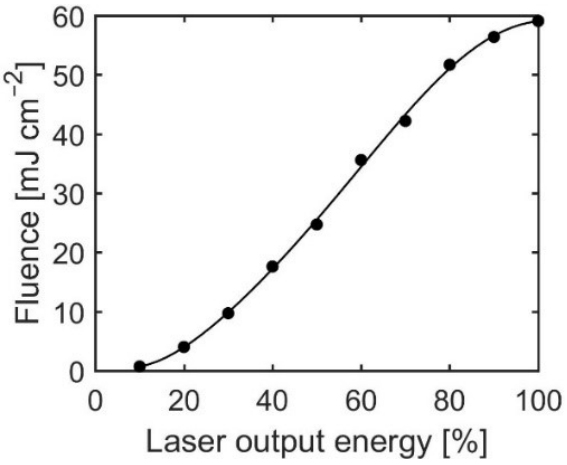

Figure 3-6: Laser fluence calculated for various fractional output energy settings controlled by a custom fit motorised phase retarder $\lambda/2$ wave-plate and the beam-area determined from the raster scan in Sec. 3.3.2.

3.3.3 Hydrophone

The UT1602 membrane hydrophone used to measure the LGUS pressure pulses was fitted with a submersible preamplifier and DC coupled to a 50 Ω output impedance. The hydrophone was calibrated for its end-of-cable loaded magnitude sensitivity response up to 60 MHz and for the phase response up to 40 MHz [29], [30]. The measured phase response was obtained using a relative

technique, which requires the magnitude sensitivity of the reference hydrophone to be flat, implying that the underlying phase response is a constant function of frequency [124]. Since the magnitude sensitivity response of the reference hydrophone was only flat up to 40 MHz, therefore, the technique used to measure the phase response of UT1602 hydrophone did not extend beyond 40 MHz.

The initial measurements from CPN sources showed that the LGUS pulses were inherently broadband with non-negligible frequency content up to and beyond 100 MHz. Therefore, in order to obtain a better estimate of the characteristics of the LGUS pulses such as the peak-positive pressure and bandwidth, the frequency response of the hydrophone was also predicted from 1–110 MHz using a 1D analytical model previously developed at NPL. The model has been validated against NPL's primary standard up to 60 MHz [125]. The accuracy of the model is reliant on knowing the acoustic properties of each hydrophone layer, and in-situ electric and piezoelectric properties of PVDF. Therefore, during model evaluation a destructive approach was taken by the authors of Refs. [28], [125] to measure for example the in-situ electric properties of a single hydrophone. The magnitude and phase responses predicted by the model for a bilaminar hydrophone (GEC Marconi Ltd) is shown in Figure 3-7. Plotted alongside the predicted magnitude response are the average and standard deviation obtained from the measurement of 14 nominally identical hydrophones calibrated on NPL's primary standard [24]. The relative standard deviation in the measured data across the frequency range is nearly 20%, which perhaps provides an indication of the tolerances associated with manufacturing membrane hydrophones.

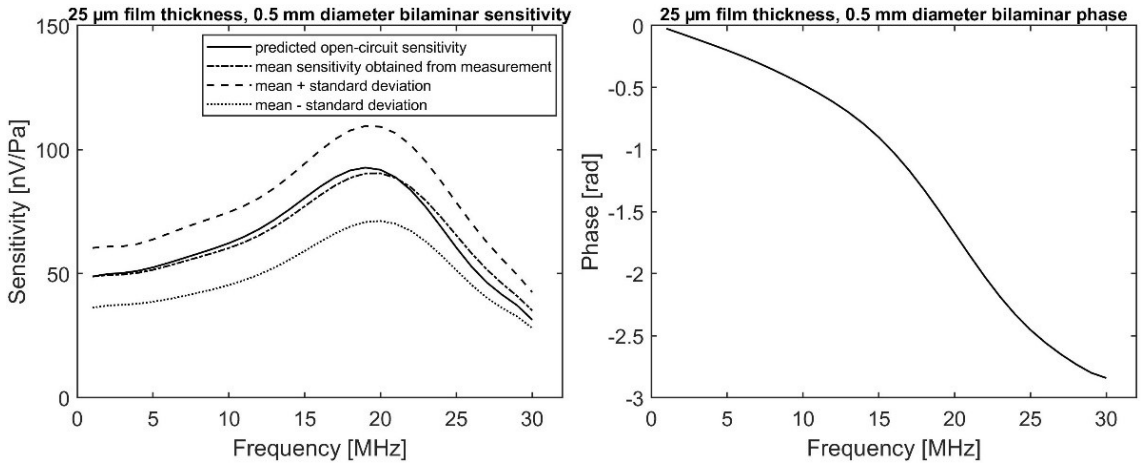

Figure 3-7: Left: Predicted end-of-cable open-circuit magnitude sensitivity response shown as continuous line for a bilaminar hydrophone whose film thickness was 25 µm and an active diameter of 0.5 mm. The dotted continuous line is an average of measured end-of-cable magnitude sensitivities from 14 nominally identical GEC Marconi hydrophones. The lower and upper curves represent one standard deviation in the measured data. Right: Predicted phase response of the hydrophone. Reproduced with format changes from [125], Copyright 2005, with permission from Elsevier.

In this thesis, to avoid having to destructively characterise the hydrophone, agreement between the measured and modelled response was obtained by solving an optimization problem. The initial estimates of the model input parameters such as the hydrophone element diameter, length and width of the signal carrying electrodes attached to the active electrode and their electrical resistance, the length of interconnect cable, preamplifier gain, and the input impedance were obtained from the manufacturer (Precision Acoustics Ltd). These parameters were varied within a manufacturer tolerance of 10–25%, except for the preamplifier values, until closer agreement was achieved with the measured data. The piezoelectric coefficient, d_{33} $[\mathrm{C\,N^{-1}}]$, and the frequency dependent complex relative permittivity, ε_r, were optimised by minimising a cost function defined as the sum of squared difference between the measured and modelled magnitude responses (up to the measured frequency). The minimisation was accomplished in MATLAB® using a quasi-Newton method implemented within an unconstrained multivariable function solver, *fminunc*. The measured and the predicted end-of-cable loaded hydrophone sensitivities are shown in Figure 3-8. The initial and optimised model input parameters returned by the solver *fminunc* are shown in Table 3-6. No uncertainty analysis was performed on the modelled data but the uncertainties on the measured data was extrapolated up to 110 MHz assuming a linear increase in uncertainty with frequency.

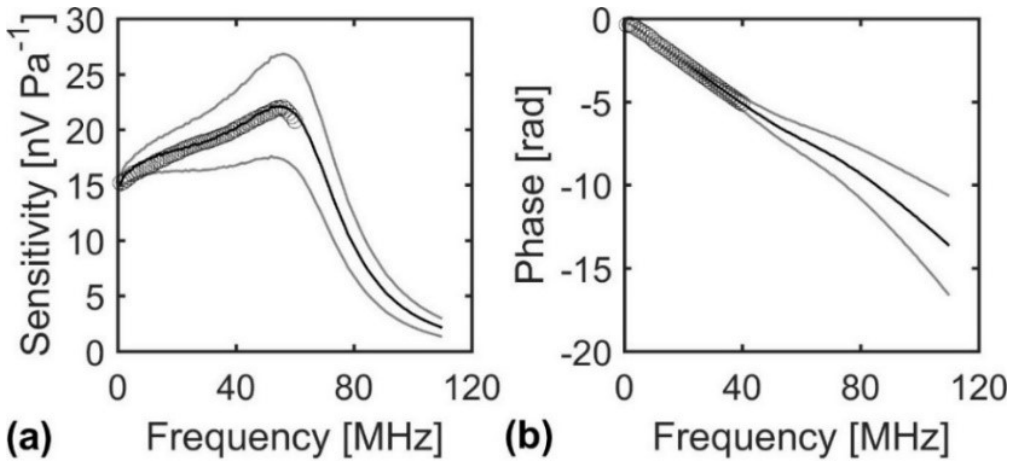

Figure 3-8: Measured (circles) and predicted magnitude sensitivity and phase responses of UT1602 hydrophone are shown in **a** and **b**, respectively. The grey uncertainty curves on the measured data up to 60 MHz was also extrapolated up to 110 MHz assuming a linear increase in uncertainty with frequency. The uncertainties are expressed at 95% coverage interval (k = 2). The uncertainties increase from 4.7% to 38% with frequency for the magnitude sensitivity and for phase it is 0.001 to 3.0 rad.

Table 3-6: The initial and the optimised model input parameters returned by MATLAB's unconstrained multivariable function solver *fminunc*.

Model input parameters	Initial values	Optimised values
Element diameter [mm]	0.2	0.22
Leg length [mm]	45	45
Leg width [mm]	0.15	0.2
Leg DC resistance [Ω]	150	114
Cable length [mm]	20	10
Cable impedance [Ω]	2	1
d_{33} [pC N^{-1}]	14	10.5
Abs. relative permittivity	$-2.82\log_{10}(f) + 26.7$	$-4.59f^{0.1403} + 10.8$
Loss tangent	$0.22 + 0.07\log_{10}(f) - 0.055\ \log_{10}(f^2)$	1 – 5 MHz: $-2.844\exp(-0.04127f) + 0.03559\exp(-1.73f)$ 6 – 110 MHz: $0.5714f^{0.5155} - 4.202$

f is in MHz.

3.3.4 Deconvolution

The electrical response of the LGUS pulse acquired from the hydrophone at an axial distance z, $u(z,t)$ was converted to a pressure pulse $p(z,t)$, via deconvolution [20]

$$p(z,t) = \mathcal{F}^{-1}\left\{\frac{\mathcal{F}[u(z,t)]}{\underline{M}(f)}\right\}. \tag{3.1}$$

Here, $\mathcal{F}$ and $\mathcal{F}^{-1}$ are the Fourier and inverse Fourier transforms in time respectively, and $\underline{M}(f)$ is the predicted complex sensitivity response of the hydrophone from Sec. 3.3.3.

The deconvolution process, though simple in implementation, requires regularisation when measuring broadband ultrasound pulses whose frequency content exceeds the known frequency response of the hydrophone. To facilitate the computation of Eq. (1.26), the $\underline{M}(f)$ data from 111 MHz to 1.25 GHz was assigned the same sensitivity value as at 110 MHz and to avoid divide by zero error, and the sensitivity at 0 Hz was assigned the same sensitivity value of 1 MHz for the same reason. The sensitivity of UT1602 hydrophone at 110 MHz is a factor of 10 lower relative to the resonance frequency (see Figure 3-7) and since the signal content beyond 100 MHz is also close to the noise floor (see Figure 3-9), the division operation in Eq. (1.26) amplifies the noise present in the voltage signal, $u(z,t)$, after deconvolution. In order to supress the high-frequency noise in the deconvolved pressure pulse (see top-row of Figure 3-11), a finite impulse response linear-phase lowpass digital filter was applied to remove frequency components beyond 110 MHz. The high-frequency cut-off for the filter and the number of filter coefficients were set to 110 MHz and 24, respectively. This resulted

in an attenuation of at least 26 dB of the magnitude components beyond twice the cut-off frequency [126]. The magnitude and phase response of the filter is shown in Figure 3-10. The filtered deconvolved pressure pulse is shown in the bottom-row of Figure 3-11.

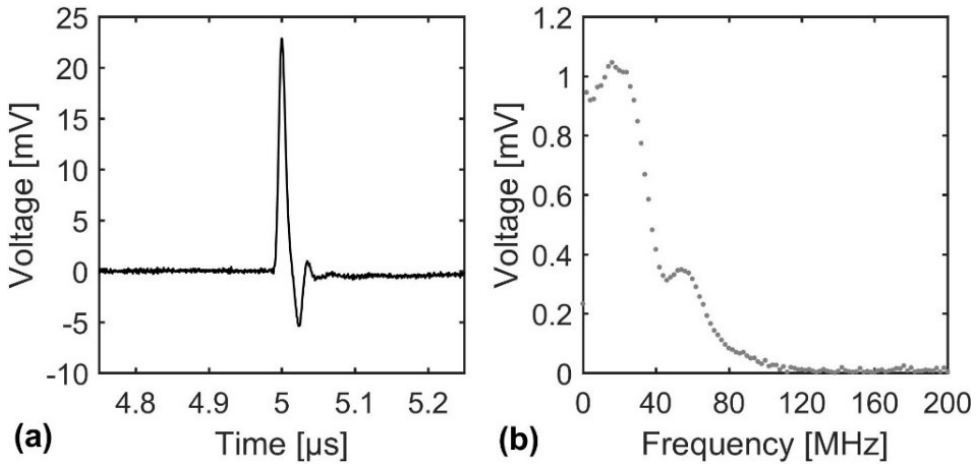

Figure 3-9: **a** Hydrophone voltage pulse acquired using UT602 hydrophone when an epoxy-based CPN source with 1.25 wt. % MWCNT was excited with a fluence of 10 mJ cm^{-2}. **b** Magnitude spectrum shown up to 200 MHz. The hydrophone pulse was acquired at a sampling frequency of 1.25 GHz and the record length was 1250 sample points.

The regularization of the deconvolution of hydrophone waveforms is currently an active field of study [30], [33], [34], [127], [128] but there exists no standardized approach. A method to estimate the uncertainty bounds of the deconvolved hydrophone time-series waveform has been recently developed [129], which may be useful when reporting of absolute exposure parameters from medical equipment is required for regulatory purposes. In contrast to all previous work, the challenges of deconvolution with a limited calibration frequency range has been partly overcome in this thesis by extrapolating the measured response of the hydrophone to beyond 100 MHz. Since the primary aim of the present study was to assess the relative performance of 27 different CPN sources for their suitability as an ultrasound source for hydrophone calibrations, the regularization procedure described here was deemed adequate.

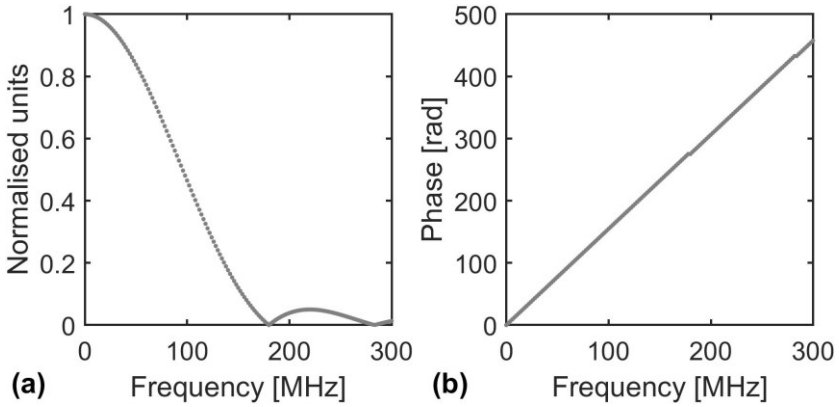

Figure 3-10: **a** Normalised magnitude response of the LABVIEW built-in finite impulse low-pass filter function whose higher cut-off frequency was set at 110 MHz and 24 filter coefficients were used. **b** Unwrapped filter phase response. For the purpose of visualisation, the filter responses are shown only up to 300 MHz rather than the Nyquist frequency of 1.25 GHz.

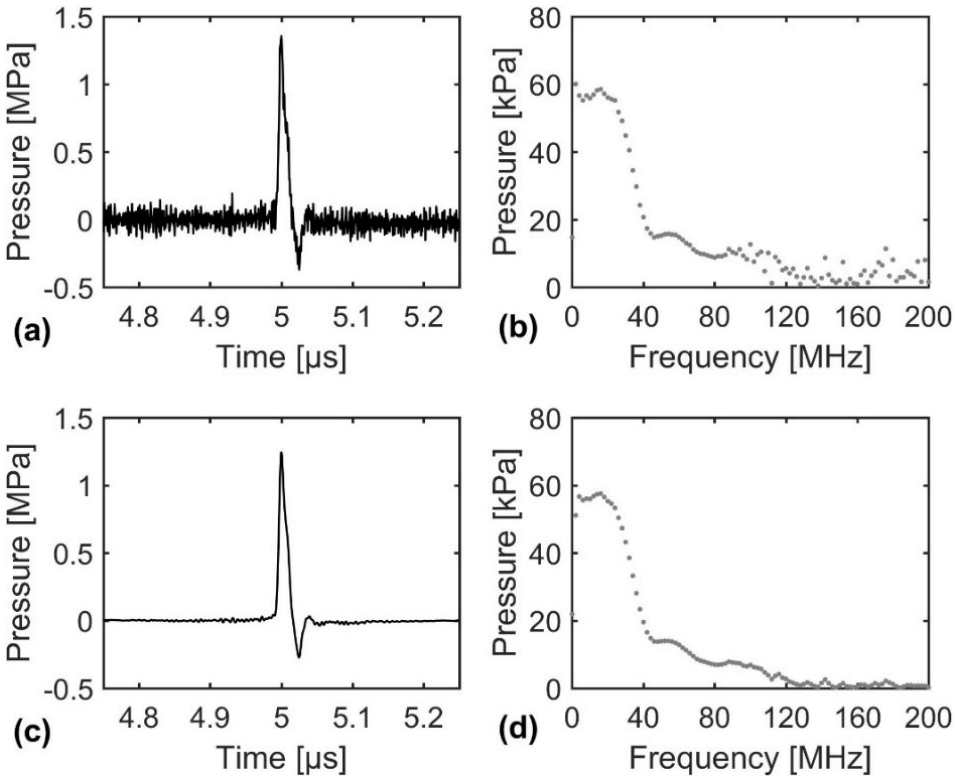

Figure 3-11: **a** Deconvolved pressure pulse obtained by applying Eq. (1.26) using the hydrophone voltage pulse shown in Figure 3-9(a) and the regularised predicted sensitivity response of the hydrophone shown in Figure 3-8. **b** Magnitude spectrum of the pressure pulse shown in **a**. **c** Post FIR lowpass filtered pressure pulse shown in **a**. **d** Magnitude spectrum of the lowpass filtered pressure pulse.

3.4 Experimental Source Characterisation

In this section, the peak-positive pressure, p_+ and –6 dB bandwidth, $BW6$, of the LGUS pulse obtained from the 27 CPN sources are compared. But first, the interfacial reflections arising from the design structure of the CPN source is described.

3.4.1 Interfacial Reflections

The extent to which the acoustic impedance of the CPN source affects the LGUS pulse is described in this sub-section. A schematic of a glass-backed CPN source sandwiched between two water half-spaces is shown in Figure 3-12. The acoustic impedance of water, glass, and CPN source are denoted as z_w, z_g and z_{cpn}, respectively. The dimensions of glass backing and CPN source along the z-axis is approximately to scale. For the sake of discussion, the source is modelled as 1D and stress confined. Therefore, the initial pressure, $p_o(z)$, leaving the CPN source will divide into two equal parts, one propagating to the left, $p_L(t)$ and the other to the right, $p_R(t)$. The hydrophone is located in water to the right of the CPN source. The two waves, when they arrive at the edge of the CPN source, are presented with CPN-glass and CPN-water interfaces respectively, where step changes in the acoustic impedance occur. Therefore, the amplitude of the waves entering into each medium is dependent on the transmission coefficient seen by the wave from the CPN source. Similarly, the amplitude of the waves reflected within the CPN source is dependent on the reflection coefficient; the polarity of the wave reflected will either remain the same or undergo 180° phase inversion.

The acoustic transmission and reflection coefficients for the three polymers for CPN-glass and CPN-water interfaces are listed in Table 3-7.

For an incident plane-wave, the equations for the pressure transmission coefficient, T, and the pressure reflection coefficient, R, for a wave entering medium 2 of acoustic impedance, z_{ac2} from medium 1 of acoustic impedance, z_{ac1} is given by [130]

$$T = \frac{2z_{ac2}}{z_{ac2} + z_{ac1}}, \tag{3.2}$$

$$R = \frac{z_{ac2} - z_{ac1}}{z_{ac2} + z_{ac1}}. \tag{3.3}$$

Table 3-7: Acoustic pressure transmission, T, and reflection, R, coefficients for a wave propagating from the CPN medium into either glass or water mediums. The acoustic impedances for each medium was calculated using sound-speeds and densities from Table 3-4. The transmission and reflection coefficients were calculated using Eq. (3.2) and (3.3), respectively.

Medium interface	$T_{\text{cpn-glass}}$	$R_{\text{cpn-glass}}$	Medium interface	$T_{\text{cpn-water}}$	$R_{\text{cpn-water}}$
Epoxy-glass	1.63	0.63	Epoxy-water	0.69	−0.31
PU-glass	1.70	0.70	PU-water	0.80	−0.20
PDMS-glass	1.85	0.85	PDMS-water	1.18	0.18

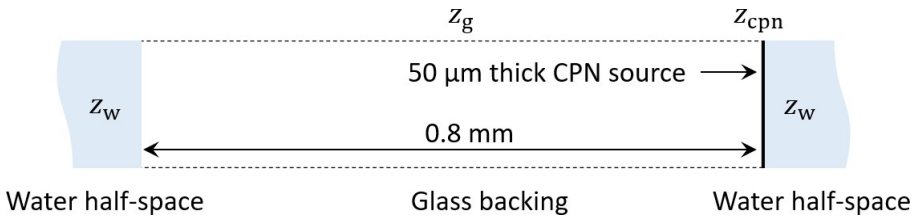

Figure 3-12: Schematic of glass-backed CPN source sandwiched between two water half-spaces. Dimensions along the z-axis is approximately to scale. The acoustic impedance of water, glass and CPN source are denoted as z_w, z_g and z_{cpn}, respectively.

Example voltage time-series acquired using UT1602 hydrophone over a long acquisition window, which includes interfacial reflections, are shown in Figure 3-13 and Figure 3-14 for epoxy and PDMS-based, glass-backed, CPN sources, respectively. In both figures, the plot area is divided into two regions. Region 1 corresponds to the initial transmitted part of $p_R(t)$ through the CPN-water interface, initial $p_L(t)$ first reflected at the CPN-glass interface and then transmitted through the CPN-water interface, and its subsequent reflections at the CPN-water and CPN-glass interfaces. Since the thickness of the CPN source is very small, the interfacial reflections immediately follow the preceding wave. The waves in Region 2 are composed of the initial part of $p_L(t)$ transmitted through the CPN-glass interface and the waves returning after reflections at the glass-water and glass-CPN interfaces. After successive interfacial reflections, the wave amplitudes continue to diminish coupled by wave attenuation within the CPN source, which is significantly higher compared to water or glass.

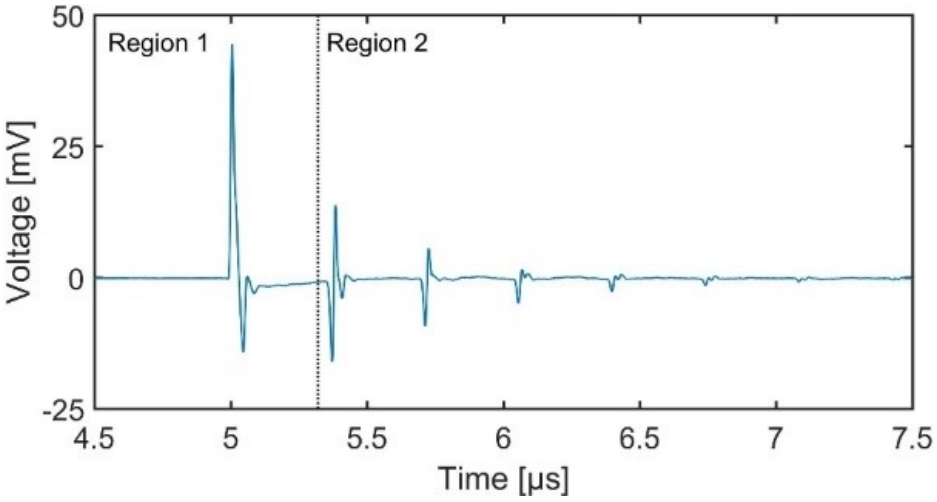

Figure 3-13: The main LGUS pulse and the interfacial reflections recorded for an epoxy-based glass-backed CPN source. The negative going wave appearing after the main pulse in Region 1 is because the reflection coefficient from epoxy-CPN into water is negative and it is positive for epoxy-CPN into glass. Similarly, the polarity of the interfacial reflections in Region 2 are affected by whether the reflection coefficient is either positive or negative at various interfaces. The CPN was loaded with 2.5 wt. % MWCNT and the applied fluence was 20 mJ cm^{-2}.

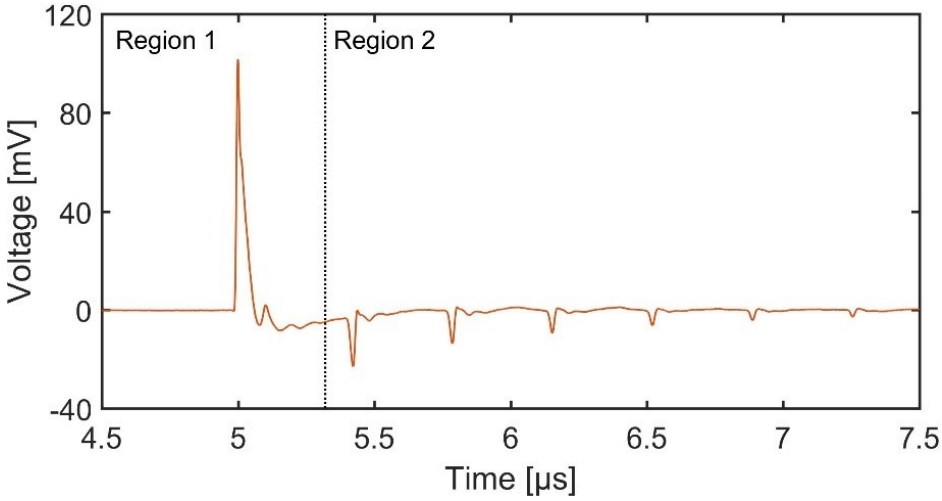

Figure 3-14: The main LGUS pulse and the interfacial reflections recorded for an PDMS-based glass-backed CPN source. The positive going wave appearing after the main pulse in Region 1 is because the reflection coefficient is positive at both PDMS-CPN into water and PDMS-CPN into glass interfaces. The polarity of the interfacial reflections in Region 2 are affected by whether the reflection coefficient is either positive or negative at various interfaces. The CPN was loaded with 2.5 wt. % MWCNT and the applied fluence was 20 mJ cm^{-2}.

3.4.2 Effect of Polymer Type

The LGUS pulses and the corresponding spectra obtained for an applied fluence of 10 mJ cm^{-2} from epoxy, PU, and PDMS-based CPN sources are shown in Figure 3-15. The CPN sources were dispersed with 3.5 wt. % MWCNT and their respective thicknesses were 26 ± 5 µm , 27 ± 4 µm and 34 ± 2 µm. The p_+ of epoxy, PU, and PDMS-based CPN sources were 1.5, 2.5 and 4 MPa, respectively. At a first glance, the increase in pressure seems to be correlated with the polymer's volume thermal expansion coefficient rather than the Grüneisen parameter (see Table 3-4). However, for a 3.5 wt. % MWCNT loading, the stress relaxation times for epoxy, PU and PMDS-based CPN sources are 2.2, 2.2, and 3.9 ns, respectively, calculated using μ_a values from Table 3-3 and c_0 values from Table 3-5. Therefore, the effect of the Grüneisen parameter of the polymer on the measured LGUS pulse cannot be appreciated when stress confinement condition is not met. According to Table 3-5, only one of the nine CPN variants i.e., PDMS with 1.25 wt. % MWCNT seems to satisfy stress confinement with $\tau_{ac} = 14.9$ ns against the laser duration of 4 ns. Also, the amplitude of the pressure wave transmitted into water from the CPN is dependent on the transmission coefficient of CPN-water interface. Therefore, even in the event of stress confinement, for absolute comparison the transmission coefficients of the three polymers must be taken in account.

The $BW6$ of epoxy, PU and PDMS-based CPN sources are 34, 20 and 14 MHz, respectively. It can been seen that there is non-negligible spectral content even at 100 MHz, which is in the range of 5–20 kPa depending the polymer type. However, $BW6$ was found to be more consistent for reporting bandwidth compared to say –10 or –20 dB as the spectral content at these threshold levels were variable depending on the p_+ levels.

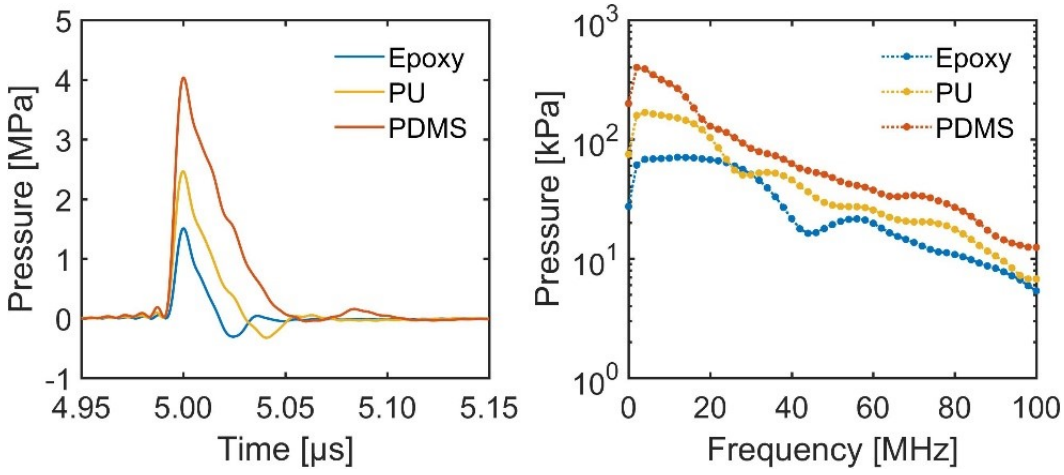

Figure 3-15: Effect of polymer type on the LGUS for an applied fluence of 10 mJ cm^{-2}. Each polymer was loaded with 3.5 wt. % MWCNT. The thickness of epoxy, PU and PDMS-based CPN sources were 26µm (5µm), 27 µm (4 µm) and 34 µm (2 µm), respectively. The parenthetical entries are one standard deviation.

3.4.3 Effect of Thickness

The optical absorption depths, $1/\mu_a$, for nominal μ_a values of 64000, 146000 and 210000 m^{-1}, which represent 1.25, 2.5 and 3.5 wt. %, are approximately 15.6, 6.8 and 4.8 µm, respectively. The CPN film thickness should be ideally equal to the optical absorption depth. If the CPN film thickness is much greater than $1/\mu_a$ then the wave must propagate through the excess region of the CPN film. This will cause it to be attenuated, since the acoustic absorption of polymers is significantly higher than water (for example, at 5 MHz the acoustic absorption in water is 0.055 dB cm^{-1} whereas for the particular polyurethane polymer used in this thesis it is 45 dB cm^{-1}, more than a factor of 800 larger than water).

The effect of thickness for the PU-based CPN source is shown in Figure 3-16. The applied fluence was 10 mJ cm^{-2} and each polymer was loaded with 1.25 wt. % MWCNT. The three thicknesses of the CPN sources were 28 µm (2 µm), 51 µm (6 µm), and 85 µm (7 µm) and their p_+ were 1.68, 1.57 and 1.34 MPa, respectively. In the spectral plots of Figure 3-16, the loss of high frequencies with increasing thickness are evidently seen particularly after 40 MHz. To know the absolute acoustic attenuation in the CPN, a measurement of pressure-pulse propagated in water-only medium and another measurement with CPN in the propagation path are required. Additionally, the acoustic impedance of the CPN also must be known to correct for the effects of impedance mismatch between water and CPN [131]. Since such a measurement was not possible, relative loss estimates were obtained in which the spectral magnitudes of 51 and 85 µm thick CPN sources were compared with the spectral magnitudes of 28 µm CPN source. This is shown in Figure 3-17 for frequencies 40 MHz and above. The loss is amplitude is nearly 40% at 100 MHz for 85 µm thick CPN source compared to 28 µm thick CPN source.

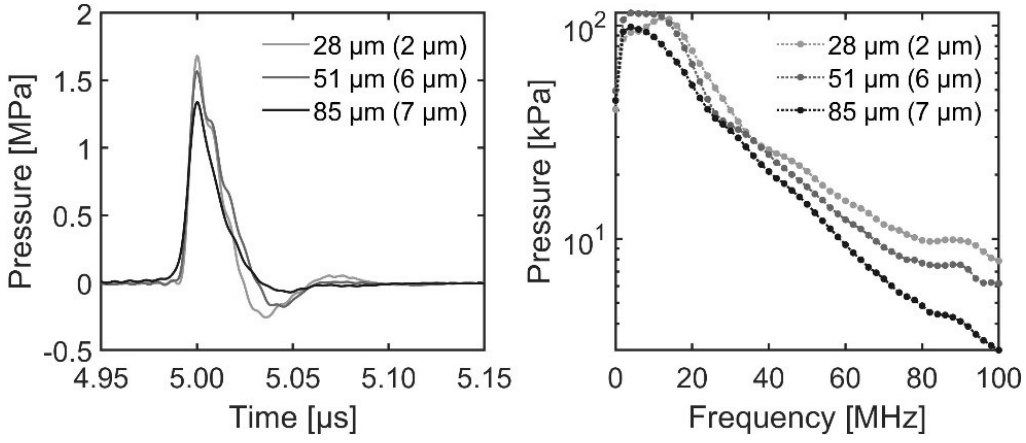

Figure 3-16: Effect of PU-based CPN source thickness on LGUS pulse and its magnitude spectra are shown. The applied fluence was 10 mJ cm^{-2} and each polymer was loaded with 1.25 wt. % MWCNT.

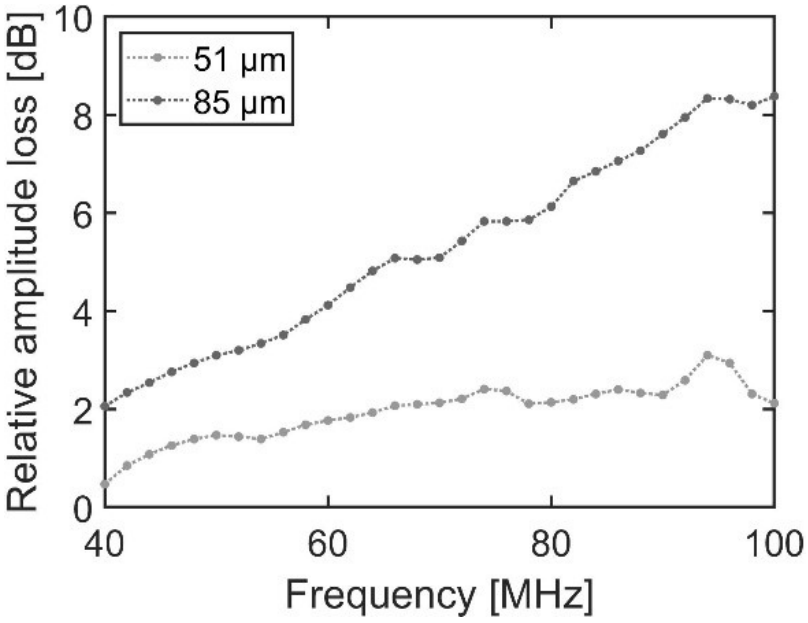

Figure 3-17: Relative amplitude loss of 51 and 85 µm thick PU-based CPN sources compared against the 28 µm CPN source calculated using amplitude spectra shown in Figure 3-16.

3.4.4 Effect of Fluence

The absorbed energy density, $\Phi\mu_a$, in a CPN can be increased for a given optical absorption coefficient, μ_a by increasing the laser fluence, Φ, which results in increased pressures generated by a CPN source. All 27 CPN sources were tested at four fluence levels of 10, 20, 30 and 40 mJ cm^{-2}. These fluence levels are in the range of those applied in various previous studies (see Table 2-1). The effect of fluence on LGUS for epoxy, PU and PDMS-based CPN sources for arbitrary CPN thickness and MWCNT wt. % are shown in Figure 3-18, Figure 3-19 and Figure 3-20, respectively. It is seen that the peak-positive pressure increases with fluence for each CPN type, but the increase is not linear. Additional measurements were made on epoxy, PU and PDMS-based CPN sources of 10 µm nominal thickness over a fluence range of 0.7–52 mJ cm^{-2} to confirm that the observed pressure versus fluence relationship was indeed nonlinear, which is shown in Figure 3-21.

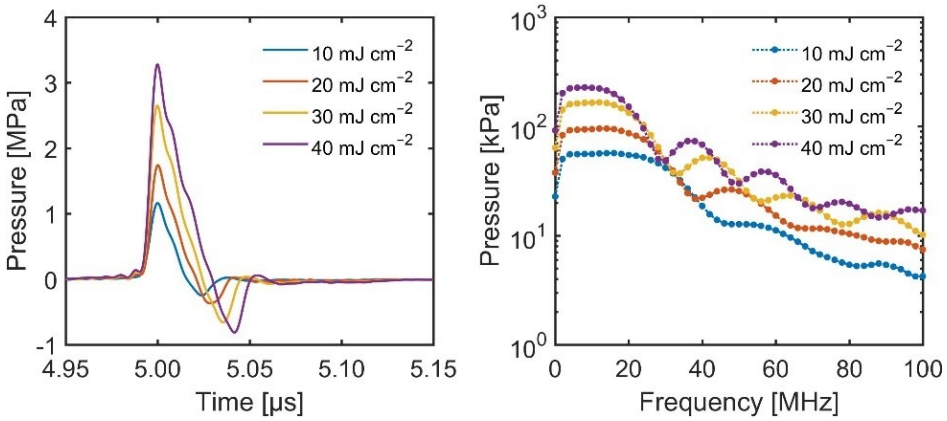

Figure 3-18: Effect of a laser fluence for an epoxy-based CPN source with 1.25 wt. % MWCNT and 27 μm thick.

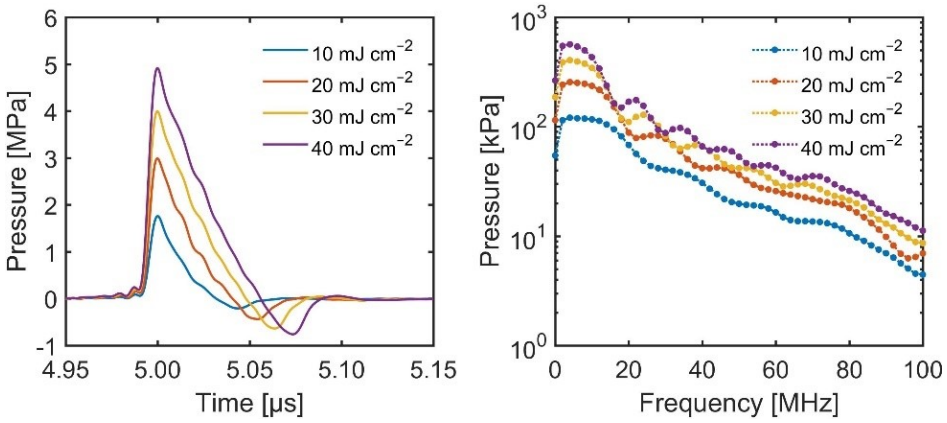

Figure 3-19: Effect of a laser fluence for a PU-based CPN source with 2.5 wt. % MWCNT and 51 μm thick.

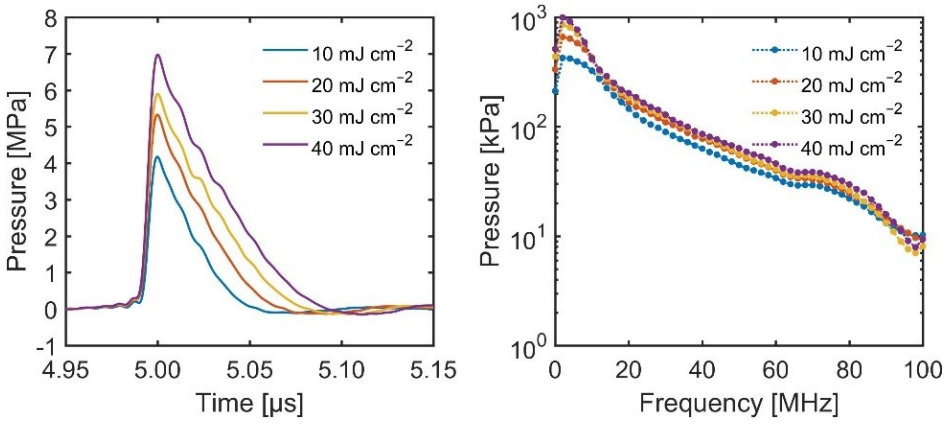

Figure 3-20: Effect of a laser fluence for a PDMS-based CPN source with 3.5 wt. % MWCNT and 55 μm thick.

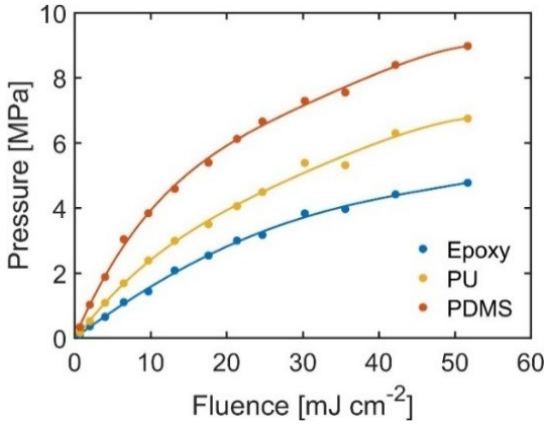

Figure 3-21: Extended fluence dependency measurement of epoxy, PU and PDMS-based CPN sources with 2.5 wt. % MWCNT and 10 µm nominal thickness. The continuous lines are fourth order polynomial fit to the measured data, which are represented in circles.

The nonlinear increase in peak pressure with fluence was common to all 27 CPN sources. This nonlinear increase in the peak-positive pressure as a function of applied fluence has been previously reported for CPN sources made of allotropes of carbon and also gold nanoparticle nanocomposites [83], [97], [132]. The reasons for this nonlinear increase have been attributed to the bandwidth limit of the hydrophone saturating its response [83], partial detachment of the nanocomposite film from the glass slide [97], and acoustic attenuation of LGUS pulse within the nanocomposite [132]. In contrast, the nonlinear increase in pressure amplitude with fluence observed in this study is attributed to the nonlinear propagation of LGUS in water. It was also observed that the nonlinear increase in pressure amplitude was accompanied by a decrease in *BW6*, which can be seen in the spectral plots of Figure 3-18 compared to Figure 3-19 and Figure 3-20. This is attributed to the broadening of the time-series pressure-pulse also as a consequence of the nonlinear propagation of the LGUS pulse and rapid absorption of high MHz frequencies relative to low MHz frequencies. It should be noted that the bandwidth is a relative measure which describes the width of the emitted spectrum relative to the spectral peak, so a decrease in bandwidth does not necessarily imply that the higher frequency spectral magnitudes have decreased, as the overall amplitude may have increased. It is seen in all the time-series pressure pulses shown in this thesis that there are undulations on the trailing side of the pulse. Because the hydrophone does not capture the full frequency content in the signal, the undulations are a consequence of this limited bandwidth, which is investigated together with nonlinear propagation in Chapter 4.

3.4.5 CPN Source Comparison

The main difficulty in comparing the nine variants of the CPN sources (polymer type and MWCNT wt. %) under identical experimental conditions is that the duration of the laser pulse used in this thesis

was not adequate to ensure stress confinement. However, intra-comparison of CPN sources such as the effect of thickness or effect of fluence is not dependent on whether there was a stress confinement or not. Nevertheless, in order to present as much of the measurement data as possible, the p_+ and $BW6$ from 30 and 50 µm nominally thick CPN sources loaded with 1.25, 2.5 and 3.5 wt. % MWCNT are shown as p_+ versus $BW6$ plots in Figure 3-22, Figure 3-23 and Figure 3-24. The trade-off of p_+ and $BW6$ as a function of laser fluence is clearly appreciable in the following plots. The pressure generated from PDMS-based CPN sources is promising compared to epoxy or PU-based CPN sources. As with bandwidth, the reduction in $BW6$ appears to be largely a consequence of nonlinear propagation, which will be investigated numerically in Chapter 4. However, the reduction in $BW6$ can be reduced by making measurements closer to the CPN source so that loss of high frequencies due to acoustic absorption are smaller.

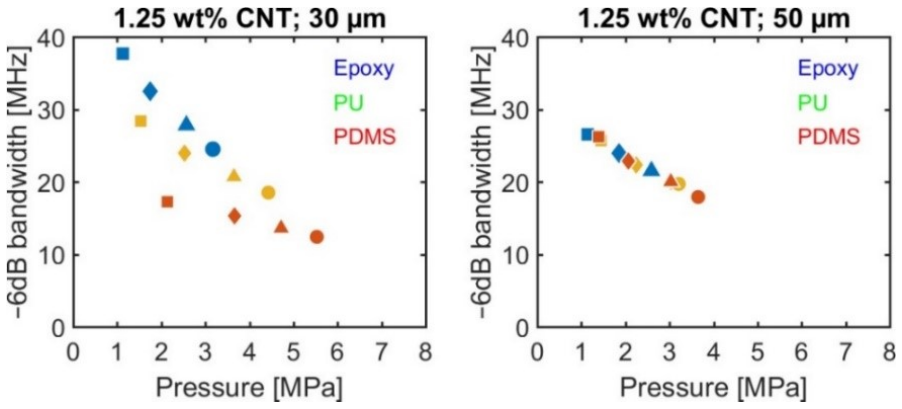

Figure 3-22: Effect of polymer type, laser fluence and CPN film thickness are shown for a MWCNT loading of 1.25 wt. %. The filled square, diamond, triangle, and circle represent applied fluences of 10, 20, 30, and 40 mJ cm^{-2}.

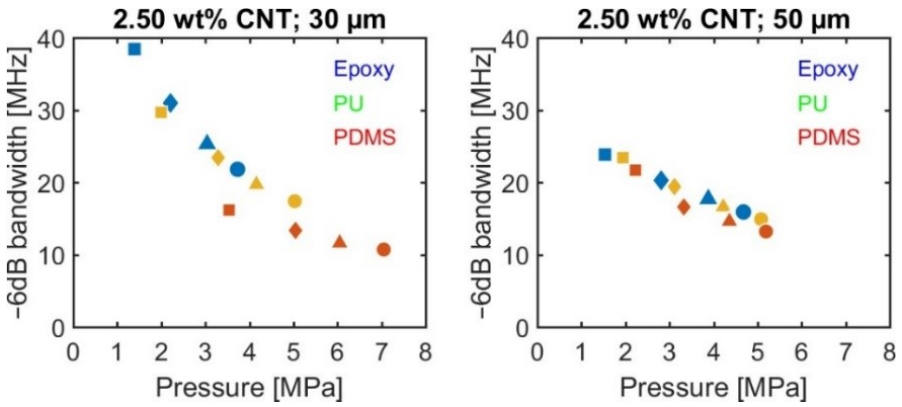

Figure 3-23: Effect of polymer type, laser fluence and CPN film thickness are shown for a MWCNT loading of 2.5 wt. %. The filled square, diamond, triangle, and circle represent applied fluences of 10, 20, 30, and 40 mJ cm^{-2}.

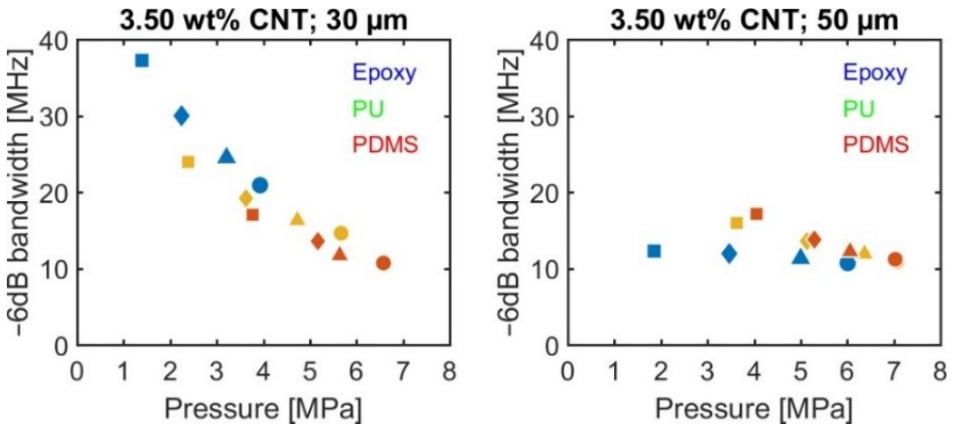

Figure 3-24: Effect of polymer type, laser fluence and CPN film thickness are shown for a MWCNT loading of 3.5 wt. %. The filled square, diamond, triangle, and circle represent applied fluences of 10, 20, 30, and 40 mJ cm^{-2}.

3.4.6 CPN Source Stability

A fundamental requirement in the calibration of hydrophones using interferometry is that the hydrophone voltage measurement and the corresponding velocity or displacement measured using a pellicle must be made in identical acoustic fields. This therefore requires the source to be stable over the duration of the calibration procedure. The stability of the acoustic outputs from CPN sources were assessed by analysing the peak-positive voltages of the hydrophone measurements under sustained laser excitation. The stability test comprised a total of 28 CPN sources including four of the sources listed in Table 3-2. There were ten epoxy-based, eight PU-based and ten PDMS-based sources. Two of the epoxy-based and three of the PDMS-based sources were of 1.25 wt. % MWCNT and the rest were of 2.5 wt. % MWCNT. The CPN film thickness ranged from 10–55 µm. The measured hydrophone voltage pulses were not corrected for pulse-to-pulse changes in the laser fluence since, after a period of one-hour warm-up, they did not make a noticeable difference to the hydrophone voltages. Each source was tested initially at 20 mJ cm^{-2} and 20 Hz PRR for a period of one hour. If the source was found to be stable, then the measurement was repeated at 30 mJ cm^{-2} and 20 Hz PRR. A select number of stable sources were tested for up to three hours and a further few sources were tested on a different day to ensure they remained stable.

Epoxy-based CPN sources were generally found to be unsuitable along with a couple of PU-based CPN sources. During the course of sustained laser excitation, the CPN film would detach itself from the glass directly over the laser illumination area, which was observed as a sudden drop in the hydrophone output voltage. The film detachment mostly occurred at a fluence of 30 mJ cm^{-2}. A combination of slow water ingression and tensile stresses at the CPN-glass interface, which increases with applied fluence, were possibly the two reasons for detachment. Also, for the three polymer-based CPN sources the surface chemistry of the glass slide was not modified to ensure glass and CPN films adhered strongly, although the glass slides were thoroughly cleaned, first with detergent and then with

acetone and methanol solvents, to remove grease and organic deposits from the surface. For epoxy-based CPN sources, after being stored for about six-month to a year, flaking or entire film detachment were observed. These observations are depicted in Figure 3-25.

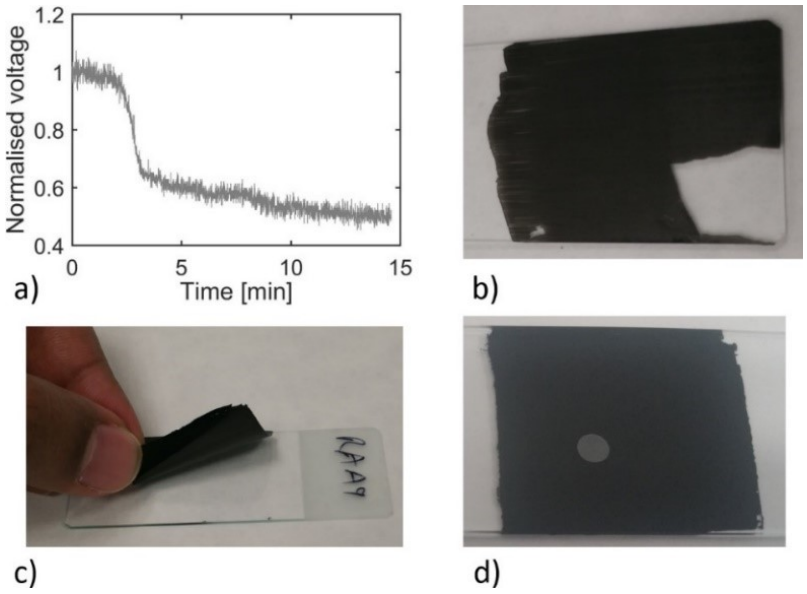

Figure 3-25: The plot and images shown are uncorrelated and represents various epoxy-based CPN sources. **a** Normalised peak-positive hydrophone voltage time history obtained from unaveraged single-shot waveform acquisitions (averaging over 32 repetitions was not used as discussed in Sec. 3.3.1) for a fluence of 30 mJ cm^{-2} and 20 Hz PRR. The CPN film detached within the first 5 min of sustained laser excitation. **b** Flaking of CPN film. **c** Complete CPN film detachment. **d** Film detachment corresponding to central laser illumination area seen as a bubble under the glass surface at 30 mJ cm^{-2} and 20 Hz PRR.

The voltage-time trends of four PU and PDMS-based CPN sources are shown in Figure 3-26 and Figure 3-27, respectively. The CPN source TAA06 in Figure 3-26 is one of the two sources that failed at 30 mJ cm^{-2} in a test batch of eight sources. As with epoxy-based CPN sources, there was a partial detachment of the PU-based CPN film from the glass over the area of laser illumination. The voltage-time trends commonly showed a behaviour in which the LGUS gradually decreased and, in some cases, increased. The maximum change occurred within the first 30-min period of about 6% except in the case of SAA16 (see Figure 3-27). After the 30-min period, the average change was about 0.5% for each successive 30-min of laser excitation.

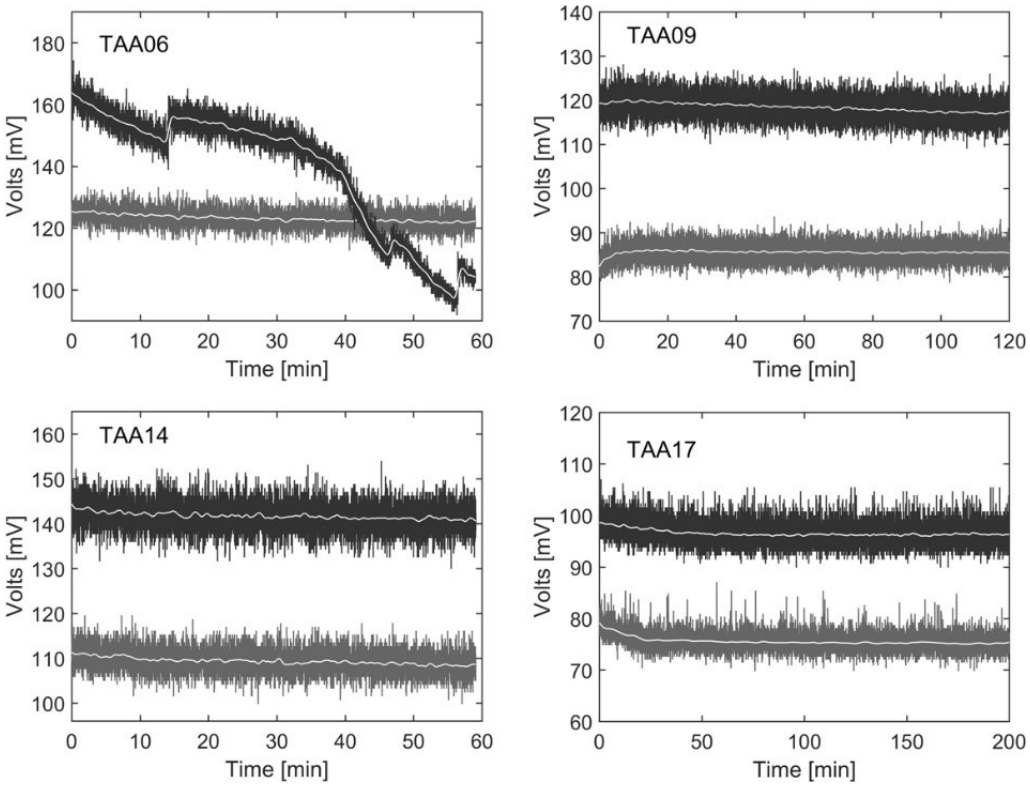

Figure 3-26: The voltage-time trends of various PU-based CPN sources acquired using a 0.2 mm diameter hydrophone. The light and dark grey plots are peak-positive voltages of unaveraged single-shot hydrophone waveform measurements (averaging over 32 repetitions was not used as discussed in Sec. 3.3.1) at a laser fluence of 20 mJ cm^{-2} and 30 mJ cm^{-2}, respectively. The underlying white curves were obtained by fitting a smoothing spline.

The observed voltage-time trends were compared with the change in temperature of the CPN medium, which was determined by measuring the surface temperature of a PDMS-based CPN source near the region of maximum laser fluence. The temperature was measured using a K-type thin-wire thermocouple connected to a data logger. For a fluence of 30 mJ cm^{-2}, the surface temperature of the CPN increased by 8.5 ℃ within 30 s from the ambient temperature and became stable in approximately 10 min (Figure 3-28). The temperature increase thereafter was only 0.2 ℃ over a 50-min measurement period. The measured CPN surface temperature profiles for other fluences are also shown in Figure 3-28. Since the Grüneisen parameter is temperature dependent, the LGUS amplitude is directly affected by the local temperature of the CPN medium. Once a temperature equilibrium is reached the change in LGUS output should be constant or minimal, which agrees with the observations presented in Figure 3-26 and Figure 3-27.

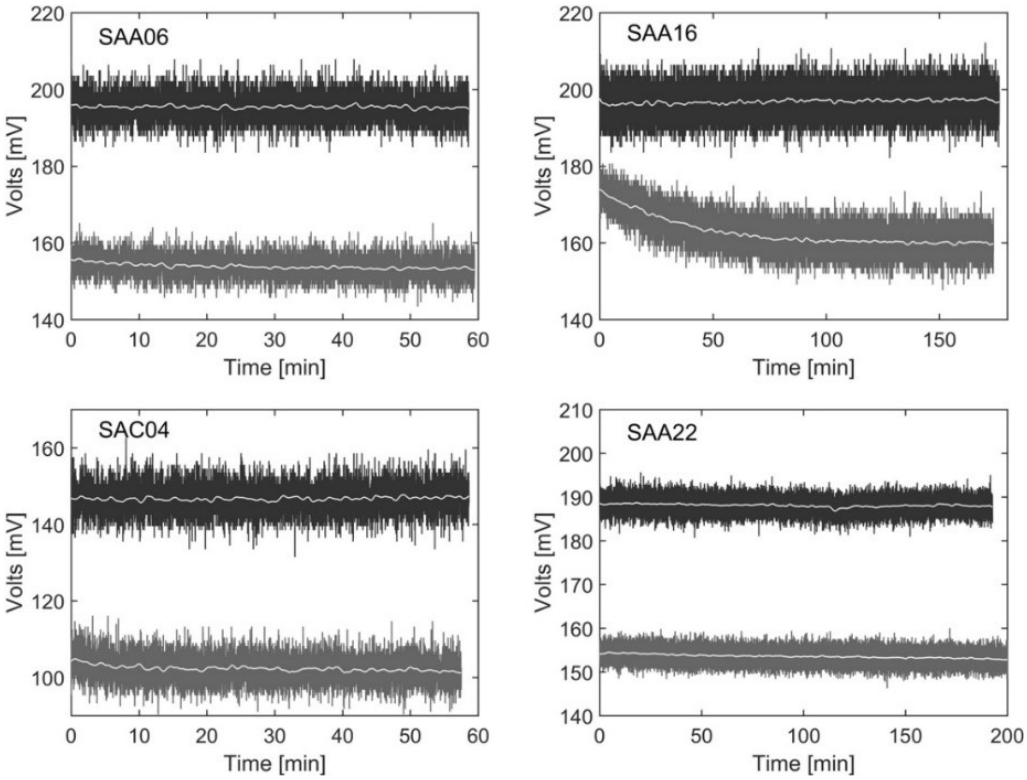

Figure 3-27: The voltage-time trends of various PDMS-based CPN sources acquired using a 0.2 mm diameter hydrophone. The light and dark grey plots are peak-positive voltages of unaveraged single-shot hydrophone waveform measurements (averaging over 32 repetitions was not used as discussed in Sec. 3.3.1) at a laser fluence of 20 $\mathrm{mJ\,cm^{-2}}$ and 30 $\mathrm{mJ\,cm^{-2}}$, respectively. The underlying white curves were obtained by fitting a smoothing spline.

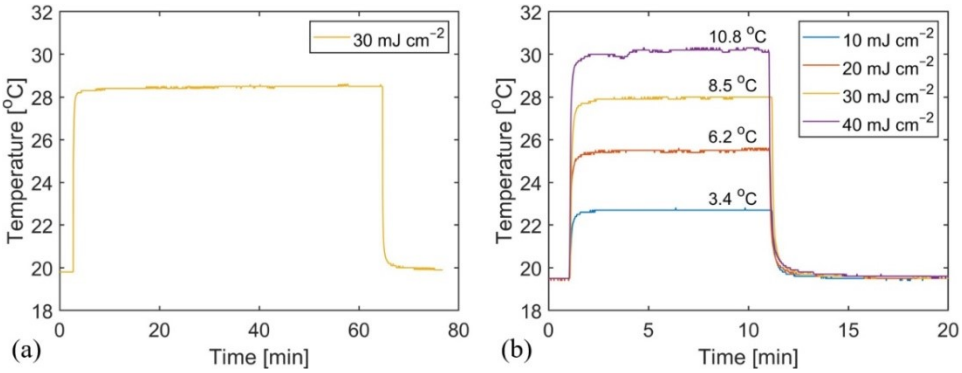

Figure 3-28: **a** Temperature profile measured on the surface of a PDMS-based CPN source at 30 $\mathrm{mJ\,cm^{-2}}$ near the region of maximum fluence within the test setup shown in Figure 3-4. **b** Surface temperature profiles measured for a short period for four different fluences. The temperature label on each curve is the CPN surface temperature just before the laser was turned off.

Though the observed CPN stability is not ideal, it is already considered adequate with regard to allowing the calibration of hydrophones with acceptable uncertainties. Equipment manufacturers normally recommend a minimum switch on time to guarantee that measurement made using their equipment are within a quoted performance envelop. Therefore, the standard operating procedures for hydrophone calibration involves switching on all equipment for at least 30 min before beginning with measurements. Since the maximum variability of the CPN source also occurs within the first 30-min period, the CPN source could be left to operate for a set duration before using it to calibrate hydrophones. Additionally, the calibration of a hydrophone on the primary standard involves obtaining a pair of measurements, i.e., a hydrophone voltage signal and the interferometer signal corresponding to either acoustic displacement or particle velocity, which are acquired consecutively. These measurements are normally completed within 20 min and at least six pairs of independent measurements are taken to obtain confidence in the calibration data. If the LGUS output gradually changes, then a gradual change in sensitivity can be expected over the duration of the calibration. A correction relative to the first sensitivity measurement could be applied retrospectively to the subsequent sensitivity data provided a gradual change is clearly identifiable.

3.5 Conclusion

The aim of the work in this chapter was to experimentally explore a suitable nanocomposite and source fabrication method guided by previous work in this area reported in the literature. This chapter has demonstrated that CPN fabrication using mechanical dispersion of MWCNT in polymer via shear mixing and coating the resulting mixture on a glass slide is an adequate method to produce LGUS sources. By varying the polymer type, weight content of MWCNT in polymer and film thickness, peak-positive pressures up to 9 MPa and bandwidth with non-negligible frequencies up to 100 MHz were realised for a laser fluence of 50 $\mathrm{mJ\,cm^{-2}}$. The key findings from the study are as follows.

An absolute comparison of CPN sources (different polymer types and fixed MWCNT wt. %) based on their LGUS conversion efficiency cannot be made with arbitrary laser pulse durations. This is because the stress relaxation occurs at different time rates for each polymer, which is governed by the polymer's sound-speed. Furthermore, for absolute comparison the transmission coefficients of the CPN into the medium to which it is coupled also should be considered.

The CPN sources are typically more absorbing than the pure matrix material, therefore, the thickness should ideally be equal to the optical absorption depth or where possible as thin as practically achievable to minimise unnecessary acoustic absorption and loss of high frequencies.

The stability of the CPN sources under sustained laser excitation revealed that generally epoxy and to a lesser extent PU-based CPN sources were unsuitable as a stable source of ultrasound. The failure in most cases was the detachment of the CPN film from glass occurring mostly at a fluence of 30 $\mathrm{mJ\,cm^{-2}}$. A combination of water ingression and tensile stresses at the CPN-glass

interface were possibly the two reasons for debonding of the CPN film from glass. PDMS-based CPN sources were found to be most stable. A steady change in LGUS output was observed from all stable CPN sources after the first 30 min at a rate of 1% per hour. Simple assumptions suggest that this steady decrease would have a negligible consequence on hydrophone calibration.

The peak-positive pressures from the CPN sources were found to be nonlinearly dependent on the laser fluence and the bandwidth scaled inversely proportionally to the peak pressure. This is hypothesised to be due to the effect of nonlinear propagation of LGUS pulse in water whose effects increases with both pressure amplitude and propagation distance. This is explored further using numerical simulations in Chapter 4.

Chapter 4

Numerical Simulations

4.1 Introduction

In this chapter, the steepening of the time-series pressure-pulse with pressure amplitude and the effect of a bandlimited hydrophone response observed in Chapter 3 are investigated using numerical simulations. Simulations were performed in 1D since, at the measurement distance of 7.4 mm, the spatial averaging effects – the effect of diffraction – for a hydrophone element of 0.2 mm diameter were negligible (see Sec. 3.3.2). Therefore, the acoustic field relative to the hydrophone element size was considered planar.

4.2 Acoustic Propagation Model

4.2.1 Governing Equations

The simulations were performed using k-Wave, a third party open-source toolbox for MATLAB® (MathWorks, Inc., Natick, MA), which is designed for modelling the propagation of broadband acoustic waves in the time-domain in 1D, 2D or 3D. k-Wave solves a set of equations, equivalent to a generalised form of the Westervelt wave equation, which account for the medium heterogeneities, absorption and nonlinearity. k-Wave has been experimentally validated for photoacoustically-generated waves in the linear and lossless case [133], propagation of nonlinear waves in homogeneous and absorbing media [134], and propagation of linear waves in biological models mimicking absorption and strong medium heterogeneities such as brain tissue and bone [135]. Therefore, k-Wave is an appropriate tool to investigate the experimental observations presented in Chapter 3, i.e., steepening of the LGUS pressure-pulses with amplitude and the distortion of the deconvolved pressure-pulses due to the bandlimited response of the hydrophone.

The equations solved in k-Wave are a system of first-order coupled acoustic equations rather than the equivalent second-order wave equation. There are two equally important benefits of solving the first-order coupled equations. Firstly, the explicit calculation of the acoustic particle velocity as well as the acoustic pressure allows the computation of acoustic intensity, from which heat deposition in a medium can be modelled for therapeutic applications. Second, there are numerical advantages: it allows the pressure and particle velocity to be computed on staggered grids which improves accuracy

when the medium properties are heterogeneous, and a special anisotropic layer known as a perfectly matched layer (PML) can be included to absorb the acoustic waves when they reach the edges of the computational domain [136].

The system of first-order coupled equations for the case of a small amplitude acoustic waves propagating in a linear and lossless isotropic fluid medium are given by [137]

$$\begin{aligned} \frac{\partial \mathbf{u}}{\partial t} &= -\frac{1}{\rho_0}\nabla p, && \text{(momentum conservation)} \\ \frac{\partial \rho}{\partial t} &= -\rho_0 \nabla \cdot \mathbf{u}, && \text{(mass conservation)} \\ p &= c_0^2 \rho. && \text{(pressure-density relation)} \end{aligned} \tag{4.1}$$

Here $\mathbf{u}$ is the acoustic particle velocity, p is the acoustic pressure, ρ is the acoustic density, ρ_0 is the ambient density, and c_0 is the isentropic sound-speed. These first-order equations can be combined together to give the familiar second-order wave equation

$$\nabla^2 p = \frac{1}{c_0^2}\frac{\partial^2 p}{\partial t^2}. \tag{4.2}$$

When absorption, nonlinearity and medium heterogeneity need to be modelled then the system of first-order coupled equations become [136]

$$\begin{aligned} \frac{\partial \mathbf{u}}{\partial t} &= -\frac{1}{\rho_0}\nabla p, \\ \frac{\partial \rho}{\partial t} &= -(2\rho + \rho_0)\nabla \cdot \mathbf{u} - \mathbf{u} \cdot \nabla \rho_0, \\ p &= c_0^2 \left(\rho + \mathbf{d} \cdot \nabla \rho_0 + \frac{B}{2A}\frac{\rho^2}{\rho_0} - \mathrm{L}\rho \right). \end{aligned} \tag{4.3}$$

The term $-2\rho\nabla \cdot \mathbf{u}$ in the mass conservation equation, represents a convective nonlinearity in which the particle velocity contributes to the sound-speed and $\mathbf{u} \cdot \nabla \rho_0$ relates to medium heterogeneities. The four terms within the brackets of the pressure-density relation separately account respectively for linear wave propagation, heterogeneities in the ambient density, material nonlinearity, and absorption and dispersion. $\mathbf{d}$ is the time-varying displacement in the medium caused by the acoustic wave, the coefficient B/A is the nonlinearity parameter of the medium, and the operator L is a linear integro-differential operator that accounts for acoustic absorption and dispersion.

The acoustic absorption model included in k-Wave has a frequency dependence of the form

$$\alpha_{\mathrm{ac}} = \alpha_0 \omega^y, \tag{4.4}$$

where, α_{ac} [Np m^{-1}] is the absorption coefficient, α_0 [Np $(\mathrm{rad/s})^{-\mathrm{y}}$ m^{-1}] is the power law prefactor and y is the power law exponent. To implement this, the operator L contains fractional Laplacians [138]

$$\mathrm{L} = \tau_a \frac{\partial}{\partial t}(-\nabla^2)^{\frac{y}{2}-1} + \eta_d(-\nabla^2)^{\frac{y+1}{2}-1}, \tag{4.5}$$

where τ_a and η_d are parameters related to the absorption and dispersion, respectively:

$$\tau_a = -2\alpha_0 c_0^{y-1} \text{ and } \eta_d = 2\alpha_0 c_0^{y} \tan\left(\pi y/2\right). \tag{4.6}$$

The exponent y, that appears in the two terms of L, has a range $0 < y < 3$ and $y \neq 1$.

Using the first-order coupled equations in Eq. (4.3), an equivalent form of the Westervelt equation for heterogenous media obeying power law absorption can be derived [136]

$$\nabla^2 p - \frac{1}{c_0^2}\frac{\partial^2 p}{\partial t^2} - \frac{1}{\rho_0}\nabla\rho_0 \cdot \nabla p + \left(1 + \frac{B}{2A}\right)\frac{1}{\rho_0 c_0^4}\frac{\partial^2 p}{\partial t^2} - \mathrm{L}\nabla^2 p = 0. \tag{4.7}$$

4.2.2 Numerical Model

4.2.2.1 Finite Difference Method

The finite-difference time-domain (FDTD) method is a commonly used numerical method of solving equations describing wave propagation. In 1D, the technique involves calculating spatial and temporal gradients of a function, say $f(x,t)$, on an equally spaced spatial and temporal discretised domain or grid to obtain an estimate of $f(x, t + \Delta t)$. A simple method to calculate an estimate of the gradient of a function of variable x is shown in Figure 4-1. More generally, approximations based on Taylor series provide the necessary mathematical framework for finite difference (FD) approximations. If a function is smoothly varying, then the function value at $f(x + \Delta x)$ can be represented exactly by an infinite sum of function's derivates at position x:

$$f(x + \Delta x) = f(x) + \frac{\Delta x}{1!}\frac{\partial f}{\partial x} + \frac{\Delta x^2}{2!}\frac{\partial^2 f}{\partial x^2} + \frac{\Delta x^3}{3!}\frac{\partial^3 f}{\partial x^3} + \cdots. \tag{4.8}$$

Truncating high order terms and re-arranging Eq. (4.8), the first-order accurate forward difference is obtained:

$$\frac{\partial f}{\partial x} = \frac{f(x + \Delta x) - f(x)}{\Delta x} + O(\Delta x). \tag{4.9}$$

Here $O(\Delta x)$ is the truncation error. Similarly, $f(x - \Delta x)$ can be expanded using a Taylor series as:

$$f(x - \Delta x) = f(x) - \frac{\Delta x}{1!}\frac{\partial f}{\partial x} + \frac{\Delta x^2}{2!}\frac{\partial^2 f}{\partial x^2} - \frac{\Delta x^3}{3!}\frac{\partial^3 f}{\partial x^3} + \cdots. \tag{4.10}$$

Truncating high order terms and re-arranging Eq. (4.10), the first-order accurate backward difference is obtained:

$$\frac{\partial f}{\partial x} = \frac{f(x) - f(x - \Delta x)}{\Delta x} + O(\Delta x). \tag{4.11}$$

Combining Eq. (4.8) and (4.10) yields a second-order accurate central difference for the second derivative:

$$\frac{\partial^2 f}{\partial x^2} = \frac{f(x + \Delta x) - 2f(x) + f(x - \Delta x)}{\Delta x^2} + O(\Delta x^2). \tag{4.12}$$

With this expression, the second-order partial differential equation for pressure, Eq. (4.2), can be expressed using second-order central differences as follows:

$$c_0^2 \frac{p_{j+1}^n - 2p_j^n + p_{j-1}^n}{\Delta x^2} = \frac{p_j^{n+1} - 2p_j^n + p_j^{n-1}}{\Delta t^2}. \tag{4.13}$$

Here n is the temporal index, j is the spatial index, and Δx and Δt are the spatial and temporal discretisation steps. After some rearrangement, a time-stepping scheme for the acoustic pressure at timestep $n + 1$ given the field at time steps n and $n - 1$ is given by

$$p_j^{n+1} = c_0^2 \frac{\Delta t^2}{\Delta x^2} \{p_{j+1}^n - 2p_j^n + p_{j-1}^n\} + 2p_j^n - p_j^{n-1}. \tag{4.14}$$

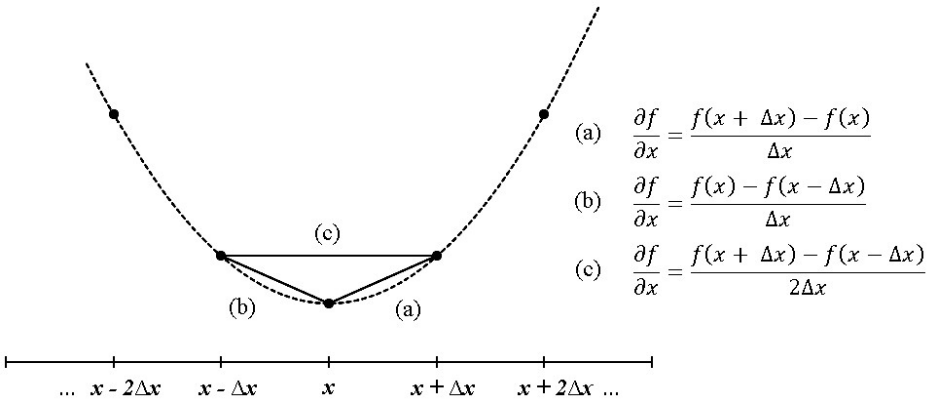

Figure 4-1: Calculation of spatial gradients of a continuous function $f(x)$ shown by the broken-line on an equally spaced grid points represented by black dots. **a** First-order accurate forward difference. **b** First-order accurate backward difference. **c** Second-order accurate centre difference.

The classical FDTD scheme is consistent and converges to the true solution to the wave equation as $\Delta t \to 0$ and $\Delta x \to 0$. However, the scheme requires very small Δt to keep the artificial numerical dispersion to a small number [139]. Also, to minimise errors in the calculation of spatial gradients either higher order finite difference approximations or increased number of grid points per wavelength (smaller Δx) are usually required. The accuracy in the calculation of spatial gradients can be improved by fitting overlapping interpolating polynomials to a small number of neighbouring grid points. This is equivalent to using higher order approximations in the Taylor Series [140]. The gradients at the grid positions are calculated by taking derivatives of the fitted polynomials. Numerical dispersion also can be reduced by using higher order time stepping schemes, based on Runge-Kutta methods for example [139].

4.2.2.2 Pseudospectral Method

k-Wave, offers significant improvement in speed and accuracy over FDTD methods, at least for homogeneous and weakly heterogeneous media, by using nonstandard pseudospectral time-domain (PSTD) schemes [141]. Instead of calculating the spatial gradients by using overlapping polynomial functions fitted to neighbouring grid points, the nonstandard PSTD uses the Fourier collocation spectral method in which the spatial field is written in term of a (truncated/bandlimited) Fourier series. The function gradient at the grid positions is calculated by taking the derivative of the Fourier series. The first advantage of using a Fourier series is that the amplitudes of the Fourier coefficients can be calculated efficiently using the fast Fourier transform (FFT). The second advantage is that since the basis functions are sinusoidal, only two grid points per wavelength are theoretically required to capture the whole field (Nyquist criterion), compared to six to ten required in FD schemes, which means relatively less memory and less computation time is required to accomplish the same task [139]. A third advantage is that the basis functions have physical meaning as plane waves, so when analysing the scheme in *k*-space, physical intuition can be used to understand what the computer code is doing.

The calculation of time domain gradients still requires conventional finite differences to be employed. However, the errors due to the numerical dispersion can be reversed by applying a correction term, $\hat{\kappa}_{tt}$ known as the *k*-space operator. It can be obtained by comparing the difference approximation and the exact integral solution of a second-order time derivative function. The nonstandard PSTD scheme for the second-order linear wave equation, Eq. (4.2) is therefore given by [141]

$$\frac{p^{n+1} - 2p + p^{n-1}}{\Delta t^2} = \mathcal{F}^{-1}\left\{-\hat{\kappa}_{tt} c_0^2 k^2 \mathcal{F}\{p^n\}\right\}. \tag{4.15}$$

Here, p, the acoustic pressure is the concise form of $p(x, y, z, t)$, $\mathcal{F}$ and $\mathcal{F}^{-1}$ are the forward and inverse spatial Fourier transforms, $k^2 = \mathbf{k} \cdot \mathbf{k} = k_x^2 + k_y^2 + k_z^2$, where $\mathbf{k}$ is the wavevector, the

term $-c_0^2k^2$ is the Fourier representation of the spatial differential operator, and $\hat{\kappa}_{tt}$ is the second-order *k*-space operator given by

$$\hat{\kappa}_{tt} = \mathrm{sinc}^2(c_0 k\, \Delta t/2). \tag{4.16}$$

4.2.3 Discrete Equations

The first-order coupled equations in Eq. (4.3), converted to discrete form using the nonstandard finite difference method [141], also known as the *k*-space PSTD method, become [139]

$$\frac{\partial}{\partial \zeta} p^n = \mathcal{F}^{-1}\left\{ik_\zeta \hat{\kappa}_t e^{ik_\zeta \Delta\zeta/2}\mathcal{F}\{p^n\}\right\}, \tag{4.17}$$

$$u_\zeta^{n+\frac{1}{2}} = u_\zeta^{n-\frac{1}{2}} - \frac{\Delta t}{\rho_0}\frac{\partial}{\partial \zeta} p^n + \Delta t S_{F_\zeta}^n, \tag{4.18}$$

$$\frac{\partial}{\partial \zeta} u_\zeta^{n+\frac{1}{2}} = \mathcal{F}^{-1}\left\{ik_\zeta \hat{\kappa}_t e^{-ik_\zeta \Delta\zeta/2}\mathcal{F}\left\{u_\zeta^{n+\frac{1}{2}}\right\}\right\}, \tag{4.19}$$

$$\rho_\zeta^{n+1} = \frac{\rho_\zeta^n - \Delta t \rho_0 \frac{\partial}{\partial \zeta} u_\zeta^{n+\frac{1}{2}}}{1 + 2\Delta t \frac{\partial}{\partial \zeta} u_\zeta^{n+\frac{1}{2}}} + \frac{\Delta t S_{M_\zeta}^{n+\frac{1}{2}}}{1 + 2\Delta t \frac{\partial}{\partial \zeta} u_\zeta^{n+\frac{1}{2}}}, \tag{4.20}$$

$$p^{n+1} = c_0^2\left(\rho^{n+1} + \frac{B}{2A}\frac{1}{\rho_0}(\rho^{n+1})^2 - \mathrm{L}_d\right), \tag{4.21}$$

where, $\mathcal{F}$ represents a discrete Fourier Transform (FFT). The discrete power law absorption term has the form

$$\mathrm{L}_d = -\tau_a \mathcal{F}^{-1}\left\{k^{y-2}\mathcal{F}\left\{\rho_0 \sum\nolimits_\zeta \frac{\partial}{\partial \zeta} u_\zeta^{n+\frac{1}{2}}\right\}\right\} + \eta_d \mathcal{F}^{-1}\left\{k^{y-1}\mathcal{F}\left\{\rho^{n+1}\right\}\right\}. \tag{4.22}$$

These equations are repeated in sequence for each Cartesian direction $\mathbb{R}^N$ where $\zeta = x$ in $\mathbb{R}^1$, $\zeta = x, y$ in $\mathbb{R}^2$, and $\zeta = x, y, z$ in $\mathbb{R}^3$ (N is the number of spatial dimensions). Here i is the imaginary unit, $\hat{\kappa}_t = \mathrm{sinc}\left(c_0 k_\zeta\, \Delta t/2\right)$ is the first-order *k*-space operator, k_ζ represents the wavenumbers in the ζ direction, $\Delta\zeta$ is the grid spacing in the ζ direction, and the total mass density is obtained by summing the acoustic densities $\rho^{n+1} = \sum_\zeta \rho_\zeta^{n+1}$. The mass density is artificially divided to facilitate the inclusion of the PML. The force-source term, $S_{F_\zeta}^n$ in Eq. (4.18) represents the input of body forces per unit mass in units of N kg^{-1} or m s^{-2} and the mass-source term, $S_{M_\zeta}^{n+1/2}$ in (4.20) represents the time rate of the input of mass per unit volume in units of kg m^{-3} s^{-1} [139]. For an initial value problem, the source terms in the above equations become zero. When pulsed heating of an optically absorbing medium needs to be modelled and there is no thermal diffusion then the heat source, S_H can be treated

as a mass sources using the relation $S_M = S_H \beta_v / C_p$, where β_v and C_p are the volume thermal expansion coefficient and specific heat capacity at constant pressure, respectively [139].

The variables, $\partial u_\zeta^{n+1/2}/\partial\zeta$, ρ_ζ^{n+1} and p^{n+1} in Eq. (4.19), (4.20) and (4.21), respectively, are calculated on the actual grid points spaced $\Delta\zeta$. The remaining variables, $\partial p^n/\partial\zeta$ and $u_\zeta^{n+1/2}$ in Eq. (4.17) and (4.18), respectively, are calculated on the staggered spatial grid, which is spaced $\Delta\zeta/2$ from the actual grid. In all the discrete equations above, the superscripts n and $n+1$ denote the function values at the current and the next time steps and $n-1/2$ and $n+1/2$ at the time-staggered points. The time-staggering by half a time-step arises because of the interleaving of the gradient calculations, Eq. (4.17) and (4.19), with the update Eq. (4.18) and (4.20).

4.2.4 Consistency, Stability and Convergence

It is always important that a numerical method for solving an equation is convergent, i.e., that the solution from the numerical scheme approaches the true solution of the continuous equation as the time and spatial steps tend to zero. Whether a scheme is convergent is dependent on the numerical scheme being both *consistent* and *stable*. This is expressed by the Lax's equivalence theorem, which states that if a finite difference scheme is consistent and stable then it will be convergent. The discrete *k*-space PSTD equations are consistent because they become the continuous equations in the limit, $\Delta t \to 0$ and $\Delta\zeta \to 0$. A scheme is stable if the errors in the numerical solution remain bounded for all times, which in this case is assured by the use of the *k*-space operator. But this is valid only for the case of a linear, lossless, and homogenous medium. The *k*-space operator is dependent on a single value for the sound-speed and therefore, for a heterogenous medium, where the ambient sound-speed is spatially varying, the *k*-space operator can no longer exactly reverse the numerical dispersion introduced by the finite difference time-step. Therefore, a reference sound-speed, c_{ref} needs to be chosen for Eq. (4.16) such that the solution is both stable and rapidly converges i.e., the phase errors quickly become negligible as the timestep decreases. One of the cases for which the stability is ensured is if $c_{ref} = \max(c_0)$ and the time-step is chosen such that $\Delta t \leq \left(2/c_{ref}k_{max}\right)sin^{-1}\left(c_{ref}/max(c_0)\right)$ [142].

A widely-used notion relating to stability when solving partial differential equations using finite difference schemes is the Courant-Friedrichs-Lewy (CFL) number [140], which is defined as the ratio of the distance travelled by a wave in one time-step, $c_0\Delta t$ to the grid spacing, $\Delta\zeta$

$$\mathrm{CFL} = \frac{c_0\Delta t}{\Delta\zeta} = \frac{PPW}{PPP}, \tag{4.23}$$

where, $\mathrm{PPW} = \lambda/\Delta\zeta$ is points per wavelength assuming $\Delta x = \Delta y = \Delta z$ and $\mathrm{PPP} = 1/f\Delta t$ is points per period. For a heterogenous medium, c_0 in Eq. (4.23) should be replaced by c_{max}. The default value of the CFL used by k-Wave is 0.3, although this can be changed by the user. This is then used to determine the time-step.

The maximum spatial frequency supported by a particular computational grid is given by the Nyquist limit of two grid points per wavelength, where $k_{max} = \pi/\Delta\zeta$ assuming $\Delta x = \Delta y = \Delta z$. The spatial wavenumber and temporal frequency are related by $k = 2\pi f/c_0$, thus the maximum wavenumber corresponds to a maximum temporal frequency of $f_{max} = \min c_0/2\Delta\zeta$. If the input signal contains higher frequencies that the grid cannot support then the frequency content is truncated, which distorts the input signal. When nonlinear propagation generates frequencies higher than the grid can support then spectral blocking can occur [143]. In the convergence tests the maximum grid frequency was chosen such that the spectral blocking did not distort the highest frequency of interest in the simulations.

The final step then is to ensure the solution computed by the numerical model has converged sufficiently closely to the true solution for the purpose at hand. This task requires gradually changing, e.g., successively halving, the values of $\Delta\zeta$ and Δt until the change in the computed solution is within an acceptable tolerance.

4.3 Nonlinear Propagation in Water

The effect of nonlinear propagation was investigated by simulating the propagation of an initial pressure distribution (IPD), assuming stress confinement, of various amplitudes. The different acoustic properties of the glass-backing and the CPN were not included in the initial study since the majority of the propagation occurs in water. The thickest CPN source tested was 85 µm, which is nearly one order of magnitude smaller than the experimental measurement distance of 7.4 mm. Therefore, any nonlinear effects occurring within the CPN source are expected to be negligible. The schematic of the 1D numerical grid is shown in Figure 4-2. The IPD, $p_0(z)$, was calculated using Eq. (2.4) with μ_a = 125,000 m^{-1}, which represents epoxy-CPN with 2.5 wt. % MWCNT (see Table 3-3). The physical properties of epoxy were taken from Table 3-4 and the thickness of the absorbing region was set to 10 µm. The total length of the grid was 10.24 mm. The IPD was launched from one end of the grid 1.2 mm away from the PML.

4.3.1 Convergence Test

A convergence test was first completed by successively halving the size of Δx and Δt. The amplitude was set to 44.8 MPa for all cases and the pressure-pulses were recorded at a distance of 7.4 mm from $z = 0$. The amplitude of the pressure-pulses at 7.4 mm were around 4.4 MPa and the pulse was nonlinearly steepened, which is discussed in more detail in Sec. 4.3.2. The spectral magnitudes (Fourier transform of the pressure-pulses) for each value of Δx and Δt were computed to identify the conditions necessary for solution convergence. For the plot shown in Figure 4-3, the spectral magnitudes at 25, 50 and 100 MHz are plotted as a function of PPW and CFL. The spectral magnitudes for each frequency are normalised using the spectral magnitude computed for the smallest Δx and Δt of the same frequency. It can be seen in Figure 4-3 that there is convergence for each frequency as PPW increases

and CFL decreases. Here, three different frequency plots are shown for the convergence test but really it is the highest frequency which is of interest. When the highest frequency converges, naturally the frequencies below the highest frequency would have already converged since they are represented by more PPW. For the 100 MHz convergence plot shown in Figure 4-3 the standard deviation in the actual pressures for PPW values of 11.9, 23.7, 47.4 and 94.9 were 4.9, 2.4, 1.2 and 0.6%, respectively. To investigate the effect of pressure amplitude on nonlinear propagation, CFL = 0.1 (or PPP = 20) and PPW = 47.4 were chosen as a trade-off between practicality (memory and time to complete the simulation) and accuracy. This corresponded to grid-size, N_x = 32768 and Δx = 312.5 nm for a grid dimension of 10.24 mm. The maximum spatial frequency supported by this grid was 2.372 GHz.

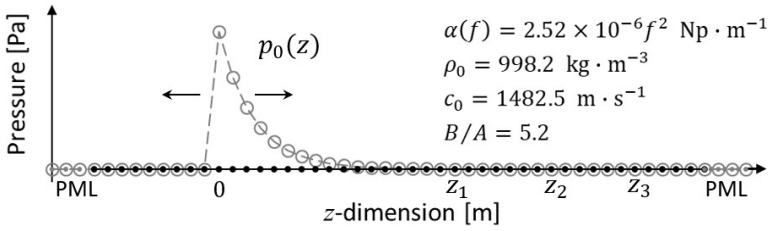

Figure 4-2: Schematic of the 1D computational grid implemented in k-Wave to investigate the wave steepening and broadening of a time-series pressure-pulse due to nonlinear propagation of a high amplitude laser generated ultrasound pulse in water. PML: perfectly matched layer, $p_0(z)$: initial pressure distribution defined using Eq. (2.4) and the physical properties of epoxy polymer taken from Table 3-4 and μ_a = 125,000 m^{-1}; B/A: nonlinear parameter of water; c_0: sound-speed of water; ρ_0: ambient density of water; f: frequency in MHz; $\alpha(f)$: frequency dependent acoustic absorption of water; z_1, z_2, and z_3: specified grid points for recording time-series pressure-pulse, $p_z(t)$.

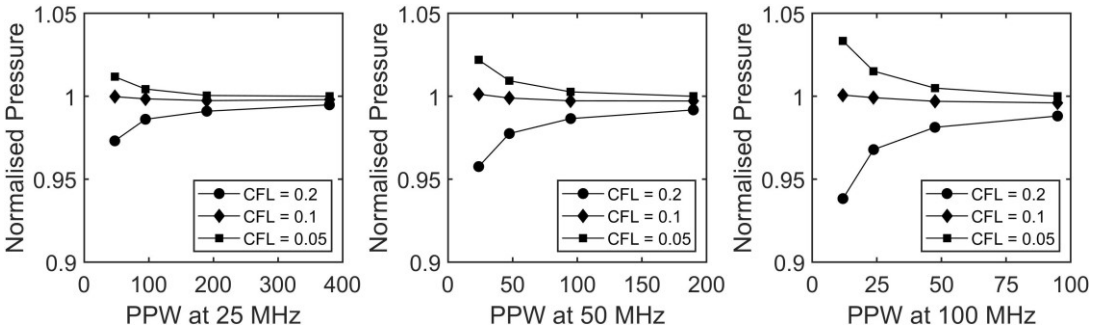

Figure 4-3: Convergence of spectral components of p(z, t) recorded at a distance of 7.4 mm on the grid, which is plotted as a function of PPW and CFL at 25 MHz, 50 MHz and 100 MHz, respectively. The spectral magnitudes at each frequency were normalised using the spectral magnitude computed for the highest N_x and lowest CFL. The three CFL values 0.2, 0.1 and 0.05 correspond to the three PPP 10, 20 and 40, respectively.

As mentioned earlier, the convergence tests were performed assuming stress confinement. Therefore, to accurately represent the step discontinuity in the IPD shown in Figure 4-2, potentially a very large number of sinusoids will be required. Also, as soon as the wave starts to propagate, absorption in the CPN and water tends to smooth the sharp discontinuity by damping the high frequencies of the pressure-pulse. Since stress confinement was generally not satisfied for the CPN sources fabricated in this thesis, a step discontinuity would not occur in practice. Therefore, the convergence tests represent a worst-case scenario.

4.3.2 Pressure versus Nonlinearity

The IPD was scaled from 5.6–44.8 MPa in steps of 2.8 MPa by scaling the fluence parameter. These amplitudes were chosen such that the recorded amplitudes of the time-series, $p(z,t)$, at 7.4 mm were within the range of experimentally measured values of 1.2–6.9 MPa. The time-series pressure-pulse, $p(z,t)$, was recorded at 0.2 mm increments from the interfacial position of the CPN source and water so that the time-series could be analysed for the effects of nonlinear propagation as a function of pressure amplitude and propagation distance.

The time-series pressure pulses shown in Figure 4-4 correspond to simulation results for an optical absorption depth of 50 μm. This thickness was specifically chosen to show the exponential pressure distribution within the CPN source and the wave shape transformation from this initial exponential shaped pressure-pulse to a steepened pressure-pulse. The time-series recorded at 0.2 mm from the interfacial position of the CPN source and water have clear exponential profiles (see Figure 4-4(a)) for all three laser fluences of 5, 22, and 40 mJ cm^{-2}. But as the wave propagates further away, the cumulative acoustic nonlinearity acts to steepen the front edge of the wave in the direction of propagation. The degree to which the wave shape transforms to a steepened wave is dependent on both the propagation distance and the amplitude of the wave. This progressive change can be seen in Figure 4-4(a)–Figure 4-4(f). The corresponding Fourier (amplitude or magnitude) spectra of a few time-series are shown in Figure 4-5.

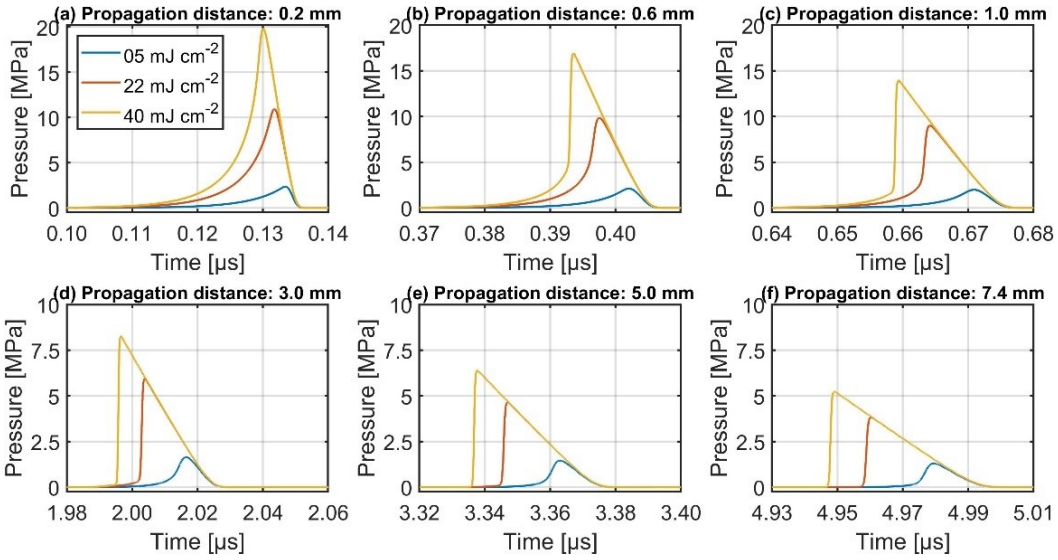

Figure 4-4: Distortion (steepening) of the time-series pressure-pulse caused by cumulative acoustic nonlinearity as a function of pressure amplitude and propagation distance for laser fluence of 5, 22, and 40 mJ cm^{-2} shown for various propagation distances from **a**–**f**. The propagation distance corresponds to the wave propagation distance from $z = 0$ shown in Figure 4-2. The steepening of the pressure-pulse is accompanied with broadening of the time-series for laser fluences of 22 and 40 mJ cm^{-2}. The optical absorption depth for this simulation was set to 50 μm.

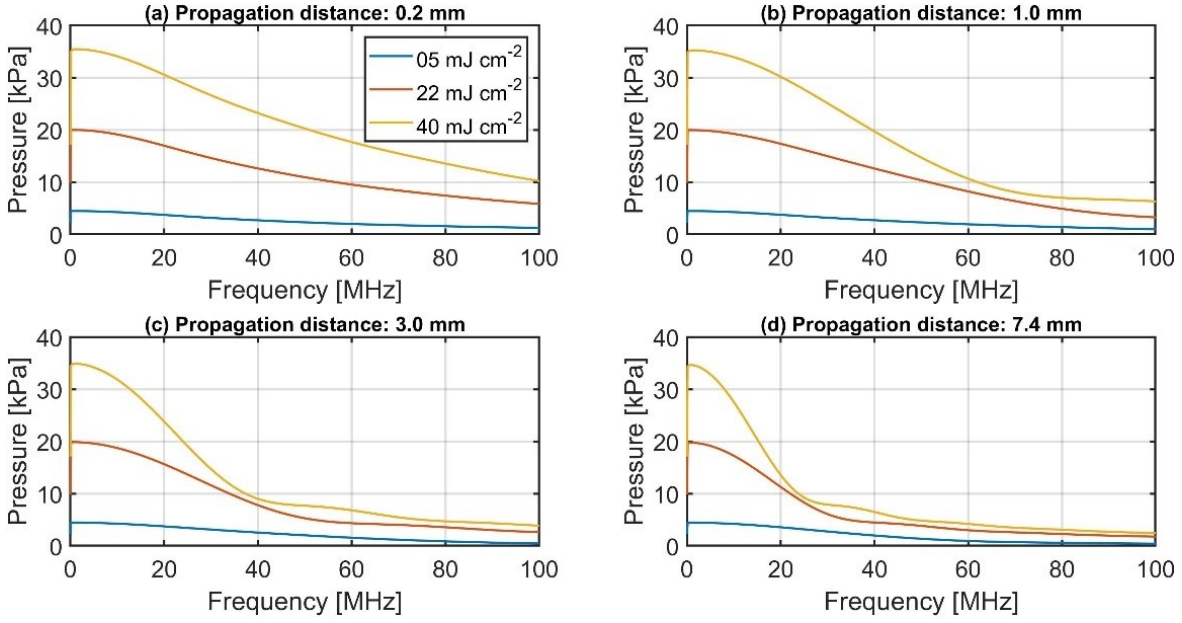

Figure 4-5: Fourier (amplitude) spectra of the time-series shown in Figure 4-4 for propagation distances of 0.2, 1.0, 3.0 and 7.4 mm.

The effect of nonlinear propagation and acoustic absorption on the pressure amplitude and −6 dB bandwidth (*BW6*) are shown in Figure 4-6 and Figure 4-7, respectively. The peak-positive (p_+) pressures of the simulated time-series pressure-pulses and the bandwidths obtained from their magnitude spectra are plotted in Figure 4-6(a) and Figure 4-7(a) as a function of source-sensor separation and fluence. For comparison, simulated data are plotted in Figure 4-6(b) and Figure 4-7(b), for the range of source-sensor distances which overlap with the source-sensor separations of the measured data. The simulations correspond to an optical absorption depth of 10 µm. The measured results from an epoxy-based CPN source of 10 µm thickness with 2.5 wt. % MWCNT are shown in Figure 4-6(c) and Figure 4-7(c) over the same fluence range but the closest source-hydrophone distance was 3.9 mm as opposed to 0.2 mm in the simulations. This is because the hydrophone signal chain was susceptible to radio-frequency noise emitted by the Q-switch of the laser, which lasted for up to 2.5 µs and hence the hydrophone could not be closer than 3.9 mm (or 2.63 µm in time-of-flight).

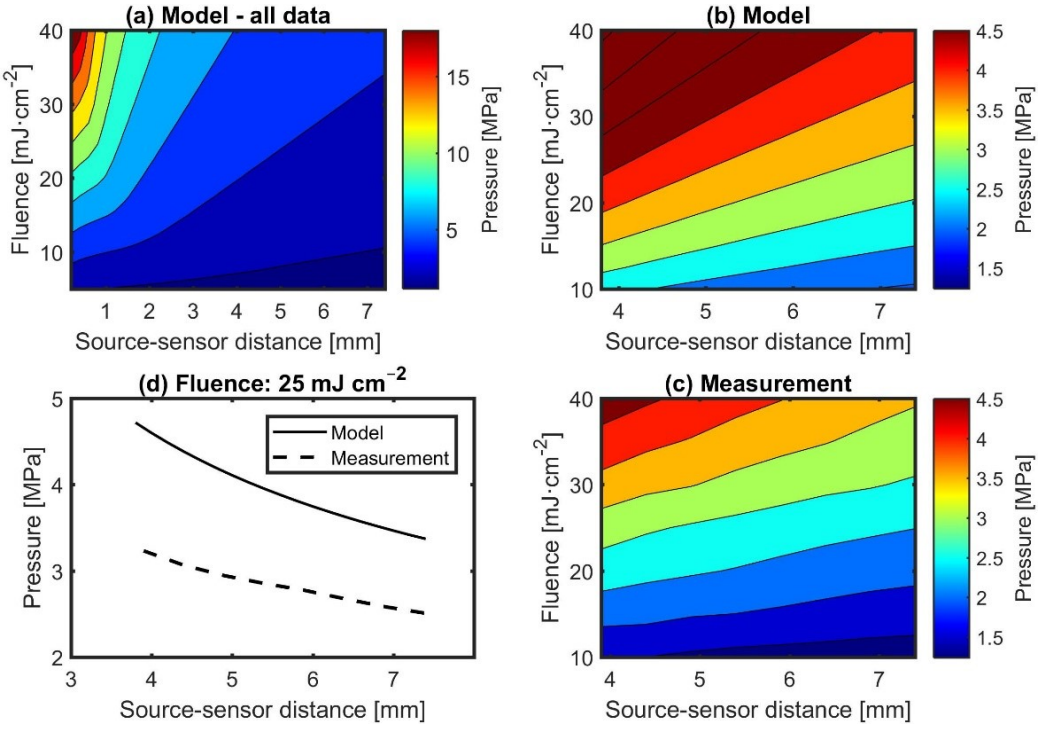

Figure 4-6: **a** Peak-positive pressures of the simulated time-series pressure-pulses using k-Wave plotted as a function of laser fluence and source-sensor separation. In the model, the thickness of the optical absorption region was set to 10 µm to match the experimental case. **b** Comparison of simulation data at the same source-sensor separation as the measured data in **c**. The experimental source was an epoxy-based CPN dispersed with 2.5 wt. % MWCNT and a thickness of around 10 µm. The hydrophone could not be positioned below 3.9 mm (or 2.63 µs in time-of-flight) due to pick up of radio-frequency noise emitted by the Q-switch of the laser, which lasted for up to 2.5 µs. **d** Line plot of model and measured pressures at 25 mJ cm^{-2}.

Whilst a comparison is shown between measurement and simulations, it should be noted that the simulation does not exactly match the conditions of the measurement. The epoxy-based CPN source has a glass backing, and the laser pulse of 4 ns duration does not satisfy stress confinement. In simulations, on the other hand, the glass backing was not modelled, and stress confinement was assumed. Therefore, care should be taken when comparing measured and modelled data. However, the important rationale for carrying out these simulations was to demonstrate that the LGUS pressure-pulse in the measurements are linear only over a short propagation distance of around 0.2 mm from the CPN source and thereafter the pressure-pulse becomes nonlinear.

The *BW6* is highest in the linear region but when the pressure-pulse starts to steepen, the preferential loss of high frequencies causes the pulse to become broader. This observation is quite counter intuitive to the general understanding of the effect of nonlinear propagation in which a single frequency low-MHz acoustic wave generated at the face of an ultrasound transducer becomes progressively nonlinear the further it propagates, thus adding more and more harmonic frequencies. When the wave is significantly steepened, i.e., $\partial p/\partial t$ or $\partial \mathbf{u}/\partial t$ reaches a maximum, then the wave is harmonically rich [130]. Thereafter the effect of absorption dominates on the harmonic frequencies, and the wave eventually becomes a single frequency wave with a diminished amplitude. However, in case of a LGUS pressure-pulse, the impact of absorption is instantaneous since the pulse is already broadband. Though the cumulative acoustic nonlinearities acts to steepen the pulse, the rapid dampening of both the high frequencies already present in the pulse and those generated via cumulative acoustic nonlinearity causes it to broaden, the effect of which increases with propagation distance as seen in Figure 4-4. The decrease in bandwidth means that the pressure amplitudes at higher frequencies will be lower, which means that the SNR will be lower. For the primary calibration of hydrophones on the interferometer, it is required that pressure levels at all frequencies are sufficiently above the SNR so that the measurement uncertainties are kept to a minimum. Therefore, during calibration, the hydrophone would need to be positioned as close as practically achievable to the CPN source.

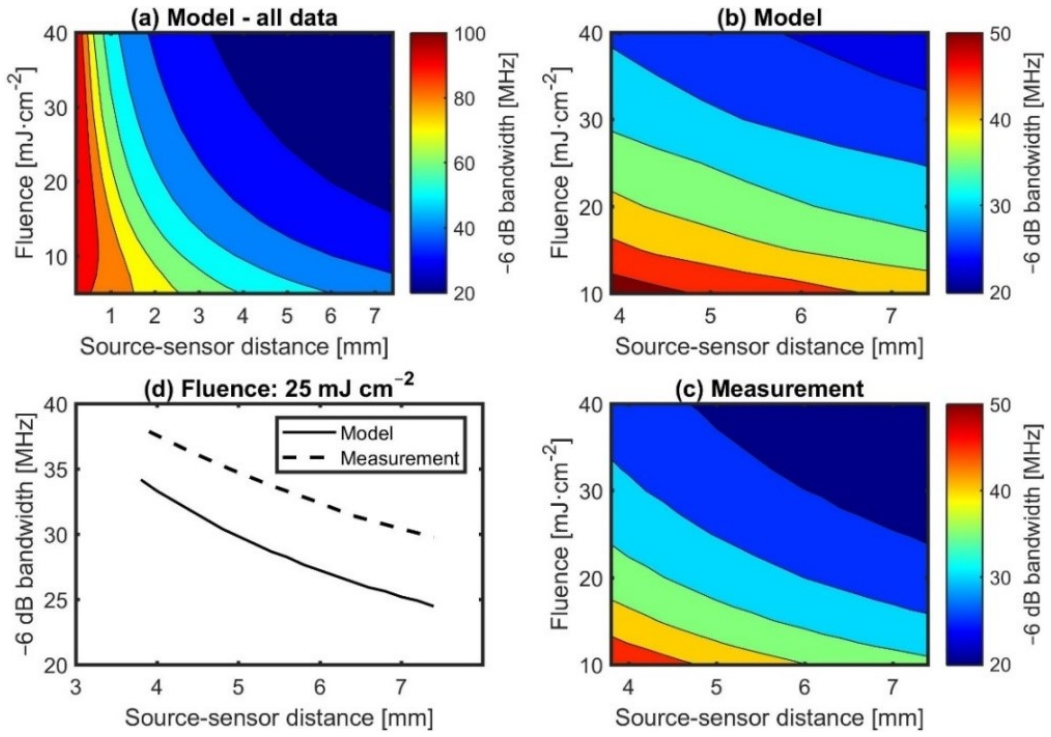

Figure 4-7: **a** −6 dB bandwidths of the simulated time-series pressure-pulses using k-Wave plotted as a function of fluence and source-sensor separation. In the model, the thickness of the optical absorption region was set to 10 µm to match the experimental case. **b** Comparison of simulation data at the same source-sensor separation as the measured data in **c**. The experimental source was an epoxy-based CPN dispersed with 2.5 wt. % MWCNT and a thickness of around 10 µm. The hydrophone could not be positioned below 3.9 mm (or 2.63 µs in time-of-flight) due to pick up of radio-frequency noise emitted by the Q-switch of the laser, which lasted for up to 2.5 µs. **d** Line plot of model and measured bandwidths at 25 mJ cm^{-2}.

4.3.3 Bandlimited Hydrophone Response

The simulated pressure-pulses in Figure 4-4 and the measured, deconvolved, hydrophone pressure-pulses in Chapter 3, for example Figure 3-15, are qualitatively different. There are undulations on the trailing side of the measured pressure-pulses which do not appear in Figure 4-4. Since LGUS pulses have a wider bandwidth than the hydrophone, it was hypothesised that the bandlimited response of the hydrophone was a likely cause for the difference between the simulation and the measurements. To test the hypothesis, pressure time-series were simulated for an epoxy-based CPN source of 10 µm thickness sandwiched between glass and water half spaces for comparison with an experimental source of similar thickness. The model input parameters are shown in Table 4-1. The time-series pressure pulse, $p(z,t)$, recorded at a grid location of 7.4 mm in water from the IPD was then

convolved with the complex sensitivity response of the hydrophone (see Sec. 3.3.4) to derive the model voltage, $u_{model}(z,t)$, as follows:

$$u_{model}(z,t) = \mathcal{F}^{-1}\{\mathcal{F}[p_{model}(z,t)] \times \underline{M}(f)\}. \quad (4.24)$$

Here, $p_{model}(z,t)$, is the simulated pressure-pulse. Since the time-steps in the simulation and measurement were different, i.e., 2.7704 and 400 ps, respectively, the simulated $p_{model}(z,t)$ was down-sampled using MATLAB's *resample* function to match with the sampling frequency of the measured oscilloscope. $\underline{M}(f)$ was set to zero at 0 Hz and beyond 110 MHz and in between it was set to the predicted response using the hydrophone model [126]. The resulting voltage time-series, $u_{model}(z,t)$, was then compared with the measured hydrophone voltage time-series, $u_{meas}(z,t)$, obtained from a 10 μm thick epoxy-based CPN with 2.5 wt. % MWCNT. The amplitude of the IPD was varied by scaling the fluence parameter such that the amplitude of $p_{model}(z,t)$ at 7.4 mm was approximately equal to the deconvolved pressure-pulse for applied fluence levels of 10, 20, and 40 mJ cm^{-2} in the experiment. The scaled values of the three fluence levels were 0.7, 0.77 and 0.8, respectively.

It was noted in Sec. 4.2.1 that the acoustic absorption within k-Wave is implemented as a power-law model using a fractional Laplacian operator. The acoustic loss model allows heterogeneous media to have different power law absorption prefactors, but the power-law exponent must be the same for all media (as a consequence of it being applied in *k*-space). Therefore, considering these limitations, the thinnest source of 10 μm was chosen as the model and measurement are most similar. For simulations, acoustic absorption within glass and epoxy-based CPN were assumed to be that of water.

The effective mass density and sound-speed of the CPN are not known, so they were estimated by fitting the simulated time series to the measurements (see Table 4-1). The reduction in sound-speed is due to the multiple scattering of acoustic waves caused by the presence of carbon nanotubes in epoxy. This is consistent with the results of a previous experimental study in which the sound-speed is reduced with increasing volume fraction of the metallic powder [144]. Also, the density of tungsten and alumina loaded epoxy composites increased with volume fraction. The 2.5 wt. % of CNT in epoxy and the bulk density of the CNT, which is around 50 kg m^{-3} [145], is too small to lower the effective density of the CNT. Therefore, the decrease in density of the epoxy-based CPN is likely to be due to the air trapped in the CPN during fabrication.

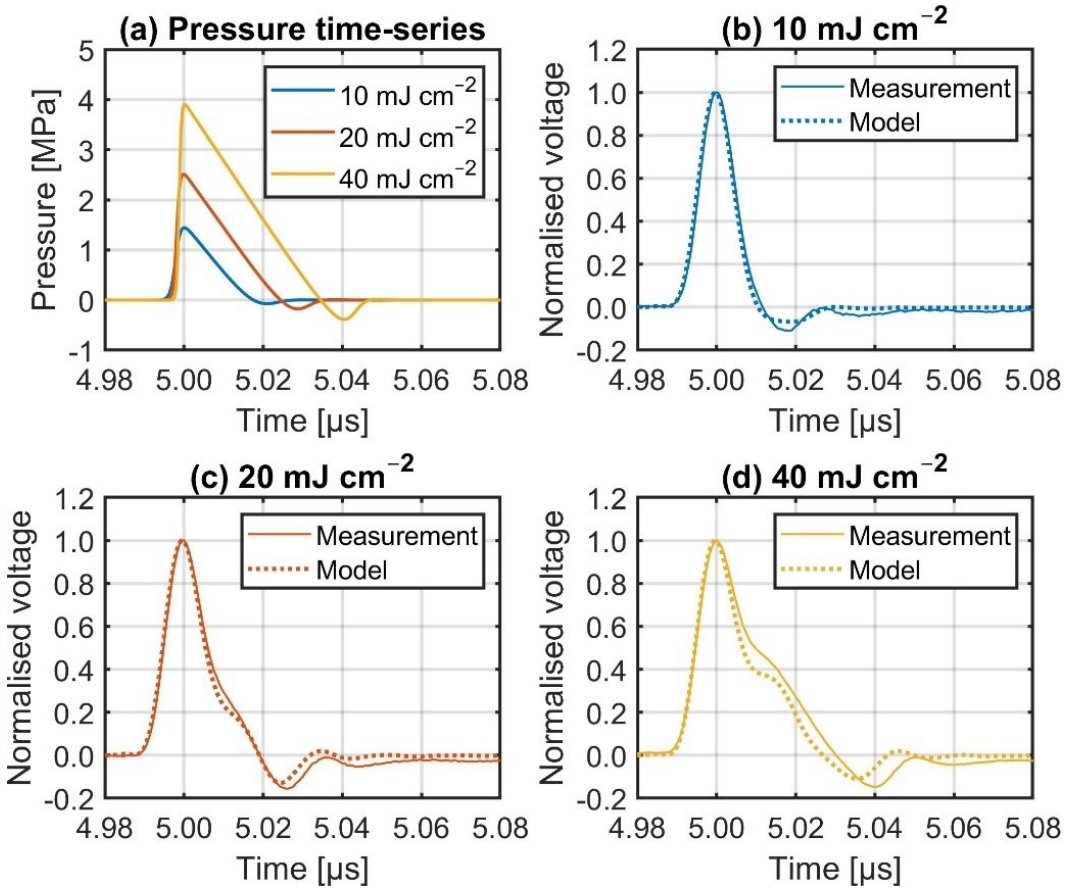

Figure 4-8: Pressure time-series simulated using k-Wave in 1D from a three layered media comprising of 10 μm thick epoxy-based CPN with 2.5 wt. % multiwalled carbon nanotubes sandwiched between glass and water half spaces. The time-series was recorded at a distance of 7.4 mm from the initial pressure distribution for laser fluences of 10, 20, and 40 mJ cm^{-2}. Normalised model derived voltage time-series obtained by convolving the pressure time-series in **a** with the complex sensitivity response of the hydrophone are plotted along with the normalised measured voltage timeseries for laser applied fluences of **b** 10, **c** 20, and **d** 40 mJ cm^{-2}. The two time-series were aligned by shifting the model derived voltage time-series with respect to the measured time-series.

There is a good agreement between measured and model derived voltage time-series for the case of 10 and 20 mJ cm^{-2} shown in Figure 4-8(b) and Figure 4-8(c), respectively, which confirms that the limited bandwidth is the dominant cause for the presence of undulations in the deconvolved time-series pressure pulses. However, in Figure 4-8(d) at 40 mJ cm^{-2}, the trailing part of the model-derived voltage time-series is slightly offset from the measured voltage time-series. It is suspected that this difference could be due to a temperature-dependent change in the material properties of epoxy-based CPN as the fluence increases beyond 20 mJ cm^{-2}. From Table 3-5, for epoxy polymer loaded with 2.5 wt. %

MWCNT the estimated initial temperature rise, T_0, for 10 mJ cm^{-2} is 8.3 ℃ and for 20 and 40 mJ cm^{-2} it increases linearly to 16.6 and 33.2 ℃, respectively. The measured sound-speed and attenuation of unfilled epoxy at 2 MHz was found to decrease by 6% and 10%, respectively [146] over the same temperature range. Therefore, the transient changes in the sound-speed and attenuation are likely to have affected the pulse shape of the LGUS pressure-pulse during the heating phase of the CPN medium.

Table 4-1: Model input parameters used in 1D k-Wave for the generation of time-series pressure pulses from an epoxy polymer nanocomposite backed on glass and radiating acoustic wave in water media. The values for sound-speed and mass density epoxy-based CPN were varied approximately by 10% and 25%, respectively, to achieve a closest agreement of model derived voltage time-series with the measurements.

Parameter	Material	Value	Units
Mass density, ρ_0	Pyrex glass Epoxy Water	2230 750 998.2	kg m^{-3}
Sound speed, c_0	Pyrex glass Epoxy Water	5640 2300 1482.5	m s^{-1}
Acoustic absorption, $\alpha(f)$	Water	$2.52 \times 10^{-6} f^2$	Np m^{-1}
Optical absorption coefficient, μ_a	Epoxy-CPN	125000	m^{-1}
Coefficient of thermal expansion, β	Epoxy	217×10^{-6}	m^{-1}
Specific heat capacity, C_p	Epoxy	1600	J kg^{-1} K^{-1}

Although PDMS-based CPN sources are favoured for practical purposes over epoxy and PU-based CPN sources, due to their more stable LGUS output under sustained pulsed laser excitation, the simulations and comparison to measurements in this section were all based on epoxy-based CPN sources because the pulse broadening due to cumulative acoustic nonlinearity is more clearly discernible in this case. The reason is that the pressure output from PDMS-based CPN source was around a factor of 2.7 higher than for epoxy-based sources, so for PDMS-based sources, the pulses had already broadened by the time they reached the measurement location whatever the fluence level. For epoxy, as the pressures were lower, the effect of the different fluence levels can be seen more clearly.

4.4 Conclusion

The purpose of this chapter was to numerically investigate the nonlinear propagation of source pulses as this has not been widely considered in the literature. The experimental observations from Chapter 3, i.e., steepening, and the effect of bandlimited hydrophone response on the deconvolved pressure-pulses were numerically investigated. The simulations were performed in k-Wave in 1D.

To investigate the effect of wave steepening, stress-confined IPDs of various amplitudes were propagated. Since the thickness of the CPN source was small compared to the experimental propagation distance of 7.4 mm in water, only a homogeneous medium of water was considered. Wave steepening due to cumulative acoustic nonlinearity was observed for all stress-confined amplitudes in the range 5.6–44.8 MPa. The degree to which the wave steepening occurred was dependent on the pressure amplitude and propagation distance. The effect of nonlinear propagation on the −6 dB bandwidth was most significant. The *BW6* was highest in the linear region but when the pressure-pulse transformed to a nonlinear pulse, the preferential loss of high frequencies caused the pulse to broaden. Hence, the *BW6* decreased with increasing nonlinearity, which agrees with the measurements.

The effect of the bandlimited hydrophone response on the measured pressure-pulses was investigated by propagating stress-confined IPD in a layered media. The layered media consisted of glass, epoxy-based CPN and water. The IPD propagated from within the CPN medium was recorded in the water layer and convolved with the complex sensitivity response of the hydrophone. The resulting model derived voltage time-series showed a good agreement with measurement, i.e., undulations on the trailing side of the hydrophone voltage time-series from a nominally identical CPN source. The undulations appear because the hydrophone's sensitivity response is limited when compared to the bandwidth of the LGUS pressure-pulse.

Chapter 5

Advanced Source Design

5.1 Introduction

In Chapter 3, the results from a study comprising 27 glass-backed carbon-polymer nanocomposite (CPN) sources fabricated by varying the polymer type, carbon nanotubes (CNT) weight percent (wt. %) and thickness were discussed. For a laser pulse of 4 ns duration, polydimethylsiloxane (PDMS) polymer-based CPN sources generated the highest pressure compared to epoxy or polyurethane-based CPN sources for nominally identical CNT wt. %, thickness, and laser fluence. Though stress confinement was generally not satisfied, PDMS-based CPN sources generated the highest pressure because the stress relaxation times were longer compared to epoxy or PU-based CPN sources. The nonlinear propagation of laser-generated ultrasound (LGUS) pressure-pulses resulted in the peak-positive (p_+) pressure and the −6 dB bandwidth ($BW6$) to be inversely related. The nonlinear propagation and the effect of the bandlimited hydrophone response were confirmed via numerical simulations in Chapter 4.

The bandwidth of the LGUS pressure-pulse can be increased by changing the design of the CPN source. Consider a CPN layer on a glass-backing in water. Due to the significant difference in acoustic impedance between the CPN and glass, one half of the initial LGUS pulse, the part propagating towards the glass, gets largely reflected within the CPN medium and immediately follows the other half propagating towards the water. Therefore, temporally, the wave exiting the CPN medium into the water will be of twice the duration taken by the acoustic wave to transit across the thickness of the CPN layer. If the CPN source is backed on an acoustically matched backing, i.e., the same polymer used as the matrix in fabricating the CPN, then the half of the LGUS pulse propagating towards the polymer-backed medium is not reflected and does not therefore contribute to the acoustic field in the water. Since the duration of the pressure-pulse from a glass-backed CPN source will be twice that of the polymer-backed CPN source, the bandwidth of the glass-backed pressure-pulse will be narrower than the polymer-backed pressure-pulse, whilst the amplitude of the pressure-pulses remain the same. This is true only in the case of stress confinement. But, when stress confinement is not satisfied as is the case for most of the experiments in this thesis, the pressure amplitude from

glass-backed CPN sources were found to be higher compared to polymer-backed CPN sources. This effect of backing on LGUS pulse amplitude was investigated with experiments using a fibre-laser with a variable pulse duration and with analytical and numerical models.

In this chapter, the fabrication of PDMS-backed PDMS-based CPN sources is described in Sec. 5.2 and the initial experimental results are discussed in Sec. 5.3. An extended experimental study involving five laser pulse durations whose full-width at half-maximum (FWHM) spanned from 10–200 ns is described in Sec. 5.4. A 1D linear analytical model was developed to obtain an intuitive understanding of how the source backing affects the amplitude of the LGUS in the absence of stress confinement is described in Sec. 5.5. In Sec. 5.6, a comparison of the results from Sec. 5.4 with simulations in k-Wave is made.

5.2 Polymer-backed Source Fabrication

The epoxy- and polyurethane-based CPN sources were not pursued further as a potential source of LGUS following their temporal instability and issues with CPN detachment from glass (see Sec. 3.4.6). The initial study into the effect of backing was carried out by fabricating glass-backed PDMS-based CPN sources with 2.5 wt. % multi-walled CNT (MWCNT) using the method described in Sec. 3.2. To fabricate PDMS-backed sources, the following approach was taken. A small amount of petroleum jelly (debonding agent) was hand spread on one surface of an optical-flat glass disc of 50 mm diameter (FSW18, Newport Spectra-Physics Ltd, Didcot, U.K.). The surface was then wiped off using lens cleaning tissue, which leaves a film sufficiently thin to be assumed to be parallel to the surface of the glass. A thin film of the CPN mixture was coated on top of the petroleum jelly coated surface using the blade film applicator. The coated glass disc was then placed in a polytetrafluoroethylene mould with coated side facing up and subsequently the mould was filled with a 5:1 ratio of PDMS:catalyst mixture. The mould was placed in an oven at 100 ℃ for 35 mins. During curing, the presence of petroleum jelly prevents bonding of the CPN film to glass and bonds only with PDMS-catalyst mixture forming a PDMS-backed source. After allowing the mould to return to laboratory temperature, the contents of the mould come free. The embedded glass discs and the PDMS-backed sources were removed using a scalpel and cut to approximate lateral dimensions of 20 × 30 mm. The combined thickness of the CPN film and the PDMS-backing was around 2–3 mm. Four glass-backed and four PDMS-backed sources were fabricated. The PDMS-backed source fabrication process is shown in Figure 5-1 in which glass discs of 25 mm diameter were used.

5.2.1 Thickness Estimate of Polymer-backed Sources

The thickness of the CPN film on glass-backed sources can be obtained by calculating the difference in thickness of the uncoated glass slide and the CPN coated glass slide (see Sec. 3.2.1). However, such an approach is not possible with PDMS-backed sources because of the fabrication process described above. Therefore, the thickness of the cured CPN film on PDMS backing was derived

indirectly. The wavelength-dependent optical absorbance, $A_o(\lambda)$, of the glass-backed and PDMS-backed sources was measured using a spectrophotometer from 400-900 nm (Lambda 800, Perkin Elmer, Waltham, MA, USA). The optical absorbances of CPN sources were measured, three times each, near to the central region of the coating over an area of 5×5 mm. The optical absorption coefficient, $\mu_a(\lambda)$, of the glass-backed sources was determined using the relation: $\mu_a(\lambda) = (A_o(\lambda) \times \ln 10)/d_{th}$, where d_{th} is the measured thickness of the CPN film coated on glass slide. By knowing $\mu_a(\lambda)$ of the CPN material, the thickness of the CPN film on PDMS was estimated using the above relation. At 600 nm wavelength, the average optical absorbance and thickness of CPN sources backed on glass was 2.03 ± 0.05 and 23 ± 2.4 μm, respectively, which results in μ_a of 203 ± 23 mm^{-1}. Using this average value of μ_a, which is expected to be the same for both glass and PDMS-backed sources, the thickness for each PDMS-backed source was estimated. The derived thickness of the PDMS-backed sources is shown in Table 5-1 along with measured values of optical absorbance of glass and PDMS-backed sources and the measured thickness of glass-backed sources.

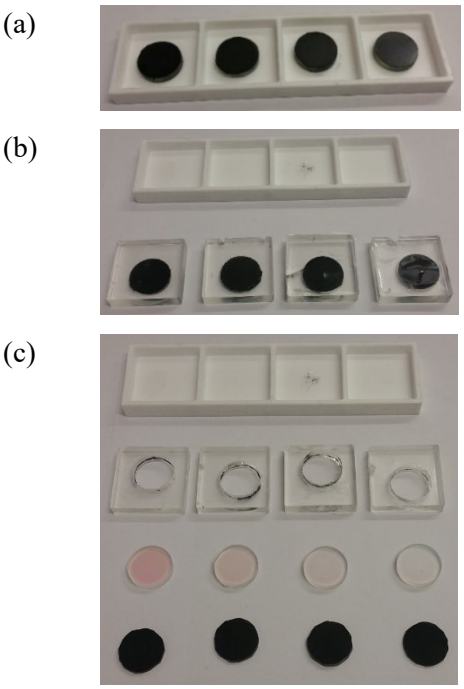

Figure 5-1: **a** 25 mm diameter optical-flat glass discs coated with PDMS-based CPN mixture with 2.5 wt. % MWCNT, which were previously coated with a thin layer of debonding agent. The CPN coated glass discs are placed in a polytetrafluoroethylene mould followed by filling the mould with 5:1 ratio of PDMS:catalyst mixture and oven cured at 100 ℃ for 35 min. **b** After allowing the mould to return to laboratory temperature, the contents come free from the mould. **c** Glass discs embedded in the cured PDMS and PDMS-backed sources were removed using a scalpel.

There is a small measurement bias in deriving the thickness of the CPN film on PDMS, firstly due to the optical loss within the clear PDMS backing and second, the refractive index of glass and PDMS are not the same. The optical absorption coefficient of PDMS at 1064 nm was measured at University College London (UCL) using a wide wavelength range dual-beam spectrophotometer (Lambda 750, Perkin Elmer, Waltham, MA, USA) for two rectangularly cast PDMS blocks of size 10 × 20 mm and of thickness 4.26 mm ± 18 µm and 7.64 mm ± 16 µm. By measuring the difference between the absorbance between PDMS blocks of different thicknesses, the effect of interfacial losses can be removed. The difference in both the optical absorbance and thickness from the two PDMS blocks were used to calculate the optical absorption coefficient, which was found to be 11 m^{-1} at 1064 nm. For a 2.5 mm thick PDMS backing this works out to be a 3% loss in intensity. The second bias arises from the difference in refractive index of glass and PDMS which are 1.47 and 1.4 [72], respectively at 1064 nm, a 5% difference. However, the relative difference in the optical intensity reflection of glass and PDMS interfaced to air which is the case during spectrophotometer measurements is only 0.8%. Therefore, these two factors affect the estimated CPN film thickness on PDMS. But these biases are small and hence no correction was applied to the estimated thicknesses of CPN film on PDMS backing. Two glass-backed sources of thicknesses 24 and 25 µm and two PDMS-backed sources of thickness 27 µm were tested on the experimental setup.

Table 5-1: Optical absorbance and thicknesses of CPN films coated on glass and PDMS backings. Parenthetical entries represent one standard deviation in the measured and derived values.

Optical absorbance, A_o (λ = 600 nm)		CPN film thickness, d_{th} [µm]	
Glass-backed	PDMS-backed	Glass-backed	PDMS-backed
2.04 (0.02)	2.36 (0.02)	24 (1.3)	27 (3.1)
2.07 (0.03)	2.55 (0.04)	25 (3.2)	29 (3.4)
1.95 (0.02)	2.43 (0.13)	20 (2.3)	27 (3.5)
2.03 (0.01)	1.23 (0.04)	23 (1.6)	14 (1.7)

5.2.2 Thickness Measurement of a Polymer-backed Source

In order to validate the method used to estimate the thickness of the PDMS-backed sources described in Sec. 5.2.1, an optical imaging technique was used. Measurements on a 14 µm thick PDMS-backed source (see Table 5-1) were performed by the Materials Testing group of NPL. Three sections of the source material were cut with a scalpel blade at the mid region, which were approximately 4 mm wide and 12 mm long (see Figure 5-2). Imaging surfaces were prepared using a ultramicrotome (Leica EM

UC7, Milton Keynes, U.K.), fitted with a temperature controlled cryochamber (Leica EM FC7, Milton Keynes, U.K.) cooled using liquid nitrogen to −140 ℃. A DiATOME diamond cryo knife with a 35° knife angle was used to cut the cooled and hardened samples. The automated cutting process was monitored by a microscope lens focussed on the cutting face. A layer removal of 2 µm thickness was used to flatten the surface, until complete sample surface cuts were observed. This thickness was then reduced to 1 µm for several cuts and finally 200 nm for several more cuts to ensure a flat even surface. The drive speed of the sample over the blade was 1 $\mathrm{mm\,s^{-1}}$. Less than 0.5 mm of the material was removed from each cut face. The maximum sample area available for cutting was 4 × 4 mm. Samples were then removed from the holder and allowed to return to room temperature prior to imaging.

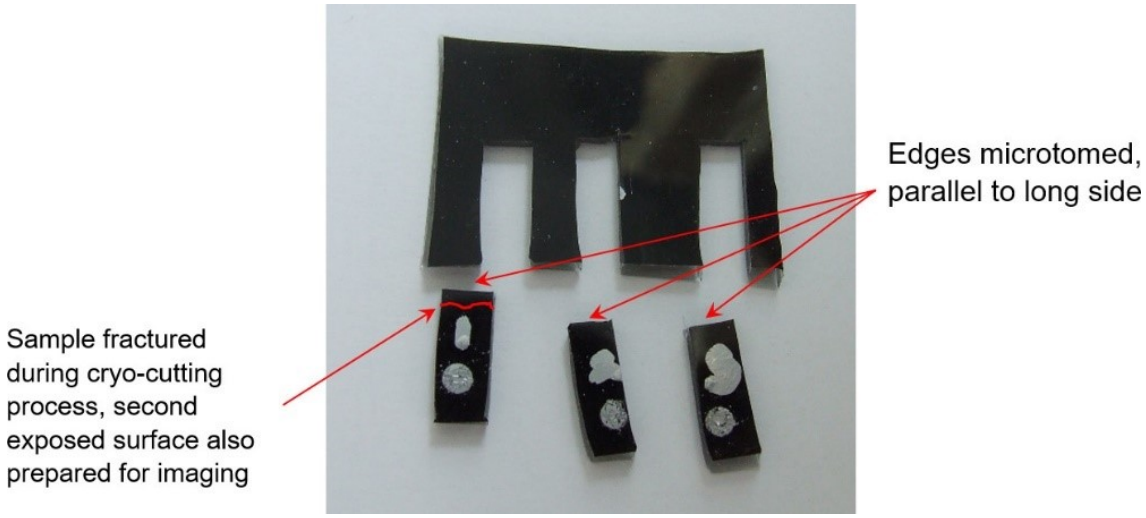

Figure 5-2: PDMS-backed source with 2.5 wt. % MWCNT. Three sections of the source material were cut as shown in the image for edgewise optical imaging of the CPN layer thickness on PDMS-backing. The surface of the cut samples are sequentially numbered as 1, 2, and 3.

Edgewise optical images of the CPN layer thickness were captured using a 3D microscope (Alicona InfiniteFocus, Graz, Austria) at 20× magnification using a combination of full ring light and coaxial lighting to illuminate the surface, filtered with a polariser. This proved the most effective way to optimise contrast between the optically absorbing CPN layer and the transparent PDMS backing without emphasising any residual surface texture after cutting (some cutting related striations can be seen on the surface in Figure 5-3). Difficulties with clamping the soft surfaces perfectly flat and perpendicular to the imaging axis limited the resultant image quality. Images were captured at 440.2 nm per pixel resolution. Edgewise optical images taken from the three samples are shown in Figure 5-3.

The thickness of the CPN layer in each sample was found by analysing the optical images. The number of pixels in the CPN layer along each pixel column of the image were separately counted using a thresholding technique using MATLAB. The pixel resolution was used to convert the pixel count to thickness, which when averaged for each sample image was found to be 12.2, 15.7 and 15.1 μm. The average CPN layer thickness from the samples was 14.4 ± 1.9 μm. This value is only 3% higher compared to 14 ± 1.7 μm obtained from the optical absorbance method.

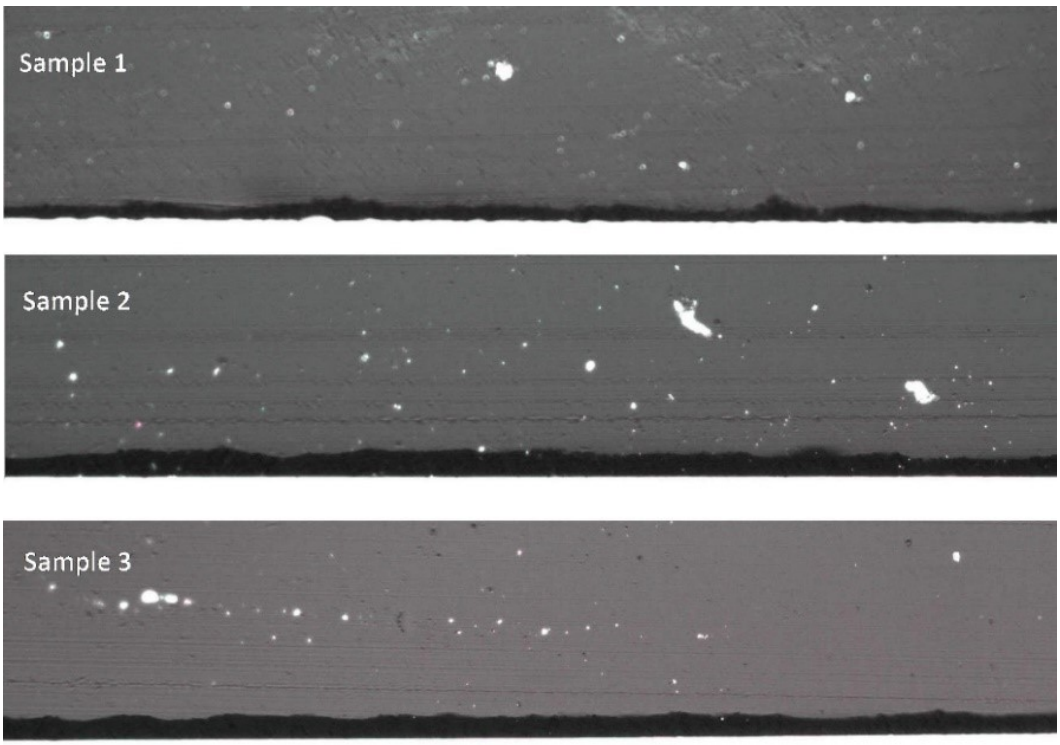

Figure 5-3: Edge wise optical image of the three samples of which only a corner region of the image is shown. The size of the image is 200 × 700 μm. The thickness of the CPN layer in each sample was found by analysing the images as described in the text.

5.3 Test of CPN Sources using Two Lasers

The experimental setup used to test the glass-backed and PDMS-backed sources was similar to the setup described in Sec. 3.3.1 except with two minor changes. An additional fibre-coupled laser was purchased with a pulse duration of 2.6 ns operating at 1064 nm. The laser (M-NANO, Montfort Laser GmbH, Götzis, Austria) is a diode pumped Q-switched Nd:YAG laser coupled with a fibre-bundle (CeramOptec GmbH, Bonn, Germany) of 5 mm aperture size. This laser was specifically commissioned for use with the final LGUS source, which is discussed in detail in Chapter 6. The UT1602 hydrophone used to measure the LGUS response from CPN sources in Chapter 3 became

unstable and its magnitude sensitivity dropped by more than 60%. The low sensitivity response of the UT1602 hydrophone deemed it unusable and therefore a different hydrophone was employed for the subsequent experiments. The hydrophone was a 0.4 mm diameter Precision Acoustics UT1604 type membrane hydrophone. The sensitivity response of the 0.4 mm diameter hydrophone was similarly extrapolated from 60–110 MHz as described in Sec. 3.3.3.

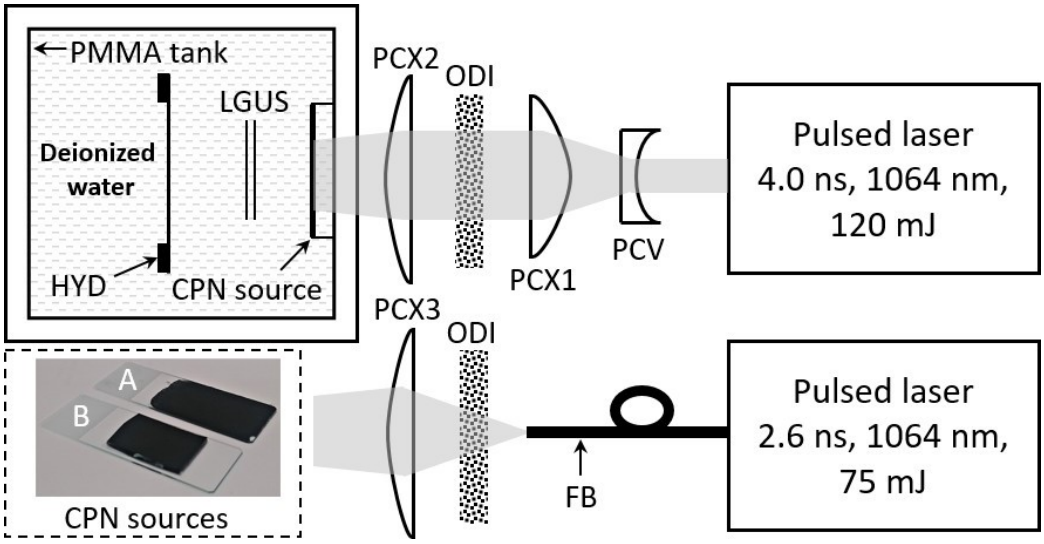

Figure 5-4: Top view of the test setup. Plano-concave lens (PCV); plano-convex lens (PCX1, PCX2 and PCX3); optical diffuser (ODI); fibre-bundle (FB); carbon-polymer nanocomposite (CPN); hydrophone (HYD); laser generated ultrasound (LGUS); Polymethyl methacrylate (PMMA); glass-backed source **A**; PDMS-backed source laid on glass slide **B**.

The top-view of the experimental test setup is shown in Figure 5-4. The output beams from both lasers were homogenized using a 1500 grit ground glass optical diffuser (ODI). The homogenized beam was weakly focused using a plano-convex (PCX) lens to reduce the losses due to scatter caused by the ODI. The focal lengths of PCX lens were 200 mm for Litron and 150 mm for Montfort lasers, which resulted in a −20 dB acoustic beam-area of 1.23 and 1.36 cm^2, respectively measured via a hydrophone raster scan at 3.7 mm from the source (see Figure 5-5). The measured acoustic beam-area was assumed to be the beam-area of the laser on the CPN source. The beam-area of the Litron laser in Chapter 3 was 0.8 cm^2, whereas here the optical beam was expanded to match closely the beam-area of the Montfort laser to allow measurements under nearly identical conditions.

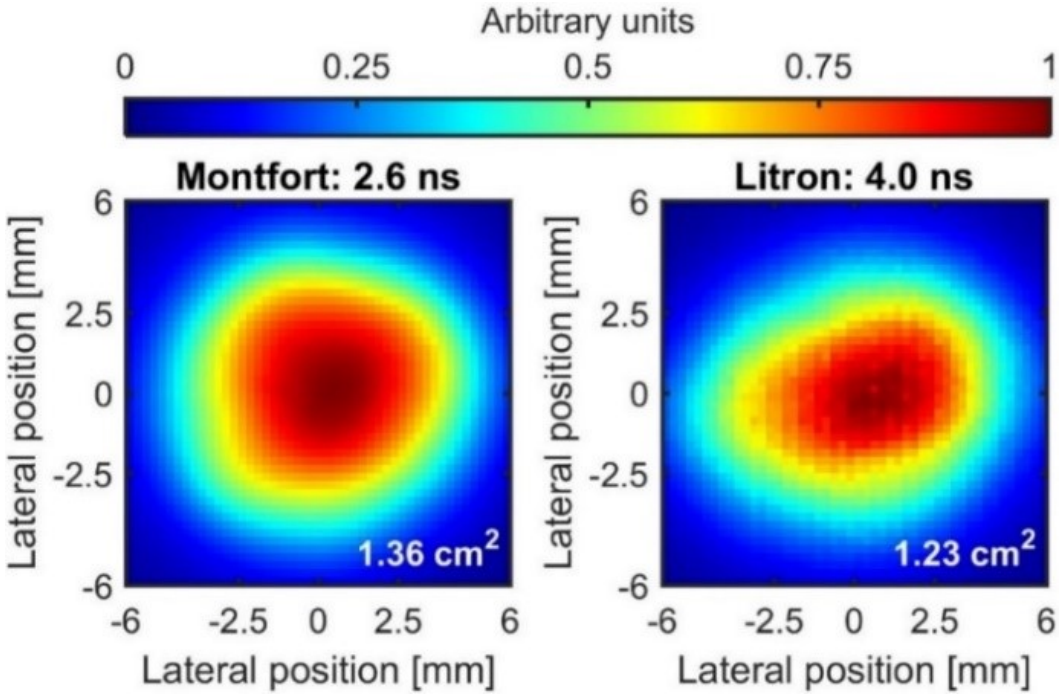

Figure 5-5: Raster scans of the LGUS field generated from a glass-backed CPN source measured using a 0.2 mm diameter membrane hydrophone (UT1602, Precision Acoustics Ltd, Dorchester, U.K). The peak positive hydrophone voltages recorded from the raster scans were rescaled between (0, 1). The areas denoted within each raster scan were estimated at the −20 dB of peak value in the image.

5.3.1 The Test Protocol

The beam-area of the Litron (4 ns) laser is 11% smaller compared to Montfort (2.6 ns) laser and, therefore, the laser energy was varied so that the laser fluence was kept the same for both lasers to allow a comparison of the effect of laser pulse duration on the CPN sources. Identical laser energies on each CPN surface was ensured as follows. A set of measurements were undertaken using the 2.6 ns laser on glass and PDMS-backed sources at 6, 9 and 11 mJ cm^{-2}. Next, measurements were repeated using the 4 ns laser by adjusting the fluence levels such that the hydrophone voltage matched with those of 2.6 ns laser for the case of glass-backed CPN source. The energy settings of the 4 ns laser were noted and used to measure the response of PDMS-backed sources.

5.3.2 Results of Two Laser Tests

The LGUS pressure time-series and their spectra from glass and PDMS-backed sources are shown in Figure 5-6 for both lasers at an applied fluence of 11 $\mathrm{mJ\,cm^{-2}}$. The average p_+ pressure measured over four independent repeat measurements from a glass-backed source using the two lasers and its standard deviation was 4.9 ± 0.01 MPa. However, for the PDMS-backed source the pressures were 3.0 ± 0.1 MPa and 2.9 ± 0.1 MPa for 2.6 and 4 ns lasers, respectively. There are two things to note. First, the maximum pressures for the glass and PDMS-backed sources are not the same, and second, there is a small decrease in pressure with increased laser pulse duration for the PDMS-backed source. These two effects were also observed at two other fluences of 6 and 9 $\mathrm{mJ\,cm^{-2}}$. The results are summarised in Table 5-2.

The *BW6* calculated from the amplitude spectra of glass and PDMS-backed sources are tabulated in Table 5-3. The *BW6* from PDMS-backed sources are nearly 35% larger compared to glass-backed sources. The duration of the pressure-pulses from PDMS-backed sources are shorter compared to glass-backed sources, which is expected due to the effect of acoustically matched backing as explained in the beginning of this chapter. But the difference is not big i.e., the pulse duration (calculated at 10% threshold of the respective time-series amplitudes) of PDMS-backed source is only 10 ns shorter compared to glass-backed source. Since the pulses are all nonlinear it appears that the effect of wave broadening due to cumulative acoustic nonlinearity, which is dependent on pressure amplitude and propagation distance (see Sec. 4.3.2) is more dominant in determining the duration of the pressure-pulse at the measured location compared to the effect of backing material. Another observation is that though the *BW6* metric suggests that there is an improvement in bandwidth from PDMS-backed sources compared to glass-backed sources, the pressure amplitudes of glass-backed sources at all frequencies are higher than PDMS-backed sources (see Figure 5-6). This is because the pressure amplitude of the LGUS pressure-pulse from glass-backed source is higher compared to the PDMS-backed sources.

The differences in the acoustic pressures between glass-backed and PDMS-backed sources, which is unexpected needs further investigation. In the first instance, this may be explained with the following argument. For efficient laser generation of ultrasound, the laser pulse duration should be short compared to the stress confinement time. Failing to meet this criterion means that the pressure wave will start to leave the optical absorption region while pressure is still being added by the laser pulse. The pressure spreads out rather than builds up, and therefore the maximum amplitude decreases as the laser pulse duration increases. This effect is seen in the case of PDMS-backed source where the measured pressures were 3.0 and 2.9 MPa for 2.6 and 4.0 ns lasers, respectively.

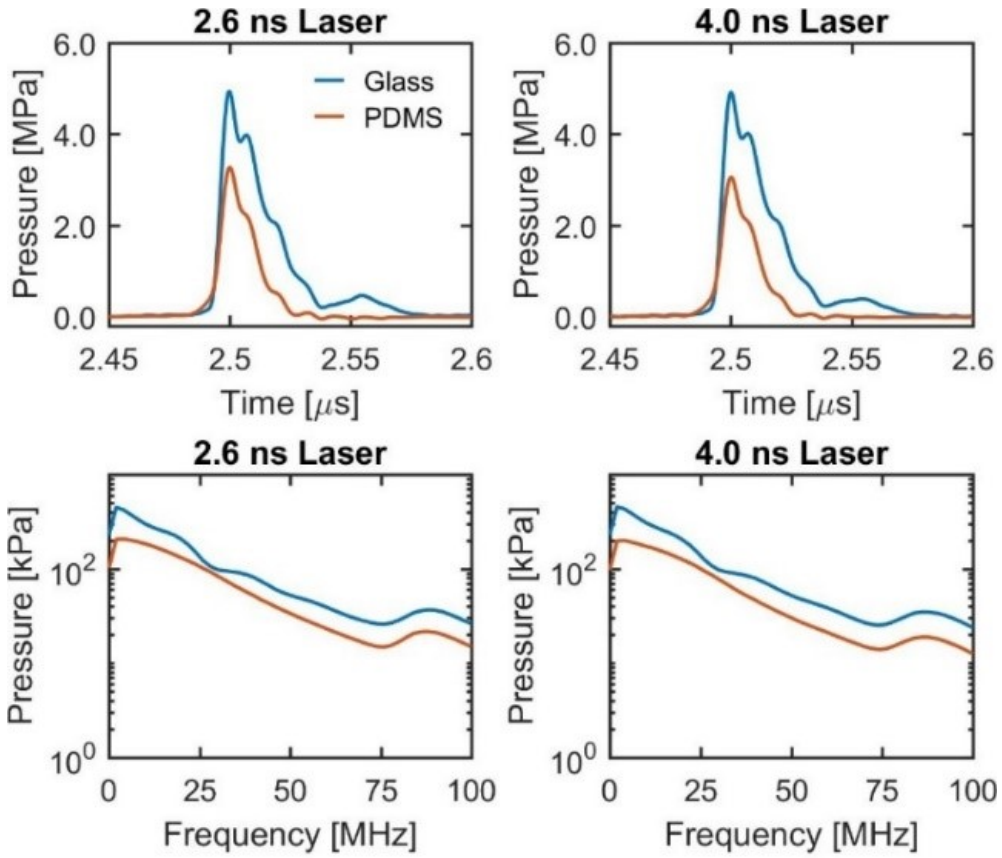

Figure 5-6: The pressure time-series (top row) and the corresponding spectra (bottom row) for a glass and PDMS-backed source for an applied laser energy of 11 mJ cm^{-2} for the two lasers. The thicknesses of the glass and PDMS-backed sources were 24 and 27 µm, respectively.

Table 5-2: Peak-positive pressures from glass and PDMS-backed sources. Glass-backed values represent an average of the measurement data from 2.6 and 4 ns lasers.

Applied laser fluence	Glass-backed	PDMS-backed	
		2.6 ns laser	4 ns laser
[mJ cm^{-2}]	[Peak positive pressure, MPa]		
6	2.9 (0.1)	1.8 (0.1)	1.7 (0.1)
9	3.7 (0.1)	2.3 (0.1)	2.2 (0.1)
11	4.9 (0.0)	3.0 (0.1)	2.9 (0.1)

Table 5-3: The −6 dB bandwidths calculated from the amplitude spectra of glass and PDMS-backed sources. Glass-backed values represent an average of the measurement data from 2.6 and 4 ns lasers.

Applied laser fluence	Glass-backed	PDMS-backed	
		2.6 ns laser	4 ns laser
[mJ cm^{-2}]	[−6 dB Bandwidth, MHz]		
6	23 (0.1)	29 (0.5)	29 (0.4)
9	21 (0.1)	29 (0.5)	29 (0.3)
11	20 (0.1)	28 (0.4)	28 (0.4)

The significant difference in amplitude of 61% and 59% in the case of the PDMS-backed source relative to the glass-backed source for 2.6 and 4 ns lasers, respectively, is caused by the presence of the acoustically strong reflective backing provided by the glass medium. The effect of glass and polymer backing on the LGUS pulse from a CPN source was previously described in the beginning of this chapter using a 1D example. For a glass-backed CPN source, and when stress confinement is satisfied, the half of the deposited pressure pulse propagating towards the glass backing is reflected and immediately follows the other half propagating towards the water. In the absence of stress confinement, the wave reflected by the glass back into the CPN during the continued optical deposition of heat causes additional pressure to build-up. The total acoustic pressure reached is therefore higher than in the absence of the reflection. In the case of PDMS-backed sources, the pressure amplitude is lower since no backing reflections are present.

5.4 Tests Using a Tuneable Duration Fibre-Laser

A second experiment was setup to further test the effect of the source backing when using a variable laser pulse duration. A variable pulse duration experimental fibre-laser was available at Photoacoustic Imaging Group of UCL whose FWHM could be varied from 10–500 ns. This laser was developed in collaboration with the Optoelectronics Research Centre of University of Southampton. A paper describing the operation of the fibre-laser is yet to be published and therefore, only a brief description is provided here. The fibre laser is based on a master oscillator power amplifier configuration, which consists in the output of a seed laser being amplified by a chain of ytterbium-doped fibre amplifiers. Such a configuration provides the ability to easily scale the output power of the laser by adding more amplifiers, but also provides the capability of shaping the excitation pulses, as the output of the fibre laser follows the shape provided by the seed laser. The custom designed fibre laser system was comprised of a superluminescent diode as a seed source and a cascade of 4 ytterbium-doped fibre amplifier stages. The final amplification stage used a custom-drawn large core diameter (200 μm) fibre to obtain pulse energies of up to 10 mJ. The system provided variable pulse durations (10–

500 ns) and pulse repetition frequencies (100 Hz to 1 kHz), and the emission wavelength was 1064 nm.

A new set of glass-backed and PDMS-backed CPN sources were fabricated such that the stress confinement duration was within the range of 10–200 ns. For this, a 1.25 wt. % MWCNT was used in PDMS, which gave a stress relaxation time of 15 ns (see Table 3-5). Four glass-backed and four PDMS-backed sources were fabricated using the method described in Sec. 5.2, from which two each with thicknesses of 24 µm and 20 µm were selected for the measurements. A sample glass-backed and PDMS-backed source of 20 µm thickness source is shown in Figure 5-7.

The experiment was conducted at UCL with Thomas Allen, as he has expertise in controlling the experimental fibre laser. The setup consisted of a variable pulse duration fibre-laser and a Fabry–Pérot Interferometric (FPI) ultrasound sensor as shown in Figure 5-8. The beam diameter on the CPN sources was around 2 cm, the pulse energy at the output of the fibre was 8 mJ for all pulse durations and the pulse repetition frequency was 100 Hz. After transmission through the 50% neutral density filter, the laser fluence at the source location was less than 1.5 mJ cm^{-2}. The neutral density filter was used to limit the number of unabsorbed photons in the CPN source reaching the FPI, which otherwise caused the FPI signal to fluctuate due to interaction of the excitation laser and the interrogating laser. Measurements were taken at five pulse durations of 10, 20, 50, 100 and 200 ns. Also, a measurement was made on the experimental setup shown in Figure 5-4 using the 4 ns duration laser at 2 mJ cm^{-2}. The p_+ pressures of the LGUS pulses from glass-backed and PDSM-backed sources using the 4 ns laser measured at a source-sensor separation of 5.2 mm was 123 kPa and 90 kPa, respectively. These pressures are nearly a factor of 20–30 lower compared to the measurements in Sec. 5.3.2. Since the laser fluence used was small i.e., less than 2 mJ cm^{-2} for experiments conducted at both UCL and NPL, no wave steepening was observed in the measurements suggesting that the any effects of nonlinear propagation was negligible.

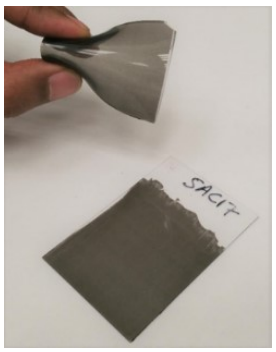

Figure 5-7: PDMS-based PDMS-backed (top) and glass-backed (bottom) CPN sources with 1.25 wt. % CNT. The PDMS-backed source is bent to show that it is not rigid as compared to glass. The thickness of the CPN film on glass and PDMS backings was 20 µm and their stress confinement duration was 15 ns.

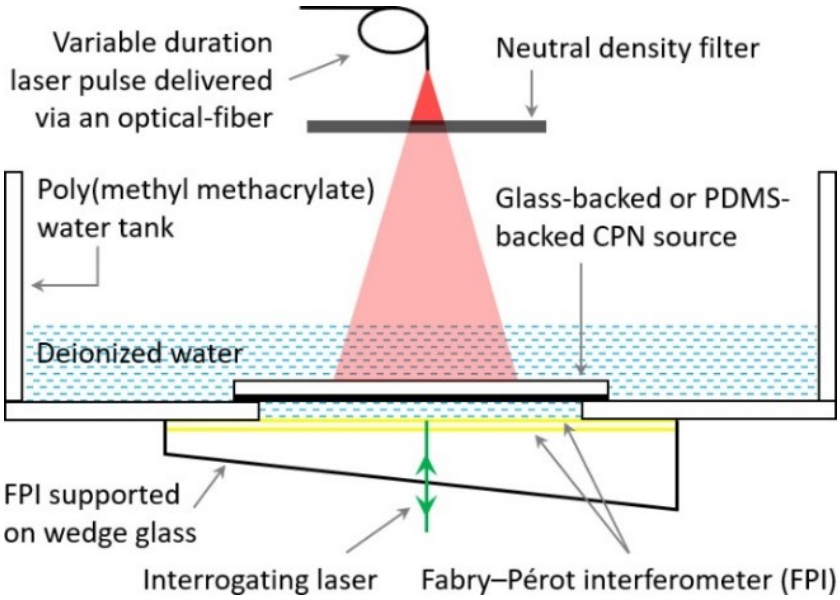

Figure 5-8: Measurement set-up used to test the effect of source backing material on LGUS from glass-backed and PDMS-backed CPN sources. A variable duration fibre laser was used to generate laser pulses of FWHM duration from 10–200 ns. A Fabry–Pérot Interferometer (FPI) was used to record the LGUS pulses.

The FPI sensor voltage waveforms acquired from the glass-backed and PDMS-backed CPN sources are shown in Figure 5-9. The sampling frequency of the digitizer attached to the FPI sensor instrumentation was 200 MHz. The acquired signal consisted of 1600 samples, which corresponds to an acquisition duration of 8 μs. The waveforms shown in Figure 5-9 are time-gated for display purposes to isolate the interfacial reflections discussed in Sec. 3.4.1. The full waveforms were multiplied with a Kaiser window function (alpha = 9) to dampen the end points to zero before calculating the Fourier spectra, which are shown in Figure 5-10.

The ratios calculated using the peak-positive voltages of the glass-backed over PDMS-backed sources and are shown in Figure 5-11. The ratio calculated from the 4 ns measurements is also included in the same figure. As described earlier, when stress confinement is not met, the LGUS spreads out and consequently the pressure amplitude decreases with laser pulse duration. This effect is clearly seen for both types of CPN sources in Figure 5-9. The ratios at 4 ns and 10 ns in Figure 5-11 are nearly identical, which suggests that there is stress confinement at these pulse durations, and as the pulse duration increases, the pressure amplitude of the glass-backed source increases relative to the PDMS-backed source. However, when there is a stress confinement, the ratio of glass-backed over PDMS-backed pressure amplitudes would be expected to be ‘1’, at least at a first glance as the theory outlined above, but this is not the case here. This may be because there is more high-frequency content in the PDMS-backed case compared to glass-backed case (see Figure 5-10). The preferential

loss of high frequencies both in CPN and water causes the overall amplitude to decrease, the effect of which should increase with propagation distance in water.

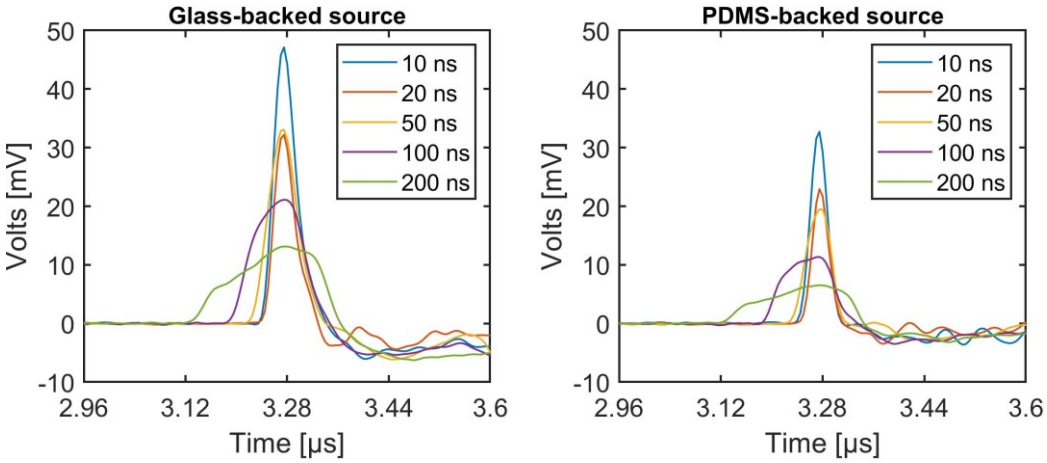

Figure 5-9: Fabry–Pérot interferometer sensor waveforms acquired from glass-backed and PDMS-backed CPN sources using the experimental arrangement shown in Figure 5-8. The waveforms are time-gated for display purposes to isolate the interfacial reflections discussed in Sec. 3.4.1. The thickness of the CPN film on the backings was around 24 μm.

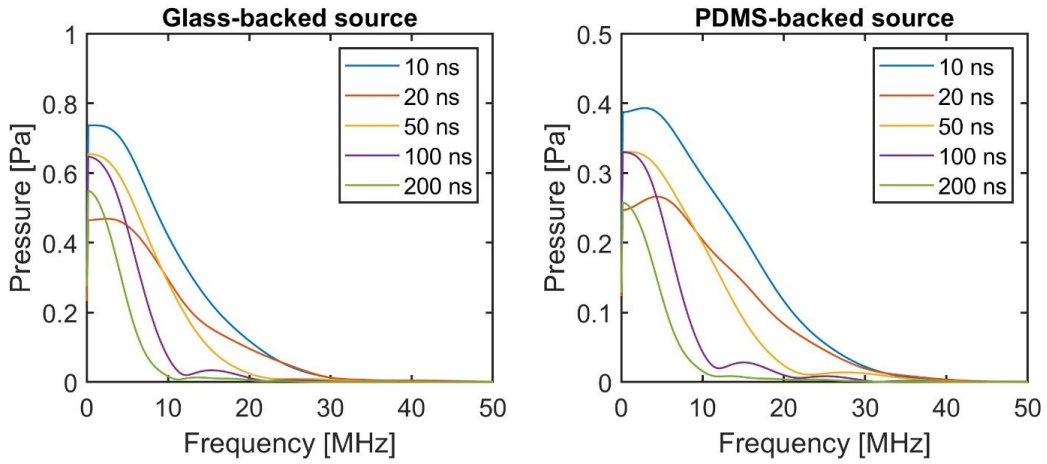

Figure 5-10: Magnitude spectra of the Fabry–Pérot interferometer sensor (full) waveforms which were multiplied with a Kaiser window function (alpha = 9) to dampen the end points to zero before calculating the Fourier spectra.

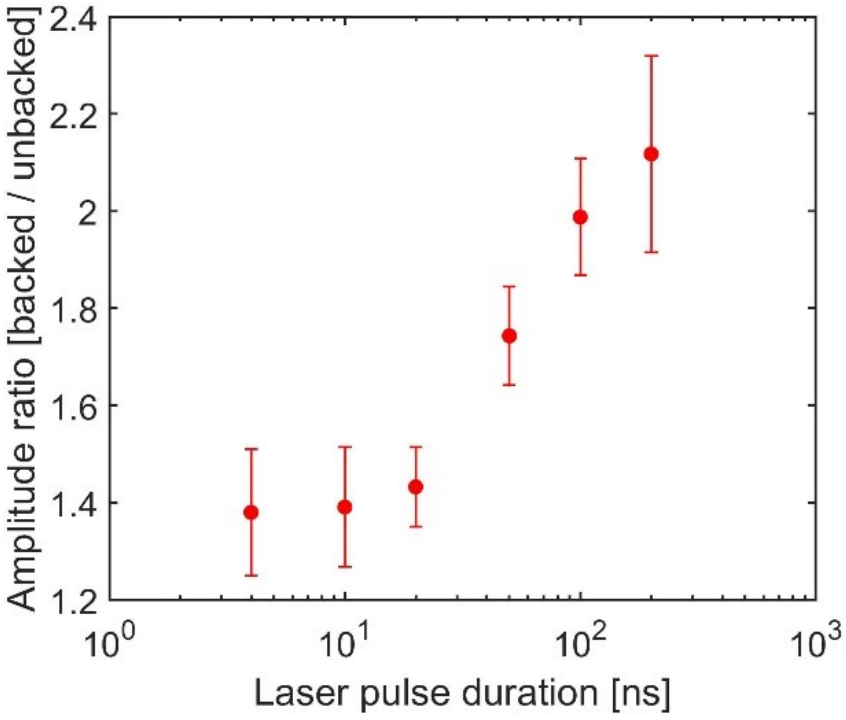

Figure 5-11: Ratios of FPI sensor peak-positive voltages from glass-backed and PDMS-backed CPN sources. The error corresponds to one standard deviation in the ratios computed using two sets of glass-backed and PDMS-backed waveforms. The ratio at 4 ns was from the experimental setup at NPL and the ratios from 10–200 ns were from that of UCL.

The *BW6* calculated from the amplitude spectra of glass-backed and PDMS-backed sources shown in Figure 5-10 and are tabulated in Table 5-4 and their ratios are shown in Figure 5-12. The stress confinement time of the glass-backed and PDMS-backed sources, which consists of 1.25 wt. % MWCNT in PDMS is approximately 15 ns (see Table 3-5). When the laser pulse durations are less than the stress confinement time (15 ns), then the gain in *BW6* from PDMS-based source is significant compared to glass-backed source. As the laser pulse durations increase, the relative difference in the pulse duration of LGUS pressure-pulses from both glass-backed and PDMS-backed sources become smaller and consequently their *BW6* are nearly identical. However, since the amplitude of LGUS pressure-pulses in the glass-backed case are always higher than the PDMS-backed case, the spectral pressure amplitudes are also higher in the glass-backed case (see Figure 5-10).

The effect of the backing on the LGUS amplitude is investigated theoretically in Sec. 5.5, including the effects of absorption and nonlinear propagation.

Table 5-4: The −6 dB bandwidths calculated from the amplitude spectra of glass and PDMS-backed waveforms shown in Figure 5-10.

Laser pulse duration	Glass-backed	PDMS-backed
[ns]	[−6 dB Bandwidth, MHz]	
10	11.2	16.1
20	12.3	17.5
50	9.5	11.9
100	6.6	6.9
200	4.9	5.2

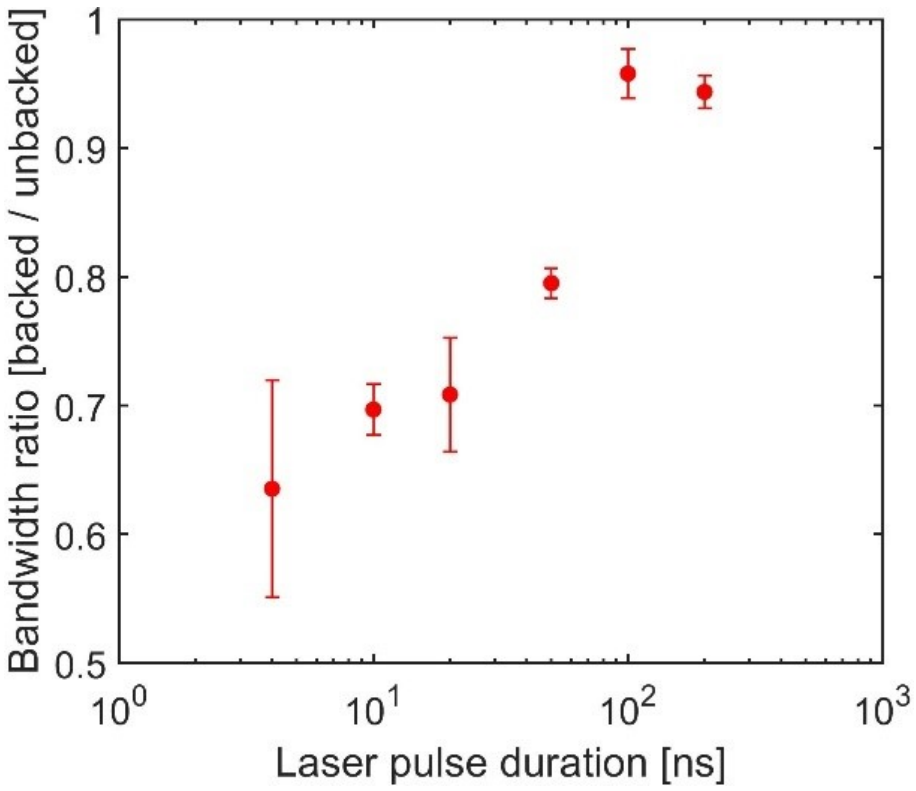

Figure 5-12: Ratios of −6 dB bandwidths calculated from the amplitude spectra of glass-backed and PDMS-backed CPN sources shown in Figure 5-10. The error corresponds to one standard deviation in the ratios computed using two sets of glass-backed and PDMS-backed waveforms. The ratio at 4 ns was from the experimental setup at NPL and the ratios from 10–200 ns were from that of UCL.

5.5 Effect of Backing Material: Analytical Model

In this section, analytical models are developed to obtain an intuitive understanding of how an acoustically-hard backing (like glass) contributes to an increased pressure amplitude compared to an acoustically-matched backing (like PDMS) when stress confinement is not satisfied. Firstly, a two-layer model, i.e., backing-absorber half spaces is developed, from which a more realistic model consisting of three layers is developed, i.e., backing-absorber-water. The results of the model were compared with k-Wave simulations to demonstrate that it is a suitable model for modelling these effects, and as well as more complicated cases including absorption, nonlinearity, and potentially multiple layers. Only linear propagation was possible in the analytical model but in all the previous experiments the LGUS pressure-pulses were nonlinear. Therefore, it is necessary to incorporate nonlinearity in general, which can be accomplished with k-Wave as shown in Chapter 4.

5.5.1 Two-layer Analytical Model

Consider two half spaces with different sound-speeds and acoustic impedances, c_0, c, z_0 and z, respectively. The interface between the two media is normal to the *x*-axis. A planar laser pulse of duration τ travels through the first media in the positive *x*-direction, which is optically non-absorbing. The second medium, medium 2, is only optically absorbing to a depth d. For mathematical convenience it is assumed that the optical energy is absorbed uniformly within the thickness d of the second medium (see Figure 5-13). (This will be approximately true when d is much less than the optical penetration depth.) The absorbed optical energy generates an acoustic wave which then propagates in both the positive and negative *x*-directions. The schematic of the two-layer model is shown in Figure 5-13.

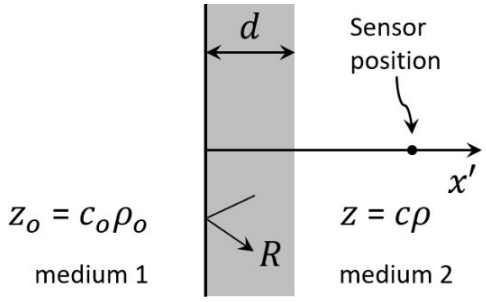

Figure 5-13: Schematic of the analytical model in which an optical absorber with uniform optical absorption in medium 2 is backed against medium 1. Medium 1 is optically non-absorbing and medium 2 in only optically absorbing for a depth d. The sound-speeds and acoustic impedances of the two mediums are, c_0, c, z_0 and z, respectively. R is the pressure reflection coefficient for the wave in medium 2 looking in to medium 1. A sensor is positioned in medium 2 outside the optical absorber.

It is assumed that the laser pulse is a rectangular pulse of energy E, irrespective of its duration, so the power in the pulse is E/τ and its pulse shape, $f(t)$, normalised to give an integral of one, is

$$f(t) = \begin{cases} 1/\tau, & -\tau/2 < t < \tau/2, \\ 0, & \text{otherwise.} \end{cases} \tag{5.1}$$

The 1D wave equation for LGUS sources which describe the waves propagating linearly in medium 2 is:

$$\frac{1}{c^2}\frac{\partial^2 p}{\partial t^2} - \frac{\partial^2 p}{\partial x^2} = \frac{₹}{c^2}\frac{\partial \mathcal{H}}{\partial t}(x,t), \tag{5.2}$$

where, $\mathcal{H}(x,t)$ is the absorbed optical power density and ₹ is the unitless photoacoustic conversion efficiency. When the photoacoustic source is not moving then the optical power density can be separated as $\mathcal{H} = H(x)f(t)$, where H and f have dimensions of J m^{-3} and s^{-1}, respectively. The absorbed optical power density for the case considered here is defined as follows:

$$H(x) = \begin{cases} E/d, & 0 < x < d, \\ RE/d, & -d < x < 0 \\ 0, & \text{otherwise,} \end{cases} \tag{5.3}$$

where, R is the acoustic pressure reflection coefficient seen by the wave from medium 2 into medium 1.

$$R = \frac{z_0 - z}{z_0 + z}. \tag{5.4}$$

Note that H here is not just the absorbed energy distribution (which is the part of H between $0 < x < d$) but also uses the idea of an image source to model the effect of the boundary (making H non-zero between $-d < x < 0$).

The 1D Green's function solution to Eq. (5.2) can be written as

$$p(x,t) = \frac{₹}{c^2}\int_0^{t^+}\int_{-\infty}^{\infty} G(x-x',t-t')\frac{\partial \mathcal{H}}{\partial t}(x',t')dx'dt', \tag{5.5}$$

where the Green's function is given by

$$G(x-x',t-t') = \frac{c}{2}U\left(t - t' - \frac{|x-x'|}{c}\right), \tag{5.6}$$

where U is the unit step function.

Since, from Eq. (5.1), $\partial f/\partial t = \big(\delta(t+\tau/2) - \delta(t-\tau/2)\big)/\tau$, where δ is the Dirac delta function, Eq. (5.5) can be written

$$p(x,t) = \frac{₹}{c^2}\int_0^{t^+}\int_{-\infty}^{\infty} G(x-x',t-t')H(x')\frac{\partial f}{\partial t'}(t')dx'dt' \tag{5.7}$$

$$p(x,t) = \frac{₹}{\tau c^2}\int_0^{t^+}\int_{-\infty}^{\infty} G(x-x',t-t')H(x')\big(\delta(t'+\tau/2) - \delta(t'-\tau/2)\big)dx'dt' \tag{5.8}$$

$$p(x,t) = \frac{₹}{\tau c^2}\int_{-\infty}^{\infty} H(x')\big(G(x-x',t+\tau/2) - G(x-x',t-\tau/2)\big)dx' \tag{5.9}$$

Substituting the expression for H from Eq. (5.3) into Eq. (5.9) gives

$$\begin{aligned} p(x,t) = \frac{E₹}{d\tau c^2}\Bigg\{&\int_0^d \big(G(x-x',t+\tau/2) - G(x-x',t-\tau/2)\big)dx' \\ &+ R\int_{-d}^0 \big(G(x-x',t+\tau/2) - G(x-x',t-\tau/2)\big)dx'\Bigg\}. \end{aligned} \tag{5.10}$$

Substituting Eq. (5.6) in Eq. (5.10) then gives

$$\begin{aligned} p(x,t) = \frac{E₹}{2d\tau c}\Bigg\{&\int_0^d \left(U\left(t+\frac{\tau}{2}-\frac{|x-x'|}{c}\right) - U\left(t-\frac{\tau}{2}-\frac{|x-x'|}{c}\right)\right)dx' \\ &+ R\int_{-d}^0 \left(U\left(t+\frac{\tau}{2}-\frac{|x-x'|}{c}\right) - U\left(t-\frac{\tau}{2}-\frac{|x-x'|}{c}\right)\right)dx'\Bigg\}. \end{aligned} \tag{5.11}$$

Since the sensor (or hydrophone) is positioned outside the optical absorber i.e., $x > d$ then Eq. (5.11) becomes

$$\begin{aligned} p(x,t) = \frac{E₹}{2d\tau c}\Bigg\{&\int_0^d \left(U\left(t+\frac{\tau}{2}-\frac{(x-x')}{c}\right) - U\left(t-\frac{\tau}{2}-\frac{(x-x')}{c}\right)\right)dx' \\ &+ R\int_{-d}^0 \left(U\left(t+\frac{\tau}{2}-\frac{(x-x')}{c}\right) - U\left(t-\frac{\tau}{2}-\frac{(x-x')}{c}\right)\right)dx'\Bigg\}. \end{aligned} \tag{5.12}$$

Eq. (5.12) can be compactly written as

$$p(x,t) = \frac{E₹}{2d\tau c}\left(\underbrace{\int_0^d g(x',t)\,dx'}_{I_1} + \underbrace{R\int_{-d}^0 g(x',t)\,dx'}_{I_2}\right), \tag{5.13}$$

Where

$$g(x',t) = \begin{cases} 1, & \dfrac{x-x'}{c} - \dfrac{\tau}{2} < t < \dfrac{x-x'}{c} + \dfrac{\tau}{2}. \\ 0, & \text{otherwise.} \end{cases} \tag{5.14}$$

The wave $p(x,t)$ recorded at an arbitrary distance x from the optical absorber is a continuous sum of the waves optically generated whilst the absorption region is being heated by a laser pulse. The waves propagating forward integrate to give I_1 and the waves propagating backwards or towards the interface integrate to give I_2. This is shown in Figure 5-14 and Figure 5-15, where the shaded region indicates where the integrand $g(x',t)$ equals one (zero elsewhere), for the cases $\tau < d/c$ (stress confined) and $\tau > d/c$ (not stress confined) respectively. From Figure 5-14 and Figure 5-15, it can be seen that the pulse durations of I_1 or I_2 individually are both $(\tau + d/c)$ regardless of the stress confinement condition, but they are offset, so when combined the pulse duration of $p(x,t)$ is $(\tau + 2d/c)$. Explicit analytical expressions for the time evolution of $I_1(x,t)$ and $I_2(x,t)$ can also be calculated from these figures geometrically, as they are simply the integral from $x' = 0$ to $x' = d$ for any given time. These expressions are given in Eq. (5.15) through to Eq. (5.18).

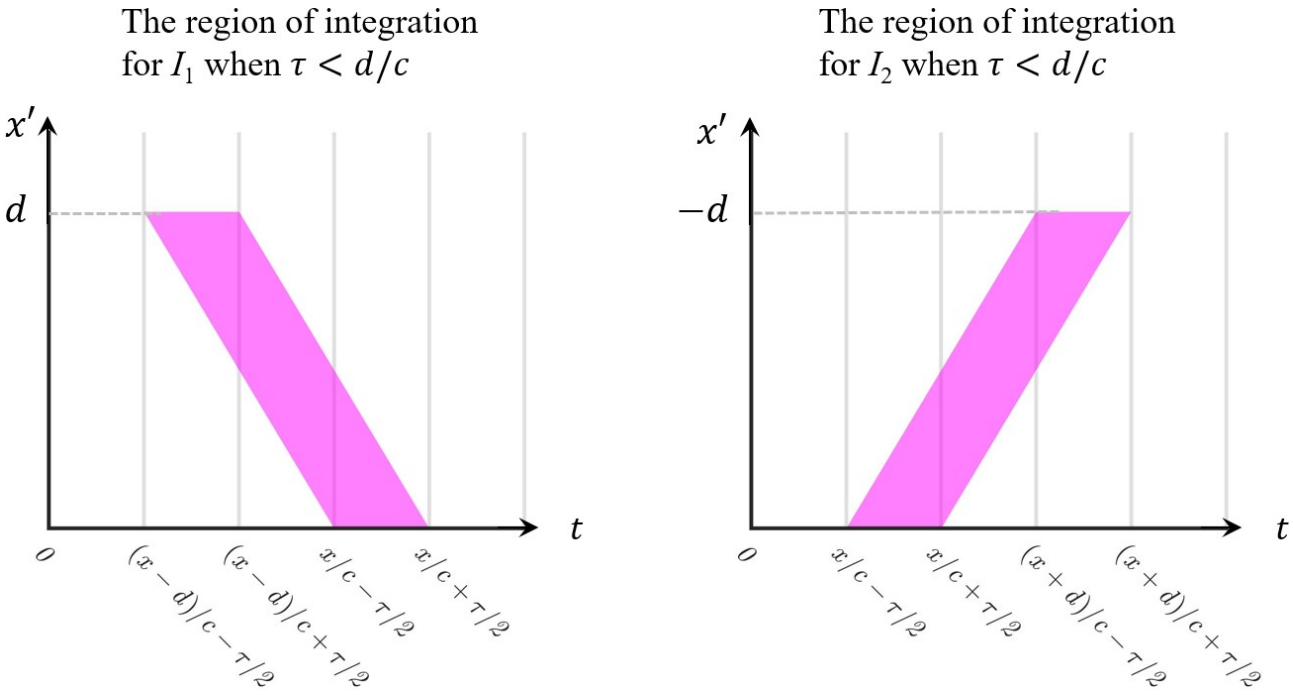

Figure 5-14: Region of integration for I_1 and I_2 when $\tau < d/c$. The shaded region shows where the integrand, $g(x',t) = 1$. It is zero elsewhere.

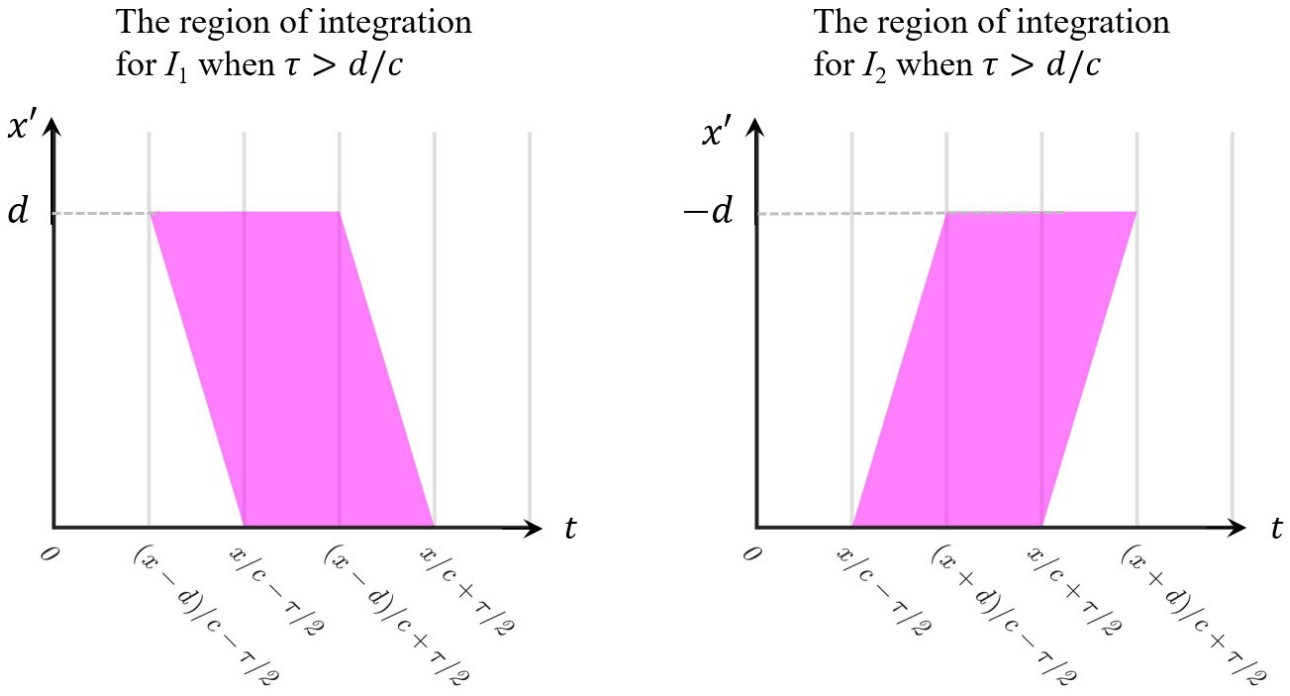

Figure 5-15: Region of integration for I_1 and I_2 when $\tau > d/c$. The shaded region shows where the integrand, $g(x', t) = 1$. It is zero elsewhere.

For $\tau < d/c$, the five parts of I_1 are

$$I_1^{\tau<d/c} = \begin{cases} 0, & t < \dfrac{x-d}{c} - \dfrac{\tau}{2}, \\ d - x + c(t+\tau/2), & \dfrac{x-d}{c} - \dfrac{\tau}{2} < t < \dfrac{x-d}{c} + \dfrac{\tau}{2}, \\ c\tau, & \dfrac{x-d}{c} + \dfrac{\tau}{2} < t < \dfrac{x}{c} - \dfrac{\tau}{2}, \\ x - c(t-\tau/2), & \dfrac{x}{c} - \dfrac{\tau}{2} < t < \dfrac{x}{c} + \dfrac{\tau}{2} \\ 0, & t > \dfrac{x}{c} + \dfrac{\tau}{2}. \end{cases} \tag{5.15}$$

For $\tau < d/c$, the five parts of I_2 are

$$I_2^{\tau<d/c} = \begin{cases} 0, & t < \dfrac{x}{c} - \dfrac{\tau}{2}, \\ c(t+\tau/2) - x, & \dfrac{x}{c} - \dfrac{\tau}{2} < t < \dfrac{x}{c} + \dfrac{\tau}{2}, \\ c\tau, & \dfrac{x}{c} + \dfrac{\tau}{2} < t < \dfrac{x+d}{c} - \dfrac{\tau}{2}, \\ d + x - c(t-\tau/2), & \dfrac{x+d}{c} - \dfrac{\tau}{2} < t < \dfrac{x+d}{c} + \dfrac{\tau}{2}, \\ 0, & t > \dfrac{x+d}{c} + \dfrac{\tau}{2}. \end{cases} \tag{5.16}$$

For $\tau > d/c$, the five parts of I_1 are

$$I_1^{\tau>d/c} = \begin{cases} 0, & t < \dfrac{x-d}{c} - \dfrac{\tau}{2}, \\ d - x + c(t+\tau/2), & \dfrac{x-d}{c} - \dfrac{\tau}{2} < t < \dfrac{x}{c} - \dfrac{\tau}{2}, \\ d, & \dfrac{x}{c} - \dfrac{\tau}{2} < t < \dfrac{x-d}{c} + \dfrac{\tau}{2}, \\ x - c(t-\tau/2), & \dfrac{x-d}{c} + \dfrac{\tau}{2} < t < \dfrac{x}{c} + \dfrac{\tau}{2}, \\ 0, & t > \dfrac{x}{c} + \dfrac{\tau}{2}. \end{cases} \tag{5.17}$$

For $\tau > d/c$, the five parts of I_2 are

$$I_2^{\tau>d/c} = \begin{cases} 0, & t < \dfrac{x}{c} - \dfrac{\tau}{2}, \\ c(t+\tau/2) - x, & \dfrac{x}{c} - \dfrac{\tau}{2} < t < \dfrac{x+d}{c} - \dfrac{\tau}{2}, \\ d, & \dfrac{x+d}{c} - \dfrac{\tau}{2} < t < \dfrac{x}{c} + \dfrac{\tau}{2}, \\ d + x - c(t-\tau/2), & \dfrac{x}{c} + \dfrac{\tau}{2} < t < \dfrac{x+d}{c} + \dfrac{\tau}{2}, \\ 0, & t > \dfrac{x+d}{c} + \dfrac{\tau}{2}. \end{cases} \tag{5.18}$$

Lastly, recall that

$$p(x,t) = \frac{E₹}{2d\tau c}(I_1 + RI_2). \tag{5.19}$$

Finally, if medium 2 is acoustically identical to medium 1 then $p(x,t) = (E₹/2d\tau c)I_1$. For $d/c < \tau < 2d/c$, the ratio, $(I_1 + RI_2)/I_1$, i.e., backed wave amplitude over unbacked wave amplitude, increases linearly with τ from 1 to $(1 + R)$. When $\tau > 2d/c$, there is at least one instance at which the amplitude of both I_1 and I_2 are going to be maximum and thus the ratio equals $(1 + R)$.

5.5.1.1 Comparison with Numerical Simulations

The analytical solutions, which comprises Eq. (5.15) and (5.16) for $\tau < d/c$ and Eq. (5.17) and (5.18) for $\tau > d/c$, were compared against linear simulations performed numerically using k-Wave. The purpose of this was to demonstrate that k-Wave is a suitable tool for modelling situations such as this, the advantage being that using k-Wave the simulations could be extended to include effects that would be difficult or tedious to include in an analytical derivation, especially including absorption and nonlinear propagation.

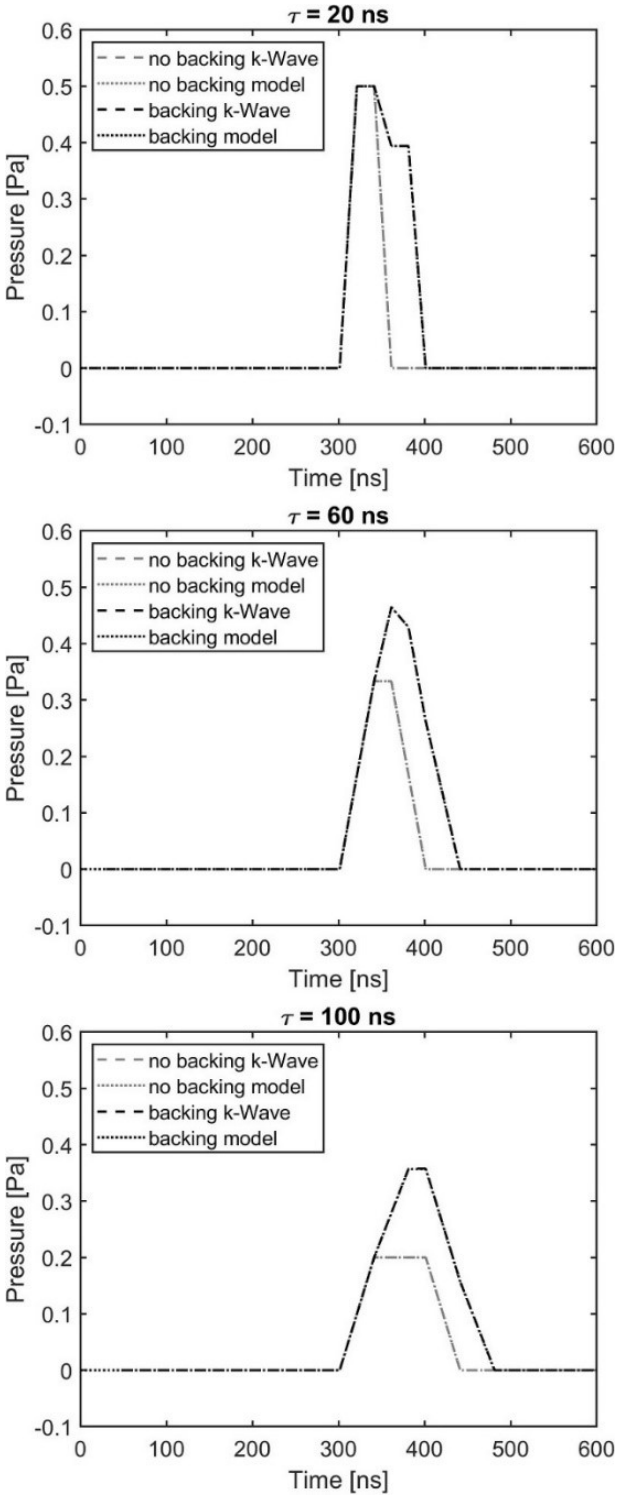

Figure 5-16: Analytical and k-Wave simulation waveforms showing the effect of acoustically reflective glass backing relative to acoustically matched water backing for laser pulse durations ranging from stress confined ($\tau < d/c$) to the unconfined ($\tau > d/c$) case. The thickness of optical absorber was 60 µm and the waveforms were computed/recorded at 128 µm from the edge of the optical absorber in water. The d/c was 40 ns.

Medium 1 was set to have the acoustic properties of glass and medium 2 was water. The thickness of the optical absorber in water was 60 µm. The optical absorption was assumed uniform across the absorbing region. The laser pulse duration τ, spanned from 20–100 ns, and its amplitude, $1/\tau$. For each pulse, two separate numerical simulations were performed to test the effect of the backing, i.e., initially medium 1 and medium 2 were both water and in the second simulation, medium 1 was glass and medium 2 was water. The optical absorber in all simulations was positioned in medium 2 (water) and backed against medium 1. The nominal sound-speeds and densities of glass and water were 5000 $\mathrm{m\,s^{-1}}$, 1500 $\mathrm{m\,s^{-1}}$, 2000 $\mathrm{kg\,m^{-3}}$ and 1000 $\mathrm{kg\,m^{-3}}$, respectively. A convergence test was run to ensure that the spatial and time steps were small enough that any purely numerical effects were negligible. The waveforms were recorded at 128 µm from the edge of the optical absorber in medium 2. Example simulation waveforms are shown in Figure 5-16 and the ratios are shown in Figure 5-17. It is clear from these simulations that k-Wave's output agrees very well with the analytical solutions.

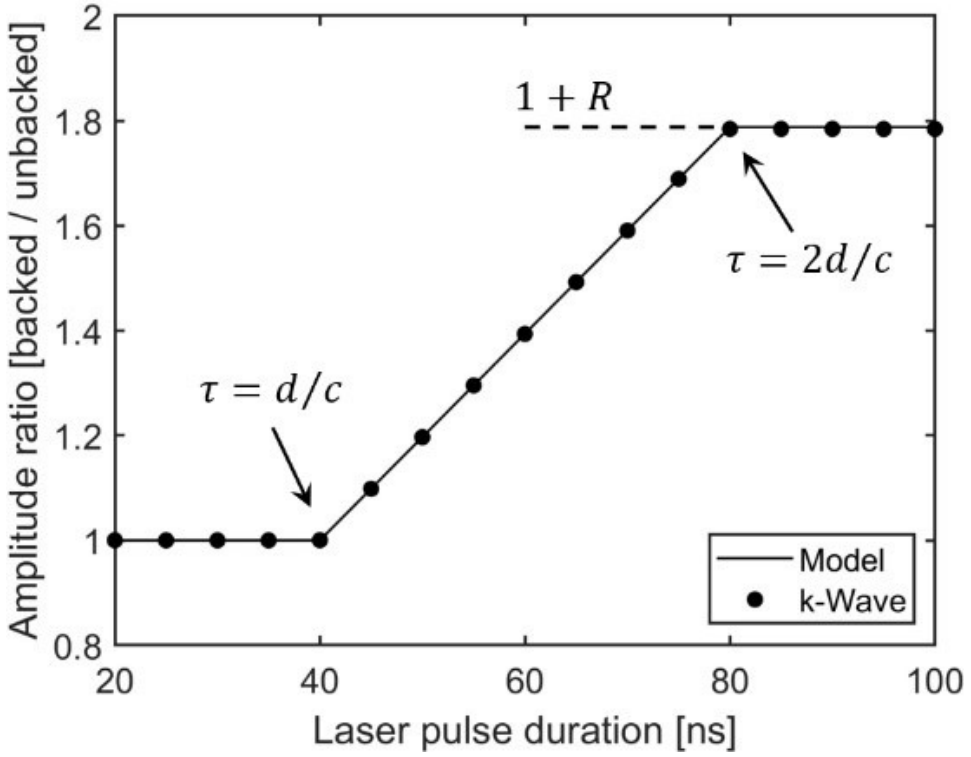

Figure 5-17: Ratios of backed ($I_1 + RI_2$) and unbacked (I_1) wave amplitudes for a laser-pulse of duration τ from 20–100 ns. R is the pressure reflection coefficient for a wave from the optical absorber looking at the backing medium, d = 60 µm is the thickness and $c = 1500\ \mathrm{m\,s^{-1}}$ is the sound-speed of the optical absorber, respectively. k-Wave simulations were performed in steps of 5 ns pulse duration and the analytical solution was computed in steps of 1 ns.

5.5.2 Three-layer Analytical Model

In this section, the above analytical model is extended to the case of an optical absorber (medium B) sandwiched between two mediums (medium A and medium C) of different acoustic properties, as shown in Figure 5-18. The thickness of the medium B is d. The sound-speeds and acoustic impedances of the three mediums are, c_A, c_B, c_C, z_A, z_B and z_C, respectively. A sensor is positioned in medium C. As in Sec. 5.5.1, the idea of image sources will be used here. The difference here is that there are two reflecting surfaces – the interfaces between media A and B and between B and C. Since acoustic absorption is ignored, the acoustic waves will bounce backwards and forwards within layer B infinitely many times and hence there will be infinite number of image sources. With this in mind, H, which incorporates the image sources, can be written as

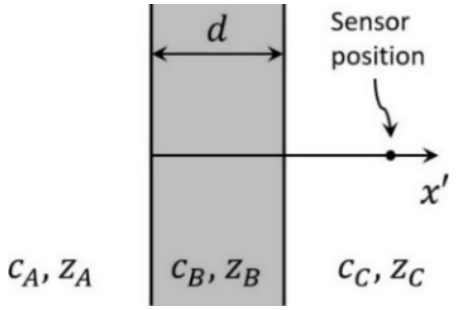

Figure 5-18: Schematic of the analytical model in which an optical absorber (medium B of thickness d with uniform optical absorption is sandwiched between two optically non-absorbing mediums, medium A and medium C. The sound-speeds and acoustic impedances of the three mediums are, $c_A, c_B, c_C, z_A, z_B, z_C$, respectively.

$$H(x) = \begin{cases} 0, & x > d, \\ TE/d, & 0 < x < d, \\ TR_{\mathrm{A}}E/d, & -d < x < 0, \\ TR_{\mathrm{A}}R_{\mathrm{C}}E/d, & -2d < x < -d, \\ \quad\cdot & \\ \quad\cdot & \\ \quad\cdot & \\ T(R_{\mathrm{A}}R_{\mathrm{C}})^{n/2}E/d, & -nd < x < -(n-1)d, \quad n\ even \\ TR_{\mathrm{A}}^{(n+1)/2}R_{\mathrm{c}}^{(n-1)/2}E/d, & -nd < x < -(n-1)d, \quad n\ odd \end{cases} \tag{5.20}$$

where, T is the acoustic pressure transmission coefficient for a wave travelling from medium B to medium C, and R_A and R_C are the acoustic pressure reflection coefficient for waves travelling in medium B and reflecting from media A and C, respectively. The even n terms correspond to the wave that initially sets off in the positive x direction, and is then multiply reflected, while the odd n terms correspond to the wave that sets off in the negative x direction and is multiply reflected.

The acoustic pressure can be found from Eq. (5.9), which in this case is written as

$$p(x,t) = \frac{₹}{\tau c_B^2}\int_{-\infty}^{\infty} H(x')\big(G(x,x',t+\tau/2) - G(x,x',t-\tau/2)\big)dx'. \tag{5.21}$$

Substituting in the expression for H from Eq. (5.20) gives

$$\begin{aligned} p(x,t) = \\ \frac{ET₹}{d\tau c_B^2}\Bigg\{ \sum_{n\ even} (R_A R_C)^{n/2} \int_{-nd}^{-(n-1)d} \big(G(x,x',t+\tau/2) - G(x,x',t-\tau/2)\big)dx' \\ + \sum_{n\ odd} R_A^{(n+1)/2} R_C^{(n-1)/2} \int_{-nd}^{-(n-1)d} \big(G(x,x',t+\tau/2) - G(x,x',t-\tau/2)\big)dx' \Bigg\} \end{aligned} \tag{5.22}$$

The relevant Green's function which takes into account the different sound-speeds in medium B and medium C is

$$G(x,x',t-t') = \frac{c_B}{2} U\left(t - t' - \frac{(d-x')}{c_B} - \frac{(x-d)}{c_C}\right). \tag{5.23}$$

Therefore, for a detector positioned at $x > d$, the acoustic pressure time-series can be written as

$$p(x,t) = \frac{ET₹}{2d\tau c_B}\left(\sum_{n\ even} (R_A R_C)^{n/2} I_n + \sum_{n\ odd} R_A^{(n+1)/2} R_C^{(n-1)/2} I_n\right) \tag{5.24}$$

where

$$I_n = \int_{-nd}^{-(n-1)d} \big(G(x,x',t+\tau/2) - G(x,x',t-\tau/2)\big)dx', \tag{5.25}$$

$$\begin{aligned} I_n = \int_{-nd}^{-(n-1)d} \Bigg(U\left(t + \frac{\tau}{2} - \frac{(d-x')}{c_B} - \frac{(x-d)}{c_C}\right) \\ - U\left(t - \frac{\tau}{2} - \frac{(d-x')}{c_B} - \frac{(x-d)}{c_C}\right)\Bigg) dx', \end{aligned} \tag{5.26}$$

$$I_n = \int_{-nd}^{-(n-1)d} g(x')dx', \tag{5.27}$$

where

$$g(x',t) = \begin{cases} 1, & -\frac{\tau}{2} + \frac{d-x'}{c_B} + \frac{x-d}{c_C} < t < \frac{\tau}{2} + \frac{d-x'}{c_B} + \frac{x-d}{c_C} \\ 0, & \text{otherwise.} \end{cases} \tag{5.28}$$

This integral can be solved using the concept of similar triangles, and Figure 5-19 and Figure 5-20 to give

$$I_n^{\tau<d/c} = \begin{cases} 0, & t < -\frac{\tau}{2} + \frac{nd}{c_B} + \frac{x-d}{c_C}, \\ c_B\left(t + \frac{\tau}{2}\right) - nd - \frac{c_B}{c_C}(x-d), & -\frac{\tau}{2} + \frac{nd}{c_B} + \frac{x-d}{c_C} < t < \frac{\tau}{2} + \frac{nd}{c_B} + \frac{x-d}{c_C}, \\ c_B\tau, & \frac{\tau}{2} + \frac{nd}{c_B} + \frac{x-d}{c_C} < t < -\frac{\tau}{2} + \frac{(n+1)d}{c_B} + \frac{x-d}{c_C}, \\ -c_B\left(t - \frac{\tau}{2}\right) + (n+1)d + \frac{c_B}{c_C}(x-d), & -\frac{\tau}{2} + \frac{(n+1)d}{c_B} + \frac{x-d}{c_C} < t < \frac{\tau}{2} + \frac{(n+1)d}{c_B} + \frac{x-d}{c_C} \\ 0, & t > \frac{\tau}{2} + \frac{(n+1)d}{c_B} + \frac{x-d}{c_C}. \end{cases} \tag{5.29}$$

$$I_n^{\tau>d/c} = \begin{cases} 0, & t < -\frac{\tau}{2} + \frac{nd}{c_B} + \frac{x-d}{c_C}, \\ c_B\left(t + \frac{\tau}{2}\right) - nd - \frac{c_B}{c_C}(x-d), & -\frac{\tau}{2} + \frac{nd}{c_B} + \frac{x-d}{c_C} < t < -\frac{\tau}{2} + \frac{(n+1)d}{c_B} + \frac{x-d}{c_C}, \\ d, & -\frac{\tau}{2} + \frac{(n+1)d}{c_B} + \frac{x-d}{c_C} < t < \frac{\tau}{2} + \frac{nd}{c_B} + \frac{x-d}{c_C}, \\ -c_B\left(t - \frac{\tau}{2}\right) + (n+1)d + \frac{c_B}{c_C}(x-d), & \frac{\tau}{2} + \frac{nd}{c_B} + \frac{x-d}{c_C} < t < \frac{\tau}{2} + \frac{(n+1)d}{c_B} + \frac{x-d}{c_C} \\ 0, & t > \frac{\tau}{2} + \frac{(n+1)d}{c_B} + \frac{x-d}{c_C}. \end{cases} \tag{5.30}$$

In the two-layer model, when $\tau > 2d/c$, the ratio of backed over unbacked wave amplitudes equals $(1 + R)$. However, in the three-layer model, the backed wave amplitude is dependent on both R_A and R_C. The duration, τ at which the ratio of backed over unbacked wave amplitudes reaches a limiting value is much longer since the acoustic pulse undergoes multiple reflections within the CPN source. However, the limiting value of the ratio can still be obtained using the geometric series.

Let $n = 2m$ and $n = 2m + 1$ in the even and odd parts of the Eq. (5.24)

$$p(x,t) = \frac{ET₹}{2d\tau c_B}\left(\sum_{m=0,1,2,\ldots}(R_A R_C)^m I_n + \sum_{m=0,1,2,\ldots} R_A^{m+1} R_C^m I_n\right), \tag{5.31}$$

$$p(x,t) = \frac{ET₹}{2d\tau c_B}\left(\sum_{m=0,1,2,\ldots}(R_A R_C)^m I_n + R_A \sum_{m=0,1,2,\ldots}(R_A R_C)^m I_n\right). \tag{5.32}$$

The two parts of the Eq. (5.32), which are geometric series, converge to the following solution [147]

$$p(x,t) = \frac{ET₹}{2d\tau c_B}\left(\frac{I_n}{1 - R_A R_C} + \frac{R_A I_n}{1 - R_A R_C}\right), \tag{5.33}$$

$$p(x,t) = \frac{ET₹}{2d\tau c_B}\left(\frac{1+R_A}{1-R_AR_C}\right)I_n. \tag{5.34}$$

For an unbacked case i.e., medium A $=$ medium B, $R_A = 0$ and hence, Eq. (5.34) becomes

$$p(x,t) = \frac{ET₹}{2d\tau c_B}I_n. \tag{5.35}$$

Therefore, the ratio of backed case, Eq. (5.34) over unbacked case, Eq. (5.35) for laser pulses $\tau \gg d/c_B$ is

$$p(x,t) = \frac{1+R_A}{1-R_AR_C}. \tag{5.36}$$

5.5.2.1 Comparison with Numerical Simulations

As above, the analytical solutions, which comprise of Eq. (5.29) for $\tau < d/c$ and Eq. (5.30) for $\tau > d/c$, were compared against linear simulations performed in k-Wave. Medium A, medium B and medium C were given the properties of glass, PDMS and water, respectively. The thickness of medium B was 60 μm. The optical absorption was assumed uniform across the absorbing region. The laser pulse duration τ, spanned from 10–1000 ns, and its amplitude, $1/\tau$. For each pulse, two separate numerical simulations were performed to test the effect of backing i.e., initially medium A and medium B were both PDMS and in the second simulation, medium A was glass and medium 2 was PDMS. The optical absorber in all simulations was positioned in medium C i.e., water. The nominal sound-speeds and densities of glass, PDMS and water were 5000 m s^{-1}, 1000 m s^{-1}, 1500 m s^{-1}, 2000 kg m^{-3}, 1000 kg m^{-3} and 1000 kg m^{-3}, respectively. The waveforms were recorded at 128 μm from the edge of the optical absorber in medium B.

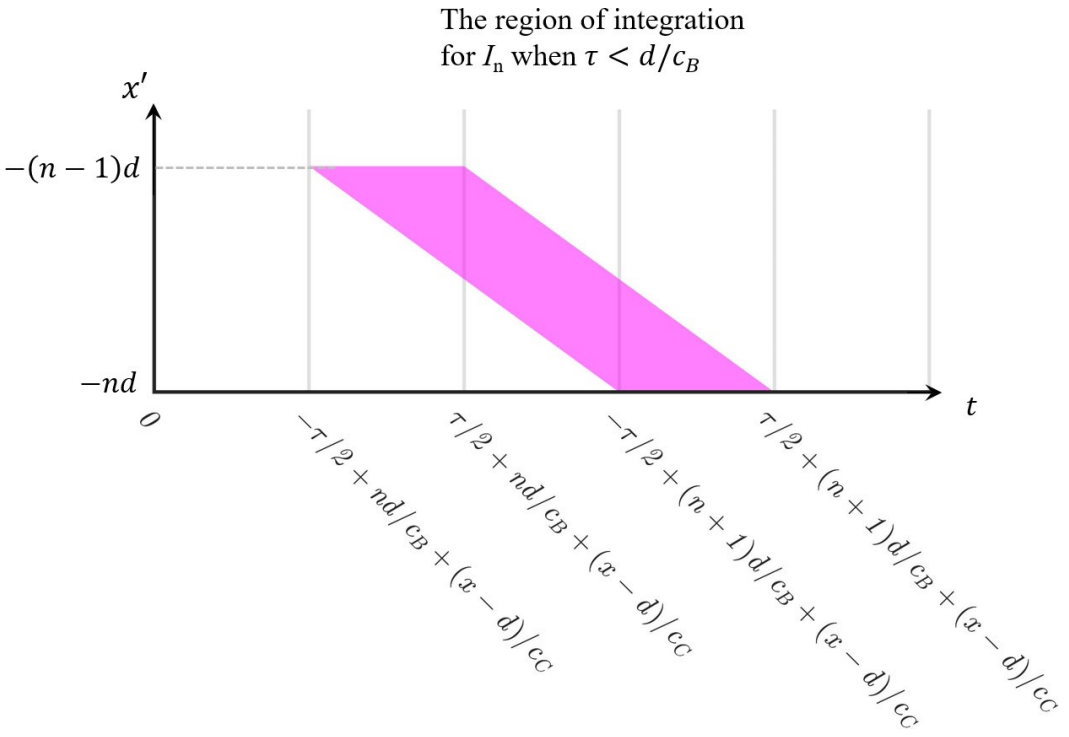

Figure 5-19: Region of integration for I_n when $\tau < d/c_B$.

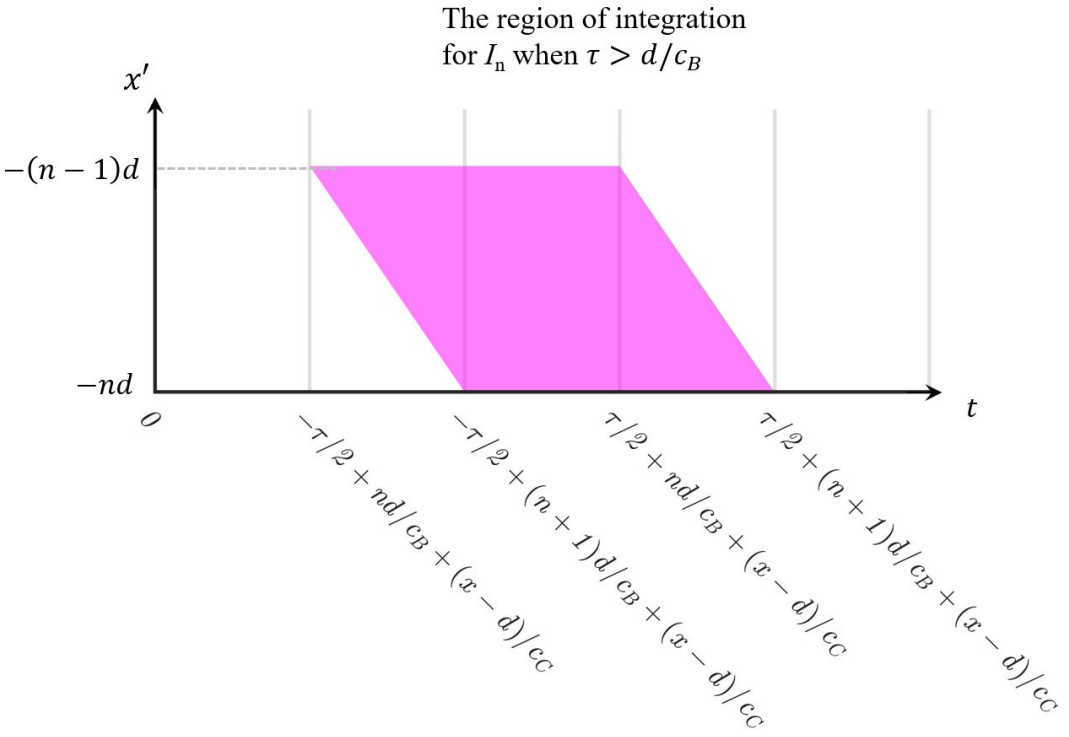

Figure 5-20: Region of integration for I_n when $\tau > d/c_B$.

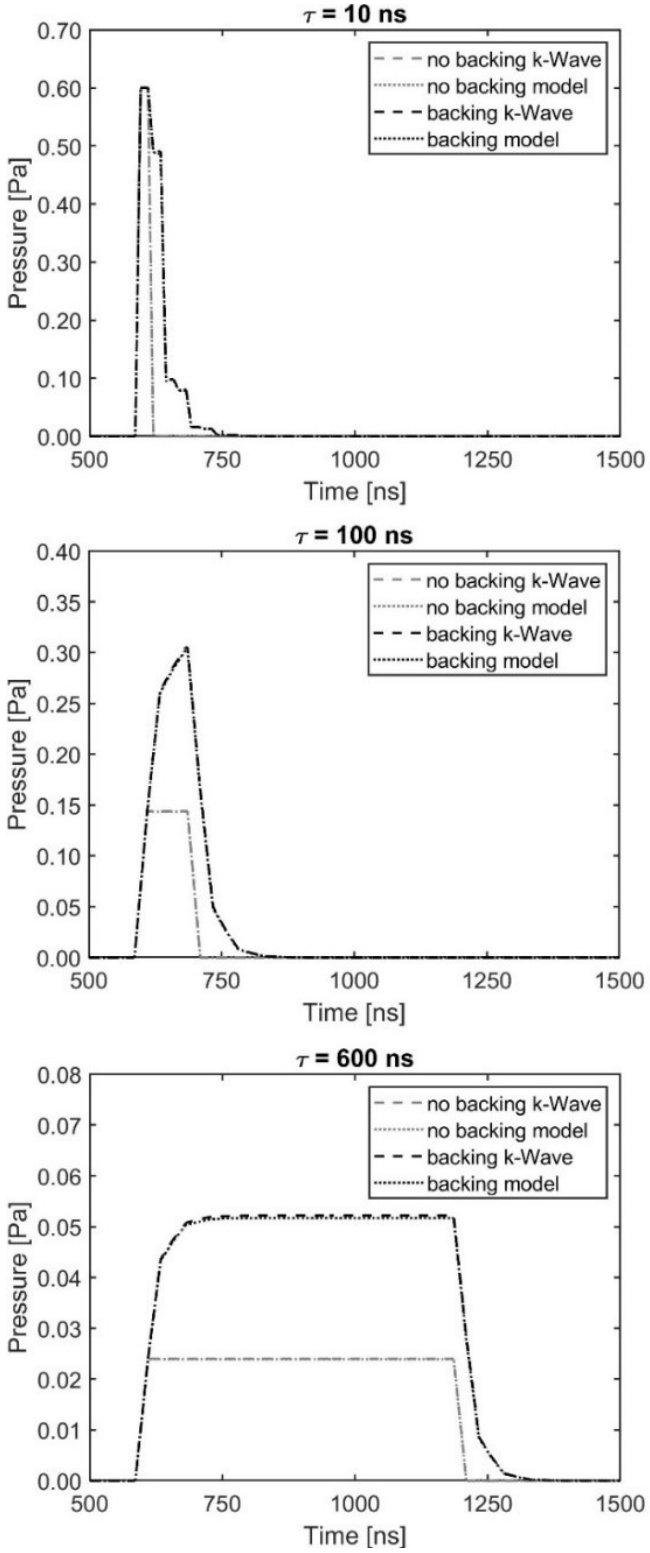

Figure 5-21: Analytical and k-Wave simulation waveforms showing the effect of acoustically reflective glass backing relative to acoustically matched PDMS backing for laser pulse durations from stress confined ($\tau < d/c$) to unconfined ($\tau > d/c$) case. The thickness of optical absorber was 60 µm, d/c_B was 40 ns and the waveforms were computed/recorded in water.

Example simulation and analytical waveforms computed with 10 image sources are shown in Figure 5-21 for laser pulse durations of 10, 100 and 600 ns, and show excellent agreement. Analytical solutions were computed from 10–1000 ns in steps of 1 ns, with 10 image sources and k-Wave simulations were completed from 10–600 ns in steps of 10 ns. The ratios of the respective peak-positive amplitudes are shown in Figure 5-22. Unlike the two-layer case, there are several transitions in the ratios which occur at multiples of d/c_B since the amplitude of the waves travelling in medium B is affected by the waves reflected at both medium A and B. The analytical simulations were also repeated to include 20 image sources but the differences with the solution of 10 image sources were too small to be noticeable.

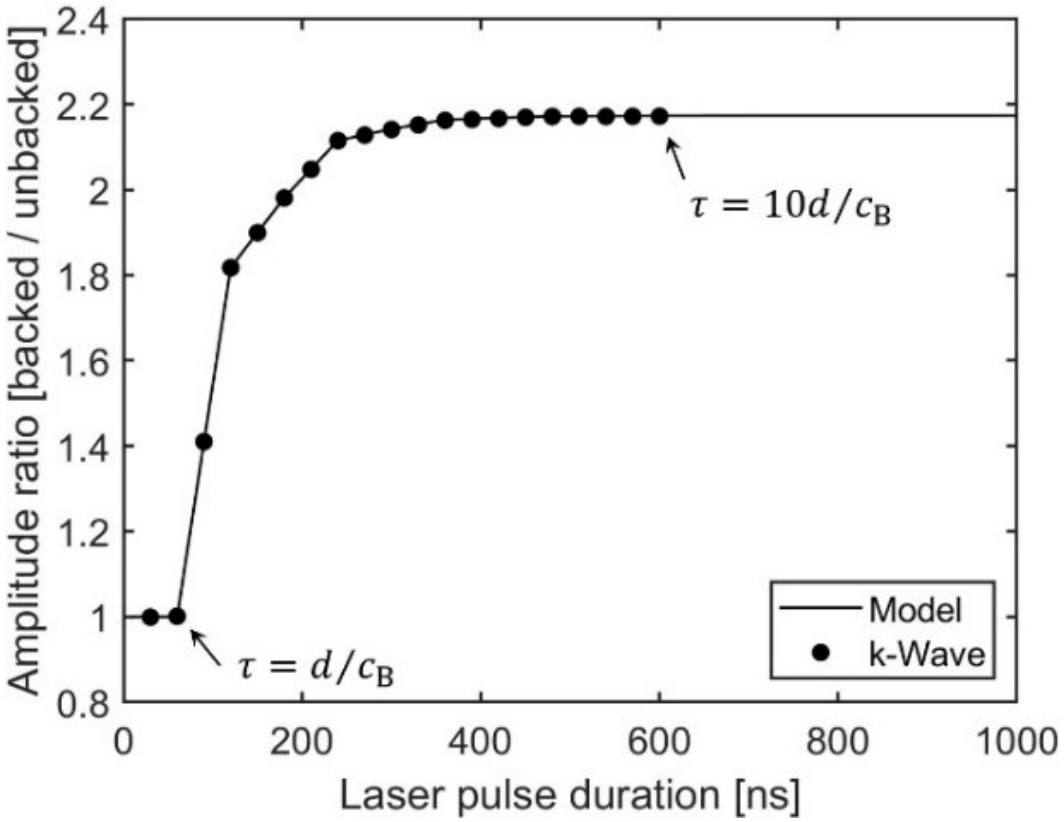

Figure 5-22: Ratios of backed and unbacked wave amplitudes for a laser pulse duration τ from 10–1000 ns. k-Wave simulations were performed in steps of 10 ns pulse duration and the analytical solution was computed in steps of 1 ns. k-Wave simulation data is plotted in steps of 30 ns for improved visualisation. For $\tau > 10d/c_B$, the ratio converges to Eq. (5.36) to within 0.005%.

5.6 Effect of Backing Material: k-Wave Simulations

The three-layer analytical model described in Sec. 5.5 is for the linear and acoustically non-absorbing case. However, in practice there is acoustic absorption in all the three layers and including this into

the analytical solution is non-trivial. Also, the optical absorption within the optical absorber in practice has an exponential profile and the laser pulse temporally has a Gaussian shape. To go further than the assumptions made in the analytical models, therefore, k-Wave was used to provide numerical solutions to more realistic scenarios. This proved to be relevant when making comparisons with the measurements of Sec. 5.4. Although LGUS sources can easily be generated with amplitudes sufficiently high that nonlinear propagation must be accounted for, as shown in Sec. 5.3, in the experiments in Sec. 5.4, the laser fluence was less than 2 $\mathrm{mJ\,cm^{-2}}$, which produced only linearly propagating waves. The effect of nonlinearity on the output of the simulations was tested for the pressures generated and shown to be negligible.

5.6.1 Setup of k-Wave Simulation

The sound-speeds and densities of glass, PDMS and water vary by a factor of two to three and acoustic absorption by two orders of magnitude (see Table 5-5). In order to model the effect of absorption, it is necessary to model the propagation over the whole propagation distance. Also, for convergence it is necessary to have a fine grid (many points per wavelength) around the acoustic boundary, and a small timestep (see Sec. 4.3.1). Consequently, because – with one simulation – that grid spacing and timestep must be used everywhere, it leads to an impractically large computational requirement.

To overcome this, the issues of the boundary and the absorption are separated into two models, and two simulations are run: one with a fine grid to model the boundaries and high attenuation within the CPN properly, and one that models the longer distance over which the effect of the absorption kicks in but doesn't need such a fine grid. In step 1, the model setup included three-layered media: glass or PDMS backing, PDMS-based CPN source and water. The time-series from the glass and PDMS-backed cases were recorded in the water medium one grid point after the CPN medium. In step 2, the time-series recorded in step 1 was propagated in a water-only model. The other advantage of splitting the model is that it will allow the use of relevant reference sound-speed, c_{ref} for the *k*-space correction factor, which improves the convergence with the time-step. In step 1 it is important to model the wave propagation accurately in the CPN medium rather than glass or water so the c_{ref} of CPN was used. In step 2, since it is a homogeneous medium the c_{ref} and the sound-speed of the medium are the same. The schematic of the simulation grid is shown in Figure 5-23.

The time-series in step 1 was injected as an interior source inside the simulation grid of water-only model as a Dirichlet boundary using the option `source.p_mode = 'dirichlet'`. At each time-step the grid value in the water-only model was replaced with simulated and down-sampled time-series recorded in step 1. With the use of such sources, it has previously been shown that the solution's amplitude will converge to within 3% of the actual solution [148]. This is because the data replacement at each time-step does not preserve the spatial gradients, which existed in the

field at the previous time-step and thus introduces numerical errors. This is not an error specific to k-Wave but a general situation present in all collocation methods, including finite differences [148]. However, this is not a limiting factor in this work since the effect is the same for all simulations, and here the ratio of the amplitudes for the glass and PDMS backings is the quantity of interest.

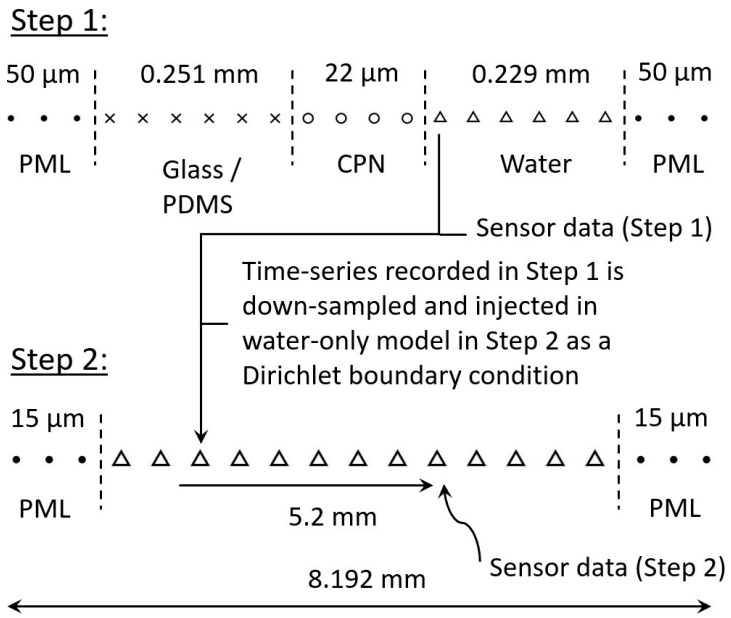

Figure 5-23: Set-up of k-Wave split-model to test the effect of CPN source backing for laser pulse durations from stress confined ($\tau < d/c$) to unconfined ($\tau > d/c$) case. PML: Perfectly Matched Layer; CPN: Carbon-polymer Nanocomposite. In step 1, Δx and Δt were 125 nm and 167 fs, respectively. The pressure time-series recorded in Step 1 was down-sampled and introduced as an interior source inside the simulation grid in Step 2 source as a Dirichlet boundary 0.2 mm away from PML on the left. In step 2, the Δx and Δt were 250 nm and 5 ps, respectively.

In step 1, the grid spacing Δx was 125 nm, Δt was 167 fs, and c_{ref} was 868 m s^{-1}. In step 2, the recoded time-series were down-sampled and propagated in a water-only medium. The grid spacing Δx was 250 nm, Δt was 5 ps and c_{ref} was 1482.5 m s^{-1}. The spatial profile of the optical absorption in the CPN medium was defined as $p(x) = Aexp(-\mu_a x)$, where μ_a is the optical absorption coefficient. The amplitude of $p(x)$ was set to $A = 250$ kPa for the glass-backed case and for the PDMS-backed case the amplitude was scaled down by 5% to account for optical absorption in the PDMS backing. Gaussian shaped pulses of FWHM from 0.25–600 ns were used in the simulations. The time-varying pressure inside the CPN medium was setup using the function `source.p`. At each time step the spatial profile of the optical absorption energy was weighted by the Gaussian shaped time pulse and added to the pressure field on the grid (see line 96 and 150 of Appendix). The acoustic attenuation of glass, PDMS, PDMS-based CPN film

and water are, $0.0209f^{1.0758}$, $1.6f^{1.47}$, $1.17f^{1.61}$ and $0.00217f^{2}$, respectively, where f is in MHz [110], [149], [150]. Since k-Wave requires the exponent of the acoustic absorption to be the same, it was set to the value for water, and the absorption coefficients in the different layers were varied by setting different pre-factors, an order of magnitude different for glass, PDMS and PDMS-based CPN. The model input parameters are shown in Table 5-5. The acoustic absorption of glass, CPN film and the adjusted values based on the variation of water absorption values are shown in Figure 5-24. Although there are differences in the two absorption values, overall the absorption based on water values represents the type of acoustic loss at least in the CPN film, which is of interest.

The experimentally obtained FPI sensor voltage waveforms acquired from glass-backed and PDMS-backed sources from Sec. 5.4 are shown in Figure 5-25 and the k-Wave simulation waveforms at the same laser pulse durations are shown in Figure 5-26 (see Sec. 5.4). The thickness of the optically absorbing layer in the model was set to 22 μm, which is an average of the source thicknesses of 20 and 24 μm used in the experiments. In the simulations (step 2), time-series were recorded at three distances of 2.2, 3.7 and 5.2 mm from the grid location where the time-series recorded in step 1 was injected. The ratios computed from the glass-backed and PDMS-backed wave amplitudes at each of the three grid locations are shown in Figure 5-27 along with the ratios computed from the FPI sensor voltage waveforms. The error bars on the experimental data represent one standard deviation in the measurement. The experimental data also includes a measurement made using a 4 ns laser pulse using the setup shown in Figure 5-4. The ratios from the experiment and from k-Wave simulations are in good agreement. The k-Wave simulations start to converge for pulse durations greater than 500 ns. Overall, the agreement between the k-Wave simulations and the experiments validates the hypothesis made at the beginning of this chapter – an acoustically reflective backing contributes to increased build-up of pressure when stress confinement criteria is not satisfied.

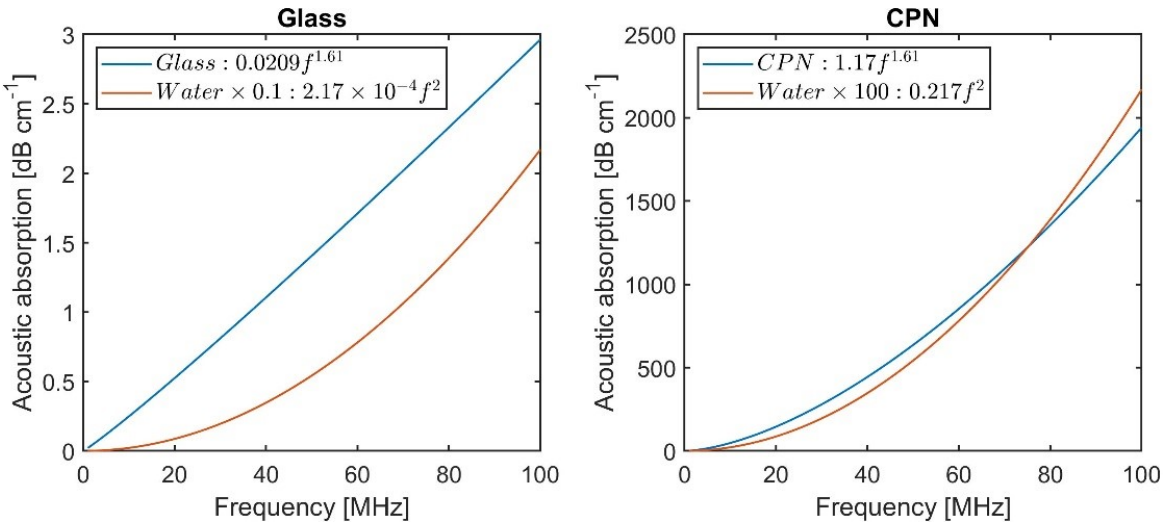

Figure 5-24: The acoustic absorption of glass [149] and CPN-based PDMS film [110] are plotted alongside the adjusted acoustic absorption used in the k-Wave simulation, which were obtained by varying the acoustic absorption of water values.

Table 5-5: Model input parameters used in 1D k-Wave to test the effect of glass and PDMS backing materials on LGUS from CPN films. Material properties were obtained from [116], [120], [126]. The mass density and sound-speed of CPN film was assumed the same as that of PDMS. Furthermore, the mass-density and sound-speed of PDMS backing and CPN film was lowered by 10% of their nominal values to obtain agreement with experimental ratios. The justification is similar to that made in Sec. 4.3.3.

Parameter	Material	Value	Units
Mass density, ρ_0	Glass	2230	kg m^{-3}
	PDMS	868	
	Water	998.2	
Sound-speed, c_0	Glass	5640	m s^{-1}
	PDMS	945	
	Water	1482.5	
Acoustic absorption, $\alpha(f^*)$	Glass	$0.252 \times 10^{-6} f^2$	Np m^{-1}
	PDMS	$252 \times 10^{-6} f^2$	
	Water	$2.52 \times 10^{-6} f^2$	
Optical absorption coefficient, μ_a	PDMS-based CPN	53000	m^{-1}
Stress-confined amplitude	–	250000	Pa

** f is frequency in MHz.*

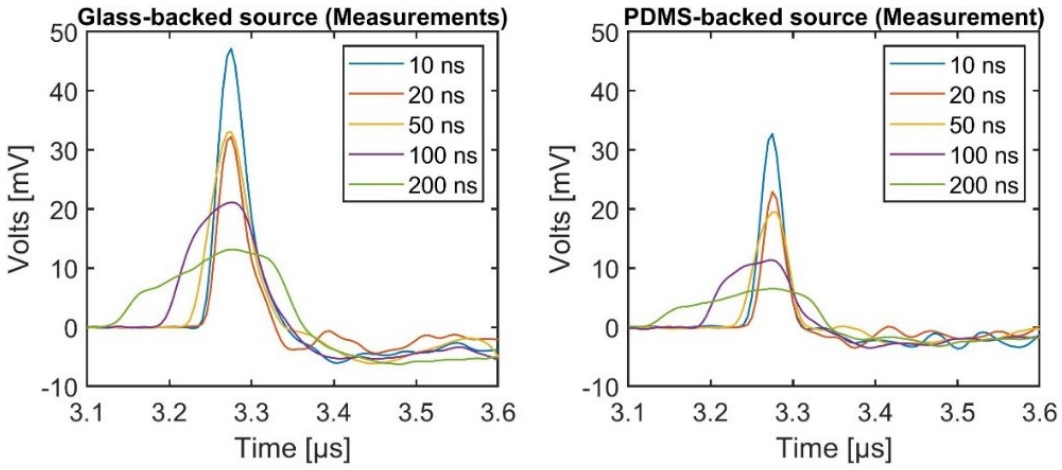

Figure 5-25: (Waveforms replotted from Sec. 5.4) Fabry–Pérot interferometer sensor waveforms acquired from glass-backed and PDMS-backed CPN sources using the experimental arrangement shown in Figure 5-8. The thickness of the CPN film on the backings was around 24 μm.

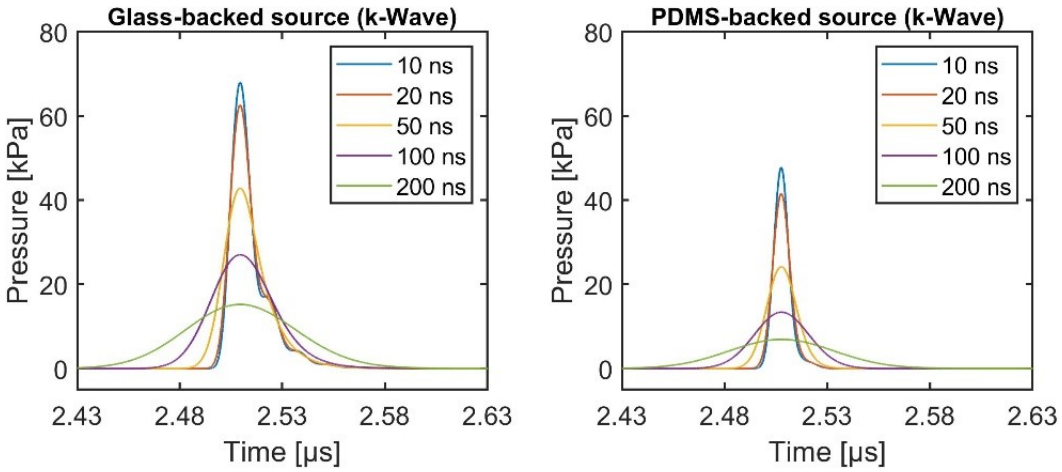

Figure 5-26: k-Wave simulations waveforms recorded from glass-backed and PDMS-backed sources using the split-model described in this section. The thickness of the CPN film was 22 μm.

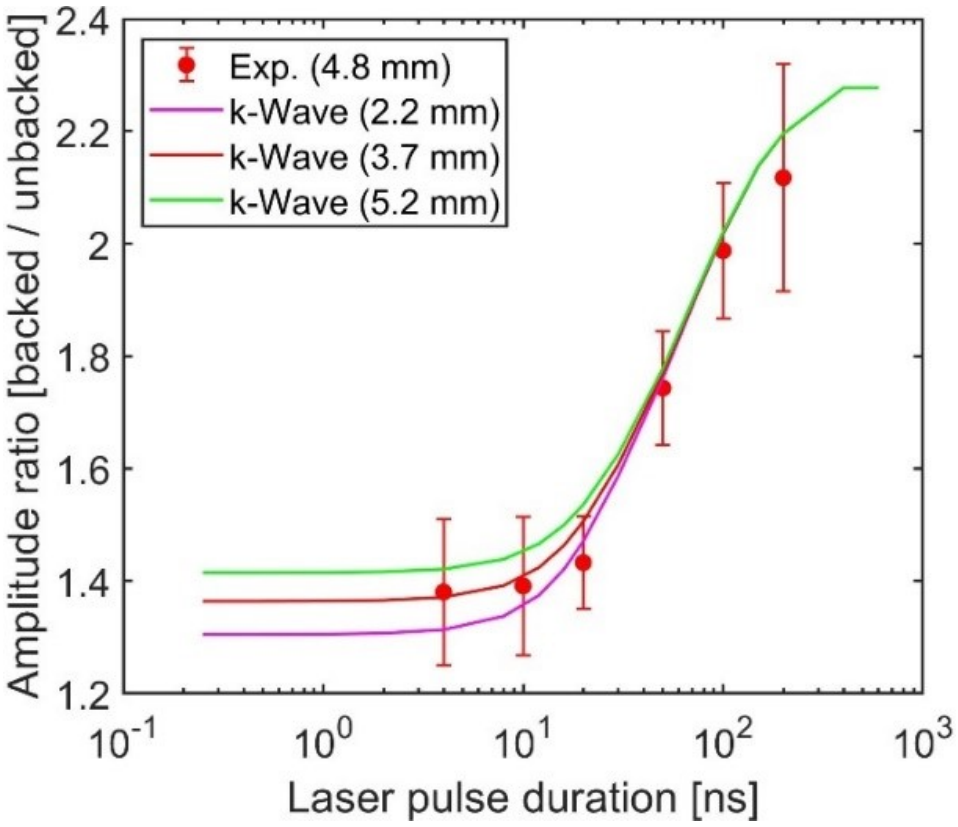

Figure 5-27: Ratios of glass-backed and PDMS-backed wave amplitudes for various laser pulse durations from stress confined ($\tau < d/c$) to unconfined ($\tau > d/c$) case. The error bars on the experimental ratios (red filled circles) represent one standard deviation in the measured data. Parenthetical entries in the plot legend are the distances at which the measurement or simulated time-series were recorded.

The simulated ratios show a small dependency with distance when $\tau < d/c$ and it is not '1' as previously seen in Sec. 5.5.2 (see Figure 5-22). This is because in stress confinement the LGUS pulses are short and hence contain more frequencies and furthermore, the duration of the LGUS pulse from the PDMS-backed source is shorter than the duration of the glass-backed source. Therefore, the LGUS pulse of the PDMS-backed source undergoes higher loss of amplitude with distance due to preferential loss of high frequencies and thus the ratios increase with distance when $\tau < d/c$. The amplitude spectra of glass-backed and PDMS-backed simulated pressure-pulses for a laser pulse duration of 10 ns are shown in Figure 5-28 for the three propagation distances at which the amplitude ratios in Figure 5-27 were computed. The *BW6* for the glass-backed case at the three propagation distances of 2.2, 3.7, and 5.2 mm, were 26.4, 25.6, and 24.8 MHz, respectively and for the PDMS-backed case it was 54.4, 49.6, and 46.2 MHz, respectively. It is seen that the relative loss in *BW6* in glass-backed case is negligible compared to the PDMS-backed case. Therefore, the amplitude loss suffered by the PDMS-based pressure-pulses are higher when $\tau < d/c$.

Simulations were repeated with no acoustic absorption both in step 1 and step 2 to check whether the amplitude ratios become '1' when $\tau < d/c$. The particular CPN source fabricated for tests in Sec. 5.4 had low optical absorption so that its stress confinement was within the range of variable pulse duration fibre-laser. Low optical absorption combined with low laser pulse energy produced nearly linear LGUS pressure-pulses. But the LGUS pulses in earlier experiments in this chapter were all nonlinear. Therefore, simulations were also performed with absorption in all three layers in step 1 and, absorption and nonlinearity in step 2. The ratios computed for the simulation cases of no absorption, absorption, and absorption and nonlinearity in water are shown in Figure 5-29. It is seen that the effect of absorption and nonlinearity is not discernible from absorption-only simulations, which suggest that any effects of nonlinear propagation in water was negligible. More importantly, when there is no absorption the ratio is almost '1' when $\tau \ll d/c$. Therefore, the higher loss in amplitude due to acoustic absorption suffered by PDMS-based pressure-pulses, which contain broader frequencies compared to glass-backed pressure-pulses is the reason why the amplitude ratio is not '1' when $\tau < d/c$.

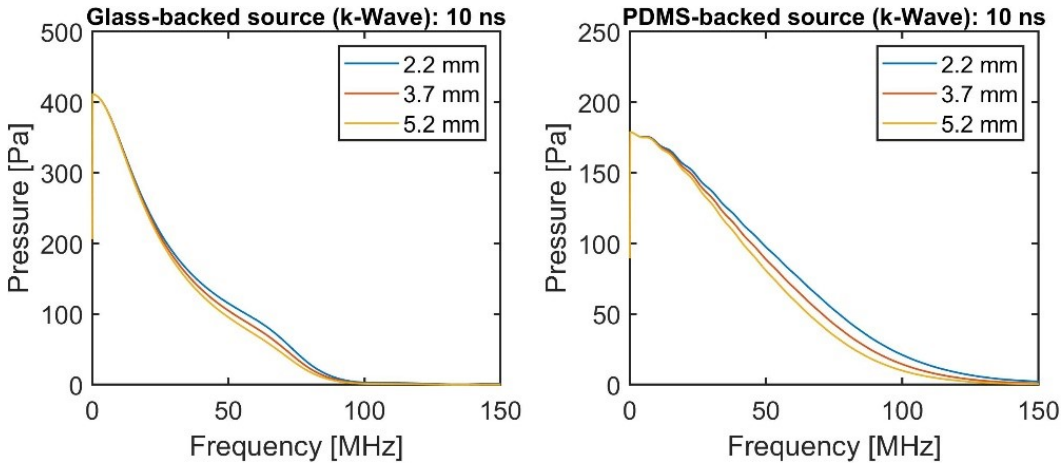

Figure 5-28: The amplitude spectra of glass-backed and PDMS-backed pressure-pulses shows the effect of acoustic absorption with propagation distance.

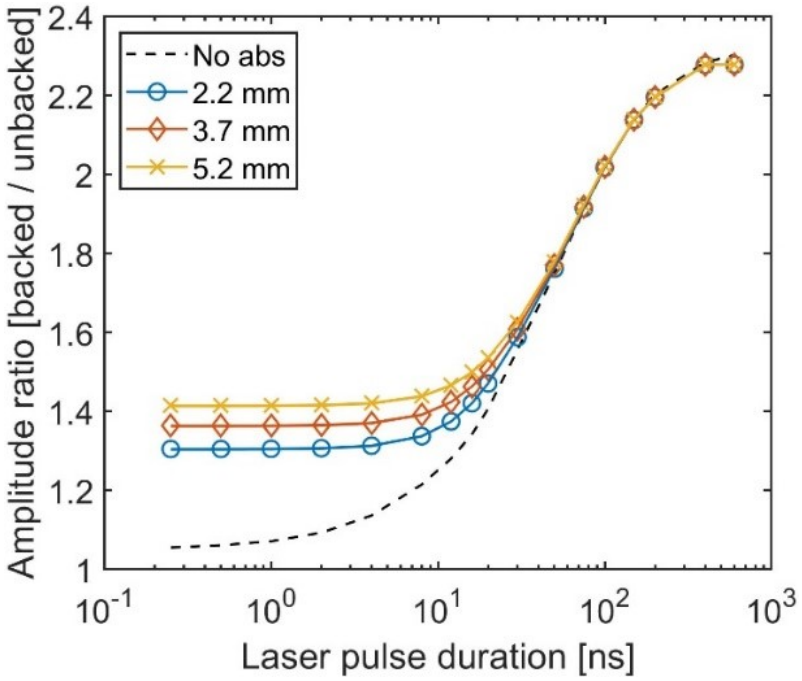

Figure 5-29: Ratios of glass-backed and PDMS-backed wave amplitudes for various laser pulse durations from stress confined ($\tau < d/c$) to unconfined ($\tau > d/c$) case. The black broken line represent no acoustic absorption case in both step 1 and step 2 of k-Wave simulations. The continuous lines represents acoustic absorption case in both step 1 and step 2. The markers on the continuous line represents acoustic absorption case in step 1, and acoustic absorption and nonlinearity in step 2.

5.7 Conclusion

The aim of this chapter was to explore the effect of source backing on the pressure amplitude and bandwidth when stress confinement was not satisfied. It is known that in stress confinement, for an acoustically reflective backing such as glass, temporally, the wave exiting the CPN medium into water will be of twice the duration taken by the acoustic wave to transit across the thickness of the CPN layer. If the CPN source is backed on an acoustically matched backing i.e., the same polymer matrix used in fabricating the CPN, then one half of the LGUS propagating towards the polymer-backed medium and the other half of the LGUS propagating towards water do not interact. Therefore, a matched source would produce twice the bandwidth compared to a reflective source. This physical effect was originally assumed to extend even when there was no stress confinement. However, it was found experimentally that the backing material has an interesting effect on the characteristics of the LGUS pressure-pulse when the laser pulse duration is greater than the stress confinement duration. When the laser pulse is longer than the stress confinement duration (as was the case for all the glass-backed CPN sources fabricated and tested in Chapter 3), one half of the LGUS wave reflected by the

glass back to the CPN medium and the continued optical deposition of heat by the laser pulse caused increased build-up of pressure. The total acoustic pressure reached was therefore higher than in the absence of the reflection i.e., in case of PDMS-backed sources.

A linear analytical model was developed to obtain an intuitive understanding of the effects of backing material on the amplitude of the LGUS from CPN sources. Green's function solution was obtained firstly for the case of a backing-absorber half-spaces followed by three-layer medium consisting of backing-absorber-water layers. The obtained solution was compared with k-Wave simulations. A full k-Wave simulation including acoustic absorption and nonlinearity was completed, which confirmed the experimental observations that when stress confinement is not satisfied, the acoustic reflections from the reflective backing contributes to increased build-up of pressure in the CPN medium.

The increased pressure output from glass-backed sources compared to PDMS-backed sources, regardless of the stress of confinement meant that the spectral pressure amplitudes of glass-backed sources were always higher. Therefore, despite the fact that *BW6* metric for PDMS-backed sources is larger than glass-backed sources, the increased pressure output from glass-backed sources compensates for the effect of lower *BW6* observed in glass-backed sources. Consequently, in this project glass-backed sources are preferred over PDMS-backed sources.

Chapter 6

Fabrication and Testing of a LGUS Source

6.1 Introduction

In this chapter, the design, construction, and characterisation of a laser-generated, plane-wave, ultrasound source device for use in high-frequency hydrophone calibration are described. The implications of the source on the uncertainties in high-frequency hydrophone calibration are discussed. The laser-generated ultrasound (LGUS) source is packaged such that it can be used in the same way as any piezoelectric transducers are used in an ultrasound laboratory. The carbon-polymer nanocomposite (CPN) source and the beam-shaping optical diffuser are housed in a water-tight cylindrical aluminium housing, a fibre-bundle with a stainless-steel casing that connects to this housing delivers the laser pulse, and the laser itself is a convenient, portable device with a small form factor. The six design factors were based on the desired characteristics of the LGUS source discussed in Sec. 2.3, which is listed here again as a reminder:

1. The LGUS pressure-pulse should have a frequency range that makes measurements possible up to 100 MHz and the amplitude of the Fourier transform of the acoustic displacement signal at all frequencies within the bandwidth should be at least 50 pm.
2. The spatial averaging of the LGUS beam by the hydrophone being calibrated should produce significantly lower errors compared to the current best practice (focused ultrasound fields) at all frequencies i.e., errors should be 1% or below.
3. The long-time temporal stability should span at least three hours, which is sufficient to calibrate at least one hydrophone on the interferometer. The variation in the calibration of a hydrophone arising from the temporal stability of LGUS pulses should be less than 2%.
4. The LGUS source must not contaminate the water (e.g., affect its conductivity) i.e., the source must not release carbon nanotubes into water.
5. The LGUS source must not present a laser hazard to the user i.e., the laser beam should be completely enclosed.
6. The temperature rise in the LGUS source must not elevate the temperature of the water, thereby affecting the temperature dependent sensitivity of the hydrophone.

6.2 Considerations for the CPN Source Material

The choice of the carbon-polymer nanocomposite (CPN) source used in the laser-generated ultrasound (LGUS) source device in this chapter was based on the findings from the work of the previous chapters. Chapter 3 dealt with an initial study of CPN sources in which a total of 27 variations of CPN sources were fabricated and tested. Three polymer types (epoxy, polyurethane and polydimethylsiloxane (PDMS)), three weight fractions (wt. %) of multi-walled carbon nanotubes (MWCNT) in polymer (1.25, 2.5, and 3.5 wt. %), and three thicknesses (17–28, 51–55, and 71–85 μm) were investigated. The CPN was prepared using a shear mixing method in which the base polymer, curing agent and MWCNT were combined using a speed mixer. The resulting paste was coated on laboratory grade glass slides using a blade film applicator and oven cured at conditions specific to the polymer type, which completed the source fabrication process. A Q-switched Nd:YAG pulsed laser of 4 ns duration was used as an excitation source and a broadband hydrophone with an extrapolated sensitivity response up to 110 MHz was used to measure the LGUS pressure-pulse from each of the 27 sources. The LGUS pressure pulses generate from 27 CPN sources were investigated against several different factors such as the effect of MWCNT wt. %, polymer type, CPN film thickness, laser fluence, nonlinear propagation and temporal stability. A brief summary is provided in the following paragraphs along with practical constrains, which determined the final CPN source material and the design of the LGUS source device discussed in Sec 6.3.

The CPN sources were found to be highly acoustically absorbing, therefore, to minimise unnecessary acoustic absorption, the CPN source should be ideally equal to the optical absorption depth or where possible as thin as practically achievable. The blade film applicator used in this thesis was not adequate to produce CPN films below 10 μm. Therefore, a thickness of 20 μm was chosen as a compromise. The variation in the reproducibility of this thickness was less than 10 μm (see Figure 3-2).

A stress confinement was generally not satisfied in any of the CPN sources for a laser pule of 4 ns duration. Nevertheless, for a given laser fluence, and nominally the same MWCNT wt. % and CPN film thickness, PDMS-based CPN source produced the highest peak-positive pressure (p_+) compared to epoxy or PU (see Figure 3-21). The pressure-pulses were all broadband with non-negligible spectral amplitude of around 10 kPa at 100 MHz for p_+ over 4 MPa (see Figure 3-18–Figure 3-20). However, the −6 dB bandwidth (*BW6*) metric showed an inverse relationship with p_+ (see Figure 3-22–Figure 3-24). The broadening of the pressure-pulses due to wave steepening from cumulative acoustic nonlinearity and the loss of consequent high frequencies due to preferential absorption decreased the bandwidth. Since cumulative acoustic nonlinearity is dependent on both the propagation distance and pressure amplitude, the *BW6* decreased as the pressure increased. This was numerically investigated using a model of nonlinear propagation using k-Wave in Chapter 4 (see Figure 4-4 and Figure 4-5). It is required that the spectral pressure amplitudes of the LGUS pressure-

pulses should generate a measurable displacement of 50 pm on the interferometer at all frequencies up to 100 MHz. Therefore, to minimise the effect of nonlinear propagation, the design of the source device must allow smaller source-sensor separations of a few millimetres. This may be possible if the LGUS source device physically mimics the design of piezoelectric piston transducers, since the ultrasound field scanning facilities at the National Physical Laboratory (NPL) are largely designed to accommodate cylindrical transducer types.

PDMS-based CPN sources were found to be both physically robust (no detachment of CPN film from glass) and produced stable LGUS pressure-pulses under sustained pulsed laser excitation over a test duration of three hours. Therefore, the LGUS source device was based on a PDMS-based CPN material.

The stress confinement times for the PDMS-based CPN sources with 1.25, 2.5 and 3.5 wt. % MWCNT was 14.9, 6.5 and 4.5 ns, respectively (see Table 3-5). The 1.25 wt. % MWNCT case although satisfies stress confinement for a laser pulse duration of 4 ns, it is not sufficient to generate significant pressure levels. The measured p_+ at 7.4 mm source-sensor separation for a fluence of 40 mJ cm^{-2} was around 3 MPa (see Figure 3-22). A 2.0 wt. % MWCNT gives a stress confinement time of 8.9 ns, which was obtained by linearly interpolating the above derived stress confinement times. A 4 ns duration laser pulse may be sufficient to satisfy a stress confinement, but this laser was not practical to use in NPL's Primary Standard and therefore, a second laser of 2.6 ns pulse duration was commissioned. This is discussed further in Sec. 6.3.1.

The planarity of the LGUS beam can be controlled by expanding the laser beam to be sufficiently wide so that the hydrophone spatial effects become small enough to be ignored. In Chapter 3, the LGUS beam-area was 0.8 cm^2 and the lateral beam profile was approximately Gaussian. For a 0.2 mm diameter hydrophone, the spatial averaging error up to 100 MHz was less than 1% (see Sec. 3.3.2). However, at the National Physical Laboratory (NPL), reference hydrophone of up to 0.5 mm in diameter are in use. Therefore, ideally the LGUS beam-area of nearly 3 cm^2 may be required to satisfy the planarity requirement. Expanding the laser beam to a bigger area will decrease the laser fluence and will directly affect the pressure amplitude and bandwidth of the LGUS pressure-pulse. This is discussed in Sec. 6.4.

In Chapter 5, the effect of an acoustically reflective (glass) and acoustically matched (PDMS) backings on PDMS-based CPN sources was investigated. The aim of using the matched backing was to increase the bandwidth relative to that obtained from glass-backed CPN source whilst keeping the amplitude the same. However, the initial experimental findings turned out to be novel in that the effect of backing material has a significant effect on LGUS when stress confinement is not satisfied. The *BW6* from the PDMS-based source was larger (34%) compared to glass-backed source as expected but the pressure amplitude was 40% lower, which was unexpected. Via experiments and modelling it was confirmed that when the laser pulse is longer than the stress confinement duration,

one half of the LGUS wave reflected by the glass back to the CPN medium and the continued optical deposition of the heat by the laser pulse caused increased build-up of pressure. Therefore, though there is a gain in *BW6* with the PDMS-backed source, the increased pressure amplitude from the glass-backed source compensates for the lower *BW6*, since the pressure amplitudes from glass-backed source at most frequencies were higher than the PDMS-backed source. Also, glass-backed sources do not flex under physical stress compared to PDMS-backed sources (see Figure 5-7), therefore, a LGUS source device based on glass-backed CPN material is better suited for use in a laboratory type environment.

6.3 Design and Construction of the LGUS Source

The three components of the LGUS source, i.e., the laser, fibre-bundle, and the glass-backed CPN encased in a cylindrical aluminium housing, are each described in this section.

6.3.1 Laser

The laser used in Chapter 3 was a Q-switched flash lamp pumped Nd:YAG system, water-cooled using a liquid pump. The main disadvantage of this system is the airborne noise of the flash lamp and liquid pump, which would penetrate the water directly interfering with the ultrasonic displacement measurements made with a pellicle using the interferometer. This has been observed on the Primary Standard at the National Physical Laboratory (NPL) where the audible noise from the cooling fan of the radio frequency power amplifier intermittently affects the stability of the phase locked loop of the interferometer. The noise from the laser system is much higher and therefore would not be tolerable (this was my personal experience when I made measurements for hydrophone calibrations on the NPL's interferometer). The next important consideration was the electromagnetic (EM) emission during the Q-switching of the laser. Most hydrophones pick up EM emissions. This is a particular problem in this application since the hydrophone will be positioned close to the source i.e., within 10 mm or as close as practically achievable. Therefore, ideally the emissions won't exist or will subside within a couple of microseconds after the laser exits from the aperture. It was shown in Chapter 3 that using a 4 ns laser and a fluence of 40 $\mathrm{mJ\,cm^{-2}}$ it was possible to generate peak-positive pressure-pulses as high as 7 MPa with non-negligible frequency content up to 100 MHz. The stress confinement time for a PDMS-based CPN with 2.0 wt. % MWCNT is 15 ns. In order to satisfy stress confinement, the duration of the laser pulse should be significantly less than 15 ns. Since cost prohibitions prevented from procuring a picosecond range laser, the minimum duration of the laser was decided to be in the range 1–3 ns. There is also a safety concern with picosecond range lasers since the peak-power will be at least one order higher than the nanosecond range lasers. Therefore, safety measures would need to be elevated by using heavy glass-based filter goggles, which also come with poor visibility. This is not practically helpful since the calibration process involves alignment of the interferometer laser beam axis and acoustic beam axis to the hydrophone and pellicle, interactions

with computer and other hardware. All these tasks would be hindered by the extra care that is required to operate safely.

Table 6-1: Required specifications of the laser for use with the LGUS source, which was sent to four laser manufacturers.

Parameter	Specification
Pulse duration	1–3 ns
Pulse energy @1064 nm	60–80 mJ
Pulse repetition rate	At least 10 Hz
Pulse-pulse stability	2%
M2 beam quality	Not relevant
Fibre coupled laser delivery	Essential
Customised trigger i.e., trigger should correspond to laser emission from the aperture	Essential
Electromagnetic emission should be contained and if present then should not last beyond 1 microsecond	Essential
Acoustic noise due to lamp discharge and fluid pump should be low. Explore options to contain the noise and obtain measurement of the decibel levels for comparison	Important
Dimensions of the laser head	$< 0.3\ m^3$
Cost	£40,000

The specifications listed in Table 6-1 was sent to four laser manufacturers. All four manufacturers suggested using a diode pumped solid state laser as a way of eliminating the noise of the flash lamp, and three of the four manufacturers needed to employ liquid pumping to cool the laser head sufficiently. Only one manufacturer, Montfort Laser GmbH (Götzis, Austria), agreed to deliver 90% of the specifications – all except the fibre-bundle which was on a best endeavour basis. The solution offered was a customised version of their M-Nano product line. The heat extraction from the laser head was by means of conduction via a large cooling plate attached to the base of the laser and convectively via a small cooling fan blowing over the laser module. On receipt of the laser from Montfort its full-width at half-maximum (FWHM) pulse duration of 2.6 ns was verified against manufacturer's test report (see Figure 6-1). The energy per pulse of 77 mJ was confirmed using a 20 mm diameter pyroelectric energy sensor (ES220C, Thorlabs, Ely, U.K). The long-time temporal stability was tested in conjunction with the fibre-bundle, which is presented in Sec. 6.4.1. The EM emission was present and decayed within 1 μs after the laser pulse emission, which is within the time period specified in Table 6-1.

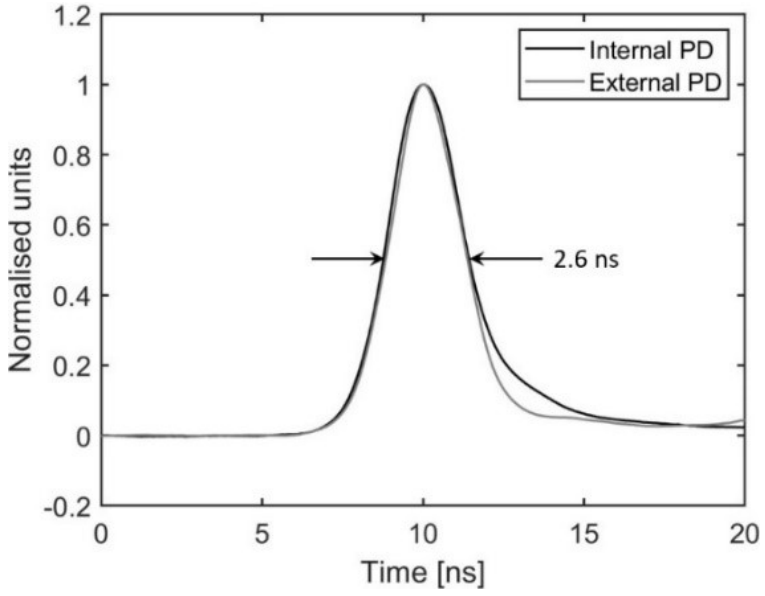

Figure 6-1: Temporal pulses of the M-Nano Montfort GmbH laser measured using a Tektronix DPO7254 digital storage oscilloscope with an analogue bandwidth of 2.5 GHz and 40 GS/s sampling rate. The laser has an internal photodetector (black line) positioned close to the exit aperture, which provides the necessary trigger signal for automated scanning measurements. An external high-speed photodetector (grey line) DET0CL (Thorlabs, Exeter, U.K.) was also used to verify the pulse duration.

6.3.2 Fibre-bundle

The experimental setup in Chapter 3 was based on an open beam laser which was directed onto a static CPN source positioned inside the water tank and the hydrophone was mounted on a motorised stage, which facilitated beam scanning. In contrast, the hydrophone in the Primary Standard measurement setup at NPL is positioned in a static mount and the source is on the motorised stage. Therefore, an open beam setup is impractical because the CPN source is not large enough, which means the source would need to move with the laser and, importantly, it increases the risk of inadvertent laser exposure to the user. The preferred option was to design the LGUS source resembling a standard piezoelectric piston source. The main challenge in this design was the delivery of the high-energy laser pulses via an optical fibre to the LGUS source.

Multimode optical fibres are commonly used for coupling high-energy laser pulses because of their large-core size (0.9 mm core diameter fibres are available from Thorlabs, Exeter, U.K.) when preserving the input beam quality is not a concern. To efficiently couple the laser, the beam size when focused should be equal to the size of the fibre core, and the cone of the focused beam should be within the acceptance cone of the fibre core (see Figure 6-2). The acceptance angle (half-angle of the acceptance cone), α_{FO} is related to the numerical aperture (*NA*) of the fibre, which in turn is related to

the refractive indices of the core, n_{core} and cladding, n_{clad}, materials: $NA = \sin(\alpha_{\text{FO}}) = sqrt\left(n_{\text{core}}^2 - n_{\text{clad}}^2\right)$, assuming the medium around the fibre is air. The two common damage mechanisms with high energy laser pulses is sparking and air breakdown at the interface of air and fibre surface, and damage down the length of the fibre, which is a consequence of angular misalignment [151], [152]. If the spatial profile of the Gaussian beam is converted to a top-hat profile then the laser fluence can be evenly spread on the fibre surface, which eliminates sparking and air breakdown. By adding beam homogenisation optics at the input of a 1.5 mm core diameter multimode fibre, laser energy as high as 65 mJ (pulse duration 3–5 ns and 532 nm wavelength) has been coupled [151]. Optical propagation losses in a single or a multimode fibre over a of couple of meters is negligible and much of the loss arises from how well the beam is coupled to the fibre core. It is possible to attain 80% efficiency when proper care is taken to align the beam into the fibre core [152].

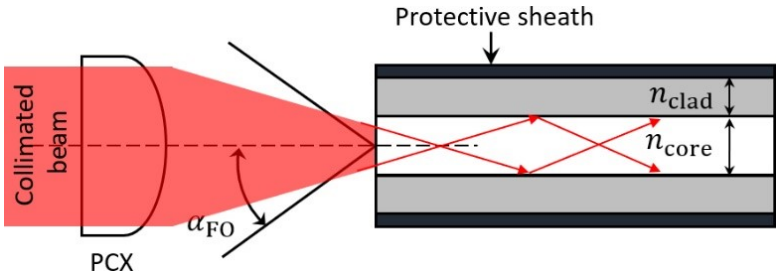

Figure 6-2: Coupling of coherent light into an optical (multimode) fibre. PCX: plano-convex lens, α_{FO}: half-angle of the acceptance cone of the fibre core, n_{core}: refractive index of the core, n_{clad}: refractive index of the cladding.

Fibre-bundles offer a robust alterative to multimode fibres in which multiple multimode large-core fibres are bundled together. Since the overall aperture of a fibre-bundle is much bigger than a single fibre, the laser launch conditions into a fibre-bundle is not constrained by tight focusing or misalignment errors. Therefore, damage occurrences are rare and even if a few of the fibres in the bundle break due to bending or twisting then there is no detrimental effect. The optical fibre-bundles are available as coherent or incoherent. In a coherent bundle there is a one-to-one correspondence at the input and output, which has applications in imaging such as endoscopy and industrial inspections. There is no such one-to-one correspondence in an incoherent bundle, which means the light exiting at the other end is diffused and relatively more divergent. This is mainly used for laser delivery applications over a short distance.

The optical loss in a fibre-bundle is greater than for a single multimode fibre. This is because the entire input face of the fibre-bundle is illuminated, so some of the light gets into the spaces or blind spots between the individual fibres and cladding of the fibres, which is invariably lost. Therefore, the optical loss is dependent on how tightly all the individual fibres are packed together (known as packing efficiency) and the relative size of the fibre core to the fibre cladding. Hexagonal

cross-section fibres, which attain this shape as a result of the fabrication process, virtually removes the gaps seen in a circular fibre design. Such a fibre-bundle from CeramOptec GmbH (Bonn, Germany) has been applied in a real-time volumetric photoacoustic tomography imaging to couple a laser pulse of less than 10 ns duration and 120 mJ at 750 nm [153]. This solution was proposed to Montfort GmbH, the laser manufacturer, who duly merged a fibre-bundle from CeramOptec GmbH into their design. The fibre-bundle is 2 m long, input and output aperture diameters are 5 mm, and it incorporates 139 hexagonal cross-section fibres of 0.4 mm core width. The coupling efficiency of the fibre-bundle was found to be close to 75% i.e., the pulse energy at the fibre input was 77 mJ and at the other end of the fibre it was 58 mJ.

The long-time temporal stability of the laser when coupled with the fibre-bundle is shown in Figure 6-3. The laser was mounted on a standard optical steel breadboard, which provided the necessary conductive cooling, and the convective cooling was from a small cooling fan positioned close to the laser module. The temporal stability was monitored from cold switch on of the laser – once with cooling fan on, once off – for one hour. It is seen in Figure 6-3 that the two plots show a similar trend. After the first 20-min, the standard deviation for both measurements is only 0.5%. It was learnt from the field scanning measurements that without the cooling fan on, the temperature of the laser casing reached the thermal shutdown temperature of 60℃ after about two hours from switch on. Consequently, for all subsequent measurements the cooling fan was kept on. There was no irreversible damage and no changes to characteristics of the laser i.e., pulse shape or stability, as a result of the thermal shutdown.

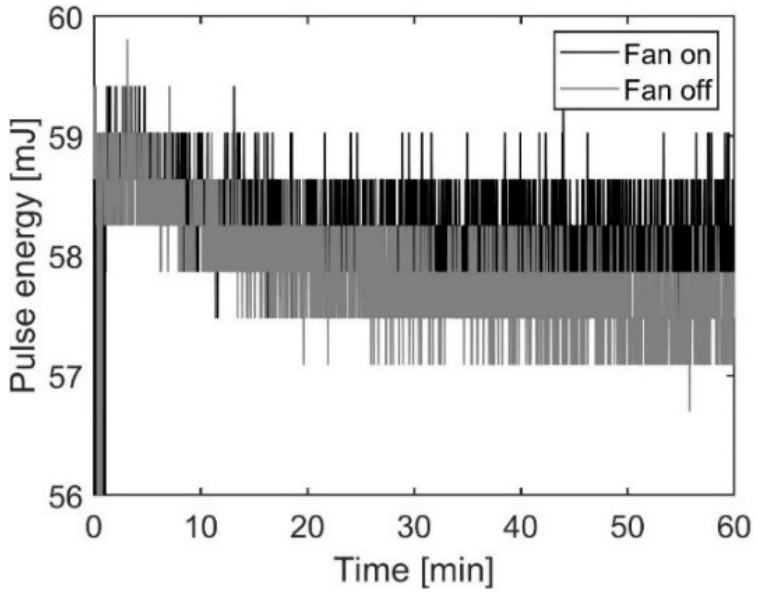

Figure 6-3: Temporal stability of the M-Nano laser with CeramOptec fibre-bundle monitored using a 20 mm diameter pyroelectric energy sensor (ES220C, Thorlabs, Ely, U.K).

6.3.3 LGUS Source

The design and construction of the LGUS source was accomplished in conjunction with NPL's Engineering Services department. First, a Computer Aided Design (CAD) in SolidWorks (Waltham, MA, USA) was drawn, Figure 6-4, and then a mock source was built using standard optical elements available from Thorlabs (Exeter, U.K.), Figure 6-5. The CPN source was designed around a fused silica parallel window of 5 mm thickness and 50 mm diameter from Newport (FSW18, Newport Corporation, U.K.). This diameter was specifically chosen to increase the laser illumination area greater than 0.8 cm^2 used in Chapter 3 to facilitate production of larger planar LGUS waves. The specified parallelism and surface flatness of the parallel window were < 5 arc seconds and 63.3 nm, respectively. The CAD drawing and the mock source were refined in discussion with Engineering Services, and then the source seen in Figure 6-6 was fabricated.

The stand-off distance between the back end of the glass disc and fibre end inside the aluminium housing was not long enough to illuminate a bigger area of the CPN surface. Therefore, a 1500 grit ground glass optical diffuser was placed inside the aluminium body, which increased the illumination diameter to nearly 30 mm. The measured pulse energy after the diffuser and before the CPN source was 43 mJ. The laser beam pattern was determined indirectly by scanning the LGUS beam using a hydrophone (see Sec. 6.4.3).

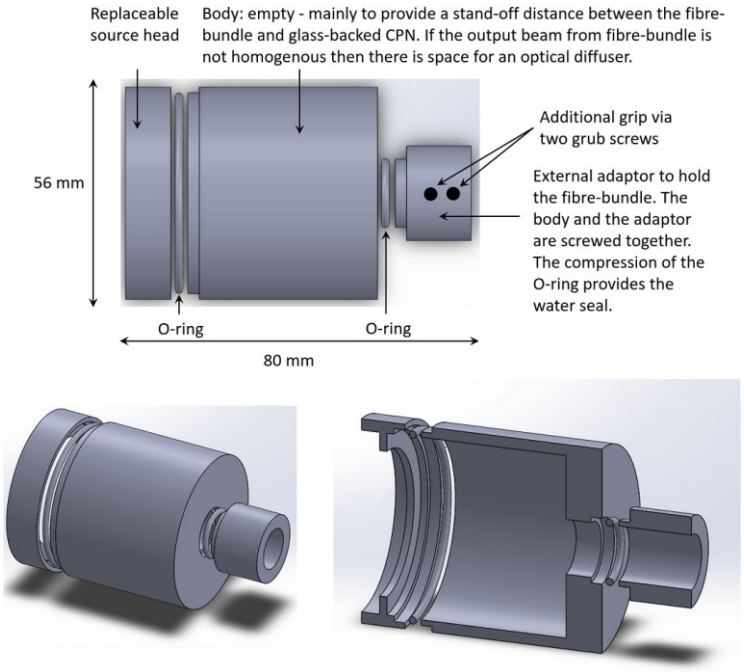

Figure 6-4: CAD drawings made using SolidWorks of the LGUS source. 3D axisymmetric models can be realised in a few simple steps using SolidWorks. A 2D profile of the resultant cross section of a quarter section is first sketched (the sketch must not cross the axis) and then the function 'revolve' is used to complete the 3D model.

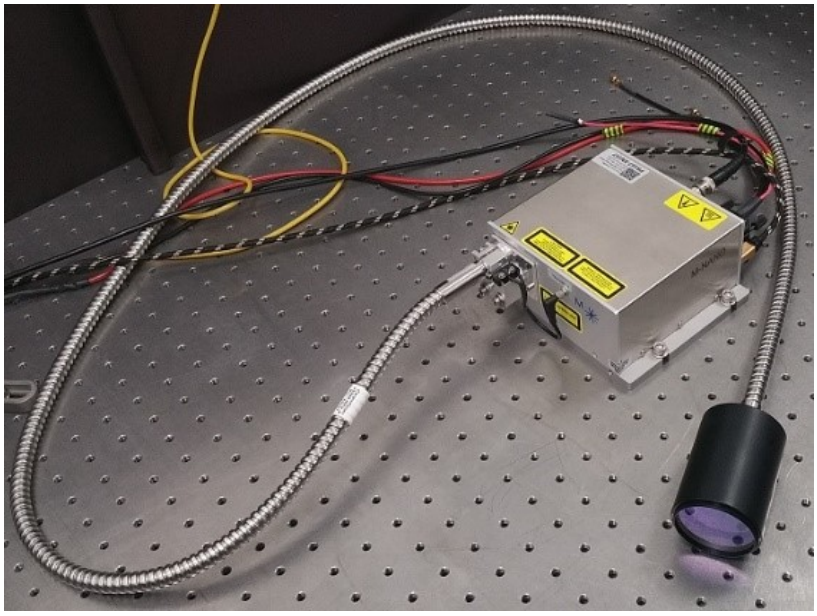

Figure 6-5: Mock LGUS source built using mechanical components purchased from Thorlabs, which is attached to the CeramOptec fibre-bundle, and M-Nano laser. The physical dimensions of the laser without the connectors are 140 × 130 × 64 mm^3. The connector holding the fibre-bundle on the laser module is equipped with a laser interlock – accidental detachment of the fibre-bundle shuts down the electrical power to the laser.

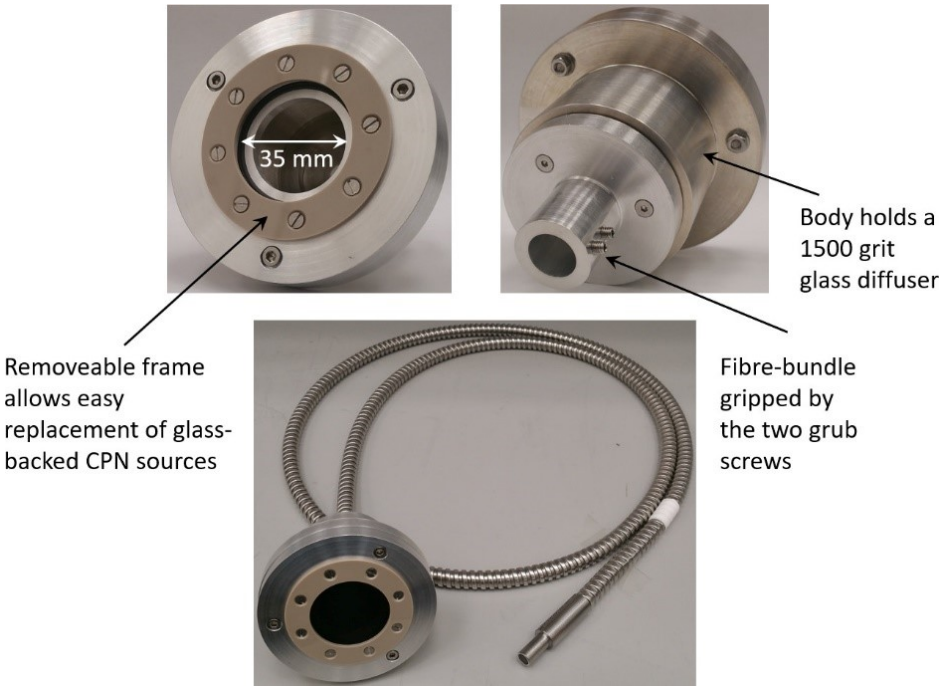

Figure 6-6: A practical LGUS source. The source element secured in the aluminium body shown in the bottom image is a PDMS-based CPN with 2.0 wt. % MWCNT and film thickness is approximately 20 µm.

6.4 Source Characterisation

Four PDMS-based glass-backed CPN sources were fabricated, which contained 2.0 wt. % MWCNT in PDMS. The four sources were sequentially numbered as Source1, Source2, Source3 and Source4. The CPN was coated using the blade film applicator and the thickness of the CPN film was approximately 20 μm. Only one aluminium body was constructed and, therefore, each source element was replaced after completing the long-time temporal stability and beam scan measurements.

6.4.1 Long-Time Temporal Stability

All four sources were tested for their temporal stability for approximately three hours. This is a reasonable length of time to complete one hydrophone calibration on the Primary Standard. The UT1604 hydrophone was positioned at 5.2 mm from the source and aligned to the maximum of the LGUS beam at the measurement plane. The hydrophone voltage signal was averaged for eight sweeps before saving each waveform. The stability was assessed by analysing the peak-positive voltages of the waveform records acquired over the three hours. Each plot shown in Figure 6-7 is normalised to the beginning of the respective measurement data set. It is seen that generally the change is within 2% compared to the measurements at the start of the test. As mentioned previously, the calibration of hydrophone requires two measured waveforms which are acquired consecutively: one from the hydrophone itself and the other from calibrated interferometer. Therefore, the effect of small short-term variations over a 10-min period tend to average out. This is further demonstrated in Sec. 6.5.2 in which the measurement standard error of the spectral ratios (amplitude ratios of the Fourier transform of the LGUS signals) computed from two membrane hydrophones in the LGUS field are comparable to that of secondary standard hydrophone calibrations.

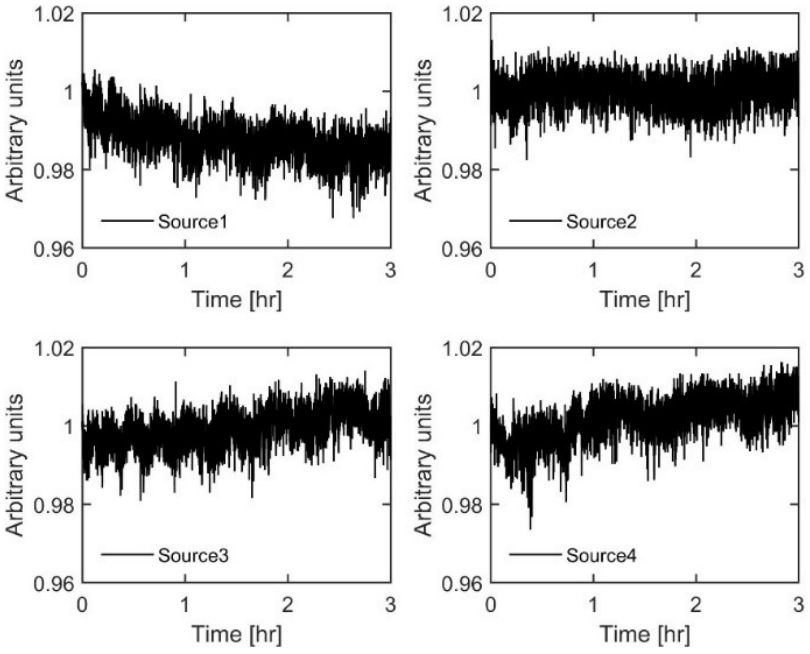

Figure 6-7: Temporal stability plots of four PDMS-based glass-backed CPN sources.

The 2% change in the LGUS output over a three-hour period seen in all four CPN sources was thought to be due to the heating of water via heating of the CPN source, which affects the temperature dependent sensitivity of the hydrophone. In a previous measurement (see Sec. 3.4.6), the surface temperature of the PDMS-based CPN source increased from 3.4–10.8 ℃ for applied fluences in the range 10–40 mJ cm^{-2}. Since the sensitivity of the hydrophone is also temperature dependent, if the temperature of the water region between the hydrophone and the CPN source goes up then accordingly the voltage output of the hydrophone varies. Two separate temperature measurements were made in the setup used for the long-time temporal stability measurements above. A K-type thin-wire thermocouple connected to a data logger was positioned on the surface of the hydrophone's active element. The LGUS source was positioned 5.2 mm away from the hydrophone. Temperature data was logged for one hour from cold switch-on of the laser. The average temperature over one hour was 19.8 ℃ and the standard deviation was 0.02 ℃, which suggested that there no changes to the temperature of water due to LGUS source. Following this measurement, the surface temperature of the CPN source was also measured after briefly turning the laser off for ten minutes to allow the CPN to cool down. The surface temperature increased by 3.3 ℃ after one minute from cold switch-on. Though this temperature change is not negligible, it is not sufficient to heat the volume of water present between the hydrophone and the CPN source. The observed variation in the LGUS output from all four CPN sources (see Figure 6-7) is maximum within the first hour (except Source 2). Since the Grüneisen parameter is temperature dependent, the LGUS amplitude may be was affected by the local temperature changes of the CPN medium over the test duration.

6.4.2 Time-series and Spectra

The LGUS pressure-pulses and their corresponding magnitude spectra acquired from all four sources are shown in Figure 6-8. The pressure-pulses were measured at a source-sensor separation of 5.5 mm. The peak-positive pressures from the four sources ranged from 7.3–8.4 MPa and their corresponding spectra has non-negligible spectral content up to 100 MHz. The effect of the bandlimited frequency response of the UT1604 hydrophone is prominently seen in all four pressure-pulses. The practical implications of the generated pressure-pulses and bandwidths shown in Figure 6-8 is considered in Sec. 6.5.3.

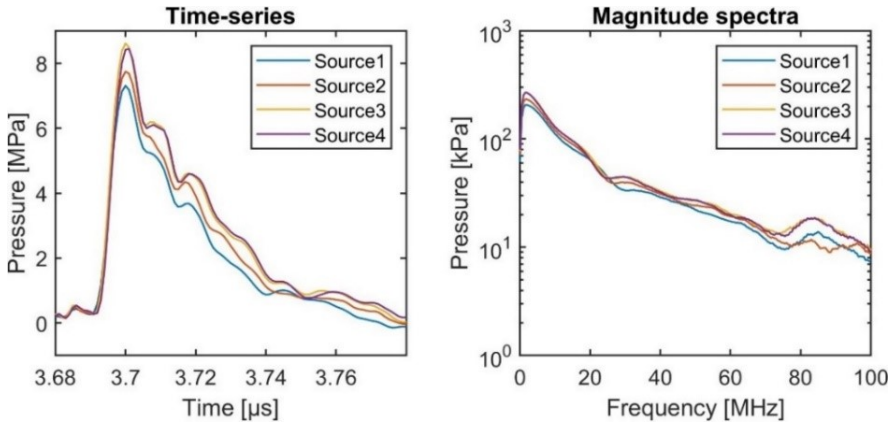

Figure 6-8: Pressure-pulses and their corresponding magnitude spectra acquired using 0.4 mm diameter UT1604 membrane hydrophone from four PDMS-based glass-backed CPN sources with 2.0 wt. % MWCNT in PDMS.

6.4.3 Beam Scans

The automated scanning tank and the LGUS source is shown in Figure 6-10. Ideally, a complete scan of the field generated by the LGUS source would be available so that both the planarity of the nominally planar part of the wavefront, as well as the significance of edge waves at various distances from the source, could be ascertained. However, such a measurement is impractical. This is because each scan position takes 3 s to complete (1 s for eight sweep averages, 1.5 s settling time between each scan step and 0.5 s overall software delay) and for a scan dimension of 30 × 30 × 10 mm^3 at 0.25 mm step size, there are 576,000 steps, which would take around 20 days to complete. Therefore, three separate scans were performed in the *x*-*y*, *x*-*z*, and *y*-*z* planes, which took around 12 hours to complete (see Figure 6-10). The closest source-hydrophone separation was 5.2 mm. Beam scans from three other sources were also completed but only in the *x*-*y* plane at the same separation (see Figure 6-11).

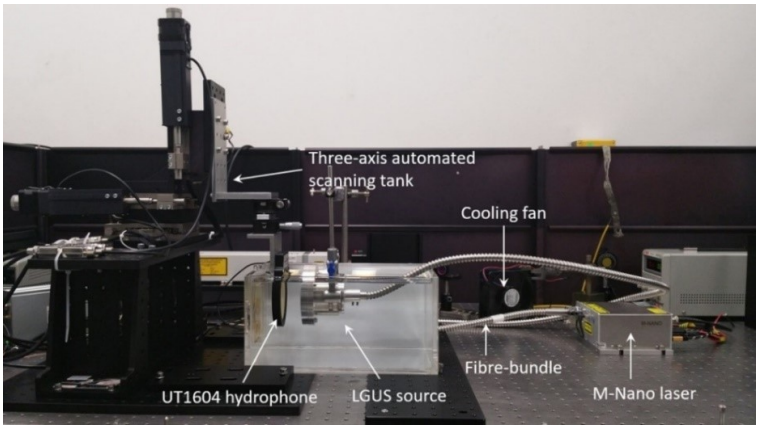

Figure 6-9: Automated scanning tank set-up with fixed LGUS source and hydrophone on the motorised stage.

The beam-area (−20 dB) was calculated using the thresholding technique described in Sec. 3.3.2. The average beam-area from the four beam scans of the four sources in the *x-y* plane was $3.19 \pm 0.08\ \mathrm{cm}^2$. The pulse energy after the diffuser was $43\ \mathrm{mJ}$, which gives a fluence of $13.4\ \mathrm{mJ\ cm}^{-2}$ on the surface of the CPN. The beam scans included only the main pulse, which was positioned in the centre of the acquisition window of 2 μs duration. This allowed to time-gate the interfacial reflections of the glass-backing arriving from the glass-air interface. Also, the lateral extent of the scan did not extend beyond the physical width of the coated surface, so it is likely that edge waves (if present) were not captured within the acquisition window. If the LGUS field was known to be linear then the measured field at a plane can be used to project the complete field in 3D using an acoustic holography method [148]. Since the LGUS waves are nonlinearly steepened, the numerical method is not straightforward and there is no accepted way of back projecting the nonlinear fields.

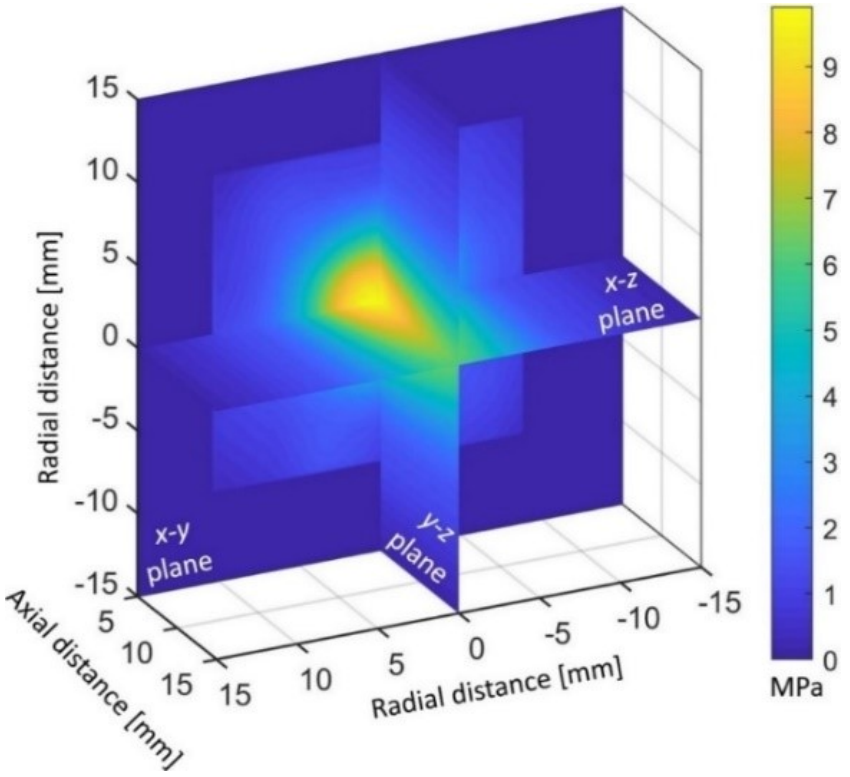

Figure 6-10: Beam scans of the LGUS field from source number 3 in x-y, x-z and y-z planes using 0.4 mm diameter UT1604 membrane hydrophone. The scan step size was 0.25 mm.

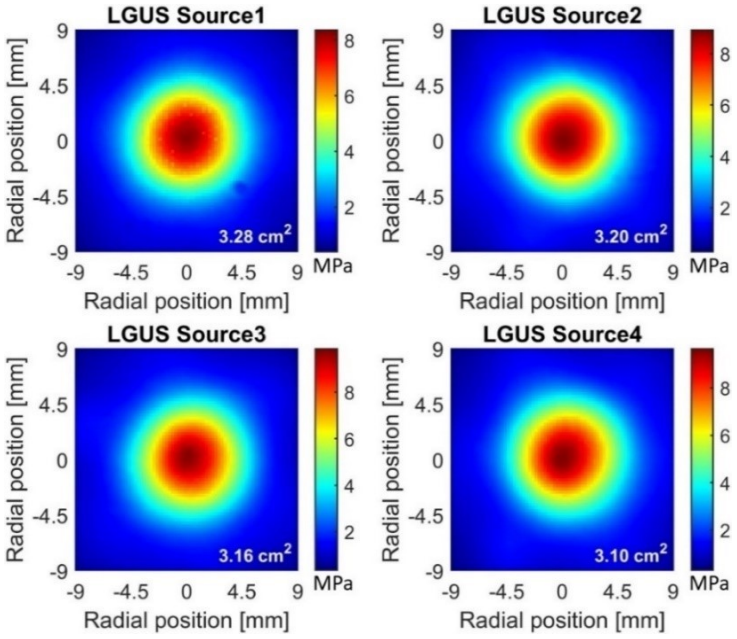

Figure 6-11: Beam scans in the *x-y* plane from all four sources measured at source-sensor separation of 5.2 mm using 0.4 mm diameter UT1604 membrane hydrophone. The scan step size was 0.25 mm. The area in each beam scan is the −20 dB beam-area.

6.5 Source Dependent Calibration Uncertainties

An essential component of hydrophone calibration is the assessment of all the uncertainties in the measurement. The three aspects of the LGUS field that contribute to the overall uncertainty in the calibration of a hydrophone are the degree of planarity, the spectral pressure amplitudes, and the long-time temporal stability. The planarity determines the spatial averaging error for a given hydrophone size, the bandwidth and sensitivity determines the SNR and the long-time temporal stability determines how reliably a measurement can be reproduced. These are discussed below.

6.5.1 Spatial Averaging Errors

The distorted waveform model discussed in Sec. 1.1.3.3 was used to calculate the spatial averaging corrections (inverse of the spatial averaging errors) for three membrane hydrophones whose geometrical diameters were 0.2, 0.4 and 0.6 mm. All three hydrophones were uncoated coplanar membrane types from Precision Acoustics Ltd whose nominal membrane thickness was 16 µm. The distorted waveform model requires two frequency dependent parameters to estimate the correction: the effective hydrophone diameter and the −6 dB beam-width measured using the same hydrophone. The effective hydrophone diameter, $d_{\mathrm{eff}}(f)$ for the three hydrophones were calculated using the empirical relationship for membrane hydrophones [123]:

$$d_{\text{eff}}(f) = 2 \times \sqrt{a_g^2 + \frac{1}{4f^2}}, \tag{6.1}$$

where, a_g is the nominal geometrical radius and f is the frequency in MHz.

The equations of the distorted waveform model from Chapter 1 are re-cast here for convenience. The empirical relationship of the spatial averaging correction, δ_{SA} is

$$\delta_{\text{SA}} = 1 + \frac{0.3}{(\alpha_{\text{SA}}^2 - 0.3)}, \tag{6.2}$$

where,

$$\alpha_{\text{SA}} = \frac{\text{measured} - 6 \text{ dB beam width}}{\text{effective hydrophone diameter}}. \tag{6.3}$$

The effective hydrophone diameters, $d_{\text{eff}}(f)$, calculated using Eq. (1.32) for 0.2-, 0.4- and 0.6-mm diameter hydrophones, are shown in Figure 6-12. Also, shown in the same figure are the measured −6 dB beam-widths through the beam maximum at a source-sensor separation of 5.2 mm, which correspond to the LGUS beam of Source3. The frequency dependent beam-widths were obtained from the magnitude spectra of each waveform recorded along the line scan in *x* and *y*-axes. The calculated spatial averaging corrections for the three hydrophones are shown in Figure 6-13. For comparison, the corrections for a 0.5 mm diameter hydrophone in a 10 MHz nonlinearly steepened focused field are in the range of 2–14% for harmonic frequencies in the range of 10–60 MHz.

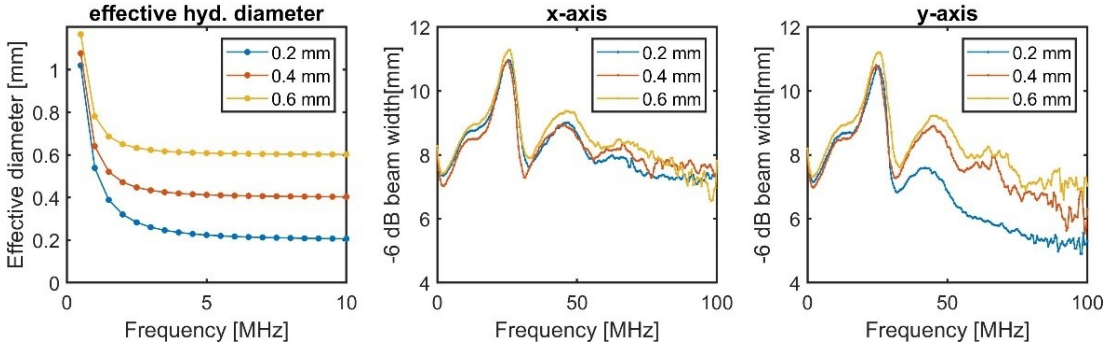

Figure 6-12: Effective diameters calculated using Eq. (1.32) for 0.2-, 0.4- and 0.6-mm diameter membrane hydrophones. The effective diameters are plotted only up to a frequency of 10 MHz since the values converge to the geometrical values beyond 10 MHz. The spectral beam-widths were measured using each hydrophone at the position of the beam maximum at a source-sensor separation of 5.2 mm in the LGUS beam of Source3.

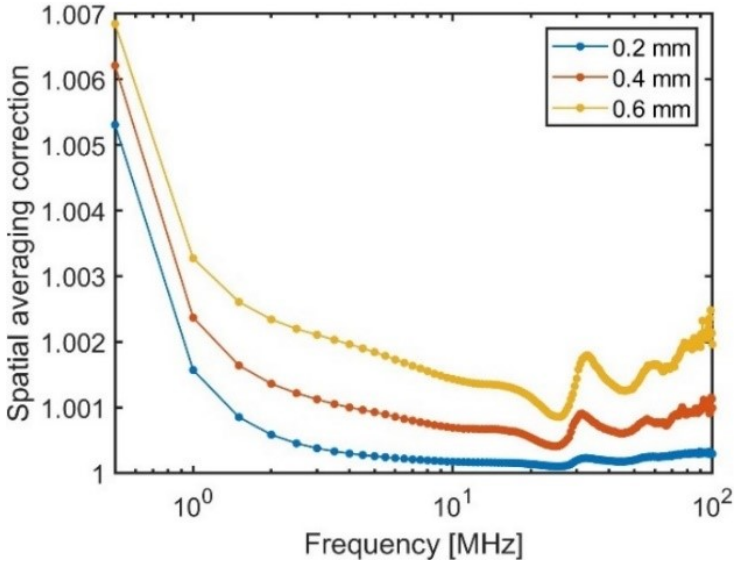

Figure 6-13: Spatial averaging corrections for 0.2-, 0.4- and 0.6-mm diameter membrane hydrophones are shown. The corrections were calculated from the average spectral beam-widths measured in x and y-axes at a source-sensor separation of 5.2 mm in the LGUS beam of Source3. The effective hydrophone diameters for the three membrane hydrophones were calculated using Eq. (1.32).

There are a couple of observations to note from the plots of the spectral beam-widths in Figure 6-12. Firstly, there are peaks and troughs, which are suspected to arise from the interfacial reflections of the LGUS pulse within the thin CPN film. The peaks and troughs in the beam-widths are consistent whether pressure-pulses or voltage-pulses are used in the analysis. Since only the UT1604 hydrophone response was extrapolated up to 110 MHz, therefore, the spectral beam-widths in Figure 6-12 were obtained using the hydrophone voltage measurements. The approximate frequencies at which the first two peaks appear are 24 and 48 MHz, respectively and the troughs appearing after the first peak are at 35 and 59 MHz, respectively. The polarity of the reflected wave within the CPN film at the CPN-glass and CPN-water interfaces are all positive because the acoustic impedance of CPN is lower than glass and water (see Sec. 3.4.1). Therefore, it is possible that these interfacial reflections constructively add-up at certain frequencies whose wavelengths correspond to a multiple of the CPN film thickness. The measured thickness of the CPN film coated on glass of Source3 was 20.0 ± 1.3 μm. The first corresponding interfacial reflection at the CPN-water interface, which arrives at the hydrophone after the main pulse should be separated by approximately 41.3 ns for a CPN sound-speed of 968 m s^{-1} [110]. Because of the undulations present in the trailing side of both the pressure-pulse (see Figure 6-8) and the voltage pulse, a clear distinction is not possible. Nevertheless, the non-smooth nature of the beam-widths is unimportant as long as the smallest beam-width is large enough to be planar across the active element of a given hydrophone.

The second observation is that the beam-widths in the *x* and *y* directions are not identical beyond 50 MHz. Also, the beam-widths of the 0.2 mm hydrophone were consistently found, in repeated measurements, to be lower in the *y*-axis compared to the 0.4 mm and 0.6 mm hydrophones. This can be more clearly seen in Figure 6-14, where the spectral line profiles for all the three hydrophones are plotted for *x* and *y*-axes. A set of beam-scan measurements were completed using the 0.2 mm hydrophone in which the LGUS source was positioned at two axes of rotations of 0° and 90°. The resulting beam-widths were nearly identical and did not suggest a distortion in the laser illumination. Another possible explanation to this could be due to the asymmetry in the circular sensing element of all the three hydrophones. This could be a plausible explanation because the hydrophone element is not perfectly circular especially at the location where the signal carrying electrodes are attached to the disc electrodes. During spot-poling, some areas around the junction of the electrodes also become polarised due to fringe fields produced by the high electric fields used in poling [154]. Consequently, IEC 62127-1 [20] standard recommends making spatial averaging corrections measurement in two orientations i.e., one along the long electrode axis of the hydrophone and another perpendicular to the long electrodes axis to account for any asymmetries of the hydrophone electrode.

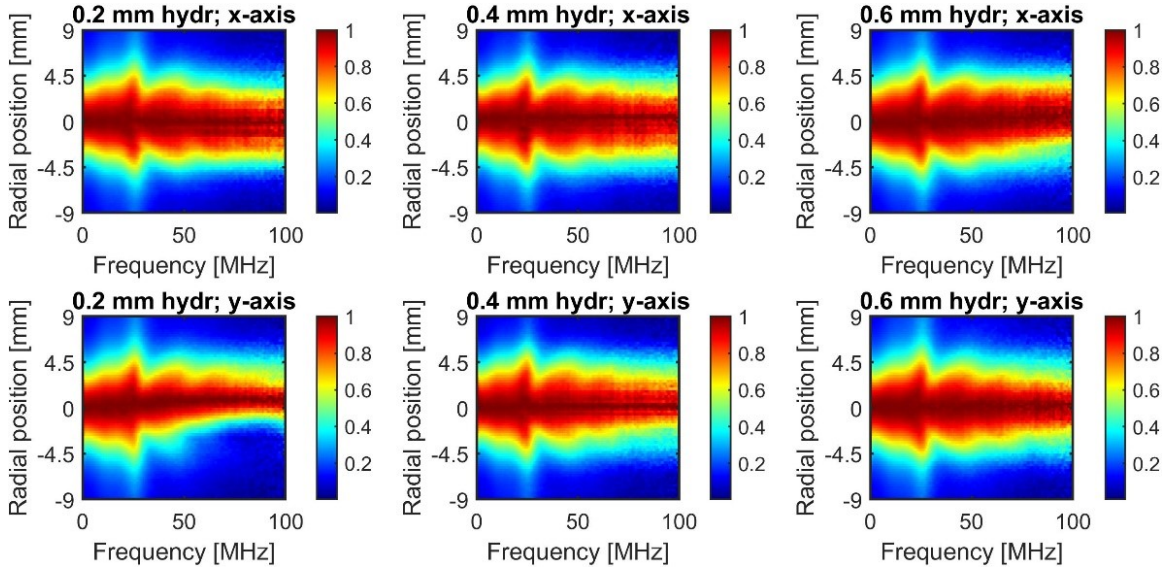

Figure 6-14: Spectral line profiles measured using 0.2-, 0.4- and 0.6-mm diameter membrane hydrophones in *x* and *y*-axes. The line profiles correspond to the maximum amplitude of the LGUS beam of Source3 at a source-sensor separation of 5.2 mm. The spectral amplitudes at each frequency is normalised to the maximum value of that frequency.

6.5.2 Measurement Repeatability

The long-time temporal stability has already been discussed in Sec. 6.4.1. Here the impact of the temporal stability is assessed via a set of comparison measurements using 0.2-, 0.4- and 0.6-mm diameter membrane hydrophones. The hydrophone signals were measured in the LGUS beam of Source1 at a source-sensor separation of 7.4 mm (or 5 μs time-of-flight). For these measurements, the automated scanning tank of the Primary Standard hydrophone calibration setup was used. In this setup, the hydrophone is on a stationary mount and the transducer is attached to a mount with a three-axis linear translation stage, as well as one rotation and one tip-tilt stage to aid angular adjustments in two orthogonal directions.

The alignment of the hydrophone to the maximum of the beam in the measurement plane was achieved by checking for the maximum of the hydrophone voltage (peak-positive) in two orthogonal directions i.e., *x* and *y*-axes. First, a line scan was performed in the *x*-axis, and the transducer was aligned to the maximum in that line scan. Next, the manual rotational stage was used to check for angular alignments. The process was repeated several times until no further adjustments were required. The process was then repeated for the *y*-axis. After a few repetitions in both axes an alignment was achieved with the maximum of the beam. Once the alignment process was completed, a hydrophone signal was acquired and this process was repeated five more times, which is normally done in a calibration to ensure measurements are independent of each other. The entire process was repeated using the other two hydrophones. This measurement sequence departs from how a hydrophone calibration is performed on the Primary Standard at NPL. For the calibration, the measurement sequence alternates between the hydrophone and pellicle displacement. Here, doing all the repeat measurements on one hydrophone in a sequence is likely to increase the random uncertainty in the measurement assuming there are temporal instabilities with the LGUS source. This is a more rigorous check of the long-time stability as drifts in the temporal stability would systematically shift the ratios with respect to the measurements made on the first hydrophone. However, no such behaviour was observed.

Standard error or Type A uncertainty, which is commonly used terminology in measurement uncertainty evaluation was computed on the spectral ratios from six repeat measurements for a pair of hydrophones i.e., 0.4 mm over 0.2 mm, 0.6 mm over 0.2 mm, and 0.6 mm over 0.4 mm. An example voltage spectrum for each hydrophone and the calculated Type A uncertainties are shown in Figure 6-15 and Figure 6-16, respectively. The Type A uncertainties up to 60 MHz are less than 2%, which is comparable to the quality of measurements on the Secondary Standard hydrophone calibration setup in which the calibration of an unknown hydrophone is obtained via a comparison to a reference hydrophone. The Type A uncertainties beyond 60 MHz and up to 100 MHz steadily increase to a maximum of 4%. These Type A uncertainties are low and comparable to those obtained from a piezoelectric transducer, which suggest that the observed long-time temporal stability of the LGUS sources is not a concern during calibrations.

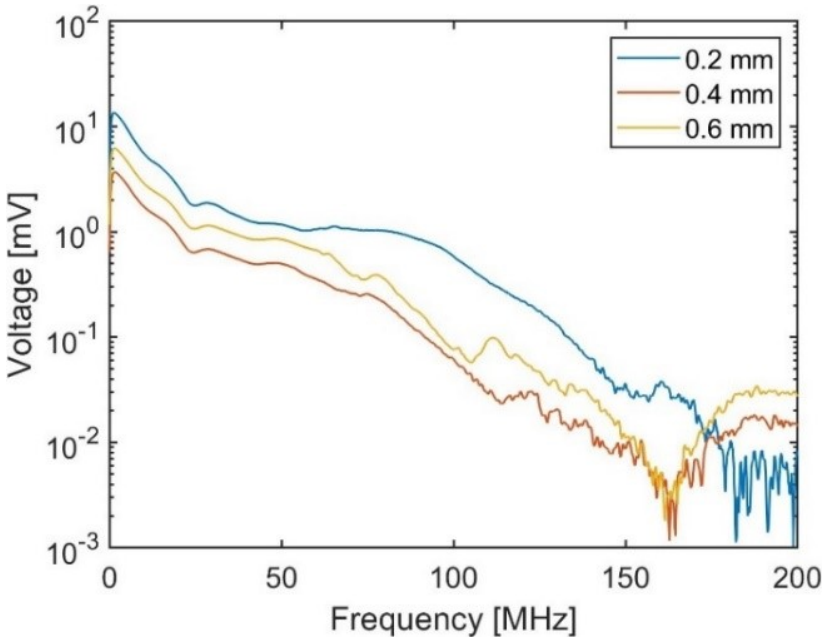

Figure 6-15: Hydrophone voltage spectrum of 0.2-, 0.4- and 0.6-mm diameter membrane hydrophones. Each hydrophone waveform from which this voltage spectra are calculated was recorded after performing 64 waveform averages. It is seen that the spectral amplitudes for the 0.2 mm hydrophone is higher compared to 0.4 mm and 0.6 mm hydrophones. This is because the 0.2 mm hydrophone used in the measurement repeatability was of a different model from Precision Acoustics Ltd. The membrane thickness was 12 µm with a bandwidth in excess of 100 MHz.

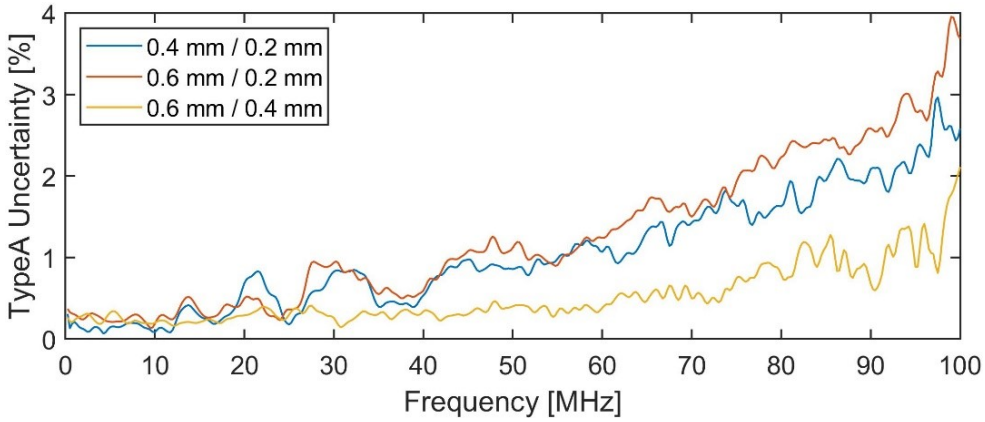

Figure 6-16: Percent Type A uncertainty in the spectral ratios for a pair of 0.2,- 0.4- and 0.6-mm diameter membrane hydrophones.

6.5.3 Signal-to-Noise

The LGUS pressure-pulse has frequencies as high as 100 MHz, as seen in the voltage spectra of the three hydrophones in Figure 6-15. However, it is not known at present whether the pressures from the LGUS source can produce a measurable displacement at 100 MHz. The current Primary Standard interferometer has not been characterised beyond 40 MHz and also its dynamic range (50 pm to 60 nm) is limited in comparison to modern heterodyne based vibrometers (few pm to more than 100 nm) [41], [52]. Therefore, only a theoretical estimate is made here to predict the maximum measurable frequency by a commercial vibrometer (UHF-120, Polytec GmbH, Waldbronn, Germany) on which the future NPL Primary Standard will be based.

The Primary Standard at Physikalisch-Technische Bundesanstalt (PTB), the German National Measurement Institute is based on UHF-120 vibrometer [41]. The standard version of the UHF-120 vibrometer has an analogue bandwidth of 600 MHz and according to the technical data sheet its displacement-amplitude resolution is 1.5 pm at 2.5 kHz resolution bandwidth (corresponds to 30 $\mathrm{fm}/\sqrt{\mathrm{Hz}}$) [155]. No information was available with regards to the frequency range over which the quoted resolution was determined i.e., 0–2.5 kHz or 99.9975–100 MHz. But, the amplitude and the phase response of the photodiode is flat up to 1.5 GHz [41]. Therefore, it is assumed the electronic noise in the vibrometer is Gaussian and that the laboratory vibration levels are small enough to not impact the displacement-amplitude resolution. Then, for a measurement bandwidth of 200 MHz, the displacement-amplitude resolution is 424 pm. This resolution in pressure at 100 MHz is 395 kPa calculated using Eq. (1.14), which is significantly high compared to 10 kPa at 100 MHz (see Figure 6-8) generated by the LGUS source. However, by performing waveform averages, the displacement-amplitude resolution can be considerably improved [51]. It is not uncommon to use 100–1000 waveform averages during hydrophone calibration. Using 1000 waveform averages may not be feasible during field mapping, but in calibration, a large number of waveform averages has no significant impact on the time taken to complete a calibration. Therefore, by taking 1000 waveform averages, the resolution can be improved by $424/\sqrt{1000}$ = 13.4 pm, which is 12.5 kPa at 100 MHz.

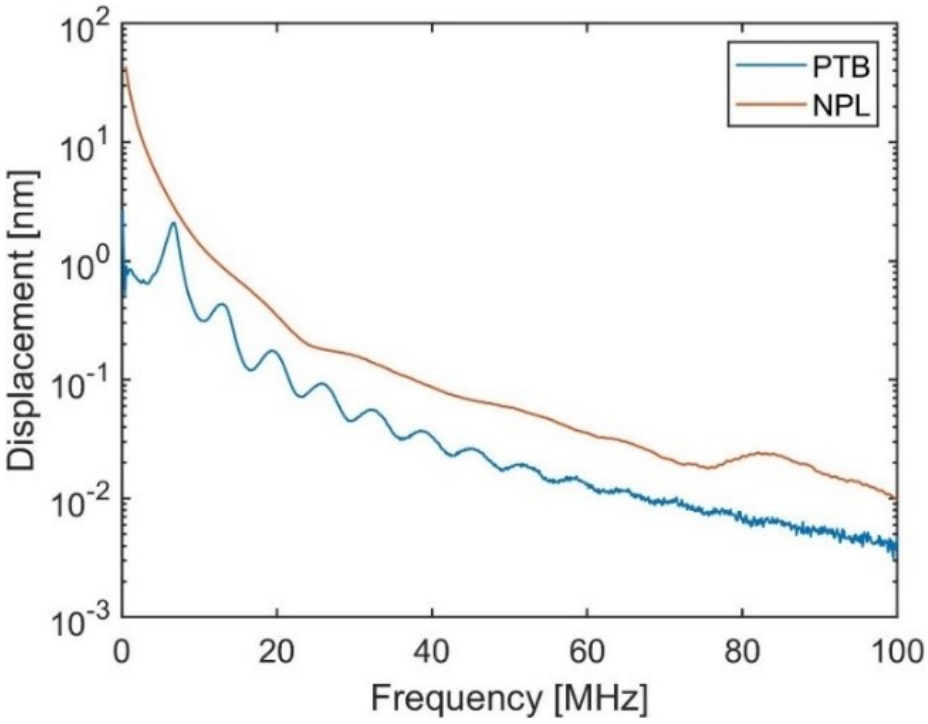

Figure 6-17: NPL: Displacement spectra calculated from the measured LGUS pressure-pulse generated by Source4 (see Figure 6-8) whose peak-positive pressure was 8.4 MPa. The frequency response of the UT1604 hydrophone used to measure the pressure-pulse was extrapolated from 60–110 MHz using a model of the hydrophone developed at NPL [125]. PTB: Displacement spectra calculated from the pellicle displacement signal measured on PTB's Primary Standard based on Polytec GmbH UHF-120 vibrometer. The source was a piezoelectric focused transducer with a nominal focal length of 50 mm, centred around 7 MHz and excited with a 1 μs voltage pulse of 236 V, which produced a peak-positive pressure of 5.5 MPa at the focus. Data reproduced with permission of the rights holder, Dr Martin Weber, and Dr Volker Wilkens of PTB.

PTB have calibrated their hydrophones using the UHF-120 vibrometer up to 100 MHz using a single focused piezoelectric transducer [41]. The peak-positive pressure of the nonlinearly steepened pressure-pulse was 5.5 MPa and which contained harmonic frequencies up to 100 MHz. A comparison is made here in order to understand the displacements levels measured by PTB's Primary Standard and the displacements contained in the pressure-pulse of the LGUS source. The laser fluence on the LGUS source is fixed and therefore no attempts were made to produce a LGUS pressure-pulse equivalent to that of PTB's focused transducer. The pressure spectra corresponding to the LGUS Source4 in Figure 6-8 was converted to displacement spectra using Eq. (1.14). A displacement spectrum was kindly provided by PTB for comparison, which corresponded to a peak-

positive pressure of 5.5 MPa. It should be noted that at PTB, the pellicle is positioned at the surface of water such that one face of the pellicle is coupled to water and other surface is coupled to air. The displacement is measured at the pellicle-air interface to avoid acousto-optic effects i.e., modulation of the refractive index of water due to passage of sound wave through the pellicle [46]. The displacement spectra shown in Figure 6-17 is not corrected for the doubling effect, which occurs at the rear side of pellicle and air interface – a pressure release boundary condition. It can be seen that the displacement levels produced in the LGUS pressure-pulse overall is at least a factor of five higher. Therefore, provided that the displacement-amplitude resolution of the vibrometer is not affected by the vibrational noise due to the laboratory environment at NPL, then it can be safely assumed that the pressure-pulse generated by the LGUS source has the potential to calibrate hydrophones up to 100 MHz.

6.6 Design Improvements

In this section, suggestions to improve on some of the characteristics of the LGUS source mentioned at the beginning of this chapter are discussed.

6.6.1 Amplitude and Bandwidth

The spectral pressure amplitudes in the frequency range of 70–100 MHz are around 10–20 kPa for a source-sensor separation of 5.2 mm. This appears to be adequate based on the theoretical estimate of the displacement-amplitude resolution of the Polytec vibrometer and also from the measurements at PTB. However, it is not known how the laboratory environment at NPL in future will affect the resolution of the vibrometer. A straightforward solution to increase the spectral amplitudes beyond 60 MHz is by decreasing the source-separation to 1 or 2 mm, which will minimise acoustic absorption and also the effect of cumulative acoustic linearity (see Sec. 4.3.2). At present the closest achievable distance is about 4 mm. This restriction is from how the front face of the LGUS is designed. The plastic frame holding the glass-backed CPN source is 2 mm thick, therefore the closest separation ever possible with this source is 2 mm. However, the overall front metallic body holding the source has a diameter of 80 mm. Since the membrane hydrophones also have a frame on the front, which means the membrane is behind the frame and depending on the manufacturer, this distance could be 2 to 5 mm. Therefore, the LGUS source cannot be positioned within the frame of the membrane hydrophone. By reducing the diameter of the front metallic body of the LGUS source a closer separation with the membrane hydrophone can be achieved.

A practical problem might occur if the source-sensor separation is 1 mm or less. This is because part of the pressure-pulse incident on the membrane hydrophone will get reflected and arrive back at the LGUS source, which in turn will again reflect and arrive back at the hydrophone. When the source-sensor separation is large enough, the reflected pulse does not fall within the acquisition window – it is time-gated out. This will not be the case if the source-sensor separation for example is

1 mm, as the reflected pulse is separated from the main pulse by only 1.4 μs. To increase the frequency resolution of the measurement, longer acquisition durations are required, which means the reflected pulse will be invariably captured. Therefore, to isolate the reflected pulse, time-gating and zero-padding will need to be performed offline before the waveforms are analysed. This is not a fundamental detrimental issue but presents a minor practical problem.

6.6.2 Laser Hazard

A potentially weak aspect of the LGUS source is the CPN layer, which is directly exposed to the environment and hence vulnerable to scratches or damage when in use. An inadvertent scratch to the CPN layer means laser light will escape through the clear scratch and the laser energy might be sufficient to put the user at risk if unnoticed. The front layer can be protected by a Parylene coat or spin coating a thin layer of PDMS. But the preferential loss of high frequencies due to acoustic absorption in the coated layer might attenuate the high-frequency pressure amplitudes to below the SNR of the vibrometer. Therefore, before each use, the coated surface must be inspected for visible scratches and if any damage is found then the user must not use the source until it is replaced with an evenly-coated CPN source.

6.7 Conclusions

In this chapter, a laser-generated, broadband, plane-wave, ultrasound source device was designed, built, and tested. Its characteristics such as pressure, bandwidth, spectral beam-widths, and long-time temporal stability were measured and assessed for their suitability as a potential source for hydrophone calibration. The CPN source consisted of 2.0 wt. % CNT dispersed in PDMS and was backed on an optical parallel glass window of 50 mm diameter and the thickness of the coated surface was around 20 μm. Four glass-backed CPN sources were fabricated for testing. The glass-backed CPN source was encased in a water-tight aluminium housing to which a laser pulse was delivered via a fibre-bundle. The optical diffuser placed inside the aluminium housing evenly homogenises the output beam of the fibre-bundle on the surface of CPN layer. The laser is a solid-state diode-pumped Q-switched system operating at 1064 nm with a PRR of 10 Hz and a pulse duration of 2.6 ns. The measured fluence on the surface of the CPN layer was 13.4 $\mathrm{mJ\ cm^{-2}}$. A laser hazard does not exist since the laser beam is completely enclosed although an inadvertent damage to the CPN coating may occur and present a hazard to the user. Contamination of water by the CPN source via increased electrical conductivity has never been observed. Nanotubes are completely encapsulated within the polymer matrix and they do not dislodge in water.

The long-time temporal stability of the ultrasound pulses emitted by the four LGUS sources tested over a period of three hours are stable to within 2%. The effect of this stability was assessed by making comparison measurements using a pair of hydrophones from a set of three different diameter membrane hydrophones. Six pressure-pulses were acquired per hydrophone after carefully aligning

the hydrophone each time to the maximum of the LGUS beam in the measurement plane. The Type A random uncertainty in the spectral ratios for any pair of two hydrophones was less than 2% up to 60 MHz with a maximum of 4% at 100 MHz. These random uncertainties are comparable to those achieved in a secondary standard hydrophone calibration. Therefore, the stability of the LGUS source is of acceptable quality for a calibration application. The LGUS source has sufficient longevity to allow a full day of measurement, which was assessed from beam scanning measurements over several days. At present, long term stability over months/years though not important is not known, but, longitudinal stability will be assessed in the future.

The planarity of the LGUS beam was assessed using a distorted waveform model for three hydrophones whose geometrical diameters were 0.2, 0.4 and 0.6 mm. The average beam-area of the LGUS field at a source-sensor separation of 5.2 mm was $3.19 \pm 0.08\ \mathrm{cm}^2$. The spectral beam-widths across the largest diameter hydrophone of 0.6 mm was found to be sufficiently large such that the resulting spatial averaging errors were below 1%.

The peak-positive pressure of the four CPN sources ranged from 7.3–8.4 MPa and their corresponding amplitude spectra had non-negligible spectral amplitudes of around 10 kPa at 100 MHz when measured at a source-sensor separation of 5.5 mm. The spectral displacement amplitudes of the LGUS pressure-pulses are at least five times larger than those produced by a focused piezoelectric transducer used by PTB. The spectral pressure amplitudes can be improved by keeping the source-sensor separation to 2–4 mm to minimise losses arising from cumulative acoustic nonlinearity and acoustic absorption in water.

All the tests conducted on the LGUS source in this chapter positively suggest that a near ideal source has been realised, which can be applied on the future Primary Standard of NPL to calibrate medical hydrophones up to 100 MHz.

Chapter 7

Conclusions and Future Work

7.1 General Conclusions

The aim of this thesis was to fabricate a laser generated, plane-wave, broadband ultrasound source device for calibrating medical hydrophones up to 100 MHz on the National Physical Laboratory's (NPL) future Primary Standard interferometer. In this thesis, such a device has been developed and tested for its suitability as a stable source of ultrasound for calibration application. In Chapter 1, the rationale behind the need for hydrophone calibrations up to 100 MHz was given, a brief overview was provided of the current Primary Standard calibration methods practised at various National Measurement Institutes, and the reasons why piezoelectric transducers are inadequate to extend the frequency range from the current limitation of 60 MHz to 100 MHz are discussed.

In Chapter 2, the physical principles of laser-generated ultrasound (LGUS) was described, a review of the fabrication methodologies of LGUS sources and the current state-of-the-art was presented. The source material primarily used for LGUS was based on a carbon-polymer nanocomposite. The optical absorption in carbon nanoparticles such as carbon nanotubes (CNT) is significantly higher than bulk forms of carbon such as graphite or graphite powder. Therefore, carbon nanoparticles have been extensively experimented with in various fabrication methodologies to increase their concentration in a polymer matrix. Historically, polydimethylsiloxane (PDMS) has been the choice of polymer matrix due to its high thermal expansion coefficient compared to other polymers. Increasing the amount of CNT in the polymer matrix increases the optical absorption. As more photons are absorbed, more heat is deposited in the optical absorption region. The increase in temperature is accompanied by an increase in pressure provided that the laser pulse heating the medium is sufficiently rapid i.e., the duration of the laser pulse would ideally be shorter than the acoustic transit time across the optical absorption depth, a condition known as the stress confinement time. If the laser pulse satisfies the stress confinement time, then the rise in pressure is maximised as the pressure pulse remains confined within the optical absorption region during the heat deposition.

Chapter 3 experimentally explored a suitable nanocomposite and reproducible source fabrication method guided by previous work in this area reported in the literature. It was demonstrated

that carbon-polymer nanocomposite (CPN) fabrication using mechanical dispersion of CNT in polymer via shear mixing is a suitable method. A thin layer of the resulting mixture was laid on laboratory grade glass slides using blade film applicator. A total of 27 variations of the CPN sources were fabricated. Three polymer types (epoxy, polyurethane (PU) and PDMS), three weight fractions (wt. %) of multi-walled CNT (MWCNT) in polymer (1.25, 2.5, and 3.5 wt. %), and three thicknesses (17–28, 51–55, and 71–85 μm) were investigated. The reason for including epoxy and PU is because the temporal stability of PDMS-based CPN sources under sustained laser excitation was not available from the literature review. Since epoxy and PU have a wide industrial use, therefore, it was initially thought that by including two additional polymers the risk in the project could be lessened. Each CPN source was tested using a 4 ns laser pulse at four fluence levels of 10, 20, 30 and 40 $\mathrm{mJ\,cm^{-2}}$. A broadband membrane hydrophone with an extrapolated sensitivity response up to 110 MHz was used to record and analyse the LGUS pulses. At a measurement location of 7.4 mm from the CPN source, the peak-positive pressure of the LGUS pulses was in the range of 1–7 MPa and the Fourier transform of the pressure-pulses at 100 MHz had a pressure amplitude of up to 10 kPa for applied fluences in the range 10–40 $\mathrm{mJ\,cm^{-2}}$.

Generally, the CPN sources fabricated in this thesis did not the satisfy stress confinement time for a given laser of 4 ns duration. Therefore, the pressure wave starts to leave the optical absorption region whilst that region is still being heated by the laser pulse. Also, an absolute comparison of CPN sources (different polymer types and fixed CNT wt. %) based on their photoacoustic conversion efficiency cannot be made with arbitrary laser pulse durations. This is because the stress relaxation occurs at different time rates for each polymer, which is governed by the polymer's sound-speed. Furthermore, for absolute comparison the transmission coefficients of the CPN into the medium to which it is coupled also should be considered.

The CPN sources are typically more absorbing than the pure matrix material, therefore, the thickness should ideally be equal to the optical absorption depth or where possible as thin as practically achievable to minimise unnecessary acoustic absorption and loss of high frequencies. Also, for a fixed CNT wt. %, increasing the fluence caused the pressure amplitude to increase and similarly for a fixed fluence, increasing the CNT wt. % caused the pressure amplitude to increase since in both cases varying one of the parameters increases the energy deposition in the optical absorption region. However, PDMS-based CPN sources always produced higher pressure amplitudes because the stress confinement duration is longer in PDMS due to its lower sound-speed compared to epoxy and PU.

The stability of the CPN sources under sustained laser excitation revealed that generally epoxy and to a lesser extent PU-based CPN sources were unsuitable as a stable source of ultrasound. The failure in most cases was the detachment of the CPN film from glass occurring mostly at a fluence of 30 $\mathrm{mJ\,cm^{-2}}$. A combination of water ingression and tensile stresses at the CPN-glass interface were possibly the two reasons for debonding of the CPN film from glass. PDMS-based CPN

sources were found to be most stable. A steady change in LGUS output was observed from all stable CPN sources after the first 30 min at a rate of 1% per hour. Simple assumptions suggest that this steady decrease would have a negligible consequence on hydrophone calibration.

The peak-positive pressures measured from the CPN sources at the measured location were found to be nonlinearly dependent on the laser fluence and the bandwidth scaled inversely proportionally to the peak-pressure. This was hypothesised to be due to the effect of nonlinear propagation of LGUS pulse in water whose effect increases with both pressure amplitude and propagation distance. Also, the effect of bandlimited sensitivity response of the hydrophone caused undulations to appear on the trailing side of the deconvolved hydrophone pressure pulse. These two effects were explored further using numerical simulations in Chapter 4 using k-Wave.

In Chapter 4, simulations were performed using k-Wave in 1D since, at the measurement distance of 7.4 mm, the spatial averaging effects – the effect of diffraction – for a hydrophone element of 0.2 mm diameter were negligible. Therefore, the acoustic field relative to the hydrophone element size was considered planar. To investigate the effect of wave steepening caused by nonlinear propagation, stress-confined initial pressure distributions (IPD) of various amplitudes were propagated. The nonlinear propagation was tested only in a homogeneous medium of water since it is the medium in which majority of the wave propagation occurs. Wave steepening due to cumulative acoustic nonlinearity was observed for all stress-confined amplitudes in the range 5.6–44.8 MPa. The degree to which the wave steepening occurred was dependent on both the pressure amplitude and propagation distance. The effect of nonlinear propagation on the −6 dB bandwidth (*BW6*) was most significant. The *BW6* bandwidth was highest in the linear region but when the pressure-pulse transformed to a nonlinear pulse, the preferential loss of high frequencies caused the pulse to broaden. Hence, the *BW6* bandwidth decreased with increasing nonlinearity, which agreed with the measurements in Chapter 3.

The effect of the bandlimited hydrophone response on the measured pressure-pulses was investigated by propagating stress-confined IPD in a layered media. The layered media consisted of glass, epoxy-based CPN and water. The IPD propagated from within the CPN medium was recorded in the water medium and convolved with the complex sensitivity response of the hydrophone. The resulting model-derived voltage time-series showed a good temporal shape agreement with measurement i.e., undulations on the trailing side of the hydrophone voltage time-series from a nominally identical CPN source. The undulations appear because the hydrophone's sensitivity response is limited when compared to the spectral content of the LGUS pressure-pulse.

The aim of Chapter 5 was to increase the bandwidth from CPN sources by changing the backing material on which the CPN was deposited. It is known that under conditions of stress confinement, for an acoustically reflective backing such as glass, temporally, the wave exiting the CPN medium into water will be of twice the duration taken by the acoustic wave to transit across the thickness of the CPN layer. If the CPN source is backed on an acoustically matched backing i.e., the

same polymer matrix used in fabricating the CPN, then one half of the LGUS propagates in the polymer-backed medium and the other half of the LGUS propagates in water. Therefore, a matched source would produce twice the bandwidth compared to a reflective source. This physical effect was originally assumed to extend even when there was no stress confinement. However, it was found experimentally that the backing material has an interesting effect on the characteristics of the LGUS pressure-pulse when the laser pulse duration is greater than the stress confinement duration. When the laser pulse is longer than the stress confinement duration, one half of the LGUS wave reflected by the glass back to the CPN medium and the continued optical deposition of heat by the laser pulse caused increased build-up of pressure. The total acoustic pressure reached was therefore higher than in the absence of the reflection i.e., in case of PDMS-backed sources.

A linear analytical model was developed to obtain an intuitive understanding of the effects of backing material on the amplitude of the LGUS from CPN sources. A solution was obtained, using a Green's function approach, firstly for the case of a backing-absorber half-spaces followed by three-layer medium consisting of backing-absorber-water layers. The obtained solution was compared with k-Wave simulations. This linear model assumed no acoustic absorption. Subsequently, a k-Wave simulation including acoustic absorption and nonlinearity was performed, which confirmed the experimental observations that when stress confinement is not satisfied, the acoustic reflections from the reflective backing contributes to increased build-up of pressure in the CPN medium.

The increased pressure output from glass-backed sources compared to PDMS-backed sources, regardless of the stress of confinement meant that the spectral pressure amplitudes of glass-backed sources were always higher. Therefore, despite the fact that *BW6* metric for PDMS-backed sources is larger than glass-backed sources, the increased pressure output from glass-backed sources compensates for the effect of lower *BW6* observed in glass-backed sources.

In Chapter 6, a laser-generated, broadband, plane-wave, ultrasound source device was designed, built, and tested. Its characteristics such as pressure, bandwidth, spectral beam-widths, long-time temporal stability were measured and assessed for its suitability as a potential source for hydrophone calibration. The CPN source consisted of 2.0 wt. % CNT dispersed in PDMS and was backed on an optical parallel glass window of 50 mm diameter and the thickness of the coated surface was around 20 μm. Four glass-backed CPN sources were fabricated for testing. The glass-backed CPN source was encased in a water-tight aluminium housing to which a laser pulse was delivered via a fibre-bundle. The optical diffuser placed inside the aluminium housing evenly homogenises the output beam of the fibre-bundle on the surface of CPN layer. The laser is a solid-state diode-pumped Q-switched system operating at 1064 nm with a PRR of 10 Hz and a pulse duration of 2.6 ns. The measured fluence on the surface of the CPN layer was 13.4 $\mathrm{mJ\,cm^{-2}}$. A laser hazard did not exist since the laser beam is completely enclosed although an inadvertent damage to the CPN coating may occur and present a hazard to the user. Contamination of water by the CPN source via increased

electrical conductivity has never been observed. Nanotubes are completely encapsulated within the polymer matrix and they do not dislodge in water.

The long-time temporal stability of the ultrasound pulses emitted by the four LGUS sources tested over a period of three hours are stable to within 2%. The effect of this stability was assessed by making comparison measurements using a pair of hydrophones from a set of three different diameter membrane hydrophones. Six pressure-pulses were acquired per hydrophone after carefully aligning the hydrophone each time to the maximum of the LGUS beam in the measurement plane. The Type A random uncertainty in the spectral ratios for any pair of two hydrophones was less than 2% up to 60 MHz with a maximum of 4% at 100 MHz. These random uncertainties are comparable to those achieved in a secondary standard hydrophone calibration. Therefore, the stability of the LGUS source is of acceptable quality for a calibration application. The LGUS source has sufficient longevity to allow a full day of measurements, which was assessed from beam scanning measurements over several days.

During the long-time temporal stability test, the surface temperature of the CPN coating increased by 3.3℃ from the ambient temperature of water at 19.9 ℃ after 1-min from the switch-on of the laser. But this increase in temperature was not sufficient to heat the volume of water between the hydrophone and the LGUS source. Therefore, the temperature dependent sensitivity of the hydrophone was not affected during the long-time temporal stability measurements.

The planarity of the LGUS beam was assessed using a distorted waveform model for three hydrophones whose geometrical diameters were 0.2, 0.4 and 0.6 mm. The average beam-area of the LGUS field at a source-sensor separation of 5.2 mm was $3.19 \pm 0.08\ \mathrm{cm}^2$. The spectral beam-widths across the largest diameter hydrophone of 0.6 mm was found to be sufficiently large such that the resulting spatial averaging errors were below 1%.

The peak-positive pressure of the four CPN sources ranged from 7.3–8.4 MPa and their corresponding amplitude spectra had non-negligible spectral amplitudes of around 10 kPa at 100 MHz when measured at a source-sensor separation of 5.5 mm. The spectral pressure amplitudes can be improved by decreasing the source-sensor separation to 2–4 mm to minimise losses arising from nonlinear propagation and acoustic absorption in water.

All the tests conducted on the LGUS source device built and tested in this thesis positively suggest that a near ideal source has been realised, which can be applied on the future Primary Standard of NPL to calibrate medical hydrophones up to 100 MHz.

7.2 Future Work

In the measurement setup at NPL, the pellicle is normally positioned in the far-field of a plane-piston transducer or at the acoustic focus of a focusing transducer. The vibration of the pellicle, which is completely submerged in water is measured by reflecting the laser from the back of the pellicle and is

aligned with the acoustic axis of the transducer. There is one systematic correction that must be accounted for based on the acousto-optic interaction, which arises specific to the measurement setup. Acousto-optic effect is the modulation of the optical refractive index of water due to the ultrasound wave causes the modulation of the optical path-length, which a laser doppler vibrometer (LDV) registers as an additional velocity component [156]. The acousto-optic corrections, which is applied to the derived pressure measurement from the LDV, is negligibly small. This is because when the optical beam is passing through a sinusoidal plane-wave along the direction of wave propagation, the light passes through an equal number of both compressional and rarefactional half-cycles, the areas under which are equal and hence the net path length change is zero. For pressure amplitudes as high as 10 MPa, where the sinusoidal wave becomes nonlinear with compressional part being narrower than the rarefactional part, the calculated correction was still only 0.05% [157]. However, the LGUS pulse is quasi-unipolar and nonlinearly steepened. Therefore, the additional velocity component persists in the LDV measurements and should be corrected.

On the future Primary Standard which will be based on a commercial LDV, the acousto-optic corrections can be obtained experimentally. For this to be possible, some modification to the existing setup (or a new setup) may be required. In the current setup, the pellicle is completely submerged in the water and hence the LDV measurements are subject to acousto-optic effects. If the pellicle is positioned on the surface of water, one side of the pellicle is beneath the water surface and the other side is in contact with air (air-backed pellicle). In this case there are no acousto-optic interactions because the laser beam does not travel through the acoustic field in water, and the LDV measures only the vibration of the pellicle. However, since the pellicle is now loaded with water on one side and air on the other – a pressure-release boundary condition – this results in doubling of the measured velocity, which should be taken into consideration. Following air-backed pellicle measurements, the level of the water is then raised so that the pellicle is backed with water and the effect of acousto-optic interactions come into play. The difference of air-backed and water-backed pellicle measurements should reveal the values for the acousto-optic corrections, which can be subsequently applied to all future measurements of LDV employing laser-generated ultrasound source device to calibrate hydrophones.

Appendix

```
function threeLayerCpnSplitKwaveSim(i)
% k-Wave split-model function script to test the effect of CPN source
% backing for laser pulse durations from stress confined to unconfined case
% This script requires installation of MATLAB 2018 or later and k-Wave
% toolbox. k-Wave is free software available under the terms of the GNU
% Lesser General Public License as published by the Free Software
% Foundation, either version 3 of the License, or (at your option)
% any later version.
% USAGE:
%     threeLayerCpnSplitKwaveSim(i)
%
% INPUTS:
%     'i' takes integer values from 1 to 18, which corresponds to laser
%     pulse durations from 0.25 ns to 600 ns stored in array vector
%     'time_pulse_vec'.
%
% OUTPUTS:
%     The script saves time-series simulation data to several text files.
% Note: The simulation was run on NPL's high-performance computing facility
% located at University of Cambridge. Each computer node is comprised of
% 2x16 cores, Intel Skylake 2.6 GHz processors with 6 GB per processor. For
% 600 ns pulse duration the total simulation time was approximately
% 12 hours and required allocation of 196 GB of RAM.
%%%%%%%%%%%%%%%%%%%%%%%% Begin: Step 1 Simulation %%%%%%%%%%%%%%%%%%%%%%%%
% array of full-width half-maximum (FWHM) laser pulse durations
time_pulse_vec = [0.25, 0.5, 1, 2, 4, 8, 10, 12, 16, 20, 30, 50,...
    75, 100, 150, 200, 400, 600]; % [ns]
```

```
% create the computational grid
Nx = 4096; % number of grid points in the x (row) direction
dx = 125e-9; % grid point spacing in the x direction [m]
kgrid = kWaveGrid(Nx, dx);
% define the source mask next to the backing
source_size = 176; % 22 um
backing_size = round(Nx/2); % 0.251 mm
source.p_mask = zeros(Nx, 1);
source.p_mask(backing_size + 1: backing_size + source_size) = 1;
% heterogeneous medium properties
% sound-speed
medium.sound_speed = zeros(Nx, 1); % [m / s]
% PDMS backing layer
medium.sound_speed(1:backing_size) = 1050;
% PDMS-based carbon-polymer nanocomposite layer
medium.sound_speed(backing_size+1:backing_size+source_size) = 945;
% Water layer, 20 C temperature
medium.sound_speed(backing_size+source_size+1:Nx) = 1482.5;
% density
medium.density = zeros(Nx, 1); % [kg / m^3]
% PDMS backing layer
medium.density(1:backing_size) = 965;
% PDMS-based carbon-polymer nanocomposite layer
medium.density(backing_size+1:backing_size+source_size) = 868;
% Water layer, 20 C temperature
medium.density(backing_size+source_size+1:Nx) = 998.2;
% add in acoustic absorption
medium.alpha_coeff = zeros(Nx, 1); % [dB/(MHz^2 cm)]
% PDMS backing layer
medium.alpha_coeff(1:backing_size) = 2.17e-1;
% PDMS-based carbon-polymer nanocomposite layer
medium.alpha_coeff(backing_size+1:backing_size+source_size) = 2.17e-1;
% Water layer, 20 C temperature
```

```
medium.alpha_coeff(backing_size+source_size+1:Nx) = 2.17e-3;
medium.alpha_power = 2; %
% define the properties of the propagation medium
medium.sound_speed_ref = medium.sound_speed(backing_size+1); % [m/s] PDMS
% set the simulation time
t_end = 8 * kgrid.x_size / medium.sound_speed_ref;
% define the time array
cfl = 0.002;
kgrid.makeTime(medium.sound_speed, cfl, t_end);
% define source time pulse: Gaussian profile
offset = 2 * time_pulse_vec(i) * 1e-9; % [s]
variance = time_pulse_vec(i) * 1e-9 / (2 * sqrt(2 * log(2))); % [s]
% total duration of Gaussian
pulse_duration = time_pulse_vec(i) * 1e-9 * 4;
% time vector corresponding to Gaussian pulse
t_array = 0:kgrid.dt:pulse_duration-kgrid.dt;
% compute Gaussian time pulse
source_signal = ...
    exp(-0.5*((t_array - offset)/variance).^2) / (variance*sqrt(2*pi));
% spatial decay of pressure
mu = 53e3; % optical absorption coefficient [1/m]
% compute spatial exponential profile
space_decay = exp(-mu * dx * (0:(source_size - 1)));
% create input signal
source.p = space_decay.' * source_signal;
% create a sensor mask next to source
pos = 2 + backing_size + source_size;
sensor.mask = zeros(Nx, 1);
sensor.mask(pos) = 1;
% amount of pressure to be added in per sample in the time series
% (remove k-Wave's built-in scaling and divide by the sum of the source
% weights)
% 0.95 below corresponds to 5% optical loss in PDMS backing
```

```
94 stress_confined_amplitude = 0.25e6 / 2 * 0.95; % [Pa]
95 scaling = stress_confined_amplitude / sum(source_signal) / cfl;
96 source.p = source.p * scaling;
97 % run the simulation
98 input_args = {'PlotSim', false, 'DataCast', 'single', ...
99     'PMLAlpha', medium.alpha_power, 'PMLSize', 400, ...
100     'PlotScale', 'auto'};
101 sensor_data_no_backing = ...
102     kspaceFirstOrder1D(kgrid, medium, source, sensor, input_args{:});
103 % re-define the source mask next to the backed boundary
104 source_size_backed = 176; % 22 um
105 backing_size = round(Nx/2); % 0.251 mm
106 source.p_mask = zeros(Nx, 1);
107 source.p_mask(backing_size + 1: backing_size + source_size_backed) = 1;
108 % re-define (add in the backing) heterogeneous medium properties
109 % sound-speed
110 medium.sound_speed = zeros(Nx, 1); % [m / s]
111 % Glass backing layer
112 medium.sound_speed(1:backing_size) = 5640;
113 % PDMS-based carbon-polymer nanocomposite layer
114 medium.sound_speed(backing_size+1:backing_size+source_size_backed) = 965;
115 % Water layer, 20 C temperature
116 medium.sound_speed(backing_size+source_size_backed+1:Nx) = 1482.5;
117 % density
118 medium.density = zeros(Nx, 1); % [kg / m^3]
119 % Glass backing layer
120 medium.density(1:backing_size) = 2240;
121 % PDMS-based carbon-polymer nanocomposite layer
122 medium.density(backing_size+1:backing_size+source_size_backed) = 868;
123 % Water layer, 20 C temperature
124 medium.density(backing_size+source_size_backed+1:Nx) = 998.2;
125 % add in acoustic absorption
126 medium.alpha_coeff = zeros(Nx, 1); % [dB/(MHz^2 cm)]
```

```
% Glass backing layer
medium.alpha_coeff(1:backing_size) = 2.17e-4;

% PDMS-based carbon-polymer nanocomposite layer
medium.alpha_coeff(backing_size+1:backing_size+source_size_backed) = 2.17e-1;
% Water layer, 20 C temperature
medium.alpha_coeff(backing_size+source_size_backed+1:Nx) = 2.17e-3;
medium.alpha_power = 2; %
% spatial decay of pressure
mu = 53e3; % optical absorption coefficient [1/m]
% compute spatial exponential profile
space_decay_backed = exp(-mu * dx * (0:(source_size_backed - 1)));
% weight the time array at each point by an exponential in space
% create input signal
source.p = space_decay_backed.' * source_signal;
% create a sensor mask
pos = 2 + backing_size + source_size_backed;
sensor.mask = zeros(Nx, 1);
sensor.mask(pos) = 1;
% amount of pressure to be added in per sample in the time series
% (remove k-Wave's built-in scaling and divide by the sum of the source
% weights)
stress_confined_amplitude = 0.25e6 / 2;        % Pascals
scaling = stress_confined_amplitude / sum(source_signal) / cfl;
source.p = source.p * scaling;
% run the simulation again
sensor_data_backing = ...
    kspaceFirstOrder1D(kgrid, medium, source, sensor, input_args{:});
% Save three-layer simulation data to a text file
file_name = ['TLM_AllAbs_0p25MPa_22um_22um_pd_', ...
    num2str(time_pulse_vec(i)),'ns', '.txt'];
dlmwrite(file_name,...
    [kgrid.t_array; sensor_data_no_backing; sensor_data_backing]',...
```

```
159     'delimiter', '\t', 'precision', 12);
160 %%%%%%%%%%%%%%%%%%%%%%%% End of Step 1 Simulation %%%%%%%%%%%%%%%%%%%%%%%%
161 %%%%%%%%%%%%%%%%%%%%%%%% Begin: Step 2 Simulation %%%%%%%%%%%%%%%%%%%%%%%%
162 % Water-only propagation 'dirichlet' boundary condition
163 % Format three-layer data for forward simulation in water
164 % read three-layer simulation data from saved text file
165 data = dlmread(file_name, '\t');
166 % re-sample three-layer simulation data to a lower 'dt'
167 P = 1; % resampling factor
168 Q = 100; % resampling factor
169 unbacked_data = resample(data(:, 2), P, Q);
170 backed_data = resample(data(:, 3), P, Q);
171 % resampled 'dt'
172 Nt = numel(backed_data);
173 dt_new = kgrid.dt * 100;
174 t_array_resampled = linspace(0, dt_new*Nt, Nt)';
175 % save downsampled data
176 resampled_data = [t_array_resampled, unbacked_data, backed_data];
177 file_name_prefix = file_name(1:end-4);
178 file_name_resampled = ([file_name_prefix, '_resampled.txt']);
179 dlmwrite(file_name_resampled, resampled_data, '\t');
180 % clear few kWave variables as these will need to be redfined for
181 % water-only simulation
182 vars = {'Nx', 'dx','kgrid', 'medium', 'source', 'sensor', ...
183     'sensor_data_no_backing', 'cfl', 'sensor_data_backing', ...
184     'source_signal', 't_array', 'pos', 'pulse_duration', ...
185     'dt_new', 'input_args'};
186 clear(vars{:})
187 % create the computational grid
188 Nx = 32768; % number of grid points in the x (row) direction
189 dx = 250e-9; % grid point spacing in the x direction [m]
190 kgrid = kWaveGrid(Nx, dx);
191 % create the time array of 5 us duration and 'dt' of 5 ps
```

```
t_forward = linspace(0, 5e-06, 1000000)';
kgrid.t_array = t_forward;
% define the properties of the propagating medium
medium.sound_speed  = 1482.5; % [m / s]
medium.density = 998.2; % [kg / m^3]
medium.alpha_coeff = 2.17e-3; % power-law absorption coeff [dB/(MHz^2 cm)]
medium.alpha_power = 2; % power-law absorption exponent
medium.BonA = 5.2; % B/A of water for nonlinear propagation
% define an interior source
source.p_mask = zeros(Nx, 1);
source.p_mask(800, :) = 1; % 0.2 mm from the left-edge
% define sensor to record time-series at 2.2, 3.7 and 5.2 mm from the left
% edge of the source mask
sensor.mask = zeros(Nx, 1);
% [800 + 14800 = 15600 or 3.7mm from source]
sensor.mask([9600; 15600; 21600], :) = 1;
% enforce, rather than add, measured time-series pressure values
source.p_mode = 'dirichlet';
% set the input arguments
input_args = {'PMLInside', true, 'PMLSize', 60, ...
    'PMLAlpha', medium.alpha_power, 'PlotPML', false, 'Smooth', false, ...
    'PlotScale', 'auto', 'DataCast', single, 'PlotSim', false};
% assign unbacked sensor data to source.p
source.p = unbacked_data';
% run the forward simulation - unbacked case
sensor_data_unbacked = ...
    kspaceFirstOrder1D(kgrid, medium, source, sensor, input_args{:});
% assign backed sensor data to source.p
source.p = backed_data';
% run the forward simulation - backed case
sensor_data_backed = ...
    kspaceFirstOrder1D(kgrid, medium, source, sensor, input_args{:});
% save water-only propagation data for the backed and unbacked case
```

```
225 file_name_forward = strrep(file_name_resampled, 'resampled', 'nl_forward');
226 forward_data = [kgrid.t_array', sensor_data_unbacked', sensor_data_backed'];
227 dlmwrite(file_name_forward, forward_data, '\t');
228 %%%%%%%%%%%%%%%%%%%%%%%% End of Step 2 Simulation %%%%%%%%%%%%%%%%%%%%%%%%
228 % End of function script
```

References

[1] T. L. Szabo, “Introduction,” in *Diagnostic Ultrasound Imaging: Inside Out*, Elsevier, 2004, p. 576.

[2] J. V. Robertson and K. G. Baker, “A Review of Therapeutic Ultrasound: Effectiveness Studies,” *Phys. Ther.*, vol. 81, no. 7, pp. 1339–1350, Jul. 2001.

[3] D. Miller *et al.*, “Overview of Therapeutic Ultrasound Applications and Safety Considerations,” *J. ultrasound Med.*, vol. 31, no. 4, pp. 623–634, 2012.

[4] J. E. Kennedy, G. R. Ter Haar, and D. Cranston, “High intensity focused ultrasound: surgery of the future?,” *Br. J. Radiol.*, vol. 76, no. 909, pp. 590–599, 2003.

[5] W. G. Pitt, G. A. Husseini, and B. J. Staples, “Ultrasonic drug delivery – a general review,” *Expert Opin. Drug Deliv.*, vol. 1, no. 1, pp. 37–56, 2004.

[6] S. Schandelmaier *et al.*, “Low intensity pulsed ultrasound for bone healing: systematic review of randomized controlled trials,” *BMJ*, vol. 356, p. j656, 2017.

[7] A. Fomenko, C. Neudorfer, R. F. Dallapiazza, S. K. Kalia, and A. M. Lozano, “Low-intensity ultrasound neuromodulation : An overview of mechanisms and emerging human applications,” *Brain Stimul.*, vol. 11, no. 6, pp. 1209–1217, 2018.

[8] K. K. Shung, “High Frequency Ultrasonic Imaging,” *J. Med. Ultrasound*, vol. 17, no. 1, pp. 25–30, 2009.

[9] “FUJIFILM VisualSonics, ‘MicroScanTM Transducers,’” 2018. [Online]. Available: https://www.visualsonics.com/product/transducers/ms-series-transducers. [Accessed: 21-Dec-2018].

[10] “ArcScan Insight® 100 System,” 2018. [Online]. Available: https://arcscan.com/products/. [Accessed: 21-Dec-2018].

[11] “DermaScan C CORTEX TECHNOLOGY,” 2018. [Online]. Available: http://www.analyse-skin.com/dermatology/dermascan-live-ultrasound/. [Accessed: 21-Dec-2018].

[12] M. S. Canney, M. R. Bailey, L. A. Crum, V. A. Khokhlova, and O. A. Sapozhnikov, “Acoustic characterization of high intensity focused ultrasound fields: A combined measurement and modeling approach,” *J. Acoust. Soc. Am.*, vol. 124, no. 4, pp. 2406–2420, 2008.

[13] G. Ter Haar, “Ultrasound bioeffects and safety,” *Proc. Inst. Mech. Eng. Part H J. Eng. Med.*, vol. 224, no. 2, pp. 363–373, Feb. 2010.

[14] T. J. Esward and S. P. Robinson, “Extending the frequency range of the National Physical Laboratory primary standard laser interferometer for hydrophone calibrations to 60 MHz,” *IEEE Trans. Ultrason. Ferroelectr. Freq. Control*, vol. 46, no. 3, pp. 737–744, 1999.

[15] IEC 62359:2010/AMD1:2017, *Amendment 1 - Ultrasonics - Field characterization - Test methods for the determination of thermal and mechanical indices related to medical diagnostic ultrasonic fields*. Geneva, Switzerland: International Electrotechnical Commission, 2017.

[16] IEC 60601-2-37:2007+AMD1:2015 CSV, *Medical electrical equipment - Part 2-37: Particular requirements for the basic safety and essential performance of ultrasonic medicaldiagnostic and monitoring equipment*. Geneva, Switzerland: International Electrotechnical Commission, 2015.

[17] IEC 60601-2-62:2013, *Medical electrical equipment - Part 2-62: Particular requirements for the basic safety and essential performance of high intensity therapeutic ultrasound (HITU) equipment*. Geneva, Switzerland: International Electrotechnical Commission, 2015.

[18] S. M. Nagle *et al.*, "Challenges and regulatory considerations in the acoustic measurement of high-frequency (>20 MHz) ultrasound," *J. Ultrasound Med.*, vol. 32, no. 11, pp. 1897–1911, 2013.

[19] E. Jafarzadeh and A. N. Sinclair, "Non-linear Wave Propagation and Safety Standards for Diagnostic Ultrasound Devices," *Ultrasound Med. Biol.*, vol. 45, no. 1, pp. 11–20, Jan. 2019.

[20] IEC 62127-1:2007+AMD1:2013, *Amendment 1—Ultrasonics— Hydrophones—Part 1: Measurement and characterization of medical ultrasonic fields up to 40 MHz*. Geneva, Switzerland: International Electrotechnical Commission, 2013.

[21] P. Morris, A. Hurrell, A. Shaw, E. Zhang, and P. Beard, "A Fabry–Pérot fiber-optic ultrasonic hydrophone for the simultaneous measurement of temperature and acoustic pressure," *J. Acoust. Soc. Am.*, vol. 125, no. 6, pp. 3611–3622, Jun. 2009.

[22] S. M. Howard, "Calibration of reflectance-based fiber-optic hydrophones," *IEEE Int. Ultrason. Symp. IUS*, vol. 2016-Novem, no. 2, pp. 2–5, 2016.

[23] E. Martin, E. Z. Zhang, J. A. Guggenheim, P. C. Beard, and B. E. Treeby, "Rapid Spatial Mapping of Focused Ultrasound Fields Using a Planar Fabry-Pérot Sensor," *IEEE Trans. Ultrason. Ferroelectr. Freq. Control*, vol. 64, no. 11, pp. 1711–1722, 2017.

[24] R. C. Preston, S. P. Robinson, B. Zeqiri, T. J. Esward, P. N. Gélat, and N. D. Lee, "Primary calibration of membrane hydrophones in the frequency range 0.5 MHz to 60 MHz," *Metrologia*, vol. 36, no. 4, pp. 331–343, 1999.

[25] B. Zeqiri and A. D. Bond, "The influence of waveform distortion on hydrophone spatial-averaging corrections—Theory and measurement," *J. Acoust. Soc. Am.*, vol. 92, no. 4, pp. 1809–1821, 1992.

[26] S. Robinson, R. Preston, M. Smith, and C. Millar, "PVDF reference hydrophone development in the UK-from fabrication and lamination to use as secondary standards," *IEEE Trans. Ultrason. Ferroelectr. Freq. Control*, vol. 47, no. 6, pp. 1336–1344, Nov. 2000.

[27] D. R. Bacon, "Characteristics of a pvdf Membrane Hydrophone for Use in the Range 1-100 MHz," *IEEE Trans. Sonics Ultrason.*, vol. 29, no. 1, pp. 18–25, 1982.

[28] P. N. Gélat, R. C. Preston, and A. M. Hurrell, "Development, validation and publication of a complete model for hydrophone/amplifier transfer characteristics," Teddington, 2001.

[29] R. A. Smith and D. R. Bacon, "A multiple-frequency hydrophone calibration technique," *J. Acoust. Soc. Am.*, vol. 87, no. 5, pp. 2231–2243, 1990.

[30] A. M. Hurrell and S. Rajagopal, "The Practicalities of Obtaining and Using Hydrophone Calibration Data to Derive Pressure Waveforms," *IEEE Trans. Ultrason. Ferroelectr. Freq. Control*, vol. 64, no. 1, pp. 126–140, 2017.

[31] A. Hurrell, "Voltage to pressure conversion: are you getting `phased' by the problem?," *J. Phys. Conf. Ser.*, vol. 1, pp. 57–62, 2004.

[32] V. Wilkens and C. Koch, “Amplitude and phase calibration of hydrophones up to 70 MHz using broadband pulse excitation and an optical reference hydrophone,” *J. Acoust. Soc. Am.*, vol. 115, no. 6, pp. 2892–2903, 2004.

[33] K. A. Wear, P. M. Gammell, S. Maruvada, Y. Liu, and G. R. Harris, “Improved measurement of acoustic output using complex deconvolution of hydrophone sensitivity,” *IEEE Trans. Ultrason. Ferroelectr. Freq. Control*, vol. 61, no. 1, pp. 62–75, 2014.

[34] V. Wilkens, S. Sonntag, and O. Georg, “Robust spot-poled membrane hydrophones for measurement of large amplitude pressure waveforms generated by high intensity therapeutic ultrasonic transducers,” *J. Acoust. Soc. Am.*, vol. 139, no. 3, pp. 1319–1332, 2016.

[35] B. Fay, G. Ludwig, C. Lankjaer, and P. A. Lewin, “Frequency response of PVDF needle-type hydrophones,” *Ultrasound Med. Biol.*, vol. 20, no. 4, pp. 361–366, 1994.

[36] A. Hurrell, “Geophysical modelling techniques and their benefit to ultrasonic measurement tools,” *J. Phys. Conf. Ser.*, vol. 1, pp. 44–49, 2004.

[37] P. Morris, P. Beard, and A. Hurrell, “Development of a 50MHz optical fibre hydrophone for the characterisation of medical ultrasound fields,” *Proc. - IEEE Ultrason. Symp.*, vol. 3, pp. 1747–1750, 2005.

[38] E. Zhang, J. Laufer, and P. Beard, “Backward-mode multiwavelength photoacoustic scanner using a planar Fabry-Perot polymer film ultrasound sensor for high-resolution three-dimensional imaging of biological tissues,” *Appl. Opt.*, vol. 47, no. 4, p. 561, 2008.

[39] J. Staudenraus and W. Eisenmenger, “Fibre-optic probe hydrophone for ultrasonic and shock-wave measurements in water,” *Ultrasonics*, vol. 31, no. 4, pp. 267–273, 1993.

[40] A. Arvengas, K. Davitt, and F. Caupin, “Fiber optic probe hydrophone for the study of acoustic cavitation in water,” *Rev. Sci. Instrum.*, vol. 82, no. 3, 2011.

[41] M. Weber and V. Wilkens, “Using a heterodyne vibrometer in combination with pulse excitation for primary calibration of ultrasonic hydrophones in amplitude and phase,” *Metrologia*, vol. 54, no. 4, pp. 432–444, 2017.

[42] IEC 62127-2:2007+AMD1:2013+AMD2:2017 CSV, *Ultrasonics - Hydrophones - Part 2: Calibration for ultrasonic fields up to 40 MHz*. Geneva, Switzerland: International Electrotechnical Commission, 2017.

[43] IEC 61161:2013, *Ultrasonics - Power measurement - Radiation force balances and performance requirements*. Geneva, Switzerland: International Electrotechnical Commission, 2013.

[44] G. Ludwig and K. Brendel, “Calibration of Hydrophones Based on Reciprocity and Time Delay Spectrometry,” *IEEE Trans. Ultrason. Ferroelectr. Freq. Control*, vol. 35, no. 2, pp. 168–174, 1988.

[45] E. G. Oliveira, R. P. B. Costa-Felix, and J. C. Machado, “Primary reciprocity-based method for calibration of hydrophone magnitude and phase sensitivity: Complete tests at frequencies from 1 to 7 MHz,” *Ultrasonics*, vol. 58, pp. 87–95, 2015.

[46] D. R. Bacon, “Primary Calibration of Ultrasonic Hydrophones Using Optical Interferometry,” *IEEE Trans. Ultrason. Ferroelectr. Freq. Control*, vol. 35, no. 2, pp. 152–161, 1988.

[47] C. Koch and W. Molkenstruck, “Primary calibration of hydrophones with extended frequency range 1 to 70 MHZ using optical interferometry,” *IEEE Trans. Ultrason. Ferroelectr. Freq. Control*, vol. 46, no. 5, pp. 1303–1314, 1999.

[48] Y. Matsuda, M. Yoshioka, T. Uchida, and T. Kikuchi, “Absolute calibration of membrane hydrophones up to 40 MHz in ultrasonic far-field,” *IEEE Int. Ultrason. Symp. IUS*, pp. 374–377, 2012.

[49] P. Yang, G. Xing, and L. He, “Calibration of high-frequency hydrophone up to 40 MHz by heterodyne interferometer,” *Ultrasonics*, vol. 54, no. 1, pp. 402–407, 2014.

[50] S. Rajagopal *et al.*, “Report on BIPM/CIPM key comparison CCAUV.U-K4: absolute calibration of medical hydrophones in the frequency range 0.5 MHz to 20 MHz,” *Metrologia*, vol. 53, no. 1A, pp. 09004–09004, 2016.

[51] C Rembe; G Siegmund; H Steger; M Wörtge, “Optical Inspection of Microsystems,” Wolfgang Osten, Ed. Boca Raton: Taylor and Francis Books, 2006, pp. 245–292.

[52] C. Rembe, S. Boedecker, A. Dräbenstedt, F. Pudewills, and G. Siegmund, “Heterodyne laser-Doppler vibrometer with a slow-shear-mode Bragg cell for vibration measurements up to 1.2 GHz,” in *Proc. SPIE 7098, Eighth International Conference on Vibration Measurements by Laser Techniques: Advances and Applications*, 2008, no. June 2008, p. 70980A.

[53] K. A. Wear, S. Member, C. Baker, and P. Miloro, “Directivity and Frequency-Dependent Effective Sensitive Element Size of Needle Hydrophones : Compared With Measurements,” *IEEE Trans. Ultrason. Ferroelectr. Freq. Control*, vol. 65, no. 10, pp. 1781–1788, 2018.

[54] E. G. Radulescu, P. A. Lewin, A. Nowicki, and W. A. Berger, “Hydrophones’ effective diameter measurements as a quasi-continuous function of frequency,” *Ultrasonics*, vol. 41, no. 8, pp. 635–641, 2003.

[55] IEC 62127-3:2007+AMD1:2013 CSV, *Ultrasonics - Hydrophones - Part 3: Properties of hydrophones forultrasonic fields up to 40 MHz*. Geneva, Switzerland: International Electrotechnical Commission, 2013.

[56] R. C. Preston, D. R. Bacon, and R. A. Smith, “Calibration Of Medical Ultrasonic Equipment-Procedures And Accuracy Assessment,” *IEEE Trans. Ultrason. Ferroelectr. Freq. Control*, vol. 35, no. 2, pp. 110–121, 1988.

[57] R. A. Smith, “Are hydrophones of diameter 0.5 mm small enough to characterise diagnostic ultrasound equipment?,” *Phys. Med. Biol.*, vol. 34, no. 11, pp. 1593–1607, Nov. 1989.

[58] M. P. Cooling, V. F. Humphrey, and V. Wilkens, “Hydrophone area-averaging correction factors in nonlinearly generated ultrasonic beams,” *J. Phys. Conf. Ser.*, vol. 279, no. 1, 2011.

[59] K. A. Wear, “Considerations for Choosing Sensitive Element Size for Needle and Fiber-Optic Hydrophones I: Spatiotemporal Transfer Function and Graphical Guide,” *IEEE Trans. Ultrason. Ferroelectr. Freq. Control*, vol. 66, no. 2, pp. 318–339, 2019.

[60] K. A. Wear and Y. Liu, “Considerations for Choosing Sensitive Element Size for Needle and Fiber-Optic Hydrophones II: Experimental Validation of Spatial Averaging Model,” *IEEE Trans. Ultrason. Ferroelectr. Freq. Control*, vol. 66, no. 2, pp. 340–347, 2019.

[61] A. G. Bell, “Upon Production and Reproduction of Sound by Light,” *J. Soc. Telegr. Eng.*, vol. 9, no. 34, pp. 404–426, 1880.

[62] W. Smith, “Effect of Light on Selenium During the Passage of An Electric Current,” *Nature*, vol. 7, no. 173, pp. 303–303, Feb. 1873.

[63] L. E. Scruby and C. B. Drain, *Laser Ultrasonics Techniques and Applications*. Bristol: Adam Hilger, 1990.

[64] F. J. M. Harren, J. Mandon, and S. M. Cristescu, “Photoacoustic Spectroscopy in Trace Gas

Monitoring," *Encycl. Anal. Chem.*, 2012.

[65] L. V. Wang, Ed., *Photoacoustic Imaging and Spectroscopy*. Boca Raton: CRC Press, 2009.

[66] G. Paltauf and P. E. Dyer, "Photomechanical processes and effects in ablation," *Chem. Rev.*, vol. 103, no. 2, pp. 487–518, 2003.

[67] B. Cox, J. G. Laufer, S. R. Arridge, and P. C. Beard, "Quantitative spectroscopic photoacoustic imaging: a review," *J. Biomed. Opt.*, vol. 17, no. 6, p. 061202, 2012.

[68] L. V. Wang, "Tutorial on Photoacoustic Microscopy and Computed Tomography," *IEEE J. Sel. Top. Quantum Electron.*, vol. 14, no. 1, pp. 171–179, 2008.

[69] T. Stratoudaki, J. A. Hernandez, M. Clark, and M. G. Somekh, "Cheap optical transducers (CHOTs) for narrowband ultrasonic applications," *Meas. Sci. Technol.*, vol. 18, no. 3, pp. 843–851, 2007.

[70] R. M. White, "Generation of elastic waves by transient surface heating," *J. Appl. Phys.*, vol. 34, no. 12, pp. 3559–3567, 1963.

[71] M. M. Tilleman, "Optical attenuation and plasmon generation on a metal grid," in *Proc. SPIE 8457, Plasmonics: Metallic Nanostructures and Their Optical Properties X*, 2012, no. October 2012, p. 84572I.

[72] M. Polyanskiy, "RefractiveIndex.INFO," 2018. [Online]. Available: https://refractiveindex.info/?shelf=main&book=Al&page=Rakic. [Accessed: 03-Feb-2019].

[73] J. P. Holman, *Heat Transfer*, 10th ed. McGraw-Hill Education, 2009.

[74] F. A. Duck, *Physical Properties of Tissues*, 1st ed. Academic Press, 1990.

[75] National Physical Laboratory, "The speed and attenuation of sound," 2018. [Online]. Available: http://www.kayelaby.npl.co.uk/general_physics/2_4/2_4_1.html. [Accessed: 08-Feb-2019].

[76] S. Kang, Y. Yoon, J. Kim, and W. Kim, "Thermoelastic response of thin metal films and their adjacent materials," *Appl. Phys. Lett.*, vol. 102, no. 2, 2013.

[77] T. Lee and L. J. Guo, "Highly Efficient Photoacoustic Conversion by Facilitated Heat Transfer in Ultrathin Metal Film Sandwiched by Polymer Layers," *Adv. Opt. Mater.*, vol. 5, no. 2, pp. 1–9, 2017.

[78] M. C. Finlay *et al.*, "Through-needle all-optical ultrasound imaging in vivo: A preclinical swine study," *Light Sci. Appl.*, vol. 6, no. 12, pp. e17103-7, 2017.

[79] E. Vannacci, S. Granchi, L. Belsito, A. Roncaglia, and E. Biagi, "Wide bandwidth fiber-optic ultrasound probe in MOMS technology: Preliminary signal processing results," *Ultrasonics*, vol. 75, pp. 164–173, 2017.

[80] S. Noimark *et al.*, "Polydimethylsiloxane Composites for Optical Ultrasound Generation and Multimodality Imaging," *Adv. Funct. Mater.*, vol. 28, no. 9, pp. 1–16, 2018.

[81] E. J. Alles *et al.*, "Video-rate all-optical ultrasound imaging," *Biomed. Opt. Express*, vol. 9, no. 8, p. 3481, 2018.

[82] B. Y. Hsieh, S. L. Chen, T. Ling, L. J. Guo, and P. C. Li, "All-optical scanhead for ultrasound and photoacoustic imaging-Imaging mode switching by dichroic filtering," *Photoacoustics*, vol. 2, no. 1, pp. 39–46, 2014.

[83] H. W. Baac *et al.*, "Carbon-nanotube optoacoustic lens for focused ultrasound generation and

high-precision targeted therapy," *Sci. Rep.*, vol. 2, pp. 1–8, 2012.

[84] M. D. Brown, D. I. Nikitichev, B. E. Treeby, and B. T. Cox, "Generating arbitrary ultrasound fields with tailored optoacoustic surface profiles," *Appl. Phys. Lett.*, vol. 110, no. 9, pp. 1–5, 2017.

[85] S.-L. Chen, "Review of Laser-Generated Ultrasound Transmitters and Their Applications to All-Optical Ultrasound Transducers and Imaging," *Appl. Sci.*, vol. 7, no. 1, p. 25, 2016.

[86] T. Lee, H. W. Baac, Q. Li, and L. J. Guo, "Efficient Photoacoustic Conversion in Optical Nanomaterials and Composites," *Adv. Opt. Mater.*, vol. 6, no. 24, p. 1800491, Dec. 2018.

[87] E. Roduner, "Size matters: why nanomaterials are different," *Chem. Soc. Rev.*, vol. 35, no. 7, p. 583, 2006.

[88] Q. Li, C. Liu, X. Wang, and S. Fan, "Measuring the thermal conductivity of individual carbon nanotubes by the Raman shift method," *Nanotechnology*, vol. 20, no. 14, 2009.

[89] Z. Han and A. Fina, "Thermal conductivity of carbon nanotubes and their polymer nanocomposites: A review," *Prog. Polym. Sci.*, vol. 36, no. 7, pp. 914–944, 2011.

[90] E. Biagi, F. Margheri, and D. Menichelli, "Efficient laser-ultrasound generation by using heavily absorbing films as targets," *IEEE Trans. Ultrason. Ferroelectr. Freq. Control*, vol. 48, no. 6, pp. 1669–1680, 2001.

[91] T. Buma, M. Spisar, and M. O'Donnell, "High-frequency ultrasound array element using thermoelastic expansion in an elastomeric film," *Appl. Phys. Lett.*, vol. 79, no. 4, pp. 548–550, 2001.

[92] S. Noimark *et al.*, "Carbon-Nanotube–PDMS Composite Coatings on Optical Fibers for All-Optical Ultrasound Imaging," *Adv. Funct. Mater.*, vol. 26, no. 46, pp. 8390–8396, 2016.

[93] R. K. Poduval *et al.*, "Optical fiber ultrasound transmitter with electrospun carbon nanotube-polymer composite," *Appl. Phys. Lett.*, vol. 110, no. 22, p. 223701, May 2017.

[94] C. Moon, X. Fan, K. Ha, and D. Kim, "Generation of planar blast waves using carbon nanotubes-poly-dimethylsiloxane optoacoustic transducer," *AIP Adv.*, vol. 7, no. 1, 2017.

[95] Z. Chen *et al.*, "Multilayered carbon nanotube yarn based optoacoustic transducer with high energy conversion efficiency for ultrasound application," *Nano Energy*, vol. 46, no. November 2017, pp. 314–321, Apr. 2018.

[96] B. Y. Hsieh, J. Kim, J. Zhu, S. Li, X. Zhang, and X. Jiang, "A laser ultrasound transducer using carbon nanofibers-polydimethylsiloxane composite thin film," *Appl. Phys. Lett.*, vol. 106, no. 2, 2015.

[97] W. Y. Chang, W. Huang, J. Kim, S. Li, and X. Jiang, "Candle soot nanoparticles-polydimethylsiloxane composites for laser ultrasound transducers," *Appl. Phys. Lett.*, vol. 107, no. 16, pp. 1–5, 2015.

[98] M. A. Park, S. H. Lee, and J. J. Yoh, "Characterization of laser-induced ultrasound signal by reduced graphene oxide thickness and laser intensity," *Appl. Phys. B Lasers Opt.*, vol. 113, no. 3, pp. 389–393, 2013.

[99] S. H. Lee, Y. Lee, and J. J. Yoh, "Reduced graphene oxide coated polydimethylsiloxane film as an optoacoustic transmitter for high pressure and high frequency ultrasound generation," *Appl. Phys. Lett.*, vol. 106, no. 8, p. 081911, Feb. 2015.

[100] S. Link and M. A. El-Sayed, *Shape and size dependence of radiative, non-radiative and photothermal properties of gold nanocrystals*, vol. 19, no. 3. 2000.

[101] P. Warrier and A. Teja, "Effect of particle size on the thermal conductivity of nanofluids containing metallic nanoparticles," *Nanoscale Res. Lett.*, vol. 6, no. 1, p. 247, Dec. 2011.

[102] J. E. Mark, *Polymer Data Handbook*, Edition 2. Oxford University Press, 2009.

[103] R. Atif and F. Inam, "Reasons and remedies for the agglomeration of multilayered graphene and carbon nanotubes in polymers," *Beilstein J. Nanotechnol.*, vol. 7, no. 1, pp. 1174–1196, 2016.

[104] P. C. Ma, N. A. Siddiqui, G. Marom, and J. K. Kim, "Dispersion and functionalization of carbon nanotubes for polymer-based nanocomposites: A review," *Compos. Part A Appl. Sci. Manuf.*, vol. 41, no. 10, pp. 1345–1367, 2010.

[105] R. J. Colchester *et al.*, "Laser-generated ultrasound with optical fibres using functionalised carbon nanotube composite coatings," *Appl. Phys. Lett.*, vol. 104, no. 17, pp. 1–4, 2014.

[106] J. Li, X. Lan, S. Lei, J. Ou-Yang, X. Yang, and B. Zhu, "Effects of carbon nanotube thermal conductivity on optoacoustic transducer performance," *Carbon N. Y.*, vol. 145, pp. 112–118, Apr. 2019.

[107] H. W. Baac, J. G. Ok, T. Lee, and L. Jay Guo, "Nano-structural characteristics of carbon nanotube-polymer composite films for high-amplitude optoacoustic generation," *Nanoscale*, vol. 7, no. 34, pp. 14460–14468, 2015.

[108] N. Bhardwaj and S. C. Kundu, "Electrospinning: A fascinating fiber fabrication technique," *Biotechnol. Adv.*, vol. 28, no. 3, pp. 325–347, May 2010.

[109] T. Buma, M. Spisar, and M. O'Donnell, "A high-frequency, 2-D array element using thermoelastic expansion in PDMS," *IEEE Trans. Ultrason. Ferroelectr. Freq. Control*, vol. 50, no. 9, pp. 1161–1176, 2003.

[110] E. J. Alles *et al.*, "Acoustical characterisation of carbon nanotube-loaded polydimethylsiloxane used for optical ultrasound generation," in *2017 IEEE International Ultrasonics Symposium (IUS)*, 2017, pp. 1–4.

[111] ASTM-D823-18, "Standard Practices for Producing Films of Uniform Thickness of Paint, Coatings and Related Products on Test Panels," 2018.

[112] M. H. Madsen, N. A. Feidenhans'l, P.-E. Hansen, J. Garnæs, and K. Dirscherl, "Accounting for PDMS shrinkage when replicating structures," *J. Micromechanics Microengineering*, vol. 24, no. 12, p. 127002, Dec. 2014.

[113] B. Zeqiri and C. J. Bickley, "A new anechoic material for medical ultrasonic applications," *Ultrasound Med. Biol.*, vol. 26, no. 3, pp. 481–485, 2000.

[114] "Araldite LY 564 - Aradur 2954 Specifications Sheet," *Huntsman Corporation*, 2011. [Online]. Available: https://www.mouldlife.net/ekmps/shops/mouldlife/resources/Other/araldite-ly564-aradur-2954-eur-e-1-.pdf%0A. [Accessed: 30-Mar-2019].

[115] "Polycraft FC 6630," *MB Fibreglass*, 2016. [Online]. Available: http://mbfgfiles.co.uk/datasheets/fc-6630_tech.pdf%0A. [Accessed: 30-Mar-2019].

[116] "SYLGARD 84 Silicone Elastomer," *Dow Chemical Compnay*, 2017. [Online]. Available: https://consumer.dow.com/content/dam/dcc/documents/en-us/productdatasheet/11/11-31/11-3184-sylgard-184-elastomer.pdf?iframe=true%0A. [Accessed: 30-Mar-2019].

[117] "Engineering ToolBox," 2003. [Online]. Available: https://www.engineeringtoolbox.com/specific-heat-capacity-d_391.html. [Accessed: 30-Mar-

2019].

[118] N. Lee, Sang-Joon John Sundararajan, “Thermal Conductivity,” in *Microfabrication for Microfluidics*, Artech House, 2010.

[119] Kaye & Laby Online Version 1.0, “Tables of Physical & Chemical Constants (16th edition 1995). 2.1.4 Hygrometry,” 2005. [Online]. Available: www.kayelaby.npl.co.uk. [Accessed: 05-Apr-2018].

[120] Kaye & Laby Online Version 1.1, “Tables of Physical & Chemical Constants. 2.1.2 Barometry,” 2008. [Online]. Available: www.kayelaby.npl.co.uk. [Accessed: 05-Apr-2019].

[121] D. K. Hsu, F. J. Margetan, M. D. Hasselbusch, S. J. Wormley, M. S. Hughes, and D. O. Thompson, “Ultrasonic Beams with Bessel and Gaussian Profiles,” in *Review of Progress in Quantitative Nondestructive Evaluation*, vol. 9, Boston, MA: Springer US, 1990, pp. 799–806.

[122] M. Frenz, G. Paltauf, and H. Schmidt-Kloiber, “Laser-generated cavitation in absorbing liquid induced by acoustic diffraction,” *Phys. Rev. Lett.*, vol. 76, no. 19, pp. 3546–3549, 1996.

[123] R. C. Preston, Ed., *Output Measurements for Medical Ultrasound*. London: Springer, 1991.

[124] C. Koch, “Amplitude and phase calibration of hydrophones by heterodyne and time-gated time-delay spectrometry,” *IEEE Trans. Ultrason. Ferroelectr. Freq. Control*, vol. 50, no. 3, pp. 344–348, 2003.

[125] P. N. Gélat, R. C. Preston, and A. Hurrell, “A theoretical model describing the transfer characteristics of a membrane hydrophone and validation,” *Ultrasonics*, vol. 43, no. 5, pp. 331–341, 2005.

[126] S. Rajagopal, T. Sainsbury, B. E. Treeby, and B. T. Cox, “Laser generated ultrasound sources using carbon-polymer nanocomposites for high frequency metrology,” *J. Acoust. Soc. Am.*, vol. 144, no. 2, pp. 584–597, Aug. 2018.

[127] K. Wear, Y. Liu, P. Gammell, S. Maruvada, and G. Harris, “Correction for frequency-dependent hydrophone response to nonlinear pressure waves using complex deconvolution and rarefactional filtering: Application with fiber optic hydrophones,” *IEEE Trans. Ultrason. Ferroelectr. Freq. Control*, vol. 62, no. 1, pp. 152–164, 2015.

[128] S. Eichstädt, V. Wilkens, A. Dienstfrey, P. Hale, B. Hughes, and C. Jarvis, “On challenges in the uncertainty evaluation for time-dependent measurements,” *Metrologia*, vol. 53, no. 4, pp. S125–S135, 2016.

[129] S. Eichstädt and V. Wilkens, “Evaluation of uncertainty for regularized deconvolution: A case study in hydrophone measurements,” *J. Acoust. Soc. Am.*, vol. 141, no. 6, pp. 4155–4167, 2017.

[130] R. S. C. Cobbold, *Foundations of Biomedical Ultrasound*. Oxford University Press, 2007.

[131] S. Rajagopal, N. Sadhoo, and B. Zeqiri, “Reference Characterisation of Sound Speed and Attenuation of the IEC Agar-Based Tissue-Mimicking Material Up to a Frequency of 60MHz,” *Ultrasound Med. Biol.*, vol. 41, no. 1, pp. 317–333, 2015.

[132] N. Wu, Y. Tian, X. Zou, V. Silva, A. Chery, and X. Wang, “High-efficiency optical ultrasound generation using one-pot synthesized polydimethylsiloxane-gold nanoparticle nanocomposite,” *J. Opt. Soc. Am. B*, vol. 29, no. 8, p. 2016, 2012.

[133] B. T. Cox, J. G. Laufer, K. P. Kostli, and P. C. Beard, “Experimental validation of photoacoustic k-Space propagation models,” in *Photons Plus Ultrasound: Imaging and Sensing*, 2004, no. 5320, pp. 238–248.

[134] K. Wang, E. Teoh, J. Jaros, and B. E. Treeby, “Modelling nonlinear ultrasound propagation in absorbing media using the k-Wave toolbox: Experimental validation,” *IEEE Int. Ultrason. Symp. IUS*, pp. 523–526, 2012.

[135] J. Robertson, E. Martin, B. Cox, and B. E. Treeby, “Sensitivity of simulated transcranial ultrasound fields to acoustic medium property maps,” *Phys. Med. Biol.*, vol. 62, no. 7, pp. 2559–2580, 2017.

[136] B. E. Treeby, J. Jaros, A. P. Rendell, and B. T. Cox, “Modeling nonlinear ultrasound propagation in heterogeneous media with power law absorption using a k -space pseudospectral method,” *J. Acoust. Soc. Am.*, vol. 131, no. 6, pp. 4324–4336, Jun. 2012.

[137] B. E. Treeby and B. T. Cox, “k-Wave: MATLAB toolbox for the simulation and reconstruction of photoacoustic wave fields,” *J. Biomed. Opt.*, vol. 15, no. 2, p. 021314, 2010.

[138] B. E. Treeby and B. T. Cox, “Modeling power law absorption and dispersion for acoustic propagation using the fractional Laplacian,” *J. Acoust. Soc. Am.*, vol. 127, no. 5, pp. 2741–2748, 2010.

[139] B. Treeby, B. Cox, and J. Jaros, “k-Wave: A MATLAB toolbox for the time domain simulation of acoustic wave fields - User Manual,” vol. 1, 2016.

[140] M. D. Verweij, B. E. Treeby, K. W. A. van Dongen, and L. Demi, *Simulation of Ultrasound Fields*. Elsevier B.V., 2014.

[141] B. E. Treeby, E. S. Wise, and B. T. Cox, “Nonstandard Fourier Pseudospectral Time Domain (PSTD) Schemes for Partial Differential Equations,” *Commun. Comput. Phys.*, vol. 24, no. 3, pp. 623–634, 2017.

[142] B. E. Treeby, B. T. Cox, and J. Jaros, “k-Wave—A MATLAB Toolbox for the Time Domain Simulation of Acoustic Wave Fields: User Manual,” 2012. [Online]. Available: http://www.k-wave.org. [Accessed: 04-Mar-2019].

[143] J. P. Boyd, *Chebyshev and Fourier Spectral Methods: Second Revised Edition*, Second Edi. Dover Publications, 2001.

[144] Haifeng Wang, T. Ritter, Wenwu Cao, and K. K. Shung, “High frequency properties of passive materials for ultrasonic transducers,” *IEEE Trans. Ultrason. Ferroelectr. Freq. Control*, vol. 48, no. 1, pp. 78–84, 2001.

[145] “Carbon nanotube, few-walled,” *Merck KGaA, Darmstadt, Germany*, 2019. [Online]. Available: https://www.sigmaaldrich.com/catalog/product/aldrich/900788?lang=en&region=GB&cm_sp=Insite-_-prodRecCold_xviews-_-prodRecCold3-2. [Accessed: 18-Jul-2019].

[146] J. M. Hugh, J. Döring, W. Stark, and A. Erhard, “Characterisation of epoxy materials used in the development of ultrasound transducers,” in *16th World Conference on NDT*, 2004, p. Vol. 9 No.11, pp.1–8.

[147] E. Kreyszig, *Advanced Engineering Mathematics*, 10th Editi. John Wiley & Sons, 2005.

[148] B. Treeby, F. Lucka, E. Martin, and B. T. Cox, “Equivalent-Source Acoustic Holography for Projecting Measured Ultrasound Fields Through Complex Media,” *IEEE Trans. Ultrason. Ferroelectr. Freq. Control*, vol. 65, no. 10, pp. 1857–1864, 2018.

[149] A. Slotwinski, “Ultrasonic Testing,” in *Handbook of Reference Data for NonDestructive Testing*, L. Mordfin, Ed. West Conshohocken, PA: ASTM International, 2002, pp. 31–48.

[150] J. M. M. Pinkerton, “The Absorption of Ultrasonic Waves in Liquids and its Relation to

Molecular Constitution," *Proc. Phys. Soc. Sect. B*, vol. 62, no. 2, pp. 129–141, Feb. 1949.

[151] M. Ai, W. Shu, T. Salcudean, R. Rohling, P. Abolmaesumi, and S. Tang, "Design of high energy laser pulse delivery in a multimode fiber for photoacoustic tomography," *Opt. Express*, vol. 25, no. 15, p. 17713, Jul. 2017.

[152] M. D. Brown, "Optical and single element transducers for the generation of arbitrary acoustic fields," University College London, 2018.

[153] D. Razansky, A. Buehler, and V. Ntziachristos, "Volumetric real-time multispectral optoacoustic tomography of biomarkers," *Nat. Protoc.*, vol. 6, no. 8, pp. 1121–1129, Aug. 2011.

[154] P. Lum, M. Greenstein, C. Grossman, and T. L. Szabo, "High-frequency membrane hydrophone," *IEEE Trans. Ultrason. Ferroelectr. Freq. Control*, vol. 43, no. 4, pp. 536–544, Jul. 1996.

[155] "UHF-120 Ultra High Frequency Vibrometer," *Polytec GmbH*, 2019. [Online]. Available: https://www.polytec.com/fileadmin/d/Vibrometrie/OM_DS_UHF-120_E_42268.pdf. [Accessed: 04-Jul-2019].

[156] M. Cooling, V. Humphrey, P. Theobald, and S. Robinson, "The Influence of the Acousto-Optic Effect on LDV Measurements of Underwater Transducer Vibration and Resultant Field Predictions," in *4th International Conference and Exhibition on Underwater Acoustic Measurements: Technologies & Results*, 2011, p. 619.

[157] D. R. Bacon, "The improvement and evaluation of a laser interferometer for the absolute measurement of ultrasonic displacements in the frequency range up to 15 MHz," 1985.